InGaN/GaN Multiple Quantum Wells for Photovoltaics

Anna Mukhtarova

UNIVERSITÉ DE GRENOBLE

THÈSE

Pour obtenir le grade de

DOCTEUR DE L'UNIVERSITÉ DE GRENOBLE

Spécialité : **Physique/Nanophysique**

Arrêté ministériel : 7 août 2006

Présentée par

Anna MUKHTAROVA

Thèse dirigée par **Joël EYMERY** et
encadrée par **Christophe DURAND**

préparée au sein du **Laboratoire Nano-Physique et Semi-Conducteurs, CNRS/CEA/UJF-Grenoble I**
dans **l'École Doctorale de Physique**

Puits quantiques de composés nitrures InGaN/GaN pour le photovoltaïque

Thèse soutenue publiquement le **6 mars 2015**,
devant le jury composé de :

M. Christian BRYLINSKI		
Professeur d'université	Villeurbanne	Rapporteur
M. Enrique CALLEJA PARDO		
Professeur	Madrid	Rapporteur
M. Abdallah OUGAZZADEN		
Professeur	Metz	Président
Mme. Eva MONROY		
Chercheur CEA	Grenoble	Examinateur
M. Christophe DURAND		
Maitre de conférence UJF	Grenoble	Encadrant de thèse
M. Joël EYMERY		
Chercheur CEA	Grenoble	Directeur de thèse

Université Joseph Fourier / Université Pierre Mendès France /
Université Stendhal / Université de Savoie / Grenoble INP

To my husband, Vadik

Acknowledgment

My thesis wouldn’t be possible without a contribution of some people.

First of all, I would like to thank my thesis advisor Dr. Joël Eymery for his useful and detailed discussions, patience, encouragement and also for his always positive attitude that gives a lot of motivation to work.

I am very grateful to Dr. Christophe Durand for his valuable advices, precise comments and for offering a fresh perspective on the work.

I would like to thank Dr. Eva Monroy for her important remarks, always informative discussions and constant help during this thesis.

My sincere thanks go to Prof. Henri Mariette, Director of the group Nanophysics and semiconductors and Prof. Jean-Michel Gerard, Director of the division on physics of materials and microstructures of INAC, for their able leadership and creation of a friendly atmosphere in the lab.

I convey my thanks to the members of the jury: Prof. Christian Brylinski, Prof. Enrique Calleja Pardo, Prof. Abdallah Ougazzaden, and Dr. Eva Monroy for accepting to serve in the jury, despite of their busy schedule.

I would like to thank Dr. Catherine Bougerol for providing us high quality TEM data and Bruno Gayral for helping me with the optical characterization of samples. I am grateful to Dr. Stéphanie Pouget, Dr. Edith Bellet-Amalric and Dr. Vincent Favre-Nicolin for their valuable help with analysis of XRD data and diffraction experiments. My special thanks go to Jean Dussaud for supporting me with his technical expertise regarding the MOVPE system. Special acknowledgements to Carmelo Castagna and Cécile Blanc, for their indispensable help related to administrative work. I would like to thank the people working in PTA clean room CEA-Grenoble: Marlène Terrier, Thierry Chevolleau, Jean-Luc Thomassin, Frédéric Gustavo, and Delphine Constantin for their technical support and advices during fabrication process of the devices.

Also, I would like to acknowledge all people working in the lab for their help in all areas, starting from technical support to some personal advices and just for smiling at me in the hall.

My sincere acknowledgements go to Dr. Sirona Valdueza-Felip and Dr. Luca Redaeilli for their help in device fabrication and electrical characterization. Sirona, I learned a

lot from you, thanks for very useful discussions and advices, it was a pleasure to share the office with you.

Special thanks go to Akhil Ajay and Arantza Núñez-Cascajero for their help with electrical characterization and optical measurements.

I would like to say thank you to my friends, Olesia, Dilyara, Sasha, Stefania, Stéphanie, Buk, Didier, Agnès, Zhihua, Matthias, Vasya, Ira, Andrey, Katya, Tanya S., Florian, Dips, Tanya K., Volodya, Kostya, Agnezhka, Yulia, Lena, Laura, Aparna, Anya K. for their constant support, patience in listening me and some distraction from this work.

Я очень благодарна моей семье за их любовь и постоянную поддержку. И, конечно, большое спасибо моему мужу за его терпение, помощь во всем, многочисленные советы и просто за то, что он есть. Вадик, без тебя я ни за что бы не справилась, спасибо тебе за все.

Résumé

Cette thèse est consacrée au développement et à l'optimisation de cellules solaires à base de puits quantiques InGaN/GaN. Tous les échantillons utilisés dans ce travail ont été crûs sur le saphir par Épitaxie en phase vapeur à partir d'organométalliques (MOVPE).

Dans le chapitre 1 de la thèse, on donne une courte information sur l'histoire des matériaux III-V et des composants optoélectroniques basés sur ces matériaux. Les avantages et les défauts des alliages InGaN dans les applications photovoltaïques sont suivis par une explication de la motivation et des objectifs de ce travail. On finit le chapitre par une description courte de la thèse.

Le chapitre 2 décrit les propriétés générales des nitrures d'éléments III: la structure cristalline avec les valeurs de paramètres de maille, la construction de diagramme de bandes et la nature des champs piézoélectriques. Les bases de la physique des cellules solaires sont données pour une meilleure compréhension du travail accompli pendant la thèse. On explique les conceptions générales de la jonction p-n et les principaux paramètres électriques tels que la masse d'air, la tension de circuit ouvert (V_{oc}), le courant de court-circuit (J_{sc}), le facteur de forme (FF), le rendement de conversion (η), le courant de saturation (J_0) et le facteur d'idéalité (n). On présente aussi un état de l'art des cellules solaires à la base d'InGaN. On discute les nouveaux concepts pour l'augmentation de l'efficacité: cellules solaires multi-jonction et cellules solaires à la base des puits quantiques. Basé sur l'analyse de l'état de l'art et en prenant en compte la spécificité et propriétés des alliages InGaN tel que les effets liés aux champs piézoélectriques et aux contraintes. On explique le choix du design de la structure pour cellules solaires utilisé dans le cadre de cette thèse.

Le chapitre 3 propose une description des techniques expérimentales utilisées pour la croissance des échantillons et leur caractérisation structurale, optique et électrique. On présente la technique MOVPE et sa spécificité pour la croissance des nitrures: la méthode de croissance du buffer de GaN, les dopages p et n, la croissance de puits InGaN/GaN. On explique le principe de la diffraction des rayons X et les différentes configurations utilisées pour les mesures. La description générale de l'équipement XRD à haute résolution qu'on a utilisé dans ce travail est donnée. On décrit aussi le principe des mesures optiques (photoluminescence et transmission) et électriques. La suite du chapitre est focalisée sur le processus de fabrication d'une cellule photovoltaïque. On introduit les méthodes de nettoyage de la surface du GaN, la gravure plasma pour former les mesas, la photolithographie, la

métallisation et la procédure lift-off. On a étudie l'influence du flux de Cp_2Mg sur les propriétés électriques de p-GaN, ce qui a permis de trouver une valeur optimale du flux de Cp_2Mg pour une meilleure conductivité et une qualité structurale des couches p-GaN. On examine également l'influence d'espace entre deux contacts (p) sur le rendement des cellules solaires. Le design optimal des contacts p a été défini et appliqué pour les échantillons de cette thèse.

Le courant de court-circuit J_{sc} est un paramètre électrique que limite le rendement dans les cellules solaires à la base d'InGaN. J_{sc} dépend fortement de l'efficacité de l'absorption des photons. A son tour, l'efficacité de l'absorption dépend de l'épaisseur de la couche InGaN. Dans les puits quantiques, l'épaisseur de la couche InGaN doit être petite pour éviter une relaxation de contraintes et une formation des défauts dans la région active. Ainsi, l'un des moyens pour augmenter l'absorption est de mettre plusieurs puits quantiques ensemble.

Dans le chapitre 4, on étudie les échantillons avec un nombre de puits quantiques InGaN/GaN variables entre 5 et 100. Il y a deux processus principaux qu'il faut prendre en compte lors d'optimisation de la cellule solaire : absorption des photons et collection des porteurs. Au début du chapitre, on présente un modèle théorique simplifié pour comprendre l'épaisseur optimale de la région active. En prenant les paramètres (durée de vie des porteurs et leurs mobilités) dans la littérature on a estimé la valeur optimale égale 1.3 µm. La qualité cristalline des échantillons reste assez élevée malgré le grand nombre de puits. Une faible relaxation apparait pour un échantillon de 100 puits d'après les mesures HRXRD et HRTEM). Les mesures optiques montrent une augmentation des fluctuations d'indium avec le nombre de puits. Toutefois, grâce à une couche d'InGaN plus épaisse, la valeur de J_{sc} augmente en raison directe du nombre de puits pour les échantillons de 5 à 40 puits. Au-delà, la valeur de J_{sc} se sature vers 0.68 mA/cm^2. Cette saturation est liée aux pertes de l'efficacité de collection de porteurs pour les régions actives trop épaisses. L'augmentation de la recombinaison est également confirmée par la valeur de V_{oc} qui diminue pour les échantillons de 60 et 100 puits. Alors, l'épaisseur optimale de la région active obtenue par les expérimentes est moins que la valeur estimée par le modèle théorique. Cette divergence peut être expliquée par une différence des paramètres physiques qu'on a pris dans la littérature (durée de vie de porteurs et leurs mobilités) par rapport aux paramètres reels de nos échantillons. Finalement, on montre que le rendement de conversion totale s'augmente de 0.05% pour l'échantillon de 5 puits à 0.88% pour l'échantillon de 60 puits.

Le chapitre 5 présente une étude sur l'influence des différents paramètres de la région active (l'épaisseur de barrière, l'épaisseur des puits et la composition d'In dans les puits) sur

les propriétés structurales, optiques et électriques des échantillons à base de puits InGaN/GaN.

L'augmentation d'épaisseur de puits induit l'approfondissement des niveaux énergétiques dans les puits et décale la longueur d'onde d'absorption vers le rouge. Malgré une basse composition d'In (~12%), la relaxation de contraintes apparait pour les échantillons avec des puits plus épais que l'épaisseur critique (3nm dans ce travail). Cela provoque une formation de défauts et une dégradation de la qualité de la région active. Les nombreux défauts représentent les centres de recombinaison pour les porteurs et réduisent V_{oc}. L'approfondissement des niveaux énergétiques empêche les porteurs de sortir des puits limitant l'efficacité quantique externe du dispositif. Ainsi, la meilleure valeur du rendement de conversion de 0.49% est obtenue pour les puits les plus fins (1.3 nm).

On analyse également l'influence de la composition d'In sur les propriétés structurales, optiques et électriques. On a augmenté la composition d'In jusqu'à 18% en réduisant la température de croissance et en augmentant le flux de TMIn. Augmentation de la composition d'In induit un décalage de 50 nm de la longueur d'onde d'absorption vers le rouge. Les mesures optiques montrent une augmentation de fluctuations d'In dans les échantillons. En même temps, grâce à une amélioration de l'absorption, la valeur de J_{sc} a été considérablement augmentée jusqu'a 2 mA/cm^2 pour plusieurs dispositifs. Cependant, l'efficacité quantique externe des échantillons riches In était inférieure à celle des échantillons avec 10% d'In. Cela montre une difficulté d'extraction des porteurs pour les puits les plus profonds.

L'extraction de porteurs du puits se réalise par émission thermique et par effet tunnel. L'augmentation de la profondeur des puits diminue la probabilité d'extraction thermique pour les porteurs. Alors, il est nécessaire de stimuler l'extraction de porteurs par l'effet tunnel. Pour vérifier cette hypothèse les échantillons avec différentes épaisseurs de barrière ont été crûs. Le courant de court-circuit J_{sc} a été augmenté avec une diminution d'épaisseur de barrière justifiant un renforcement de l'effet tunnel dans le J_{sc}. La meilleure valeur de rendement de conversion a été obtenue pour un échantillon avec des barrières les plus fines (3.7 nm).

Dans le chapitre 6, on résume les résultats de ce travail et on donne la structure optimisée pour l'obtention de meilleures performances. Le rendement maximal obtenu dans le cadre de la thèse est de 2.00% pour puits quantiques $15\times In_{0.18}Ga_{0.82}N$/GaN crûs sur saphir (0001). Ce rendement est comparable avec l'état de l'art actuel (2.95% pour $12\times In_{0.35}Ga_{0.65}N$/GaN crûs sur saphir [Dahal, 2010]). Les perspectives de continuation de ce travail sont également proposées.

Content

Chapter 1

Introduction

1.1 Short history of nitride-based materials

The semi-conductor group of III-nitrides is widely used in many areas of our modern life: light-emitting diodes (LEDs), lasers, ultraviolet detectors, high electron mobility transistors (HEMTs)… and it is only the beginning of the list of all their possible applications. Before starting an active exploitation of the nitride-based materials, it was necessary to understand their properties and solve several material problems to create operational devices.

The first deposition of gallium nitride (GaN) grown by hydride vapor phase epitaxy and suitable for optical and electrical characterization was demonstrated by Maruska and Tietjen in 1969 [Maruska, 1969]. They estimated the value of a direct band gap E_g = 3.39 eV and carrier concentration $n = 10^{19}$ cm^{-3} for undoped GaN layer. Such a high value of background n-doping was attributed all this time to a high density of nitrogen vacancies. Different methods were employed to improve the structural quality of GaN films. The most successful one was proposed by Nakamura *et al*. and included the growth of a low-temperature GaN buffer layer to filter dislocations formed at the GaN/sapphire interface. Using this way of GaN layer growth, Nakamura *et al*. were able to achieve a very high electron mobility of 900 cm^2/Vs and a relatively low background electron concentration $n \approx 2\times10^{16}$ cm^{-3} [Nakamura(1), 1992]. In spite of improved quality, it was still difficult to obtain p-type conductivity in GaN samples. This fact was explained by the influence of hydrogen that forms acceptor-H complexes in p-doped GaN film causing hole compensation [Nakamura(2), 1992]. Post-growth thermal annealing of Mg-doped GaN samples under N_2 was applied to destroy these complexes allowing to reach hole concentration $p = 3\times10^{17}$ cm^{-3} and hole mobility of 10 cm^2/Vs [Nakamura(3), 1992]. Thanks to the successful growth of p- and n-type GaN layers Amano *et al.* demonstrated the first LED based on p-n GaN junction [Amano, 1989]. Later, LED structure was further improved by insertion of InGaN layer between n- and p-GaN. LEDs based on a single InGaN quantum well and emitting different colors (blue, green and yellow) were demonstrated by Nakamura *et al.* in 1995 [Nakamura, 1995]. The colors were adjusted by changing the In-composition from 20 to 70% in the alloy. In 2014 the Nobel prize

has been awarded to I. Akasaki, H. Amano and S. Nakamura "for the invention of efficient blue light-emitting diodes which has enabled bright and energy-saving white light sources". Currently, InGaN is the usual material used in modern blue and green LEDs.

A long time ago, it was believed that the band gap of InN is about 1.9 eV. In 2002 several studies confirmed the band gap to be close to 0.7 eV [Davydov, 2002; Wu, 2002]. It means that InGaN is one of the few systems that can provide band gaps from 0.7 (InN) to 3.4 eV (GaN). The adjustment of the band gap could be directly realized by changing In composition in InGaN alloys. Figure 1.1 shows the comparison of the band gap and lattice parameter values for different groups of semiconductors.

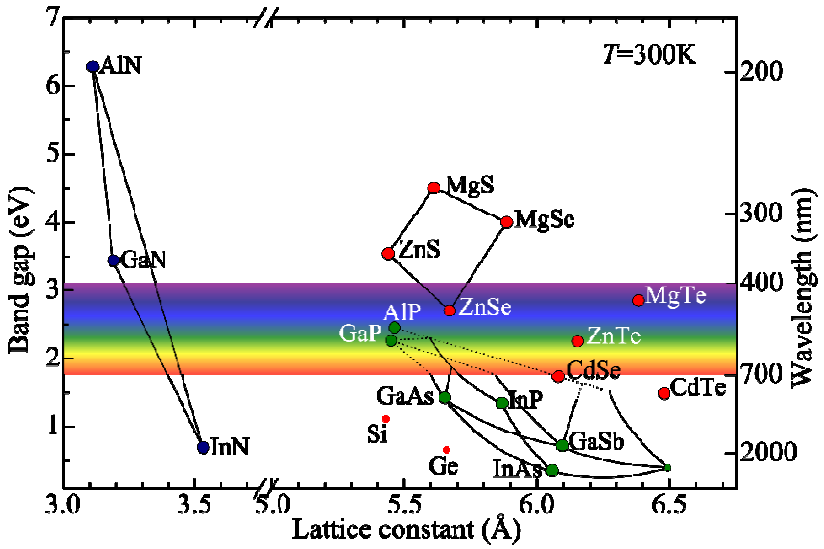

Figure 1.1. Band gap energy versus lattice constant for different groups of semiconductors.

From Figure 1.1, it can be seen that the range of energies covered by InGaN alloys perfectly corresponds to the solar spectrum. Therefore, one more possible application for InGaN materials was proposed: solar cells.

1.2 InGaN for photovoltaics: advantages and challenges

In addition to the appropriate band gap covering most of the solar spectrum, InGaN has other advantages to be applied in solar cells. Thanks to a direct band gap, the absorption coefficient of InGaN alloys is very high and reaches ~10^5 cm^{-1} for a photon energy of ~0.5 eV above the absorption edge for all range of In compositions [Wu, 2002]. Moreover, Wu *et al.* showed that optical and electronic properties of InGaN alloys have a very high resistance to high-energy photon irradiation (2 MeV) much better than what is currently used in GaAs and

GaInP solar cell materials [Wu, 2003]. This makes InGaN a good candidate in the radiation-hard solar cells for space applications. High thermal stability of the electrical and optical properties of InGaN demonstrated by Shen *et al.* makes possible the use of this material in solar cells working under concentrated light [Shen, 2012]. In addition, Hsu *et al.* showed that addition of the p-n $In_{0.46}Ga_{0.54}N$ junction to p-n Si solar cell can improve the energy conversion efficiencies of more than 50% compared to solar cell composed of only Si (27% vs 17%). Moreover, the alignment of Si valence band with $In_{0.46}Ga_{0.54}N$ conduction band obviates the necessity for heavy doping at the InGaN/Si heterointerface [Hsu, 2008].

In spite of all listed above advantages, very poor quality of In-rich InGaN layers limits its expansion in the solar cell market. This quality degradation is related to the features of InGaN material listed hereafter:

Lattice mismatch

Unfortunately, there is no lattice-matched substrate for the growth of InGaN III-nitrides and sapphire remains the most commonly used. But, a large lattice mismatch (29% between InN and sapphire and 14% between GaN and sapphire) creates a lot of defects at the InN, GaN/sapphire interface damaging the material quality. GaN thick template layer is usually grown to match the materials by dislocation bendings and annihilation. Although the lattice mismatch between InN and GaN is lower (only 11%) compared to GaN/sapphire and InN/sapphire, it is still enough to provoke strains at the GaN/InGaN interface [Lu, 2003]. There is a critical thickness for InGaN layers above which the strains are relaxed forming dislocations. This critical thickness is very low for InGaN grown on GaN substrate and reaches less than 5 nanometers for In compositions more than 20% [Holec, 2008]. Once the critical thickness is reached, threading dislocations are formed, degrading the device performance. These threading dislocations may terminate at the layer surface as V-defects and absorb photons above and below the InGaN band gap, resulting in a shadowing of the solar cells [Kim, 1998]. One of the possible ways to overcome this difficulty is to replace a thick InGaN layer with multi-quantum wells (MQWs) or superlattices (SL) keeping the QW thickness below the critical one.

Phase separation and In fluctuations

A large difference in interatomic spacing and chemical affinity between InN and GaN causes a solid phase miscibility gap and phase separation in InGaN materials [Ho, 1996]. Phase separation is a formation of micro- or nano-scale regions with high In-content within

the layer [Oliver, 2010]. These small regions behave like recombination centers decreasing the carrier lifetime and reducing the device performance. Optimization of the growth conditions (decrease of the growth rate for InGaN layers with low In composition and increase of the growth rate for high In compositions, decreasing the growth temperature) of the samples and their active region design (growing of the strained layers) can help to suppress the phase separation [Pantha, 2010; Singh, 1996; Yamamoto, 2014].

Fluctuations of In-content are also an important issue for PV devices. Composition fluctuations, which create local variation of the electron potential can be considered as beneficial in the operation of violet and blue LEDs. However, for photovoltaic applications, Lai *et al.* showed that carriers trapped in the shallow quantum wells created by In fluctuations, significantly reduce the value of solar cell fill factor causing device performance degradation [Lai, 2010].

Low In incorporation

Because of a weak In-N bond strength and high In volatility, relatively low temperatures (700–800 ^{0}C in MOCVD and 550–650 ^{0}C in MBE machines) are needed to grow InGaN alloys with high In-content [MacChesney, 1970]. There are two ways to enhance In incorporation: increase the indium flow and decrease the growth temperature. The increase of indium flow is generally not effective and causes the formation of In droplets on the sample surface [Guo, 2010]. The increase of In incorporation decreasing the growth temperature occurs at the price of the crystalline quality. This problem is especially critical for the layers grown by metal-organic vapor phase epitaxy (MOVPE). Low growth temperatures reduce the cracking efficiency of ammonia (NH_3) that is a main source of nitrogen in most MOVPE machines [El Gmili, 2013]. This results in an increase of nitrogen vacancies inside the InGaN layer causing a low quality of grown InGaN film.

1.3 Motivation and targets

Since 2009, the solar cell industry has been rapidly growing more than 30% per year. But, in spite of the fast increase, the solar energy production makes less than 1% of the overall produced energy. The limited utilization of the solar energy is partly related to its high cost.

Levelized Cost of Electricity (LCOE) is a method to compare the prices of different energy technologies. It shows the ratio between the expected cost of the system during its lifetime (including construction, financing, fuel, maintenance, taxes, insurance etc) and the working lifetime of this system for a given technology.

Figure 1.2 shows the dependence of LCOE in Germany for different electricity sources. This study was done by Fraunhofer Institute for Solar Energy Systems (ISE) for the 2013 year.

LCOE for photovoltaic panels varies from 0.078 to 0.142 €/kWh that is 2 times more expensive than coal: brown coal costs from 0.038 to 0.053 €/kWh and hard coal costs 0.063 – 0.08 €/kWh. One of the ways to decrease the cost of the solar cells is to improve their performance. Currently, photovoltaic market is dominated by photovoltaic panels based on crystalline silicon. However, Si modules are limited to a maximum efficiency of 20% in production.

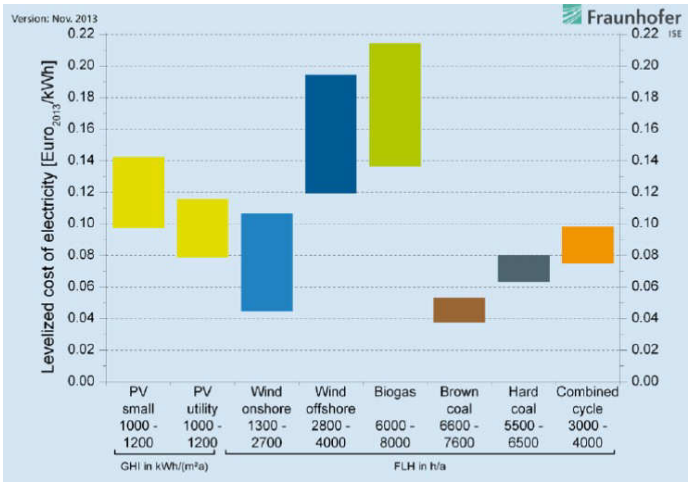

Figure 1.2. Levelized Cost of Electricity of renewable energy technologies and conventional power plants in Germany for 2013 [http://www.ise.fraunhofer.de/en/publications/studies/cost-of-electricity].

Figure 1.3 shows the development of solar cells in terms of conversion efficiency. The statistics is made by the National Renewable Energy Laboratory (NREL), Golden, USA. The highest values of efficiency are obtained with several-junction III-V solar cells under concentrated sunlight. Current efficiency record is held by a four-junction solar cell based on III-V semiconductors at 44.7% under concentrated light (297 Suns) (Fraunhofer Institute for Solar Energy Systems (ISE), Soitec, CEA-Leti and Helmholtz Center Berlin, 2013). This value is close to the predicted achievable theoretical limit of 49.6% [Bhuiyan, 2012]. Approaching to the 50% efficiency requires an exploration of new materials and device designs.

Theoretical simulations of the multi-junction solar cell showed that, over four-junction device, a material with a band gap larger than 2.4 eV is required [Bhuiyan, 2012]. Indium Gallium Nitride demonstrated properties that can be promising for its further use in photovoltaic applications, particularly as material for absorption of high-energy photons (> 2.4 eV) in multi-junction solar cells. Low quality of InGaN layers hinders the development of InGaN-based photovoltaics. But the electrical performance of the InGaN-based solar cells can be improved by an accurate choice of the active region design.

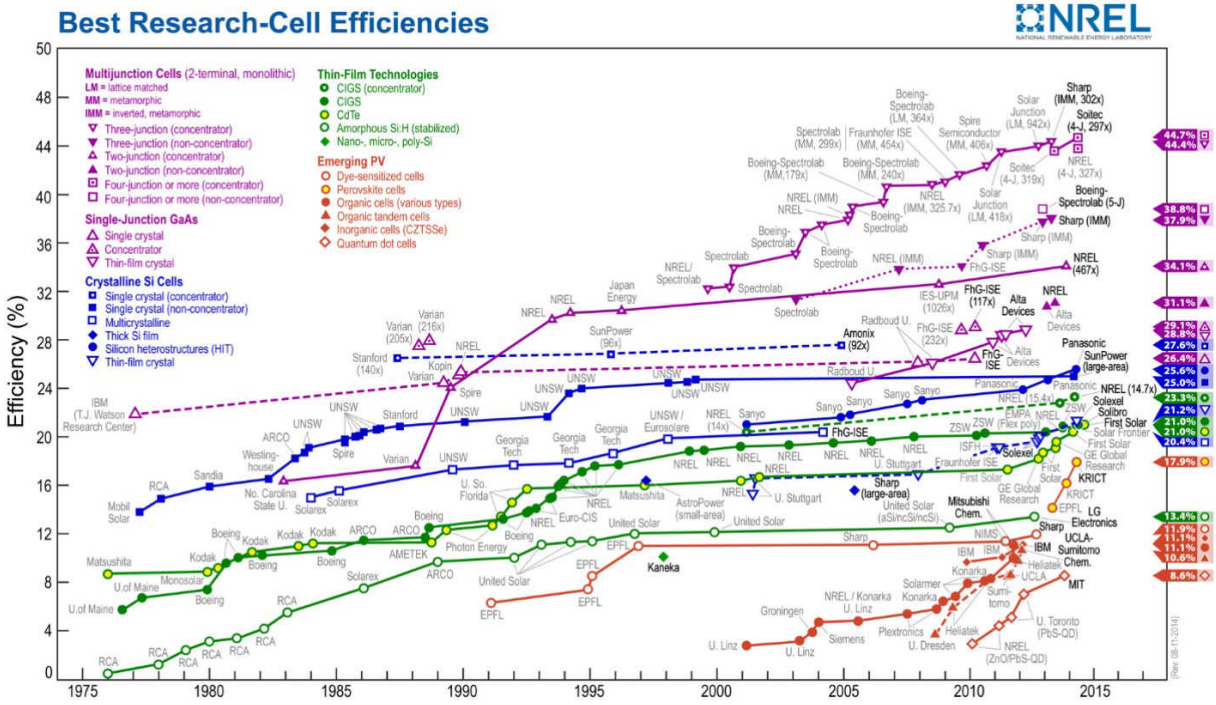

Figure 1.3. The evolution of the solar cell performance [http://www.nrel.gov/ncpv/].

Therefore, in the frame of this thesis, we focus on the epitaxial growth and investigation of different active region designs and their influence on structural, optical and electrical properties of InGaN solar cells. The aims of this work are:

- the optimization of the growth of InGaN/GaN MQWs on (0001) sapphire substrate by MOVPE and their structural characterization
- the fabrication of the devices and their electrical characterization
- the investigation of the influence of the different structure designs on crystalline, optical and electrical properties of the solar cells
- the solar cell structure optimization in order to obtain the maximum conversion efficiency
- the discussion of the use of this solution in different device applications

In this work, all samples were grown by metal-organic vapor phase epitaxy (MOVPE) on *c*-plane sapphire substrate. InGaN/GaN quantum wells were chosen as an active region in order to limit the phase separation and reduce the number of defects in InGaN layers. X-ray diffraction (XRD), photoluminescence spectroscopy (PL) and atomic force microscopy (AFM) were carried out to assess the structural quality of the samples. Additional data to extend the structural and optical characterization was provided by transmission electron microscopy (TEM) performed by Dr. Catherine Bougerol, phototransmission measurements carried out by Dr. Sirona Valdueza-Felip, Dr. Luca Redaelli, master student Akhil Ajay and PhD student Arantza Núñez-Cascajero, capacitance-voltage measurements to obtain the carrier concentration of p-GaN layers were performed by Dr. Christophe Durand and Hall measurements were done by our collaborators from CEA-LETI Dr. Walf Chikhaoui. A help with HR-XRD measurements at the European Synchrotron Radiation Facility (ESRF) has been provided by Dr. Vincent Favre-Nicolin.

After the structural characterization, samples were processed into devices in clean room CEA-Grenoble (PTA, Plateforme Technologique Amont) by Dr. Sirona Valdueza-Felip and Dr. Luca Redaelli. To investigate the solar cell performance, electrical characterization of the devices such as responsivity measurements and preliminary electrical measurements of *J(V)* curves were carried out by Dr. Sirona Valdueza-Felip, Dr. Luca Redaelli and master student of University of Grenoble Akhil Ajay. Capacitance-voltage measurements have been performed by Dr. Sirona Valdueza-Felip. Finally, the measurements of the solar cell *J(V)* curves under 1 Sun AM1.5G illumination were done in CEA-LITEN by Dr. Sirona Valdueza-Felip, Dr. Louis Grenet, Dr. Giovanni Altamura and Dr. Luca Redaelli. Also, part of the *J(V)* curve measurements under 1 Sun AM1.5G illumination were performed in the frame of our collaboration with Dr. Jérôme Faure-Vincent from the laboratory Structures et Propriétés d'Architectures Moléculaires (SPRAM) CEA, INAC by Dr. Sirona Valdueza-Felip, Dr. Luca Redaelli and master student of university of Grenoble Akhil Ajay. I have also parcticipated in processing of some samples into devices and carried out their following electrical characterization.

1.4 Organization of the manuscript

This manuscript is divided in six chapters:

- **Chapter 1** presents a short history of the III-nitride materials and their expansion in the LED market. The interest of InGaN alloys in photovoltaics is explained, clarifying the main advantages and challenges on the way to effective InGaN-based solar cells. Motivation and main targets of this work are also described.

- **Chapter 2** introduces the main definitions and concepts of the solar cell physics to understand the device behaviour. General properties of the III-nitrides in terms of crystalline and electronic structure as well as a discussion about the origin of the piezoelectric fields are presented. The chapter finishes with the current state-of-the-art of InGaN-based solar cells. The choice of the structure design of the devices developed in this work will also be explained.

- **Chapter 3** presents the MOVPE deposition technique and the main issues related to the MOVPE III-nitrides growth. General techniques are presented such as X-ray diffraction, photoluminescence and transmission spectroscopy, responsivity measurements that were used to assess the structural and electrical properties of the solar cells together with its basic concepts. Main steps of the device fabrication process (photolithography, inductively plasma etching (ICP), contact deposition) are discussed. Finally, the choice of the materials to form contacts and the choice of the contact design are explained.

- **Chapter 4** describes the optical and structural properties of $In_{0.1}Ga_{0.9}N$/GaN multiple quantum wells (supposedly completely strained layers with low density of structural defects). Influence of the quantum well number on photovoltaic properties is investigated. A simplified theoretical model is developed in order to understand the processes happening inside the p-i-n junction with the increase of the active region thickness. Advantages and disadvantages of the thick active region for solar cell application is discussed.

- **Chapter 5** investigates the ways of the device performance improvement by optimizing the active region design. Several series of samples are grown varying the quantum well and quantum barrier layer thicknesses and In-composition. The influence of the active region parameters on the structural quality, optical and electrical properties of the InGaN/GaN QW-based samples are discussed.

- **Chapter 6** summarizes the main results obtained in the frame of this thesis for InGaN/GaN QW-based solar cells. Based on the obtained results, an optimal structure design is proposed. Several perspectives for further structure optimization that were not done in this work are suggested and discussed.

Chapter 2

III-nitride semiconductors for photovoltaics

In this chapter we will consider firstly the basics of the solar cell physics, i.e. general processes that take place in a p-n junction, and the main electrical parameters that define the photovoltaic performance. In the second part, we will briefly review the structural and electronic properties of III-nitrides followed by the discussion on the polarity and origin of the spontaneous and piezoelectric polarization. Finally, we summarize the current state-of-the-art of InGaN-based materials for photovoltaic applications. The choice of the structure design for samples grown in this work will be also explained.

2.1 Basics of solar cells

2.1.1 Solar spectrum, air mass and absorption by semiconductors

The energy for solar cells comes directly from the sunlight composed of energetic particles called photons. Every photon has its own energy that depends on the wavelength of the incoming light and can be expressed through the Planck-Einstein relation:

$$E = hc/\lambda, \tag{2.1}$$

where h - Planck constant ($h = 4.135\times10^{-15}$ eV·s), c - speed of light ($c = 3\times10^{8}$ m/s), and λ - light wavelength.

Figure 2.1 shows the dependence of the spectral power density on the photon energy for a black body with temperature of 6000 K compared with the spectral power density of the Sun in the space and on the Earth surface. The maximum of emission spectrum depends on the irradiation source temperature. For the black body with T = 6000 K, the maximum is at $\lambda \approx$ 500 nm that corresponds to a photon energy of E = 2.48 eV. The total power density of the solar radiation outside the atmosphere at the mean Earth-Sun distance on a plane perpendicular to the direction of the Sun is 1353 W/m^2. Deep fails in the solar spectrum intensity at the Earth surface (AM1.5 radiation) are related to the light absorption: in infrared region by water vapor (H_2O), carbon dioxide (CO_2), nitrous oxide (N_2O), methane (CH_4), etc., and in ultraviolet region by ozone and oxygen.

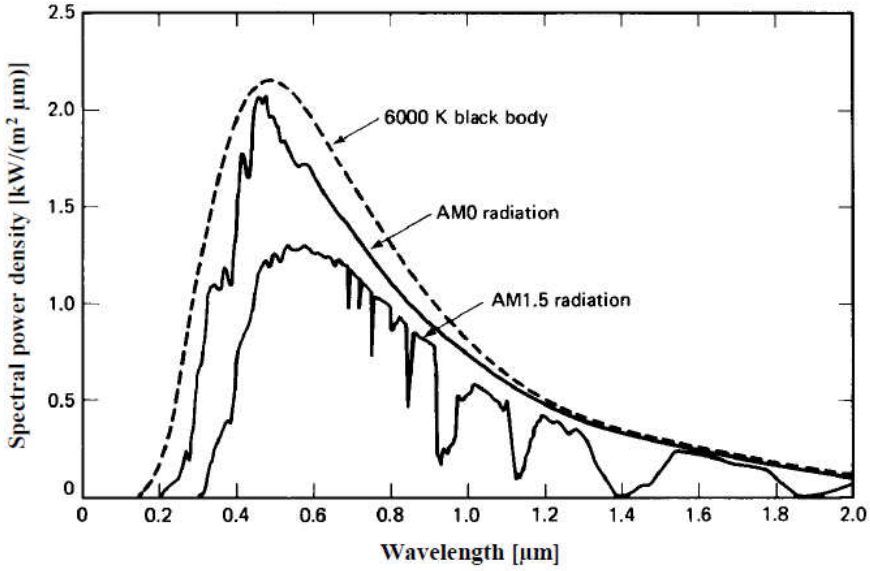

Figure 2.1. Spectral power density of the Sun as a function of the wavelength: on the Sun surface (dotted line), in the space (AM0 radiation) and on the Earth surface (AM1.5 radiation) [Green, 1982].

The absorption increases with the mass of air through which the radiation goes. The air mass coefficient is used to take into account the change of the solar spectrum intensity with the mass of air it passes. It presents the ratio between the actual path length of the sunlight through atmosphere l to the minimal distance l_0:

$$\text{Air mass} = (\cos \alpha)^{-1} = l/l_0, \qquad (2.2)$$

where α is an angle of the Sun to the zenith. For example, if the Sun is 60^0 to the zenith, the air mass is called AM2. AM0 corresponds to the solar spectrum outside the atmosphere. To allow a comparison between different solar cells, AM1.5 was chosen as a standard that corresponds to an angle of 48.8^0 between Sun position and zenith.

The sunlight coming to the Earth can be divided in two components: direct (the light that comes directly from the Sun to the Earth) and diffuse (the sunlight that was scattered by atmosphere). There is a special abbreviation to indicate these components. AM1.5G means a global radiation (takes into account all sunlight components) and AM1.5D (takes into account only direct radiation). Normally, AM1.5G is used as a standard and it gives a solar irradiance of 970 W/m^2. For convenience, this value was normalized to 1000 W/m^2 (1 Sun).

Photons coming to the semiconductor surface can be absorbed only if their energies are equal or higher than the band gap of the semiconductor (Figure 2.2). But if photons have energy larger than the semiconductor band gap, the excess of energy is lost and transformed into heat through electron-phonon interactions.

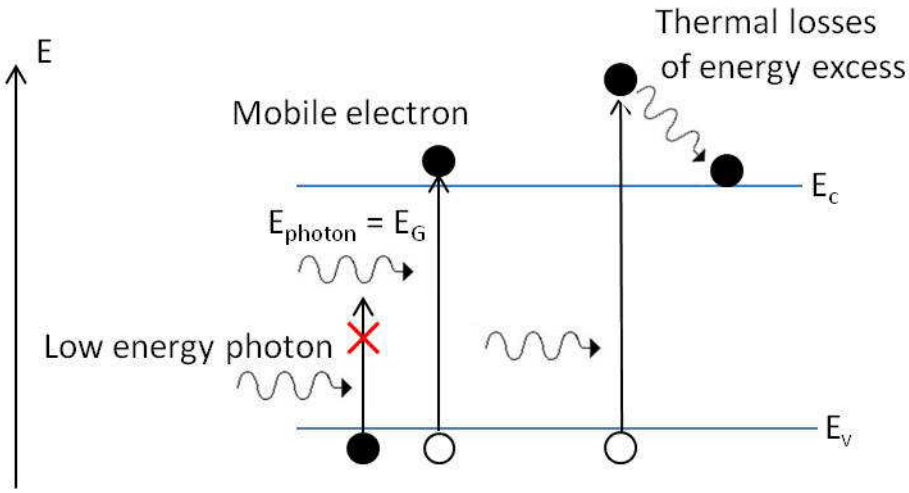

Figure 2.2. Absorption of incoming photons with creation of electrons in the conduction band.

Incoming photons, even if they have an appropriate energy to be absorbed, can also be reflected or transmitted. These photons are considered as lost as they do not create any electron-hole pairs. To decrease the photon reflection, different surface designs are applied to the solar cell, such as texturing and roughening, or introducing antireflection coatings [Bae, 2011; Farrell, 2011; Young, 2014]. To decrease the photon transmission, an appropriate thickness of the absorbed layer should be chosen. This absorption thickness can be determined, knowing the absorption coefficient[*] α of the material, via the Beer-Lambert law:

$$I(x) = I(0)e^{-\alpha x}, \quad (2.3)$$

where $I(x)$ - light intensity transmitted through material, $I(0)$ - incident light intensity, α - absorption coefficient and x – thickness of absorption layer. As an example, for an InGaN layer with $\alpha \approx 10^5$ cm^{-1}, 95% of the incoming light will be absorbed in the first 300 nm [Wen, 2007].

[*] Absorption coefficient determines how far the light can penetrate the material without being absorbed.

2.1.2 P-n junction

Usual solar cells are based on a p-n junction, meaning joining two semiconductor materials with different p- and n-type doping. We will call them homojunctions if the junction is formed by the same material and heterojunction if two different materials are used. For simplicity, we will consider only p-n homojunction basics.

In the dark

The band diagrams of two differently doped semiconductors before and after connection are shown in Figure 2.3.

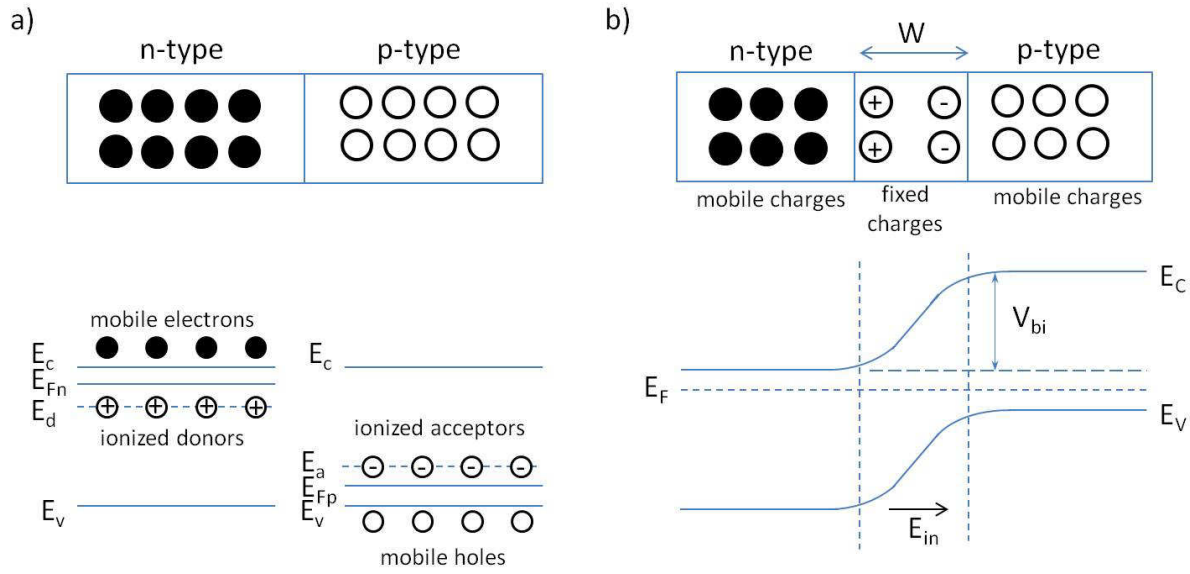

Figure 2.3. Band diagrams of p- and n-type semiconductors: a) before and b) after connection.

When p- and n-type semiconductors are connected together, electrons from n-type semiconductor diffuse towards p-type, leaving behind positive charges, holes from p-type semiconductor diffuse to n-type leaving behind negative charges. The charges left after leaving of major carriers produce the difference of the electric potentials (built-in or internal electric field) close to the semiconductor interface that accelerate carrier diffusion. In the band diagram this potential difference is shown as a barrier for diffusing carriers (Figure 2.3 (b)). The height of this energy barrier is equal to the difference in work functions of both semiconductors and called the built-in voltage:

$$V_{bi} = \frac{1}{q}\left(\Phi_n - \Phi_p\right), \tag{2.4}$$

where V_{bi} - built-in voltage, q – electron charge, Φ_n and Φ_p – work functions of n- and p-type semiconductors. Equilibrium is reached when the Fermi levels of both semiconductors are aligned (Figure 2.3 (b)).

The space free of mobile electric charges that is formed at the semiconductor interface by electric field is called the depletion region. Ionized donors or acceptor impurities are the only electric charges inside this zone. As the depletion region has no free carriers inside, it is highly resistive compared to n- and p-doped parts. The final net potential is the difference between internal and applied electric potentials. The following formula is used to calculate the depletion width inside the p-n junction:

$$W = \sqrt{\frac{2\varepsilon_r \varepsilon}{q}\left(\frac{1}{N_a} + \frac{1}{N_d}\right)(V_{bi} - V)}, \tag{2.5}$$

where N_a, N_d – acceptor and donor concentrations, ε_r – relative dielectric permittivity of the semiconductor, ε – dielectric permittivity of the air, V – applied voltage.

From Eq. (2.5), we see that the depletion width depends on the carrier concentration in both semiconductors. Higher carrier concentration results in a smaller depletion width. The width of the depletion region can also be changed by applying the external bias. Figure 2.4 describes the band diagrams of p-n junction under applied forward and reverse bias.

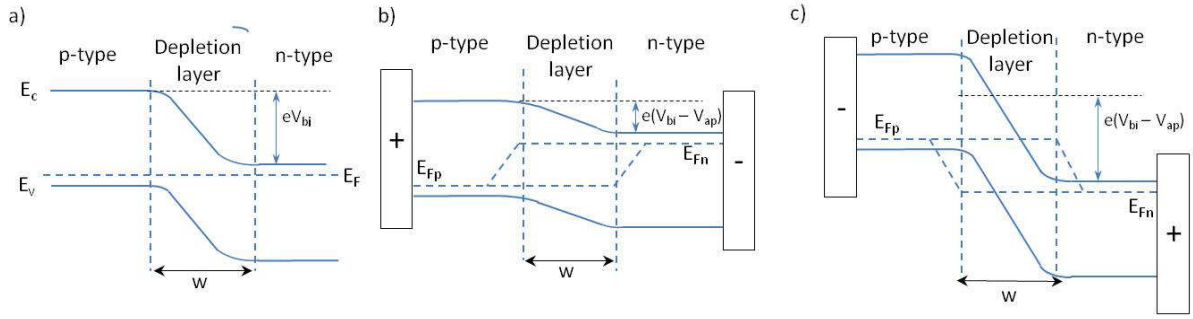

Figure 2.4. Energy band diagram for p-n junction: a) without applied bias; b) under forward bias; c) under reverse bias.

When an increasing forward bias is applied to p-n junction (positive voltage is applied to p-type and negative voltage to n-type semiconductor), the major carriers (holes in p-type and electrons in n-type) are pushed towards the semiconductor interface, reducing the width of the depletion region untill it is completely eliminated. In the reverse bias regime, the carriers are attracted towards the undepleted zone and pulled away from the junction. It induces an increase of the depletion width and energy barrier for carrier diffusion. Therefore, a very small current will flow through the junction, that is called the dark saturation current

J_0. At very high reverse voltage, a carrier leakage through the p-n junction appears. This breakdown process is usually reversible, if the current did not reach a value high enough to overheat the sample and destroy it. The typical current-voltage dependence for p-n junction in the dark is presented in Figure 2.5.

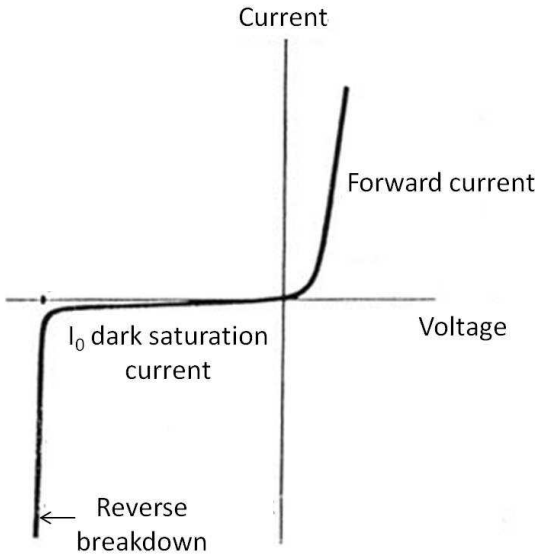

Figure 2.5. Typical current-voltage dependence for p-n junction in the dark.

Under illumination

When the p-n junction is illuminated, light creates hole-electron pairs in the all three regions (depleted, p-doped and n-doped regions). Electrons and holes photogenerated in the depletion region are separated by the built-in electric field (drift transport) giving rise to a photocurrent. This implies that it is preferable to have a depletion region larger than the absorption length. Electron-hole pairs photogenerated in the p- or n- regions can still contribute to the photocurrent, provided they are generated within one diffusion length of the depletion region. If electron-hole pairs are created at a distance much farther than their diffusion length L from the depletion region, they recombine and do not participate in the creation of useful current. Diffusion length is the average distance that carriers can move before they recombine, and it is defined as a square root of the product of diffusion coefficient and the carrier lifetime:

$$L_{n(p)} = \sqrt{D_{n(p)}\tau_{n(p)}}, \tag{2.6}$$

where $D_{n(p)}$ is the diffusion coefficient of electrons (holes) and $\tau_{n(p)}$ is the electron (hole) lifetime. Using the Einstein relation, we can express $D_{n(p)}$ through carrier mobility $\mu_{n(p)}$ ($D_{n(p)} = \mu_{n(p)}kT/q$). So, we obtain for diffusion length the following equation:

$$L_{n(p)} = \sqrt{\frac{\mu_{n(p)}kT}{q}\tau_{n(p)}}, \tag{2.7}$$

where k is the Boltzmann constant, T is the temperature, q is the electron charge.

The diffusion length depends on the lifetime and mobility of the carriers and can be different for electrons and holes. If carriers are created at a distance lower than the diffusion length from the depletion region, they can diffuse there, be separated by the internal electric field and driven to the regions where they become major carriers (therefore, electrons are driven towards the n-zone and holes towards the p-zone). Figure 2.6 depicts the current-voltage dependence for a solar cell under illumination.

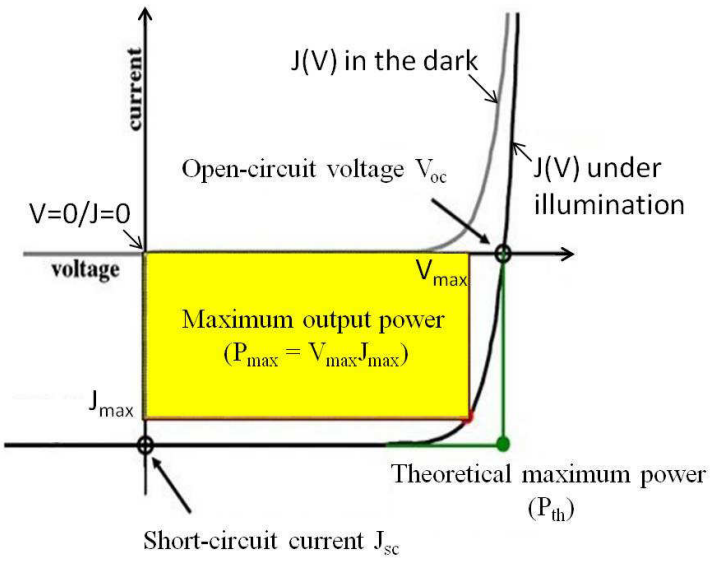

Figure 2.6. Current-voltage dependence for ideal solar cell under illumination.

Applying forward bias to illuminated p-n junction, the potential barrier decreases (as in the case of p-n junction in the dark) resulting in the diffusion of carriers. As long as the diffusion current is small, the total current is almost constant and depends on the current induced by illumination. With a voltage increase, the barrier that prevents the carrier diffusion becomes so small that most of the carriers are able to overcome it. Then, the diffusion current increases with the voltage and becomes dominant. A forward bias induces a decrease of the electric field inside the p-n junction leading to the reduction of the depletion zone and losses in collection efficiency.

At reverse bias, the p-n junction under illumination behaves the same as a p-n junction in the dark. The current induced by light flows untill the voltage becomes too high and breaks down the p-n junction.

There are two particular points on the *J(V)* curve under illumination (Figure 2.6): the current that flows at V = 0V is called the short-circuit current (J_{sc}), and the voltage at which the current becomes 0 is called the open-circuit voltage (V_{oc}). The value of V_{oc} is related to the value of J_{sc} by the following formula:

$$V_{oc} = \frac{nkT}{q} \ln\left(\frac{J_{sc}}{J_0} + 1\right), \tag{2.8}$$

where n – ideality factor, J_{sc} – short-circuit current, J_0 – saturation current.

The ideality factor represents the difference between the behaviors of the ideal diode and that of the real diode. For ideal diode with no recombination n = 1. If recombination within the depletion region occurs, then n = 2. Normally, ideality factor has a value less than 2, but in heterojunctions based on nitride-based materials (for example for solar cells based on InGaN/GaN quantum wells), the ideality factor is reported to be anomalously high (> 2) [Zhu, 2009]. Fedison *et al.* explained such a large ideality factor by an additional recombination through deep-level-assisted tunneling. Deep levels inside a band-gap can be formed by defects such as nitrogen vacancies, dislocation resulting from the lattice mismatch, etc [Fedison, 1998]. One more explanation was proposed by Shah *et al.*, who developed a theoretical model showing that the final ideality factor comes from a sum of ideality factors of the individual rectifying heterojunctions inside the structure [Shah, 2003]. The value of ideality factor can be estimated from *J(V)* curves in the dark when plotting *ln(J)* versus *V*, according to Eq. (2.8) the slope gives *q/nkT*.

While J_{sc} changes slightly from one device to another, the value of saturation current J_0 can be changed in orders of magnitude, since it is strongly related to the quality of the material. J_0 can be calculated as:

$$J_0 = Aqn_i^2 \left(\frac{D_n}{L_n N_a} + \frac{D_p}{L_p N_d}\right), \tag{2.9}$$

where A – cross-sectional area of the device, q – electron charge, n_i – intrinsic carrier concentration, D_n, D_p – diffusion coefficients of electrons and holes, L_n, L_p – diffusion lengths of electrons and holes, N_a, N_d – acceptor and donor concentrations.

2.1.3 Conversion efficiency and parasitic resistances

Conversion efficiency is the main parameter that allows comparing the performance of different solar cells. There are three types of efficiency that can be used for the description of solar cells: internal quantum efficiency (IQE), external quantum efficiency (EQE) and conversion efficiency (η).

- **Internal quantum efficiency** shows the ratio between the number of absorbed photons at a given energy and the number of collected electrons;
- **External quantum efficiency** corresponds to the ratio between the number of incident photons at a given energy and the number of collected electrons;
- **Conversion efficiency** is the ratio between the electrical power that is given by the solar cell and the incoming power of the incident light.

Conversion efficiency strongly depends on the intensity of incoming light and the temperature of the solar cell. Therefore, it was standardized to measure the conversion efficiency at 25 $^{\circ}$C and at irradiance of 1000 W/m^2 (1 Sun) with AM1.5 conditions. We can determine the value of conversion efficiency using main electrical parameters of solar cell derived from the *J(V)* curves:

$$\eta = \frac{J_{sc}V_{oc}FF}{P_{in}}, \tag{2.10}$$

where J_{sc} – short-circuit current, V_{oc} – open-circuit voltage, FF – fill factor, P_{in} – incoming power of sunlight.

Fill factor shows the ratio between the maximum power that is obtained from the solar cell and the product of V_{oc} and J_{sc}:

$$FF = \frac{J_{max}V_{max}}{J_{sc}V_{oc}}, \tag{2.11}$$

Graphically, FF can be presented as a measure of "squareness" of the solar cell *J(V)* given by FF = P_{max}/P_{th} curve (the ratio between yellow square and green square in Figure 2.6).

In real solar cells, the incoming power can be lost through parasitic resistances: series (R_s) and parallel (R_p) resistance. As it can be shown in the diode equivalent electric scheme in Figure 2.7, it is necessary to increase the value of R_p and decrease the value of R_s to avoid the current losses and maximize the output power.

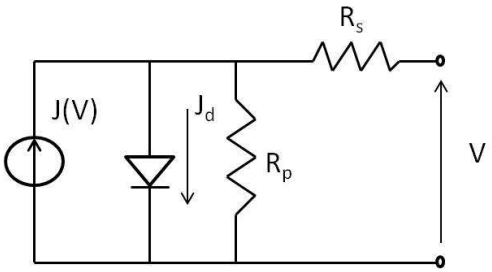

Figure 2.7. Diode equivalent circuit scheme with series and parallel resistances.

Normally, the origin of the R_s comes from the resistance of the contacts (resistance between the metal and semiconductor and resistance of contacts itself) and the bulk resistance of the non-depleted regions (n- and p-semiconductors). Parallel resistance originates from leakage current through the cell and surface recombination. Both of the parasitic resistances provoke a decrease of fill on the *J(V)* curve. R_s also decreases the value of short-circuit current and R_p leads to a decrease of open-circuit voltage. Figure 2.8 shows the effect of series and parallel resistances on *J(V)* curve of the solar cell under illumination.

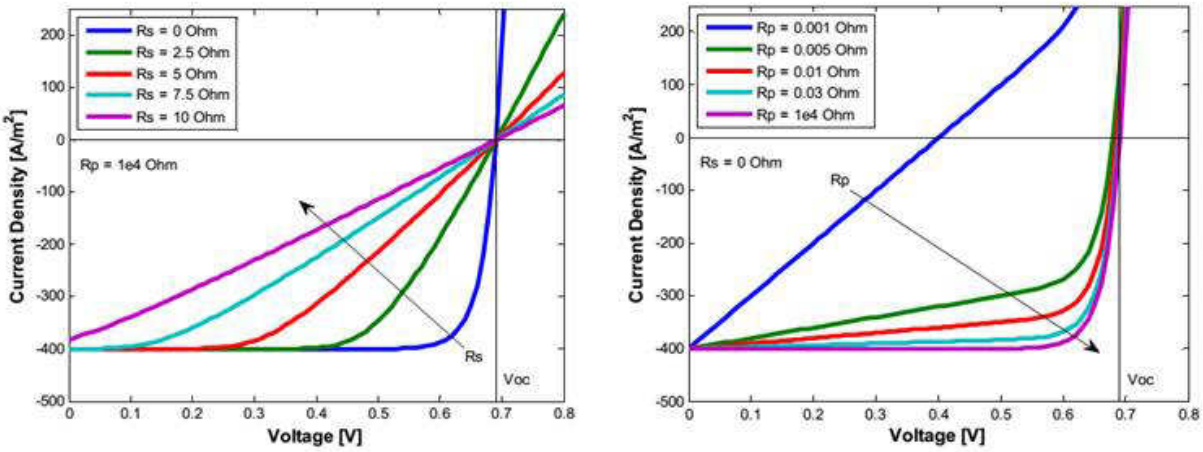

Figure 2.8. Effect of parasitic resistances on J(V) curve shape of crystalline silicon solar cell: a) the effect of series resistance (R_s) ; b) the effect of parallel resistance (R_p)[Zeman].

2.1.4 New solar cell concepts: multi-junction and quantum well-based solar cells

Multi-junction solar cell

The maximum theoretically achievable limit for one junction solar cell was calculated by Shockley and Queisser [Shockley, 1961]. The calculations were done using the principle of detailed balance taking into account several assumptions:

- one photon creates one electron-hole pair

- all photons with the energy more than the semiconductor band gap are absorbed
- there is only radiative recombination of the carriers inside the semiconductor

Finally, they found the maximum value of theoretical conversion efficiency of 33.7% for a semiconductor with a band gap of 1.34 eV. Solar cells that are currently used in industry and mass-production are based on silicon that has a band gap of 1.1 eV. Therefore, the theoretical limit of conversion efficiency that a silicon solar cell can really achieve was calculated to be about 29% under 1 sun AM1.5G illumination [Swanson, 2005]. There are different loss mechanisms that reduce this conversion efficiency: carrier recombination inside the solar cell, resistance losses, reflection, etc., but the most important one is spectral losses (more than 50% of incoming energy) [Glunz, 2012]. These losses are related to the spectral mismatch between the absorption of one-junction photovoltaic cell and solar spectrum. Therefore, to improve the sunlight absorption and decrease the thermalization losses, it is necessary to adapt the design of the solar cell to the Sun spectrum.

Multi-junction solar cells appear as an optimal solution, since each cell is designed to absorb photons with energy close to its band gap. Theoretically, the conversion efficiency of 86% can be reached using a cell with infinite number of materials with different band gaps under concentrated light. The schematic of the muti-junction solar cell concept is presented in Figure 2.9. Wide band gap materials should be on the top of the multi-junction solar cell to absorb high energy photons and transmit low energy photons to the next junction with lower energy band gap.

Theoretical calculations predict an achievable conversion efficiency of about 50% using a four-junction solar cell. Table 2.1 presents optimum band gaps for multi-junction solar cells and their maximum conversion efficiency that can be achieved [Bhuiyan, 2012].

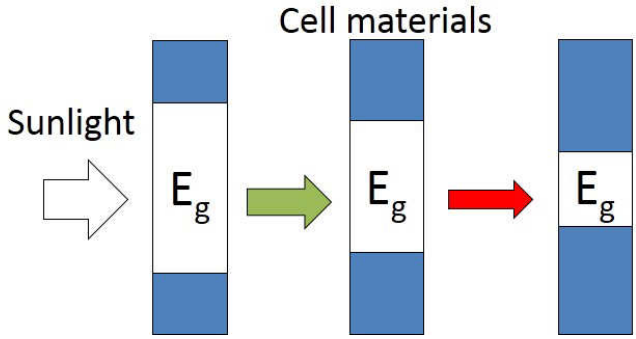

Figure 2.9. Schematic of the multi-junction solar cell concept [Cakmak, 2012].

Table 2.1. Optimum band gap, maximum and achievable limit conversion efficiency of multi-junction solar cell with different number of junctions [Bhuiyan, 2012].

Number of junctions	Band gaps (eV)	Maximum limit, η (%)	Achievable limit η×0.8 (%)
3	0.7 1.37 2.0	56	44.8
4	0.6 1.11 1.69 2.48	62	49.6
5	0.53 0.95 1.4 1.93 2.68	65	52
6	0.47 0.84 1.24 1.66 2.18 2.93	67.3	53.84
7	0.47 0.78 1.191 1.56 2.0 2.5 3.21	68.9	55.12
8	0.44 0.78 1.09 1.4 1.74 2.14 2.65 3.35	70.2	56.16

The present state-of-the-art shows that maximum achieved conversion efficiency for four-junction solar cell of 44.7% under concentrated light* is close to the theoretical limit (49.6%). There is still a room for efficiency improvement creating a tandem cell with 5 and more junctions.

Quantum well-based solar cell

The concept of quantum well-based solar cell was proposed by Barnham *et al.* in 1990 [Barnham, 1990]. The insertion of material with a low band gap surrounded by material with a higher band gap appears as a well on a band diagram (Figure 2.10) and allows the absorption of low energy photons. This additional absorption improves the conversion efficiency of the solar cell at longer wavelengths increasing the short-circuit current (improved solar spectrum matching). The open-circuit voltage MQW-based p-n junction lies between the value of V_{oc} given by the p-n junction consisting from barrier material and p-n junction composed from well material.

If the QW thickness is small enough to be comparable to the de Broigle wavelength ($\lambda_B = h/p$, where h – Planck constant and p – momentum of the particle), the continous energy levels split up into discrete energy levels. The position of the discrete levels in QW with infinite barriers can be calculated using the following formula:

$$E_n = \frac{-\hbar^2}{2m}\left(\frac{n\pi}{L_z}\right)^2, \qquad (2.12)$$

where E_n – position of the energetic level, $\hbar$ – reduced Planck constant, m – effective electron (hole) mass, n – number of the discrete energy level, L_z – quantum well thickness.

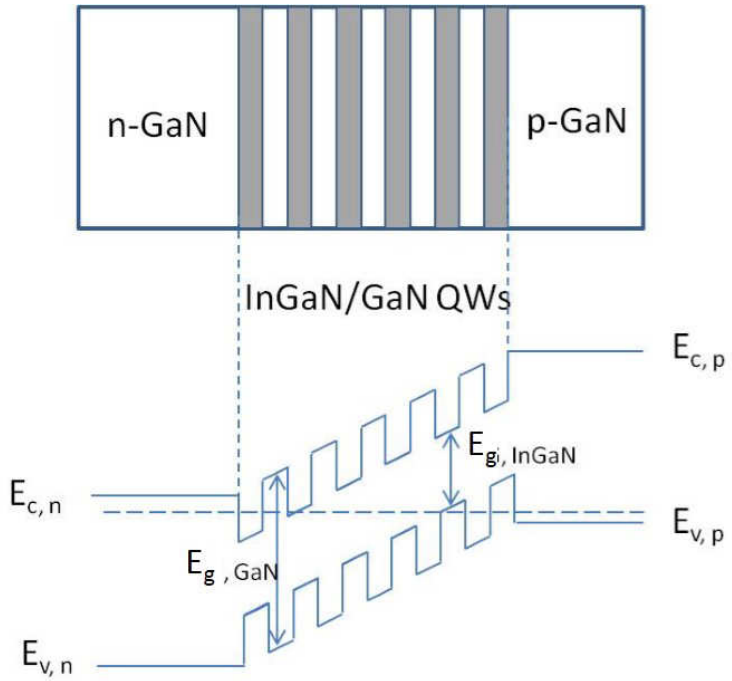

Figure 2.10. An example of the structure and band diagram of InGaN/GaN quantum well-based solar cell.

From the Eq. (2.12) we see that the space between energy levels becomes larger with the increase of the QW thickness and the levels start to shift-up in energy. Therefore, the choise of the QW thickness allows changing the effective band gap of the QW. If levels are very deep located inside the quantum well, the carriers have difficulties to escape outside and this increases the probability of the recombination losses. The use of thinner barriers can be able to solve this problem. Figure 2.11 compares the wave function inside the QW with infinite and finite barriers. We see that wave functions become zero at the well edges for structures with infinite barriers. For finite barriers the wave functions penetrate inside the barriers allowing the tunneling of the carriers from well to well in the structures with thin barriers.

Therefore, by adjusting the active region design: number and thickness of wells and barriers, doping level and alloys composition, we can control absorption properties of the solar cell and improve the conversion efficiency. From this point of view QW-based and multi-junction solar cells are similar and theoretically, should be able to reach equivalent efficiencies.

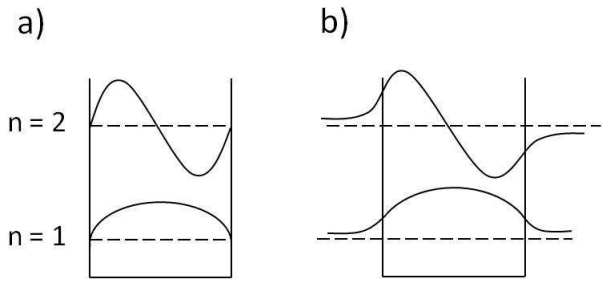

Figure 2.11. (a) Quantum well with infinite barriers. (b) Quantum well with finite barriers.

2.2 General properties of III-nitrides

2.2.1 Peculiarity of the crystalline structure

Nitride-based materials such as GaN, AlN and InN are widely used for optoelectronic applications. These materials can exist in wurtzite, zinc blende and rocksalt crystalline structures. In this chapter, we will focus only on the wurtzite structure properties because it is the most thermodynamically stable configuration that is usually grown by MOCVD (and in this thesis). Schematic of the wurtzite structure is presented in Figure 2.12.

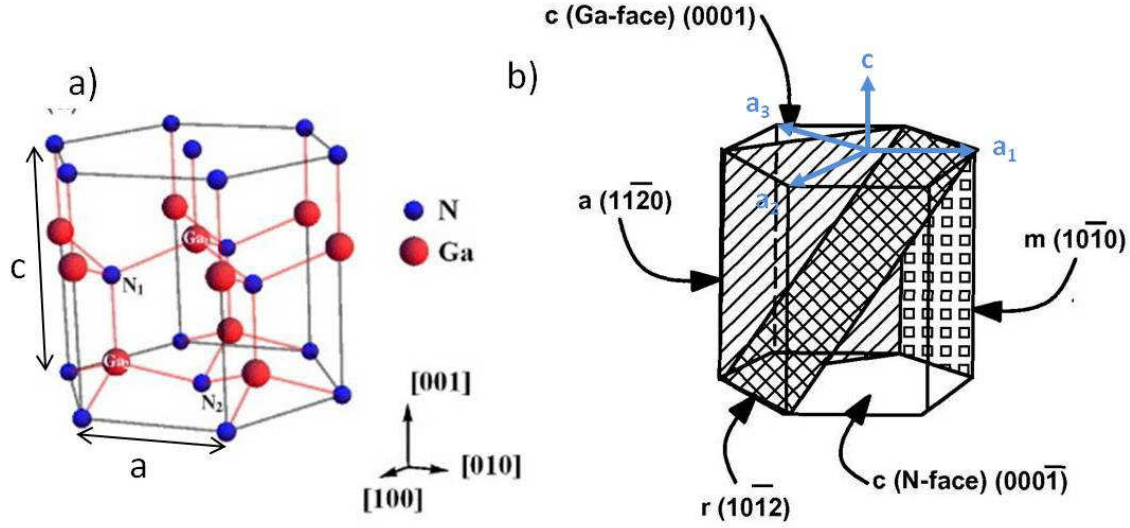

Figure 2.12. Wurtzite structure: a) atom positions with ondication of lattice parameters a and c; b) main atomic planes.

Each of the atoms (nitrogen and metal) forms an individual sublattice arranged in a hexagonal close pack system that is shifted along (0001) *c*-axis by 3/8 of *c*-lattice parameter. Miller indices *(hkil)* are used to index atomic planes in the crystal. In hexagon system these four-digit indices are based on a coordinate system with four axes (Figure 2.12(b)). There are

three basal axes a_1, a_2, and a_3, which make 120° with each other. The fourth axis or *c*-axis is a vertical axis of the hexahedron [Ayers, 2007].

Three common types of crystal planes are usually used in a wurtzite system. The *c*-plane that is perpendicular to the [0001] direction is called polar. Crystal planes that are parralel to the *c*-axis are called non-polar (*a*- and *m*-planes in Figure 2.12). The planes that make an angle different from 0^0 and 90^0 with *c*-axis are called semipolar planes (*r*-plane in Figure 2.12).

Lattice parameters of GaN, AlN and InN are summarized in Table 2.2. In an ideal wurtzite crystal, the *c/a* ratio is 1.633. Because of the different metal cations, the bond lengths and the resultant *c*/*a* ratios of AlN, GaN, and InN are different. The experimental values for GaN is close to the ideal ones, whereas those of AlN deviate slightly, which indicates that the AlN lattice is distorted with respect to a pure wurtzite structure. This fact is very important because the degree of non-ideality is a significant factor in determining the strength of polarization in III-nitrides.

Table 2.2. Lattice parameters of GaN, InN and AlN at room temperature [Pearton, 2000; Angereer, 1997; Davydov, 2002].

Parameter	GaN	InN	AlN
a, Å	3.189	3.537	3.113
c, Å	5.185	5.704	4.982
c/a	1.626	1.608	1.6

The lattice parameters of nitride-based alloys are usually supposed to vary linearly with composition following the Vegard's law [Vegard, 1921]:

$$a\ (A_xB_{1-x}N) = x * a(AN) + (1-x) * a(BN)$$
$$c\ (A_xB_{1-x}N) = x * c(AN) + (1-x) * c(BN) \quad (2.12)$$

2.2.2 Spontaneous and piezoelectric polarization

The wurtzite structure of nitrides of space group P63mc is characterized by the lack of a center of inversion symmetry. Therefore, the two [0001] and [000-1] directions are not equivalent. This leads to different properties of materials grown along these two directions:

different surface morphology, dislocation density and chemical stability [Monroy, 2004; Toumisto, 2005; Shen, 2000].

Nitrogen atoms have a large electronegativity compared to metal atoms leading to the creation of the electrostatic dipoles. Because of lattice deformation by the interactions between N and metal atoms, the charge distribution is not completely compensated leading to the spontaneous polarization P_{sp} along the [0001] direction. Values of spontaneous polarization calculated by Bernardini *et al.* are presented in Table 2.3 [Bernardini, 1997]:

Table 2.3. Calculated values of spontaneous polarization for GaN, AlN and InN.

	GaN	**AlN**	**InN**
P_{sp} (C/m^2)	-0.029	-0.081	-0.032

The value of spontaneous polarization for InGaN ternary alloys varies nonlinearly with the composition and can be calculated via [Bernardini, 2001; Ambacher, 2002]:

$$P_{sp}(In_xGa_{1-x}N) = x * P_{sp}(InN) + (1-x) * P_{sp}(GaN) - b * x * (1-x), \quad (2.13)$$

where b – bowing parameter is defined as:

$$b = 2P_{sp}(InN) + 2P_{sp}(GaN) - 4P_{sp}(In_{0.5}Ga_{0.5}N) \quad (2.14)$$

The mechanical stress can modify atom positions and the charge distribution in the superlattice creating a piezoelectric component P_{pz} of the polarization fields. The following equation can be used to estimate the value of P_{pz} in the hexagonal structure [Rom, 2006]:

$$\vec{P}_{PZ} = \begin{pmatrix} 0 & 0 & 0 & 0 & e_{15} & 0 \\ 0 & 0 & 0 & e_{15} & 0 & 0 \\ e_{31} & e_{31} & e_{33} & 0 & 0 & 0 \end{pmatrix} \times \begin{pmatrix} \varepsilon_{xx} \\ \varepsilon_{yy} \\ \varepsilon_{zz} \\ \varepsilon_{yz} \\ \varepsilon_{xz} \\ \varepsilon_{xy} \end{pmatrix} \quad (2.15)$$

where e_{ij} - piezoelectric coefficients of the material and ε_{ij} - strain tensor.

The value of piezoelectric polarization for the growth direction along *c*-axis with layers under in-plane biaxial stretching or contraction can be calculated as:

$$\begin{aligned} P_{pz} &= e_{31}(\varepsilon_{xx} + \varepsilon_{yy}) + e_{33}\varepsilon_{zz}, \\ \varepsilon_{xx} &= \varepsilon_{yy} = (a(x)-a_0)/a_0, \\ \varepsilon_{zz} &= (c(x)-c_0)/c_0, \end{aligned} \quad (2.16)$$

where *a(x)* and *c(x)* - lattice parameters of alloy obtained through Vegard's law (Eq. 2.12) and a_0 and c_0 - lattice parameters of the film under stress. Taking into account the absence of stress along the growth direction, we obtain for piezoelectric polarization:

$$P_{pz} = 2\frac{(a(x)-a_0)}{a_0}(e_{31} - e_{33}\frac{C_{13}}{C_{33}}), \quad (2.17)$$

where C_{13} and C_{33} are the elastic constants.

Values of piezoelectric coefficients and elastic constants for GaN, InN and AlN are listed in Table 2.4. Parameters for $In_xGa_{1-x}N$ alloys can be calculated through Vegard's law approximation [Christmas, 2005].

Table 2.4. Values of piezoelectric coefficients and elastic constants for GaN, InN and AlN [Bernardini, 1997; Wright, 1997].

	C_{13}, GPa	C_{33}, GPa	e_{31}, C/m^2	e_{33}, C/m^2
GaN	103	405	-0.49	0.73
InN	92	224	-0.57	0.97
AlN	108	373	-0.60	1.46

The total polarization is a sum of spontaneous and piezoelectric polarizations $P_{tot} = P_{sp} + P_{pz}$. For QW-based structures, the polarization causes non-compensated charges at the barrier/well interfaces creating an electric field inside the well. The representation of the polarization field and charge distribution in InGaN QW grown along *c*-axis is shown in Figure 2.13 (a).

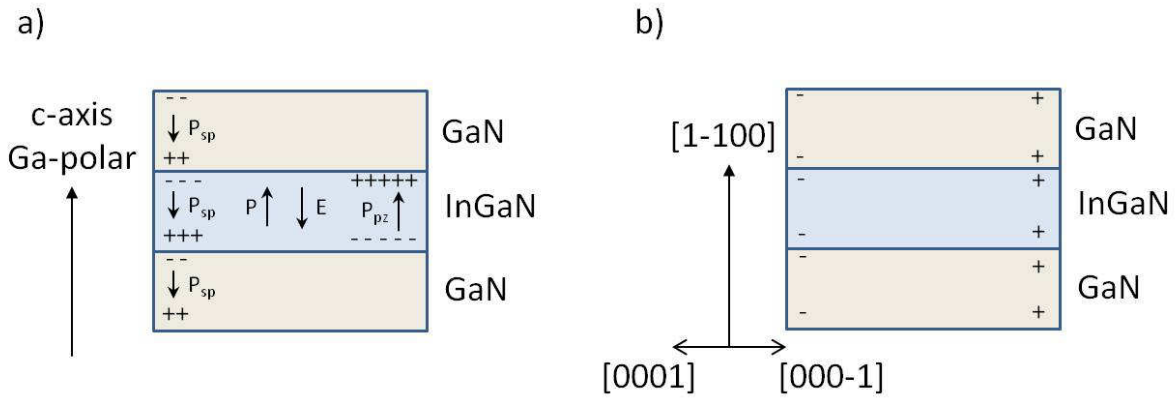

Figure 2.13. (a) Graphical representation of the polarization field direction inside InGaN/GaN QW structure grown along c-axis and biaxially strained on GaN. (b) Graphical representation of charge distribution inside InGaN/GaN QW structure grown along m-plane.

If barriers are thin enough they also can be deformed and piezoelectric polarization can take a place inside the barriers, in the case of Ga-polar InGaN/GaN QWs, the direction of

the piezoelectric fields inside the barriers has a direction opposite to the piezoelectric field inside the well. The values of electir field inside the barriers are not the same as in QWs and depnds on the doping level.

The electric field in a single QW with infinite barriers can be derived via [Grandjean, 1999]:

$$E_w = \frac{(P_b - P_w)}{\varepsilon_w}, \tag{2.18}$$

where P_b, P_w – total piezoelectric polarization in barriers and wells, ε_w –well dielectric constant.

Electric field induced by polarization for InGaN/GaN MQW-based structure depending on In-composition in the wells was calculated by Hangleiter *et al.* Values of 0.5- 3.5 MV/cm^2 for In-content varied from 5 to 24% were obtained [Hangleiter, 2003].

For non-polar orientations (for example along *m*-direction) the piezoelectric fields are perpendicular to the growth direction. Therefore, there is no charge accumulation at the interfaces and no induced electric field (Figure 2.13 (b)). Along *c*-axis the charges of adjusent dipoles cancel each other [Sun, PhD thesis].

2.2.3 Electronic structure of nitride semiconductors

Nitride-based semiconductors have a direct band gap that means that the minimum of the conduction band and the maximum of the valence bands are located at the same value for the wavenumber. Band diagrams calculated by Goano *et al.* for GaN, InN and $In_{0.2}Ga_{0.8}N$ are presented in Figure 2.14.

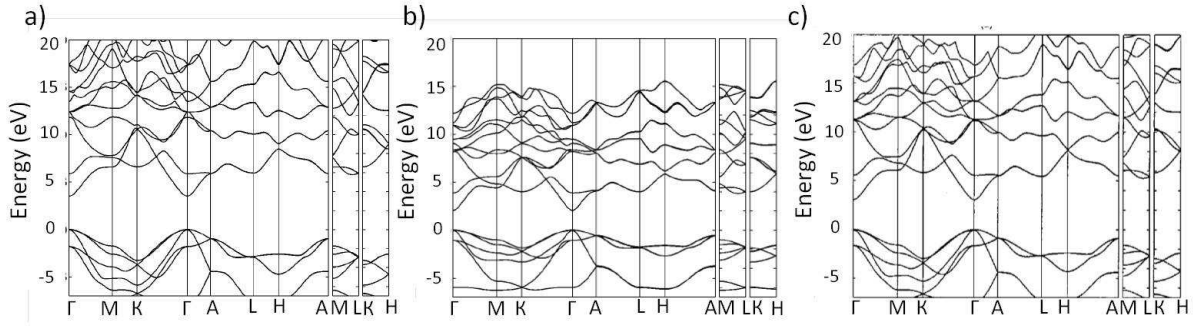

Figure 2.14. Band structure calculated by Goano et al. for a) GaN; b) InN and c) $In_{0.2}Ga_{0.8}N$ [Goano (1), 2000; Goano (2), 2000].

Band structure of nitrides consists of one conduction band and three valence bands. The valence band is degenerated in three sub-bands because of the crystal field presence and spin-orbit coupling. These sub-bands are called heavy holes (HH), light holes (LH) and spin-orbit

holes by analogy with cubic semiconductors. The valence bands around Γ point calculated by Rezaei *et al.* for GaN and InN are depicted in Figure 2.15 [Rezaei, 2006]. There is an evident asymmetry of the light hole sub-band along k_x and k_z directions of the wavevector. This asymmetry leads to a strong anisotropy of light hole effective masses depending on the wave-vector direction. Along k_x direction the hole effective mass is lower than along k_z direction.

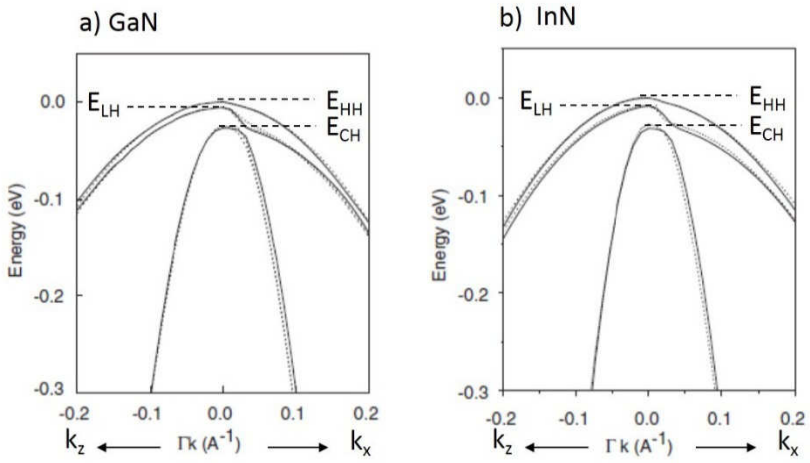

Figure 2.15. The k.p. (solid line) and empirical pseudopotential method (dotted line) calculations of valence band for a) GaN and b) InN [Rezaei, 2006].

Effective masses of electrons, heavy, light and spin-orbit holes for GaN and InN are listed in Table 2.5.

Table 2.5. Values of hole and electron effective masses at the center of Brillouin zone (Γ point) for GaN and InN taken from [Rezaei, 2006]. ∥ and ⊥ correspond to the values parallel and perpendicular to c-axis. m_0 is electron mass (9.11×10^{-31} kg).

Effective mass	GaN	InN
$m_e^{\parallel}$	0.16 m_0	0.12 m_0
$m_e^{\perp}$	0.13 m_0	0.11 m_0
$m_{hh}^{\parallel}$	1.45 m_0	1.39 m_0
$m_{hh}^{\perp}$	1.52 m_0	1.41 m_0
$m_{lh}^{\parallel}$	1.45 m_0	1.39 m_0
$m_{lh}^{\perp}$	0.168 m_0	0.12 m_0
$m_{ch}^{\parallel}$	0.14 m_0	0.1 m_0
$m_{ch}^{\perp}$	1.96 m_0	1.69 m_0

The band gap energy varies with temperature and its dependence is usually described by the Varshni's law [Varshni, 1967]:

$$E_g(T) = E_g(0) - \frac{\alpha T^2}{\beta + T} \quad , \tag{2.19}$$

where $E_g(0)$ is the gap at 0 K, α and β are Varshni thermal coefficients. The values of Varshni's constants together with values of band gaps for GaN and InN are given in Table 2.6.

Table 2.6. Values of band gap E_g and Varshni's parameters α and β for GaN and InN taken from [Vurgaftman, 2003].

	E_g at 0 K, eV	α, meV/K	β, K
GaN	3.51	0.909	830
InN	0.78	0.245	624

In contrast with lattice parameters, the value of the band gap for ternary alloys shows a nonlinear behavior as a function of alloy composition that can be estimated by:

$$E_g(A_xB_{1-x}N) = x\,E_g(AN) + (1-x)\,E_g(BN) - x(1-x)\,b(ABN), \tag{2.20}$$

where b – bowing parameter showing a nonlinearity of a band gap dependence on composition. Recommended value of the bowing parameter for InGaN alloys is 1.4 eV. [Vurgaftman, 2003].

2.3 State-of-the-art of InGaN-based solar cells

The proposal to use InGaN alloys for solar cell application has been done in 2003 by Wu *et al.* [Wu, 2003]. But the first announcement about a InGaN-based device has been published only two years later [Jani, 2005]. Different structure designs were verified to optimize photovoltaic properties of InGaN solar cells. Generally, all proposed structures can be divided on two main groups that are discussed in this sub-section: homojunctions and heterojunctions.

Homojunctions

Homojunction p-InGaN/n-InGaN and p-InGaN/i-InGaN/p-InGaN solar cells were grown in parallel by two techniques: molecular beam epitaxy (MBE) and metal-organic vapor phase epitaxy (MOVPE). In 2008 Misra *et al.* obtained V_{oc} = 0.55V and J_{sc} = 0.24 mA/cm^2 under AM0 equivalent illumination for p-$In_{0.31}Ga_{0.69}N$/n-$In_{0.31}Ga_{0.69}N$ homojunction solar cell

grown by MBE [Misra, 2008]. In the same year Yamamoto *et al.* grew p-$In_{0.23}Ga_{0.77}N$/n^+-$In_{0.23}Ga_{0.77}N$ solar cell by MOVPE reaching the values of V_{oc} = 1.5V and J_{sc} = 0.5 mA/cm^2 under 1 sun AM1.5G illumination [Yamamoto, 2008]. The photovoltaic characteristics for this solar cell are presented in Figure 2.16 (a). From this figure it can be seen that the value of *FF* is quite poor. This effect was explained by very high leakage current through the device because of a low quality of grown InGaN layers. In 2010, Jampana reported improved V_{oc} and *FF* (1.73 V and 61.04%, respectively under AM0 equivalent illumination) growing strained n-$In_{0.16}Ga_{0.84}N$/p-$In_{0.175}Ga_{0.825}N$ layers inserted between p-GaN/n-GaN layers [Jampana(1), 2010]. Current density-voltage measurements for these devices are shown in Figure 2.16 (b). This leaded to a conversion efficiency of 0.17%. Almost the same results were achieved by Boney *et al.* for n-$In_{0.14}Ga_{0.86}N$/p-$In_{0.14}Ga_{0.86}N$ solar cell grown by MBE (V_{oc} = 1.8V, *FF* = 52%) [Boney, 2011].

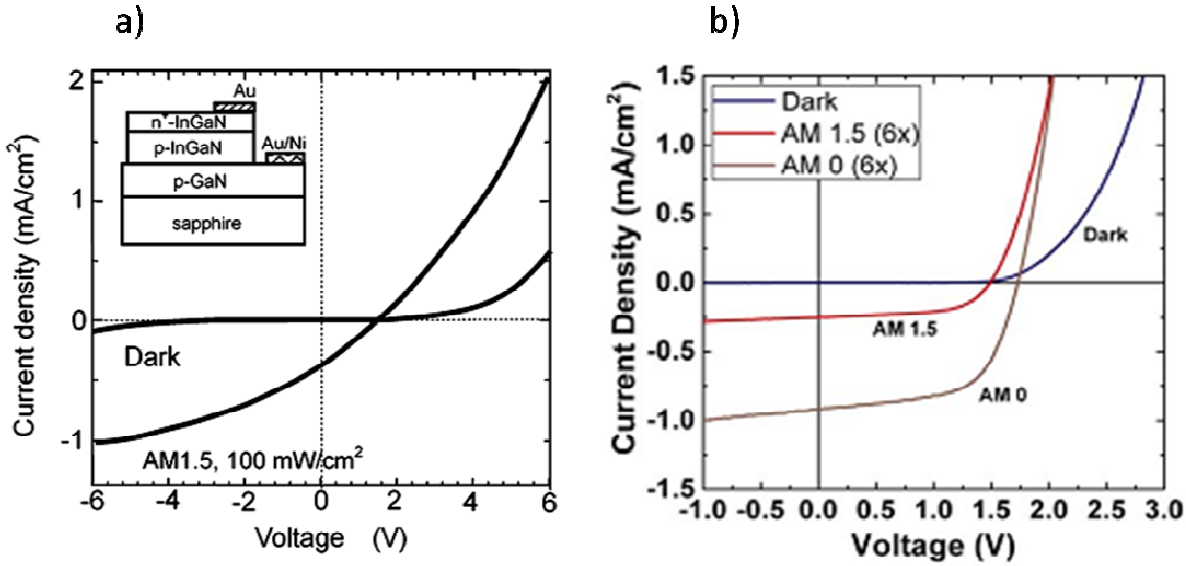

Figure 2.16. Current density-voltage measurements of InGaN-based homojunction solar cells. The images are taken from a) [Yamamoto, 2008], inset shows the structure of the device; b) [Jampana(1), 2010].

Cai *et al.* compared the performance of p-i-n *homojunction* InGaN and p-GaN/i-InGaN/n-GaN *heterojunction* solar cells [Cai, 2013]. The structure of investigated devices is presented in Figure 2.17 (a, b). Figure 2.17 (c) shows the photovoltaic performance of homojunction (HOJ) and heterojunction (HEJ) solar cells with different In-content. HOJ-L, HOJ-H, HEJ-L, HEJ-H have In-content of 12, 15, 13.5 and 16%, respectively. It was demonstrated that heterojunction samples show two times higher performance (η = 0.62% for HEJ-L) compared to homojunction solar cells (η = 0.32% for HOJ-L) under 1 Sun AM1.5G equivalent illumination.

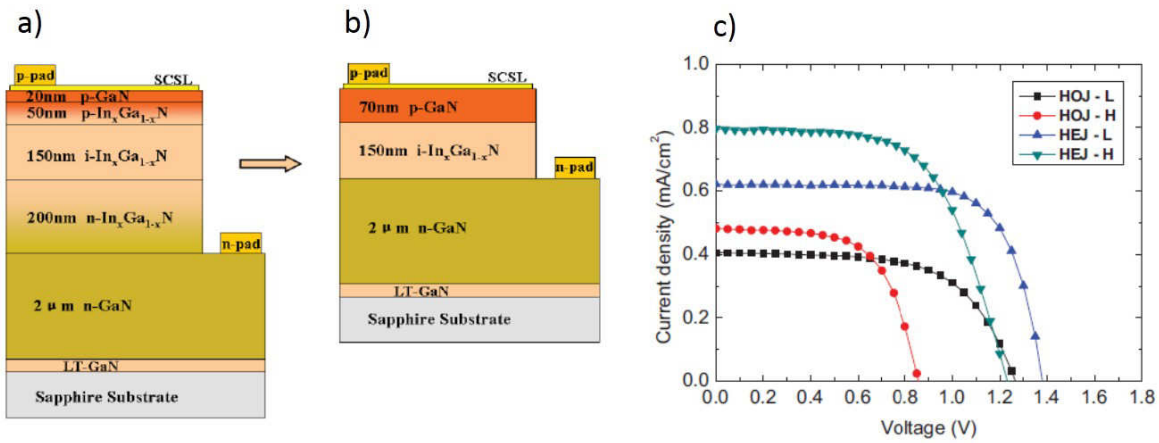

Figure 2.17. Structure of the InGaN-based solar cells: a) homojunction; b) heterojunction; c) photovoltaic characteristics for homojunction and heterojunction solar cells with In composition 12–16% under 1 Sun AM1.5G equivalent illumination [Cai, 2013].

To have a more extended review, the state-of-the-art for InGaN-based homojunction solar cells is shown in Table 2.7.

Table 2.7. State-of-the-art for InGaN-based homojunction solar cells [Bhuiyan, 2012; Lu, 2013].

Structure	Growth technique	Substrate	In content	Electrical parameters	Reference
p-n	MOVPE	(0001) sapphire	0.18	V_{oc} = 0.43 V; J_{sc} = 0.04 mA/cm^2 (360 nm illumination)	[Yang, 2007]
p-n	MOVPE	(0001) sapphire	0.1-0.2	V_{oc} = 2.1 V; J_{sc} ≈ 0.2 mA/cm^2 (light enhanced by UV)	[Jani(1), 2007]
p-i-n	MBE	(0001) sapphire	0-0.3	V_{oc} = 2.5 V; J_{sc} = 30 mA/cm^2 ; η = 0.23% (325 nm laser, 200mW/cm^2)	[Chen, 2008]
p-n$^+$	MOVPE	(0001) sapphire	0.23	V_{oc} = 1.5 V; J_{sc} ≈ 0.5 mA/cm^2 (AM1.5, 100 mW/cm^2)	[Yamamoto, 2008]
p-n	MBE	(0001) sapphire	0.31	V_{oc} = 0.55 V; J_{sc} ≈ 0.24 mA/cm^2 (AM0)	[Misra, 2008]
p-n	MOVPE	(0001) sapphire	0.31	V_{oc} = 1.5-2 V; J_{sc} ≈ 0.04 mA/cm^2 (1 sun)	[Jani, 2008]
p-n	MOVPE	(0001) sapphire	0.02 - 0.15	V_{oc} = 2.24-0.96 V; J_{sc} ≈ 1.4-1.87 mA/cm^2 (Xe lamp)	[Cai, 2009]
p-n	MOVPE	(0001) sapphire	0.02	V_{oc} = 2.24-2.36 V; J_{sc} ≈ 1.36-1.71 mA/cm^2 (Xe lamp)	[Zeng, 2010]

p-n	MOVPE	(0001) sapphire	0.14 - 0.16	V_{oc} = 1.73 V; J_{sc} = 0.91 mA/cm^2 (AM0)	[Jampana(1), 2010]
p-i-n	MBE	GaN template	0.14 - 0.54	V_{oc} = 1.8-0.02 V; J_{sc} ≈ 1-2.2 mA/cm^2 (AM0)	[Boney, 2011]
p-n$^+$	MOVPE	GaN template	0.16	V_{oc} = 1.4 V; J_{sc} ≈ 0.25 mA/cm^2 (AM1.5, 100 mW/cm^2)	[Islam, 2013]
p-i-n	MOVPE	(0001) sapphire	0.12 – 0.15	η = 0.32 – 0.26% (AM1.5, 100 mW/cm^2)	[Cai, 2013]

Heterojunctions

The progress in InGaN-based heterojunction was faster compared to homojunction solar cells. Already in 2008 Zheng *et al.* reached the conversion efficiency of 0.5% under AM1.5 (100 mW/cm^2) conditions for p-GaN/i-$In_{0.1}Ga_{0.9}N$/n-GaN solar cells [Zheng, 2008]. Kuwahara *et al.* compared p-GaN/i-InGaN/n-GaN devices grown on (0001) sapphire and on *c*-plane GaN free-standing substrates [Kuwahara, 2010]. Figure 2.18 depicts the current density-voltage characteristics for this solar cells under 1 sun AM1.5G illumination. The devices grown on free-standing GaN showed better values of V_{oc} and FF that leads to the overall improvement of conversion efficiency (1.41% for solar cells grown on GaN free-standing substrate compared to 0.98% for devices grown on sapphire). This effect was explained by the decrease of the pit density and quality amelioration of the samples grown on GaN substrate. Finally, the best result was obtained for p-GaN/i-InGaN/n-GaN solar cells by Matioli *et al.* who improved the conversion efficiency from 1.16 to 1.57% by top p-GaN surface roughening [Matioli, 2011].

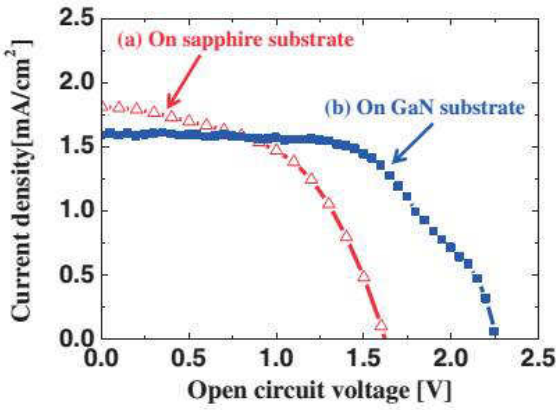

Figure 2.18. Comparison of the photoresponse under 1.5 suns AM1.5G equivalent illumination from InGaN-based solar cells grown on sapphire and on free-standing GaN substrates [Kuwahara, 2010].

In parallel with the development of p-i-n solar cells based on InGaN layer, QWs were proposed as an alternative approach to improve the solar cell performance. Some comparative studies of QW-based and InGaN layer-based samples demonstrated that QWs allow improving the structural quality of the samples [Gmili, 2013]. Moreover, theoretical simulations show that QW-based samples have better values of J_{sc} while keeping the value of open-circuit voltage similar to the layer-based samples [Cavassilas, 2014]. Already in 2009, Jeng *et al.* reported the conversion efficiency of 1.06% under 1 sun AM1.5 equivalent illumination growing 5×$In_{0.2}Ga_{0.8}N$/GaN MQWs on (0001) sapphire substrate by MOVPE [Jeng, 2009]. Farrell *et al.* demonstrated the conversion efficiency of 2.3% by roughening of the sample surface and increasing the number of $In_{0.28}Ga_{0.72}N$/GaN QWs to 30 [Farrell, 2011]. Kywahara *et al.* improved the result to η=2.5% by growing $In_{0.17}Ga_{0.83}N$ (3 nm)/$In_{0.07}Ga_{0.93}N$ (0.6 nm) SL on GaN-substrate with insertion of 10×$In_{0.1}Ga_{0.9}N$ (3 nm)/n-GaN (3 nm) to adjust the strains. The detailed structure of the device, together with photovoltaic characteristics are presented in Figure 2.19 [Kuwahara(2), 2010].

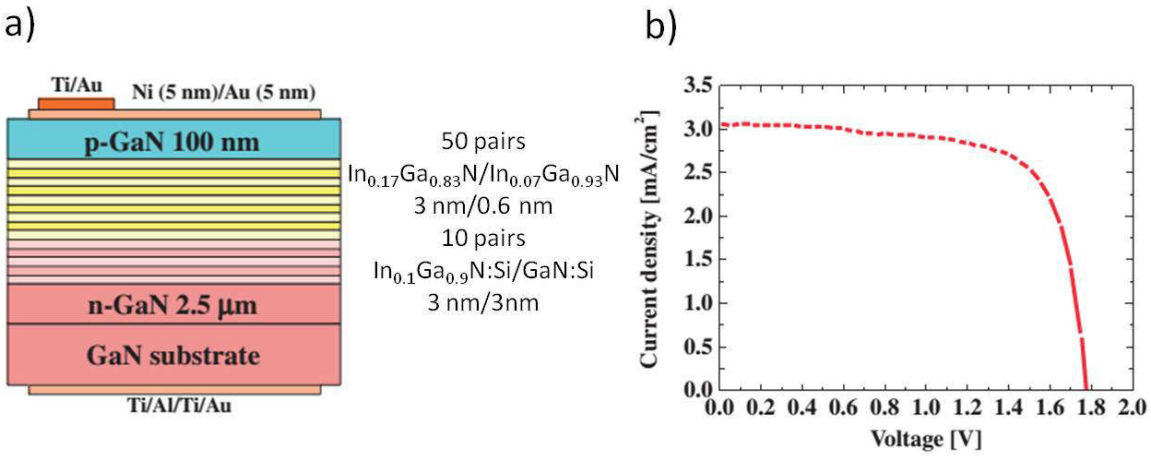

Figure 2.19. a) InGaN/GaN solar cell device structure; b) J-V characteristics under 1.5 sun AM1.5G illumination [Kuwahara(2), 2010].

Dahal *et al.* succeeded to get 2.95% of efficiency for 12×$In_{0.35}Ga_{0.65}N$/GaN QW-based solar cell [Dahal, 2010]. The device schematic and current density-voltage characteristics are shown in Figure 2.20.

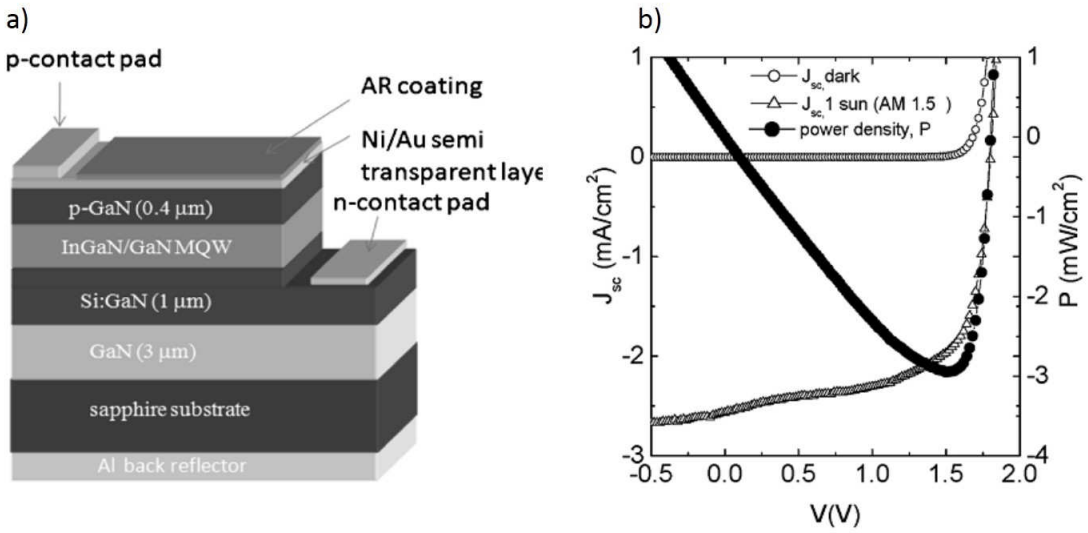

Figure 2.20. a) Schematic of the InGaN/GaN MQW-based device; b) Current density-voltage measurements under 1 Sun AM1.5G irradiation [Dahal, 2010].

Up to now, it is the best result of conversion efficiency obtained for InGaN-based solar cells grown on sapphire substrate. There were several attempts to improve the conversion efficiency of InGaN-based solar cells by growing on other types of substrates, such as r-plane sapphire [Nakao, 2011] and using AlGaN/InGaN superlattice instead of InGaN/GaN [Yang, 2010], but none of them has shown a significant improvement. Jampana *et al*. did a comparative study of $4\times In_{0.155}Ga_{0.845}N$/GaN QWs grown on (111) silicon and (0001) sapphire. The devices showed a comparable values of photovoltaic parameters indicating a possibility to create InGaN-based solar cell on silicon [Jampana(2), 2010]. Liu *et al.* grew $6\times In_{0.15}Ga_{0.85}N$/GaN MQWs on (111) Si-substrate using AlGaN/AlN superlattice to adjust the lattice mismatch between Si and GaN [Liu, 2013]. After every period of AlGaN/AlN they inserted Si_xN_y layers to stop the propagation of threading dislocations toward the active region. Conversion efficiency of 0.2% was obtained under 1 Sun AM1.5G solar illumination. Recently, Young *et al*. grew 30 periods of $In_{0.2}Ga_{0.8}N$/GaN MQWs on (0001) GaN substrate [Young, 2014]. The structure together with electrical characteristics are shown in Figure 2.21. To minimize the reflection from the top-side of the device and maximize the rear reflection they applied front-side anti-reflective coating and a back-side dichroic mirror. The value of conversion efficiency for the best samples reached 3.33%. Up to now, it is the best value of performance obtained for InGaN-based solar cells.

Values of conversion efficiency obtained on modern solar cells based on InGaN seem quite low. This is mostly because all of them obtained for InGaN layers and wells with In-composition lower than 20%. It means that such solar cells are able to absorb only a small part of the sunlight in blue-violet range of the solar spectrum. Therefore, this kind of solar

cells can not be used as an independent device but they can be used as a good complement to improve the spectral matching and, therefore, the conversion efficiency of already exsited solar cells based on silicon or GaAs.

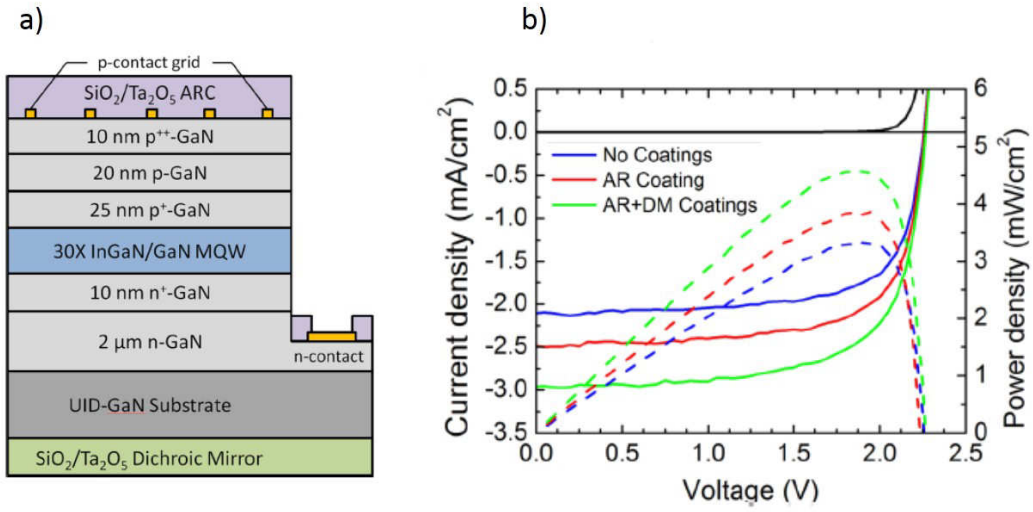

Figure 2.21. a) Schematic of a solar cell structure with 3.33% conversion efficiency; b) J(V) curves under 1 sun AM0 equivalent illumination [Young, 2014].

To conclude, an overview of the state-of-the-art for InGaN-based heterojunctions is summarized in Table 2.8. All heterojunction solar cells presented in Table 2.8 are grown by MOVPE.

Table 2.8. State-of-the-art for InGaN/GaN-based heterojunction solar cells [Bhuiyan, 2012; Lu, 2013].

Structure	Active region	Substrate	In content	Electrical parameters	Reference
p-i-n	layer	(0001) sapphire	0.04 – 0.05	V_{oc} = 2.4 V (light enhanced with UV)	[Jani(2), 2007]
p-i-n	MQWs	(0001) sapphire	0.1	V_{oc} = 2.1 V; J_{sc} = 0.46 mA/cm^2 (AM1.5)	[Zheng, 2008]
p-i-n	layer	(0001) sapphire	0.12	V_{oc} = 1.81 V; J_{sc} = 4.2 mA/cm^2 (concentrated AM0)	[Neufeld, 2008]
p-i-n	layer	(0001) sapphire	0.1	η = 0.8 %	[Horng, 2009]
p-i-n	MQWs	(0001) sapphire	0.2-0.28	η = 1.06 – 1.02 %	[Jeng, 2009]
p-i-n	MQWs	(0001) sapphire	0.19	η = 0.58 %	[Sheu, 2009]

Structure	Active region	Substrate	In content	Electrical parameters	Reference
p-i-n	MQWs	(0001) sapphire	0.35	**η = 2.95 %**	[Dahal, 2010]
p-i-n	layer	GaN substrate	0.1	η = 1.41 %	[Kuwahara, 2010]
p-i-n	layer	(0001) sapphire	0.08	η = 0.57 %	[Tsai, 2010]
p-i-n	layer	GaN substrate	0.11	η = 1.2 %	[Shim, 2011]
p-i-n	MQWs	GaN substrate	0.17/ 0.07	η = 2.5 %	[Kuwahara, 2011]
p-i-n	layer	(0001) sapphire	0.11	η = 0.51 %	[Lee, 2011]
p-i-n	layer	(0001) sapphire	0.12	η = 1.57 %	[Matioli, 2011]
p-i-n	layer	r-plane sapphire	0.15	η = 1.6 %	[Lee, 2011]
p-i-n	MQWs	(0001) sapphire	0.12	η = 2.29 %	[Farrell, 2011]
p-i-n	MQWs	(0001) sapphire	0.21	η = 1.66 %	[Wierer, 2012]
p-i-n	MQWs	GaN substrate	0.2	η = 2.4 %	[Young, 2013]
p-i-n	MQWs	(111) Si substrate	0.15	η = 0.2 %	[Liu, 2013]
p-i-n	MQWs	(0001) sapphire	0.135 – 0.16	η = 0.62 – 0.6 %	[Cai, 2013]
p-i-n	MQWs	(0001) sapphire	0.12	η = 0.23 %	[Mukhtarova, 2013]
p-i-n	layer	(0001) sapphire	0.157 – 0.071	η = 0.66 %	[Cakmak, 2013]
p-i-n	MQWs	(0001) sapphire	0.19	η = 2.0 %	[Valdueza, Mukhtarova, 2014]
p-i-n	MQWs	GaN substrate	0.20	**η = 3.33 %**	[Young, 2014]

2.4 The choice of the InGaN solar cell structure design

In our case, p- and n-GaN are used to create a p-n junction. Usually, n-GaN is chosen to be relatively thick to overgrow the defects created at the GaN/sapphire interface because of the lattice mismatch of about 15% [Meng, 2008]. Insertion of the intrinsic layer (*i*-layer) between p- and n-type materials was developed in the latest 1950's and allows to extend the depletion region making all carriers created inside it to be influenced by internal electric field. In practice, InGaN layer with low residual doping is used as an intrinsic region. Thanks to a lower band gap compared to GaN, the absorption of low-energy photons will mostly take place in *i*-layer, that can possibly improve the value of the short-circuit current.

There are a lot of difficulties to grow a thick high-quality InGaN layer. Because of a large lattice mismatch (about 11% between InN and GaN) the critical thickness of the InGaN layer (the thickness after which dislocation formation begins) is very small (about 10 nm for 20% of In-content) [Leyer, 2008].

One way to improve the crystal quality of the InGaN layers is to keep them pseudomorphically strained [Chen, 1993]. It was shown that growth of InGaN/GaN MQW heterostructures with small InGaN thickness can suppress the phase separation and improve photovoltaic properties of the InGaN-based solar cells [Singh, 1997; Dahal, 2009]. At the same time the presence of strain inside pseudomorphically grown InGaN layers creates a large polarization field inside *c*-oriented wells (about 2 MV/cm^2 for 10% In) [Beach, 1999]. The direction of polarization fields depends on crystallographic orientation of the structure. In the usual case of the [0001] Ga-polar oriented device, the direction of polarization field is opposite to the electric field created inside the depletion region reducing the internal electric field and damaging collection efficiency [Wierer, 2010]. It was shown that increased doping on the both sides of the active region can screen the existing piezoelectric field improving the carrier collection [Neufeld, 2011]. Also, doping level of the top p-GaN layer, which is difficult to increase without affecting crystalline quality, has to be optimized to improve the p-contact.

Within these constrains, a solution for a PV structure is presented in Figure 2.22.

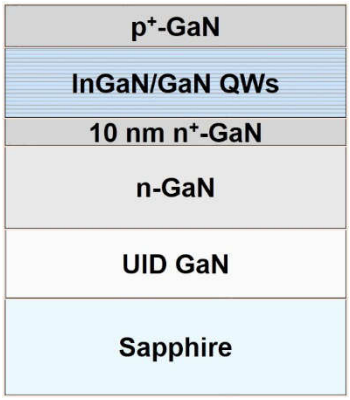

Figure 2.22. Schematic of the PV structure that is studied in this thesis.

In this structure, every layer has a clear advantage to solve the physical problems discussed in this chapter. It can be summarized in the following Table 2.9.

Table 2.9. Structure layers and its purposes.

Layer	Purpose
Thick undoped GaN layer	To overgrow the defects created at the GaN/sapphire interface
Si-doped GaN layer	To create a p-n junction
Highly doped n^+-GaN layer	To screen polarization charges
InGaN/GaN QW region	To manage strains inside InGaN layers and increase light absorption
p^+-GaN layer	To create a p-n junction and to screen piezoelectric fields

Chapter 3

Experimental techniques and device fabrication process

This chapter consists of three parts and describes experimental techniques used during this work. In the first part, we will focus on the metal-organic vapor epitaxy (MOVPE) growth technique and its basic principles for nitride's growth. The second part is related to the structural (x-ray diffraction), optical (photoluminescence and transmission spectroscopy) and electrical characterization techniques. In the third part, we will finally discuss the main steps of the solar cell fabrication process combining photolithography, metallization and inductively coupled plasma (ICP) etching. The choice of the metals to form contacts and the selected contact design will be presented as well.

3.1 Growth by Metal-Organic Vapor Phase Epitaxy

Many different techniques are employed to grow III-nitride based heterostructures, the more developed being molecular beam epitaxy (MBE) and metal-organic vapor phase epitaxy (MOVPE) [Ruterana, 2006; Kung, 2000; Ambacher, 1998].

In solide-source MBE, the materails are evaporated and deposited on the crystal substrate. This process requires ultra-high vacuum (about 10^{-10} – 10^{-11} Torr) to guaranty the purity of the materials. Gaseous-source MBE machines also excist. The gaseous elements condense on the wafer, where they react with each other. MBE technique has been used in many research laboratories because it allows a very precise control of layer thickness and doping level and the possibility to grow different type of nanostructures with high homogeneity and small number of defects. A very low growth rate (about 0.2-0.5 μm/h) and the difficulty to keep ultra-high vacuum are main disadvantages of this technique that limit its utilization for mass-production.

In industry, MOVPE is the most common technique for the growth of III-nitride based heterostructures as demonstrated by its use in the large blue and white Light-Emitting Diodes (LED) market. Unlike MBE growth, MOVPE does not need a very high vacuum, but only

high purity carrier gases and can reach a high growth rate (more than 2 μm/h). As all samples presented in this thesis are grown by MOVPE, we will discuss this technique in more details.

Chemical elements to deposit (In, Al, Ga) are combined with organic molecules to create precursors of the MOVPE growth. Triemethyl- or Triethyl-Gallium (TMGa or TEGa), Triemethyl-Indium (TMIn), Triemethyl-Aluminium (TMAl) and Bis(cyclopentadienyl)-magnesium (Cp_2Mg) are used as sources of Ga, In, Al and Mg. More simple non-organic molecules (silane (SiH_4) and ammonia (NH_3)) are used to add Si and N elements.

Precursors mixed with a carrier gas (H_2 or N_2) are injected into the reactor through separated inlets to avoid prereactions during the gas transport. We examine the growth of GaN from TMGa to illustrate chemical reactions that take place in the growth chamber during the deposition.

Metal-organic precursors react with ammonia inside the reactor chamber. The net reaction for the specific case of GaN growth from TMGa and ammonia is:

$$Ga(CH_3)_3 + NH_3 \rightarrow GaN + 3(CH_4),$$

In reality, the chemical reactions are much more complicated and include numerous sub-reactions. A detailed schematic of the one of the possible chemical processes during GaN growth is shown in Figure 3.1 [Parikh, 2006; Moscatelli, 2007].

The chemical reaction of TMGa can be divided in two sets: immediate decomposition of TMGa on the substrate or the pre-reaction of TMGa with ammonia in the gas phase. These are two competitive processes that both contribute in the growth of GaN layer. The growth rate depends on the substrate temperature in the reactor. Based on that, three growth regimes exist depending on the temperature:

- at low temperature: the growth rate is limited by the speed of chemical reactions and reaction rate, that are temperature dependent (kinetically limited regime);

- at intermediate temperature: the growth rate is limited by the mass transport of the materials and shows little dependance on the temperature;

- at high temperature: the growth rate is limited by the material desorption from the surface.

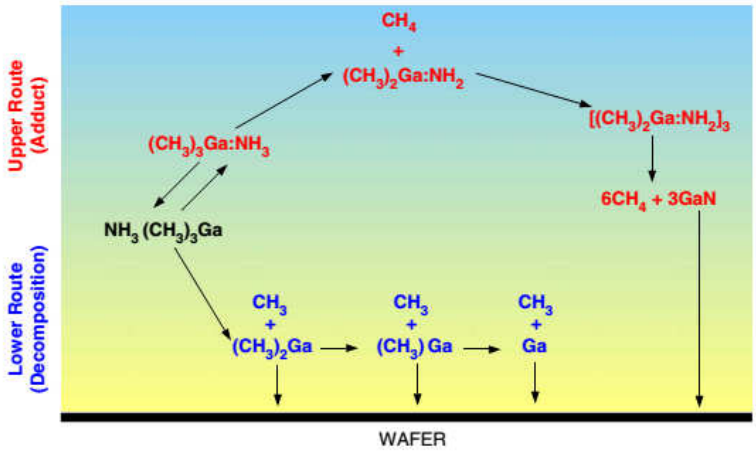

Figure 3.1. A schematic of the chemical reactions inside the reactor chamber during GaN growth proposed by Parikh [Parikh, 2006].

The scheme of the growth mechanism is depicted in Figure 3.2. After chemical reaction, the species can diffuse to the growing surface. There they can absorb, react with other surface species and then diffuse along the surface before the final incorporation reactions take place. The rest of the reaction products leave the growth chamber through the exhaust system.

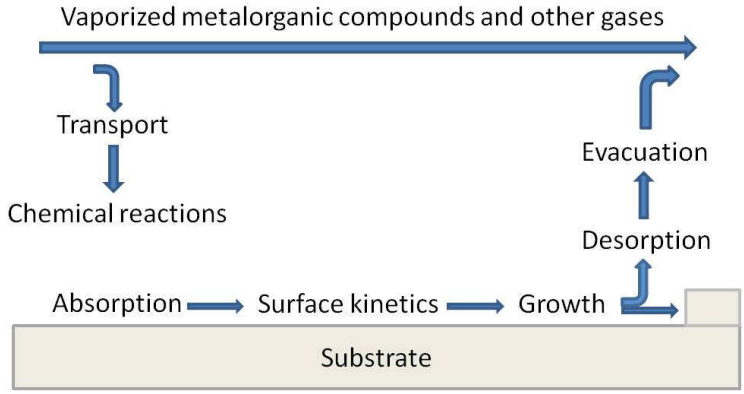

Figure 3.2. Scheme of the mechanisms occurring inside the reactor during the growth.

3.1.1 Standard process of growing GaN layers on sapphire

Commercial free-standing GaN substrates with a low density of dislocations (less than 10^7 cm^{-2} [Andre, 2007]) are still expensive. Therefore, a cheaper sapphire substrate is currently used to grow GaN on it for most applications. For the growth reported in this manuscript, we used a standard (0001) 2" sapphire substrate with 330 μm thickness and 0.25 ^{o} misorientation from Kyocera.

The quality of the first GaN layers grown directly on the sapphire substrate was quite poor. A large lattice mismatch of about 14% creates numerous dislocations at the GaN/sapphire interface. Different approaches were proposed to improve the quality of GaN films. Amano *et al.* showed that a low-temperature AlN buffer layer grown on the sapphire before GaN allows a significant improvement of GaN film quality obtaining a crack-free surface [Amano, 1986]. Nakamura *et al.* obtained high-quality GaN film with good Hall mobility (~900 $cm^2/(Vs)$) of the carriers using a low-temperature GaN buffer layer [Nakamura, 1991]. This last solution has been preferred in this work.

We will detail three main processes that were used during GaN film growth:

- surface preparation
- growth of low-temperature GaN buffer layer (LT-GaN)
- growth of high-temperature GaN thick layer (HT-GaN)

An in situ red diode interferometer (λ = 635 nm) is used to monitor all steps of the GaN growth. Figure 3.3 presents a standard reflection spectrum written during the GaN growth.

Before starting the growth process, sapphire substrates are annealed under H_2 during 5 min. This step is necessary to remove organic contaminations from the substrate surface such as a dust, water, adsorbed gas etc. Afterwards, the rector temperature is decreased and samples are annealed under NH_3 for 5 min. During this step, a thin AlN layer is naturally created on the sapphire surface. Keller *et al.* showed that this AlN layer helps to improve the structural quality and to reduce a number of dislocations in GaN film [Keller, 1996].

Then, without temperature change, we grow a nucleation GaN buffer layer. In the reflectivity spectra, this process is accompanied with a reflectance increase due to increased refractive index *n* (*n* = 2.3 for GaN and *n* = 1.8 for sapphire) (Figure 3.3 (a)). Following the LT-GaN growth, the temperature is rapidly increased to 1030 ^oC. High-temperature annealing under NH_3 etches a GaN layer forming islands on the surface, reflectivity falls down because of surface roughening (Figure 3.3 (b)). With time, the islands become smaller because of material desorption, surface becomes smoother and reflectivity increases (Figure 3.3 (c)). At the point, when the islands become small, it is necessary to start a HT-GaN growth. Nucleation islands become bigger and coalesce creating 2D GaN film (Figure 3.3 (d)). The following growth of GaN forms periodic peaks in the reflectivity curve (Figure 3.3 (e)). Knowing the refractive index of GaN film (*n* = 2.3) and the laser wavelength (λ = 635 nm), we can deduce the grown film thickness using the formula $d = \lambda/(2n)$. The layer thickness between two maxima is calculated to be 138 nm for GaN. An increase of the fringe visibility

is observed as a function of time. It denotes an improvement of the surface roughness and good interference at the layer interface.

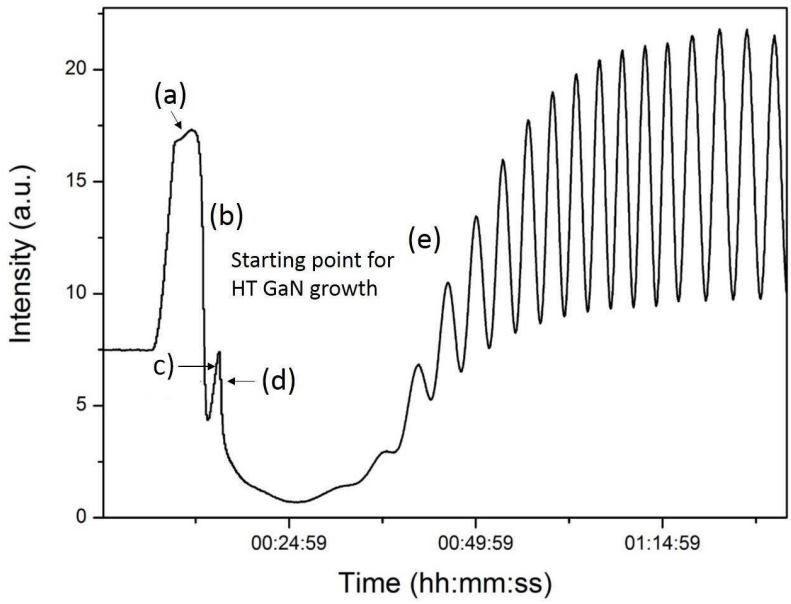

Figure 3.3. Standard reflectivity spectra during GaN growth: (a) LT-GaN buffer layer on sapphire; (b) increase of the temperature etches LT-GaN layer forming islands; (c) reduction of the islands because of material desorption; (d) start of HT-GaN deposition, increasing the size of islands; (e) islands coalesce in 2D film.

Typical atomic force microscopy (AFM) measurements of n- and p-GaN layer surfaces grown on sapphire substrate by MOVPE are presented in Figure 3.4. GaN layers show a smooth surface conserving a step-morphology of the substrate (atomic steps are clearly seen). The disturbance of the step regularity is usually related to the presence of dislocations.

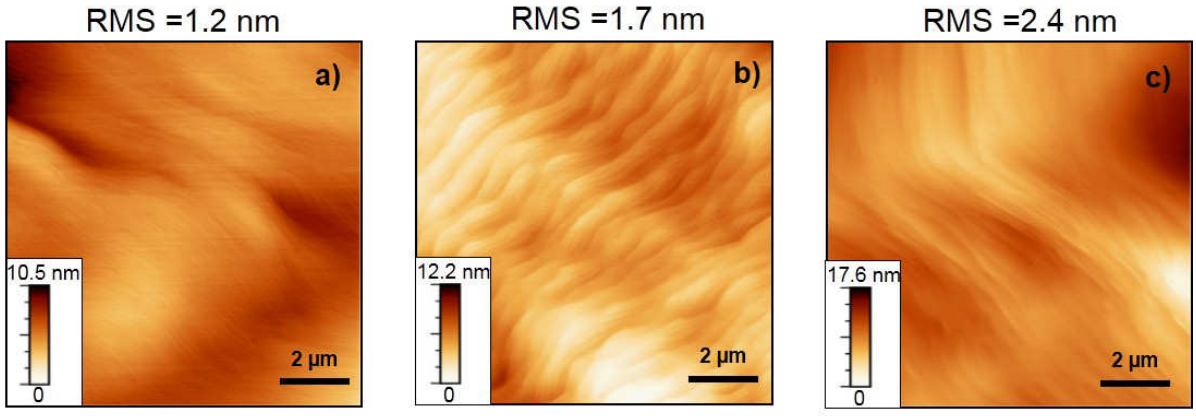

Figure 3.4. 10×10 µm AFM images: a) n-GaN layers grown on sapphire substrate; b) p-GaN layer grown on InGaN/GaN MQWs; c) p-GaN grown on n-UID GaN layer by MOVPE. Measured root mean square (RMS) is indicated on each image.

3.1.2 GaN doping

Unintentonally doped (UID) GaN is n-type and residual doping of GaN in our samples is equal 3×10^{16} cm^{-3} [Koster, 2010]. To form p-n junction based on GaN materials, it is necessary to control the doping level. In most cases, silicon is used for n-type and magnesium for p-type doping.

N-type doping

Good quality n-type doping is quite easy to obtain, as GaN is already unintentionally n-type. Very high Si-doping concentration till more than 10^{19} cm^{-3} can be simply achieved by increasing the SiH_4 flow [Zhihao, 2009; Eiting, 1998]. High Si-doping decreases carrier mobility (μ~100-200 cm^2/Vs for $n = 10^{19}$ cm^{-3} concentration compared to 800 cm^2/Vs for $n = 10^{16}$-10^{17} cm^{-3}) because of carrier scattering [Iliopoulos, 2006]. It was also noticed that at high concentration silicon introduces a significant amount of tensile stress inside GaN layers originating from edge dislocations. Recently, germanium was also proposed as a possible alternative to silicon for n-doping of GaN layers [Dadgar, 2011].

In this thesis we used SiH_4 as a source of Si in our MOVPE machine. The temperature for n-GaN growth was chosen the same as for UID-GaN (T_{gr} = 1040 ^oC). The carrier concentration directly depends on silane molar flow and a value of 6 nmol/min leads to a doping concentration about 4×10^{18} cm^{-3} in our system for 2D growth. The molar flow was increased to 31 nmol/min to reach about 10^{19} cm^{-3} doping concentration for growth of highly-doped n^+-GaN layer.

P-type doping

Cp_2Mg is usually used in MOVPE systems as a source of Mg atoms. The incorporation of Mg atoms increases almost linearly with the increase of Cp_2Mg flow [Sugiura, 1998], but the hole concentration does not follow the same trend. Sheu *et al.* showed, that at high Cp_2Mg flows, the value of active holes starts to decrease [Sheu, 2002]. The proposed possible explanation was the formation of the nearest-neighbour pair $Mg_{Ga}V_N$, a double donor. This leads to the filling of the acceptor levels with electrons provided by the created negatively charged defects.

Besides, hydrogen creates acceptor-H neutral complexes during the growth that causes a high resistivity of p-GaN film. Nakamura *et al.* showed that these acceptor-H complexes can

be dissociated by post-growth annealing under N_2 [Nakamura(2), 1992]. Nevertheless, only about 1% of incorporated Mg atoms produces active holes because of a very large activation energy (the energy between acceptor levels and valence band, $E_A - E_V$) of Mg (about 200 meV) [Gotz, 1996]. Therefore, a high quantity of magnesium atoms should be incorporated to to reach a good concentration of free hole carriers. But a very high doping degrades the quality of GaN film reducing the hole mobility ($\mu_p \approx 10$ cm^2/Vs) [Kaufmann, 2000; Chang, 2002].

A trade-off between high doping concentration and good quality of p-GaN layer should be found. The optimization of p-GaN layer for structures grown in this work is presented in section 3.1.4.

3.1.3 InGaN/GaN quantum well growth

InGaN layers are very sensitive to the deposition temperature because of a high nitrogen equilibrium vapor pressure and a high volatility of indium [Ju, 2007; MacChesney, 1970]. Indium incorporation increases with the growth temperature, leading to an increase of emission wavelength of the device. Empirically, it was observed about 1.5 nm emission wavelength shift per 1 Kelvin of growth temperature change. For InGaN-based materials for photovoltaics, the In composition should be relatively high (about 25-40%). Therefore, relatively low growth temperature (about 600 - 750 ^{o}C) compared to GaN is needed for InGaN wells [O'Steen, 1999].

At the same time, for the growth of good quality GaN barrier, the temperature should be elevated till about 900 ^{o}C. A fast temperature ramping is preferred and a thin GaN cap-layer is grown at the same temperature as for the InGaN well during the temperature increase, in order to protect InGaN well from indium evaporation. Koukitu *et al.* showed that H_2 etches In away from InGaN layers [Koukitu, 1999]. Therefore, the growth of QWs is done under N_2. Typical thickness of GaN barrier is about 10-15 nm and InGaN well is 2-5 nm in MQW heterostructures.

In Chapter 2, we showed that the absence of a center of inversion symmetry in GaN wurtzite structure causes the presence of spontaneous polarization along the *c*-axis. Besides, an additional polarization component contributes to the total piezoelectric field if the film is under stress (that is often the case for QWs). For InGaN QWs grown on (0001) substrate, the piezoelectric field along the growth direction builds up electrical charges at the InGaN/GaN

interfaces resulting in the appearance of electric field inside quantum wells. This field depends on the force of the stress and can reach relatively high values, about 1.08 MV/cm for $In_{0.13}Ga_{0.87}N$/GaN QW [Takeuchi, 1997]. Internal electrical fields in QWs cause a red-shift of the emission wavelength and a decrease of the electron and hole wave function overlap. Such effect is called Quantum Confined Stark Effect (QCSE). The change of energetic level position induced by polarization field directly depends on QW thickness as $E = eFd$, where e - electron charge, F – piezoelectric field in the well and d – well thickness. Usually, for QW thickness less than 2 nm, the influence of QCSE on the emission wavelength is negligible. An example of the piezoelectric field influence on the QW band diagram is presented in Figure 3.5.

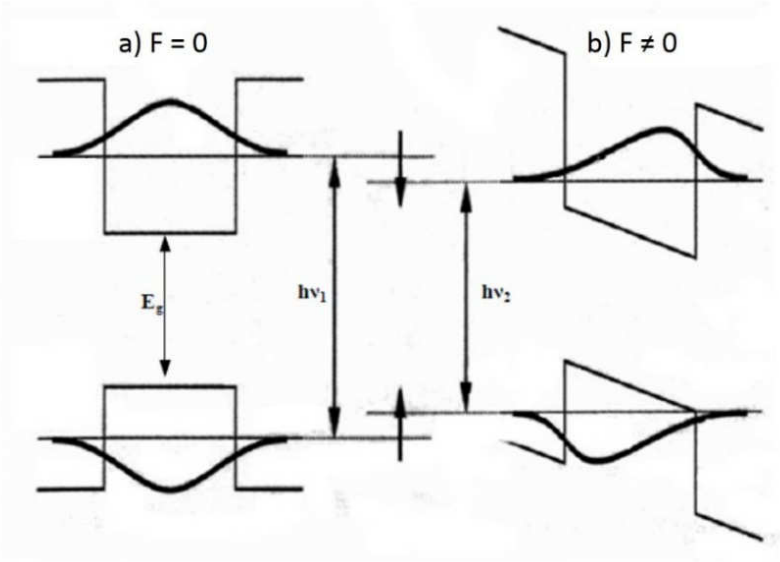

Figure 3.5. Band diagram of the QW grown along the c-axis: a) QW without piezoelectric field; b) QW with piezoelectric field. Image is taken from [Aneeshkumar, 2004].

3.1.4 P-GaN layer optimization to improve the carrier transport

Cp_2Mg flow is one of the most important parameters that determines the doping concentration in p-GaN. To evaluate its effect, we grew several samples changing the value of Cp_2Mg flow from 150 to 700 sccm. Schematic of the sample's structure is presented in Figure 3.6. Growth temperature for 1-µm-thick p-GaN layer is 920 ^oC. After the growth, samples were *in situ* annealed during 20 minutes under N_2 at T = 750 ^oC. A thin p^+-GaN layer was grown on the top of the structure at 1020 ^0C with Cp_2Mg flow = 450 sccm in order to improve the metallic contact for Hall measurements.

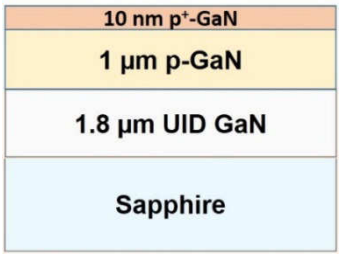

Figure 3.6. Schematic of the structure for p-GaN layer optimization.

Capacitance-voltage (C-V) measurements* were performed to estimate the concentration profile. The results are presented in Figure 3.7. The acceptor concentration changes in the range of 2×10^{18} to 5×10^{18} cm^{-3} changing Cp_2Mg flow from 150 sccm to 700 sccm. With increase of the Cp_2Mg flow the concentration of ionized acceptors also increases reaching the maximum value at Cp_2Mg flow = 500 sccm. The next increase of the flow till 750 sccm is followed by the decrease of ionized acceptors probably related to the occupation of the acceptor levels by electrons induced by charged defects created in GaN layers at high doping. For the 10 nm-thin top p^+-GaN layer the concentration of 1×10^{19} cm^{-3} is obtained.

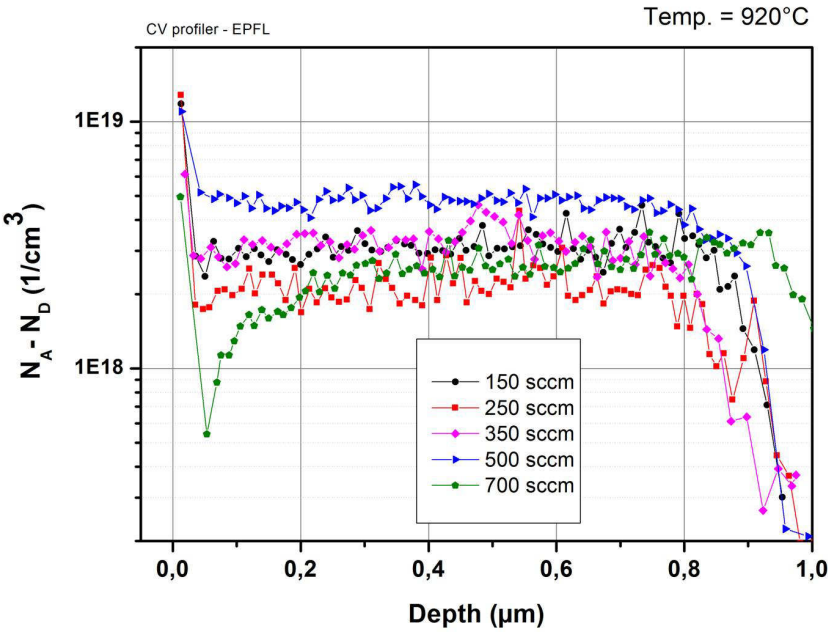

Figure 3.7. Acceptor concentration-depth profile of the p-GaN layers grown with Cp_2Mg flow varied from 150 to 700 sccm [Mukhtarova, 2013].

* Capacitance-voltage technique consists of placing a contact on the semiconductor surface and applying a voltage to create the depletion region (the region with no carriers inside) under the contact. The sample is periodically etched with a liquid electrolyte on a certain depth (other configuration used liquid metals as contacts and etc can be used). The capacitance measurements are done at every etch point. The measurements were performed by C. Durand in Ecole Polytechnique Fédérale of Lausanne (EPFL).

Hall measurements* were performed to analyze electrical characteristics of grown p-GaN layers. Pd (5 nm)/Ag (100 nm)/Ni (20 nm)/Au (50 nm) are used as a contact to verify electrical properties of the layers. Before measurements, all samples were annealed at 500 ^{o}C in oxygen atmosphere.

Table 3.1 presents the values of the hole concentration, carrier mobility and resistivity for p-GaN layers grown with different Cp_2Mg flow.

Table 3.1. Values of hole concentration p, mobility μ_p and layer resistivity ρ for p-GaN layers grown at different Cp_2Mg flow [Mukhtarova, 2013].

Cp_2Mg flow, sccm	p, cm^{-3}	μ_p, $cm^2/(Vs)$	ρ, Ωcm
250	7.3×10^{16}	11.5	7.75
350	5.7×10^{16}	10	10.7
500	4.0×10^{16}	30	5.25
700	x	x	x

There is no big difference in hole concentration between samples with a value of 4-7×10^{16} cm^{-3}. The layer grown at 700 sccm Cp_2Mg flow showed n-type behavior. The same effect (inversion of the conductivity type) was also seen for highly doped p-InGaN layer [Tuna, 2013]. The authors suggested that it could be related to the creation of negatively charged defects that can compensate the hole concentration or to the formation of compensation defect complexes such as Mg-V_N. The values of mobility and resistivity are similar to those obtained by other groups for p-doped GaN layers [Kaufmann, 2000; Svensk, 2007]. The layer grown at Cp_2Mg flow = 500 sccm shows the best characteristics in terms of mobility and resistivity and was chosen in the following.

3.2 Characterization techniques

In this section, we discuss the basics of the main characterization methods and experimental setups that we used to analyze structural and optical properties of the grown samples: high-resolution X-ray diffraction (HRXRD) setup, photoluminescence spectroscopy (PL) and transmission measurements. The principal electrical characterization techniques for photocurrent and current-voltage measurements of the device will be also discussed.

* Hall measurements were performed at room temperature by W. Chikhaoui in CEA-LETI.

3.2.1 X-ray diffraction

X-ray diffraction is a wide-used, powerful, non-destructive experimental technique to analyze the structural quality and morphological parameters of the investigated samples such as layer thicknesses, strain state, lattice parameters, crystalline orientation, composition etc.

X-rays, usually produced from cupper (Cu) or molybdenum (Mo) sources, have a very small wavelength (comparable with interatomic distance of the crystal) that can be efficiently scattered by atoms. This unique property gives a possibility to analyze the atomic and chemical structure of the materials.

3.2.1.1 Bragg's law and Laue conditions for diffraction

In 1912, Bragg developed a simple equation that shows a relation between diffraction angles of the peaks and interplanar atomic distance. The graphical illustration of Bragg's law is presented in Figure 3.8. For having a constructive interference, the difference in the paths of the incident and reflected waves of each plane must be equal to an integer number of the incident X-ray wavelength (nλ). To satisfy this, the Bragg's law can be written as following:

$$2d\ sin(\theta) = n\lambda, \tag{3.1}$$

where d - interplanar atomic distance, θ - angle between the incident beam and diffracting planes, λ - X-ray wavelength, n - integer number corresponding to the order of reflection.

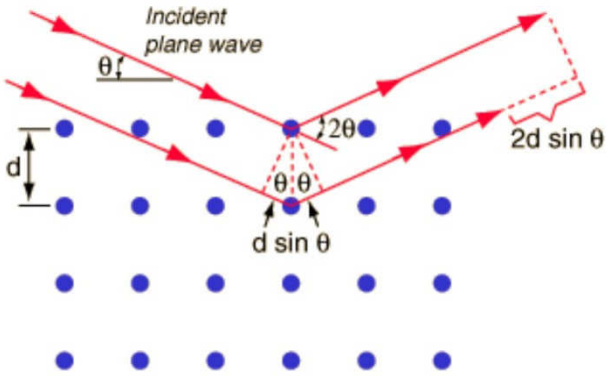

Figure 3.8. A graphical representation of Bragg's law.

In this view, we consider only the planes constituted by discrete atoms. In a more precise point of view, the atoms scatter X-rays and dislike the planes, they can scatter the waves in all three dimensions. Figure 3.9 (a) shows a more realistic picture of the X-ray diffraction. If φ_0 is an angle between the incoming X-ray wave and a row of scattering atoms

and φ is an angle between the reflected wave and a row of scattering atoms, then condition for constructive interference looks as following:

$$h\lambda = a\,(\cos(\varphi) - \cos(\varphi_0)), \tag{3.2}$$

where a – is the distance between two atoms, h is an integer.

Therefore, the X-rays will be scattered only in defined directions that lay on the surface of imaginary cone (diffraction cone) (Figure 3.10 (b)).

For three-dimensional case (3D), we have:

$$\begin{aligned} h\lambda &= a\,(\cos(\varphi) - \cos(\varphi_0)) \\ k\lambda &= b\,(\cos(\alpha) - \cos(\alpha_0)) \\ l\lambda &= c\,(\cos(\beta) - \cos(\beta_0)) \end{aligned} \tag{3.3}$$

Eq. (3.3) represents Laue conditions for diffraction. Three resulting cones will intersect at defined points. Using Eq. (3.3), Bragg's law and supposing an angle 2θ between incoming and reflected waves, we can write Laue equation as:

$$\left(\frac{h^2}{a^2} + \frac{k^2}{b^2} + \frac{l^2}{c^2}\right)^{1/2} = \frac{2sin\theta}{\lambda} = \frac{n}{d}\,, \tag{3.4}$$

where h, k, l are Miller's indexes (they define a family of planes from which the scattering occurs).

For hexagonal lattice Laue equation can be simplified and is written:

$$\left(\frac{4(h^2+hk+k^2)}{3a^2} + \frac{l^2}{c^2}\right)^{1/2} = \frac{2sin\theta}{\lambda} = \frac{n}{d} \tag{3.5}$$

a) b)

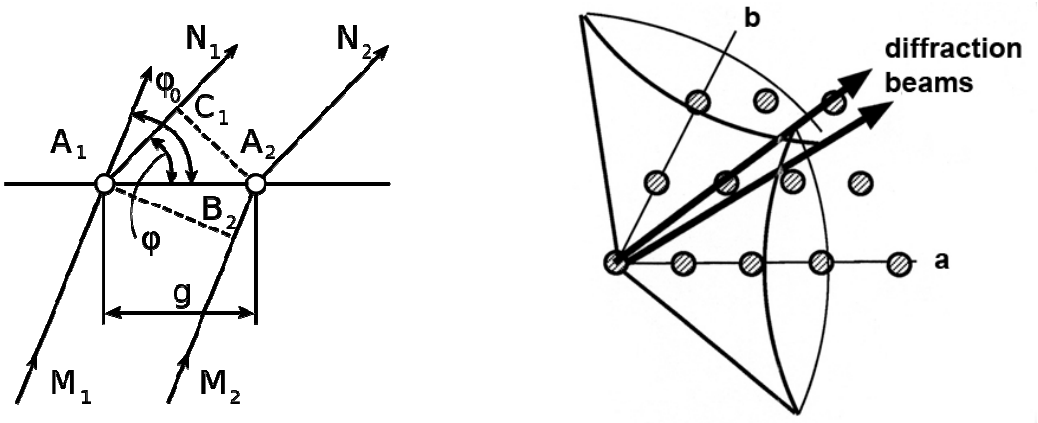

Figure 3.9. a) Graphical representation of Laue conditions for diffraction. $M_{1,2}$ are incoming waves, $N_{1,2}$ are reflected waves, $A_{1,2}$ are atoms ; b) Diffraction cones for 2D rows of atoms.

Therefore, Laue equation says that we observe reflection at scattering angle 2θ for certain values h/a, k/b, l/c, that can be written as a^*, b^*, c^* in the reciprocal space, where

$a^*=1/a$, $b^*=1/b$, $c^*=1/c$. $1/d$ is called a scattering vector $K = ha^* + kb^* + lc^*$. K can also be written as a difference in wave vectors between incident k_i and reflected k_f waves: $K = k_i - k_f$ with $|k_i| = |k_f| = 2\pi/\lambda$.

3.2.1.2 Different configurations for XRD measurements

We can choose different configurations for measurements depending on information we want to get from HRXRD techniques.

In-plane configuration ({hk0} family of planes)

In-plane configuration is used to measure intensities from lattice planes that are perpendicular to the sample surface. This configuration is applied to measure very thin films as it allows eliminating the high-intensity background signal from a thick substrate.

The configuration for in-plane XRD measurements is shown in Figure 3.10.

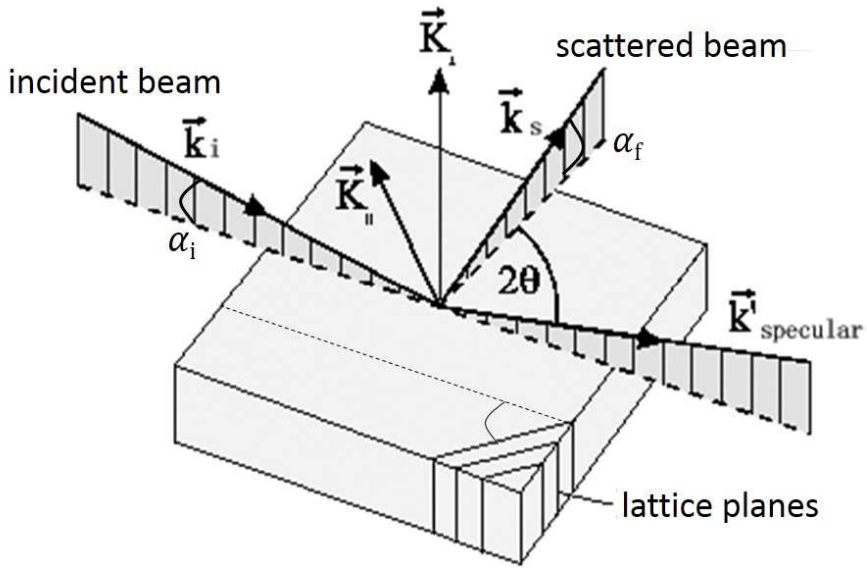

Figure 3.10. Configuration for in-plane XRD measurements.

The angle of the incident wave to the sample surface α_i is very small (close to critical angle) to limit the wave penetration into the sample. The reflected beam has an angle α_f to the sample surface. 2θ is an angle between reflected and incident waves. During the measurements, the sample is rotated around the normal to the surface until the particular lattice plane lying perpendicular to the surface satisfies the Bragg's conditions with in-plane Bragg angle $2\theta = \theta_i + \theta_f$, where $\theta_{i(f)}$ are angles between incident (reflected) wave and the

diffracted lattice plane. From {hk0} measurements, we can obtain an information about in-plane lattice parameter and surface structure. But if we want to obtain an information about planes parallel or inclined under a certain angle α to the sample surface, we have to choose another configuration for HRXRD measurements.

Out-of-plane configuration

In its turn, out-of-plane configuration can be divided on two configurations: symmetrical ({00l}) and asymmetrical ({hkl}) (Figure 3.11). For symmetrical scan, we are able to measure the interatomic distance between the planes that are parallel to the sample surface (in hexagonal symmetry for (0001)-oriented GaN, it corresponds to *c*-lattice parameter).

Symmetrical scan

During symmetrical scan, the sample and detector are turned keeping the ratio $\omega/\theta = 1$, where ω is an angle between the incident x-ray wave and the sample surface, and 2θ is an angle between the incident and reflected waves (Figure 3.11(a)).

Two types of scan are usually performed in this configuration: ω-scan that allows determining the mosaicity of the sample (the existence of different orientations in the crystal) and ω-2θ scan from which we can derive the value of out-plane lattice parameter (*c*-parameter for hexagonal GaN), sample structure (layers or superlattice), lattice period, layer thicknesses etc. To get an information about strain states and in-plane lattice parameter (*a*-lattice parameter for hexagonal structure), we have to use complementary asymmetrical scans.

Asymmetrical scan

Asymmetrical scan conditions allow the measurements of the interplanar distance between planes inclined by an angle α with respect to the sample surface. To perform this kind of measurements, we have to tilt the sample around ω (angle between the incident wave and sample surface). The sample can be tilted in two ways: towards to lower or higher omega values. So, $\omega_{a-} = \theta - \alpha$ (Figure 3.11 (b)) or $\omega_{a+} = \theta + \alpha$ (Figure 3.11 (c)). These two configurations allow for some reflections to have grazing incidence or emergence geometries.

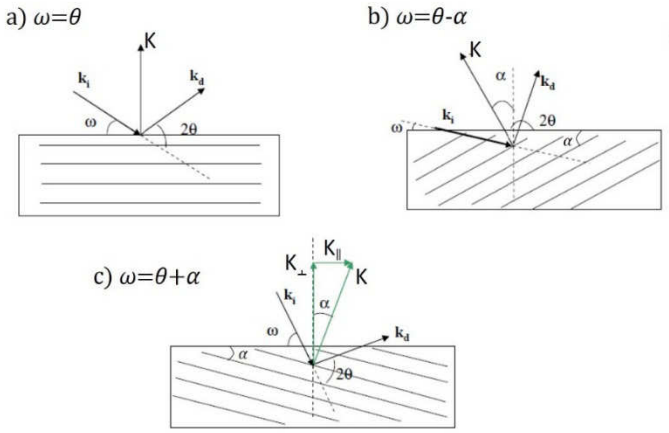

Figure 3.11. Different configurations to measure the interatomic distance: a) symmetrical scan; b) and c) asymmetrical scans.

The value of scattering vector K in the asymmetrical configuration has two components: in-plane component $K_{/\!/}$ and out-of-plane component $K_{\perp}$ (Figure 3.11(c)). Taking into account Eq. (3.4) and given ω and θ angles, we derive the values of $K_{\parallel}$ and $K_{\perp}$ as a function of θ and ω:

$$K_{\parallel} = \frac{4\pi}{\lambda}\sin\theta\,\sin(\omega-\theta) \tag{3.6}$$

$$K_{\perp} = \frac{4\pi}{\lambda}\sin\theta\,\cos(\omega-\theta) \tag{3.7}$$

3.2.1.3 HRXRD setup

Figure 3.12 presents a schematic of our HRXRD setup. The setup consists of four main parts: x-ray source, monochromator, analyzer and detector. A Cu anode is used as a source of X-rays with the $K_{\alpha 1}$ wavelength of 1.54056 Å that is selected by a monochromator. Monochromator consists of 2 monocrystals of (220) Ge that are placed in 4 crystal (-++-) configuration (Figure 3.12). This kind of configuration allows reducing the wavelength spreading and angle divergences. The maximum resolution that can be achieved is: $\Delta\theta$ = 0.0033^{o} and $\delta\lambda/\lambda = 1.4\times10^{-4}$. Analyzer has the same configuration as monochromator, but with only two (220) Ge that allows to improve the angular precision of the collected beam ($\leq$ 0.001^{o}). The detector has an aperture of 2^{0} that can be reduced by inserting slits in front of it. The picture of the experimental setup used in this work is shown in Figure 3.13.

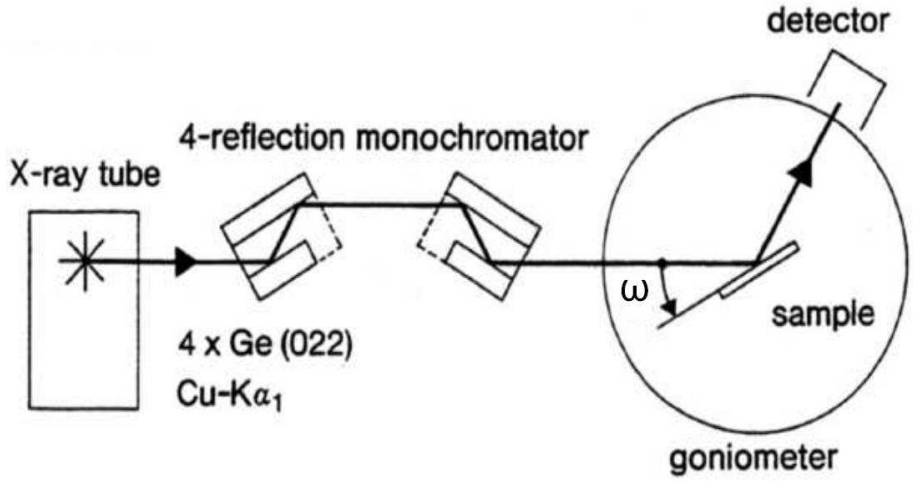

Figure 3.12. Schematic of (-++-) monochromator configuration [Das, 2012].

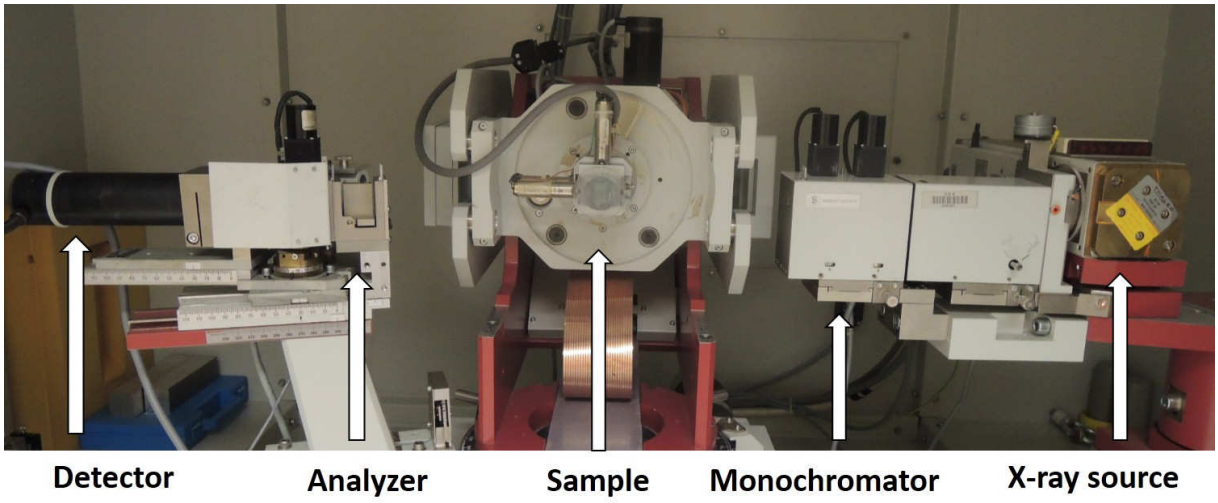

Figure 3.13. Picture of the HRXRD setup used in this work.

The sample orientation is controlled by a goniometer that adjusts angles between incoming beam and atomic planes. Four angles can be adjusted independently: ω (angle between incident beam and sample surface), 2θ (angle between incoming and outcoming beam), φ (rotation angle around z-axis), and χ (rotation angle around x-axis) (Figure 3.14). The goniometer allows also the movement along *x*, *y* and *z* axis, to center the sample.

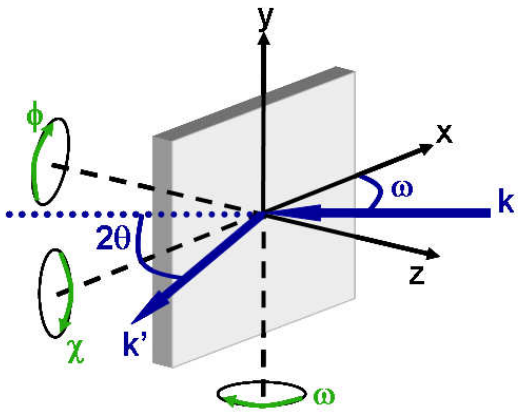

Figure 3.14. Schematic of the angles available for alignment of the sample [Das, 2012].

In this work, we mostly used only out-of-plane configuration for the measurements: symmetric *ω-2θ* scan and asymmetric types of scan (reciprocal space map). *ω-2θ* scan around (0002) reflection was used to estimate the sample quality (from intensity and full-width-half-maximum of the peaks), *c*-lattice parameter (from the peak angular position) and superlattice period (from the angular distance between satellite peaks). Using simulation with X'pert Epitaxy 4.0 from Philips Analytical software, it is also possible to estimate the values of quantum barrier and well thicknesses as well as In-composition. Assymetrical (10-15) scan was also performed in the frame of this thesis to get an information about sample's strain state and *a*-lattice parameter. From that type of scan, we can obtain the values of $\parallel$ and $\perp$ components of scattering vector *K* using Eq. (3.6) and (3.7). The *a* and *c*-lattice parameters for hexagonal structure are related to $K_{\parallel}$ and $K_{\perp}$ as:

$$a = \frac{2\pi}{K_{\parallel}}\sqrt{\frac{4h}{3}} \tag{3.8}$$

$$c = \frac{2\pi l}{K_{\perp}} \tag{3.9}$$

where *a* and *c* are lattice parameters, *h* and *l* are Miller's indexes.

3.2.2 Photoluminescence and phototransmission spectroscopy

For the optical characterization of the samples, we used two main methods: photoluminescence and phototransmission.

Photoluminescence

Photoluminescence is a spontaneous emission of light under optical excitation. Simplified mechanism of photoluminescence is depicted in Figure 3.15.

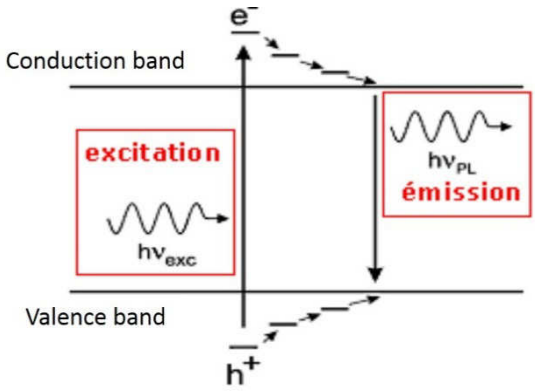

Figure 3.15. Schematic of the photoluminescence process.

Incoming photons with energy larger than the material band gap are absorbed by the sample. The absorbed photon creates an electron-hole pair inside semiconductor that recombines rapidly emitting another photon. The energy of emitted photon depends on the material properties and is approximately equal to the band gap of the sample. In the first approximation, the lowest energy of emitted photon in QW-based sample is given as:

$$E = E_g + E_{e1} + E_{h1}, \tag{3.10}$$

where E_g - band gap of the semiconductor, $E_{e1(h1)}$ – first confinement level of electrons (holes).

From intensity and shape of the photoluminescence peaks, we can derive an information about the structural quality of the sample and about the nature of acceptors and donors. The presence of emission at energies lower than a band gap, can be associated with impurities and defects.

The photoluminescence setup used in this work is presented in Figure 3.16. A 244 nm frequency-doubled continuous wave Ar^+ laser serves for optical excitation of the samples. The diameter of laser spot is about 50 μm. The signal from the sample is collected in a 45 cm focal-length Jobin-Yvon monochromator and detected by an ultraviolet-enhanced charge-coupled device (CCD). A regulated helium cryostat is used to perform the measurements at low temperatures (from 5 to 300 K).

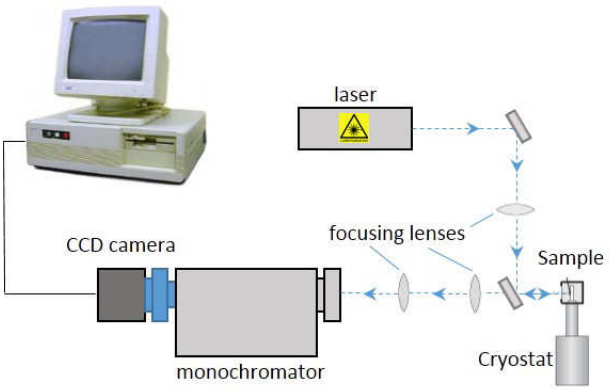

Figure 3.16. Schematic of the photoluminescence setup.

Phototransmission

Optical transmission measurements show the quantity of light that passed through the sample without absorption. We can determine a layer thickness, linear refractive index, linear absorption and effective optical band gap from transmission spectra analysis. The schematic of the setup is presented in Figure 3.17.

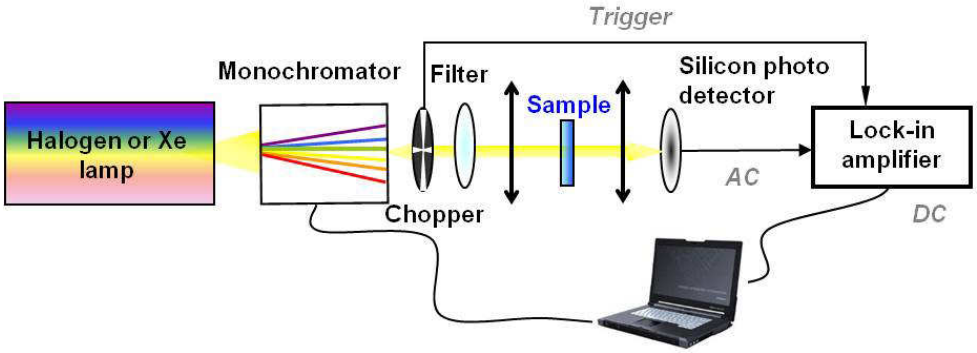

Figure 3.17. Schematic of the setup for optical transmission measurements used in this work.

In this work, we used two different lamps for visible and ultraviolet spectral ranges. 150W Xe-arc lamp coupled to a Gemini-180 double monochromator was used for 250-430 nm and 100W halogen lamp coupled with an Omni Lambda 300 monochromator for 430-900 nm spectral range. Both lamps were calibrated with a reference Si photodetector. All measurements were done at room temperature. The wavelength is chosen by a *xyz* monochromator. The chopper is connected to a lock-in amplifier to chop the signal in order to remove the external noise. Finally, we measure the dependence of the light intensity on the wavelength with $[I(\lambda)]$ and without $[I_0(\lambda)]$ the sample. The transmission coefficient spectrum is extracted using the Beer-Lambert law (see Eq. (2.3)).

3.2.3 Electrical characterization techniques

We used two types of electrical characterization to analyze photovoltaic properties of the devices. Responsivity measurements show the photovoltaic response of the device at every wavelength and allow deriving the value of external quantum efficiency (EQE). Current density-voltage measurements allow determining the main solar cell parameters such as short-circuit current, open-circuit voltage and fill factor. Based on these data the overall conversion efficiency of the device can be calculated with Eq. (2.10).

Responsivity measurements

To measure responsivity *R* of the device we used almost the same setup as for transmission mesurements. The schematic of the setup is presented in Figure 3.18**.**

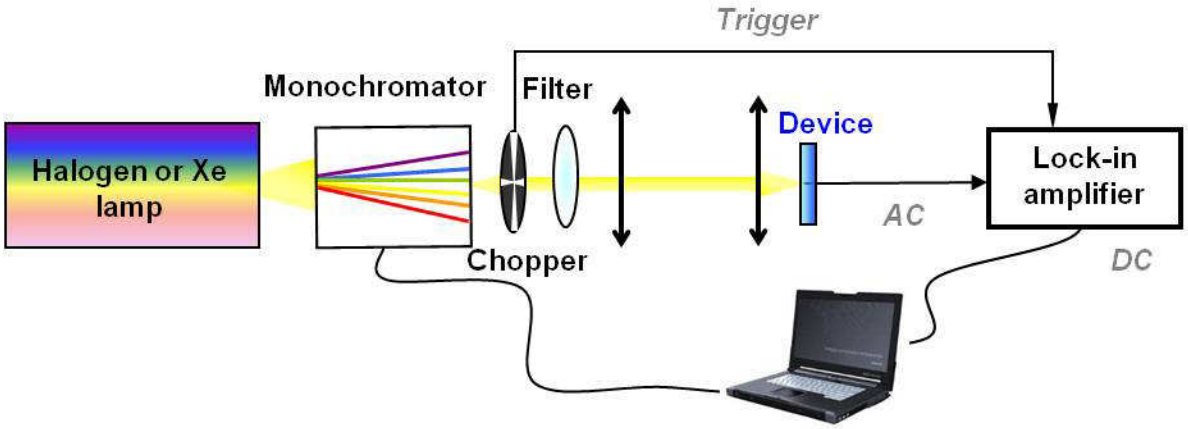

Figure 3.18. Schematic of the setup for responsivity measurements.

The difference between setups consists in the replacement of the Si photodetector by the device we want to measure. We used the same lamps as for transmission measurements: 150W Xe-arc lamp coupled to a Gemini-180 double monochromator was used for 250-430 nm and 100W halogen lamp coupled with an Omni Lambda 300 monchromator for 430-900 nm spectral range. With the lock-in amplifier, we measure the value of voltage depending on the incident wavelength. The responsivity is usually found as the ratio between the input irradiance and the output electrical signal. As the power of the incident light is unknown, we measure only the shape of the responsivity curve. To obtain the quantitative values of responsivity, a He-Cd laser with 325 nm wavelength is used. Knowing the power of the incident light from the laser (typically, the power of laser is set to 50 μW), and after

measuring output current given by the device, we can estimate the value of the responsivity at λ_0 = 325 nm as:

$$R(\lambda_0) = \frac{I(\lambda_0)}{P_{opt}}, \tag{3.11}$$

where $I(\lambda_0)$ – measured current given by the device at λ_0, P_{opt} – laser power.

The unit of responsivity is A/W. Knowing the value of responsivity at λ_0 = 325 nm, the multiwavelength curve can be normalized to this point.

Having values of responsivity, we can calculate the external quantum efficiency (EQE) of the device by the formula:

$$EQE = R\frac{hc}{q\lambda}, \tag{3.12}$$

where R – responsivity at the wavelength λ, h – Planck's constant, c – speed of light, q – electron charge.

Current-voltage measurements

Current-voltage measurements in the dark and under 1 sun AM1.5G solar illumination were recorded with an Agilent 4155C parameter analyzer.

The equivalent solar illumination was provided by solar simulator. We used two solar simulators. The first one is the *Oriel 3A Solar Simulator* equipped with a 450 W ozone-free Xe lamp located at CEA-Grenoble/INAC laboratory of Structure and properties of molecular architectures (SPRAM) (Dr. Louis Grenet and Dr. Giovanni Altamura). The second one is The *Spectra-Nova CT Series Solar Cell Tester* located at CEA/LITEN (Dr. Jérôme Faure-Vincent). All measurements were performed at room temperature.

3.3 Device fabrication process

After structural characterization of as-grown samples, they were processed into solar cells. Device fabrication was performed in a clean room of the Institute for Nanoscience and Cryogenics (INAC) CEA-Grenoble (PTA, Plateforme Technologique Amont) and included three main technological stages for the realization of solar cells: photolithography, metallization and etching. In this section, we will shortly detail all of them, step by step.

3.3.1 Surface cleaning

Different contaminations can occur on the sample's surface. Before starting any of the above-mentioned steps, the surface of the samples must be cleaned. It is recommended to clean the sample directly before the processing to avoid the contamination during sample storage. First cleaning (before any contact deposition) includes firstly, the cleaning in acetone in ultrasonic bath in order to remove organic contaminations; secondly, as acetone is not dissolvable in water, the sample should be put in methanol to clear away its residues. Afterwards, the sample is blown by dry nitrogen.

It was shown by Smith *et al.* that HCl + deionized (DI) water is quite effective for removing oxygen and carbon from the GaN surface [Smith, 1996]. Therefore, following the cleaning with solvents, the samples are left in 37% of hydrochloric acid for 3-5 minutes and rinsed in DI water. After contact depositions, all cleaning of the samples is done using only acetone and methanol.

3.3.2 Mesa formation

The size of the mesa determines the size of the device. In the literature, different techniques were used to form mesas on GaN: reactive ion etching (RIE), chemically assisted ion beam etching, inductively coupled plasma etching (ICP) etc. [Lin, 1994 Lee, 1998; Rawal, 2012]. In this work, we used BCl_3/Cl_2 ICP etching to form mesas with 2 sizes: 0.5×0.5 mm^2 and 1×1 mm^2. ICP etching has a good selectivity, high etching rate and it leaves smooth etched surface. The last point is important for solar cell devices, as very often they suffer from the carrier losses because of surface recombination. The etching rate of GaN in our ICP setup was about 400 nm/min and it increases with In-composition. Because of relatively strong bond strength of nitrides, we had to use quite high dc-voltage ~ 450 V [Shul, 1998]. The final etched thickness (depening on the thickness of the active region) was checked by a *Dektak profilometer*. The surface morphology after etching was examined with scanning electron microscope (SEM) showing a smooth surface of the device edges after etching. An example of the SEM images of the etched sample is shown in Figure 3.19.

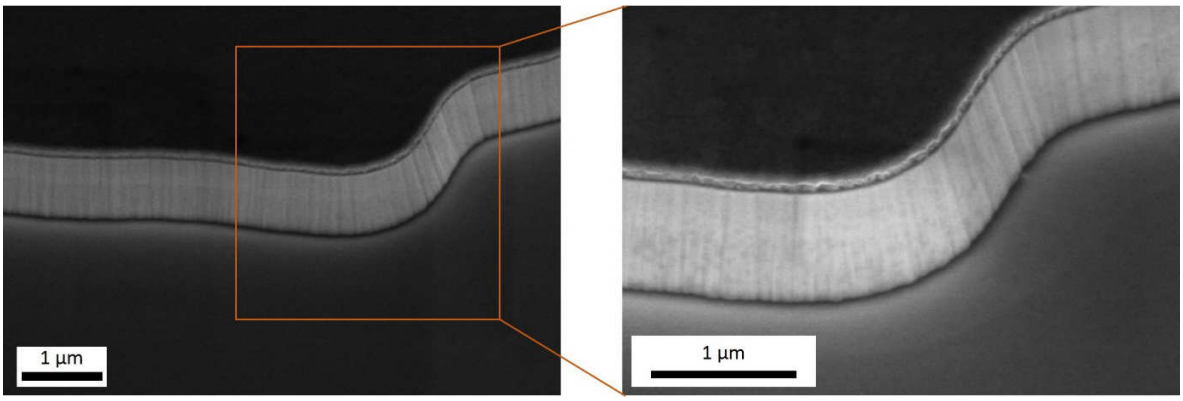

Figure 3.19. SEM images of the device edge after ICP etching.

3.3.3 Photolithography

Photolithography is the most common method used to pattern the devices. One of the important advantages of photolithography process is its ability to fabricate a lot of complex devices simultaneously and in a relatively short time. The resolution of the photolithography is determined by the wavelength of the exposure source. In our case, we have relatively large devices (the size of mesa is 0.5×0.5 mm^2 and 1×1 mm^2) and we used ultra-violet (UV) light with 365 nm wavelength. When the desired size of the device is smaller, it is necessary to decrease the exposure wavelength. Usually deep UV or electron lithography can be used as a solution for sub-micronic pattern. Schematic of the photolithography process is depicted in Figure 3.20.

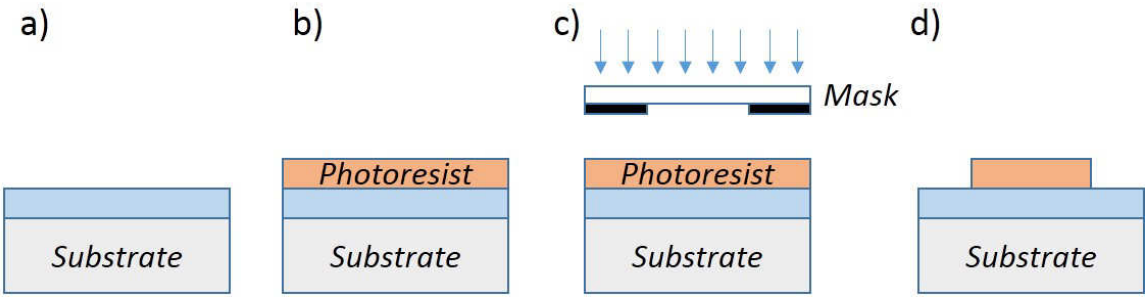

Figure 3.20. Schematic of the photolithography process: a) net substrate with GaN layer on it; b) the resist is spun on the sample; c) exposure of the resist through the mask; d) resist development.

Here, we use AZ5214E resist that allows to obtain a resolution of about 1 µm. It is spun on the sample during 1 min at the speed of 4000 rounds/min leading to the 1.4 µm resist thickness. As the resist always contains some solvents to have a liquid phase application, the sample is baked after resist spinning during 2 min at 100 ^{0}C. This bake helps to evaporate the excess of solvents, stabilizes the resist film and improves the adhesion of the resist to the wafer. After that, the sample is ready for UV light exposure. In this work, we used MJB4 setup with UV 365 nm wavelength. UV exposure changes chemical properties of the resist making it more (for positive) or less (for negative) soluble in the developer solution. In our case, we used AZ5214E as a negative resist. During the first exposure (the duration of exposure is 5.5 sec), the wafer was in a direct contact with a mask. This technique allows higher resolution but may damage the mask as well as the sample. After, the samples were baked at 120 ^{0}C during 2 minutes. This procedure helps to transform AZ5214E resist into negative one. This reversal capability is obtained by a special crosslinking agent in the resist formulation which becomes active at temperatures above 110°C and only in exposed areas, leading to an almost insoluble (in developer) and no longer light sensitive substance, while the unexposed areas still behave like a normal unexposed positive photoresist. After, it is required one more exposure (without mask) during 33 sec, that is called flood-exposure. The last step of photolithography process is the development. It determines the final shape of the photoresist profile and the line width. The samples are developed in the solution of water and AZ developer (1:1) during 25-40 sec. The time of the development slightly varies from sample to sample depending on the resist thickness.

3.3.4 Metallization and lift-off

Metallization is a very important process for electrical contact of the device. There are two main types of metal deposition: evaporation and sputtering. In our work, we used metal evaporation technique in which the metals are heated and evaporated in a high vacuum forming a thin film on the sample surface. The nature of the materials to form contacts should be carefully chosen to make either ohmic or schottky contact.

In photovoltaic cells ohmic contact is typically the most desirable because the carriers can easily move between semiconductor and metal. Low contact resistance allows minimizing the power consumption of future device and prevents the internal heating of the contact. One

of the possible mechanisms to produce the current flow between metal and semiconductor is a thermal emission. Therefore, to let the carriers freely flow from semiconductor to metal, it is necessary to decrease the barrier (schottky barrier) that is formed at the metal/semiconductor interface. The height of schottky barrier is determined as a difference between the metal work function and the electron affinity of semiconductor. Sometimes it can be difficult to find an appropriate metal to produce an ohmic contact through thermal emission, especially for semiconductors with wide band gap such as GaN. Therefore, there is one more way to allow free movement of the carriers between metal and semiconductor. If the semiconductor is highly doped at the semiconductor surface, as a consequence of that the depletion layer between metal and semiconductor becomes very thin allowing carriers to tunnel through the barrier.

When, the current dependence on applied voltage is not linear, this type of contact is called schottky. Schottky contact has a rectifying behavior allowing no or very small current to flow through the contact till the critical voltage is reached. The schemes of the band diagram for ohmic and schottky contact are presented in Figure 3.21.

Ohmic contact

At the moment of contact formation between metal and semiconductor, electrons from metal come to semiconductor aligning Fermi levels (Figure 3.21 (a and b)). If the value of metal work function is close to the electron affinity of the semiconductor, the height of the barrier created at the metal/semiconductor interface is quite small and electrons freely go from metal to semiconductor and in opposite way depending on applied voltage.

Schottky contact

For schottky contact, electrons from semiconductor go to metal leaving positive charges behind. These positive charges create a space charge region appearing as a barrier on a band diagram. If the difference in work function and electron affinity is high, the height of the barrier increases blocking further movement of electrons from semiconductor to metal and from metal to semiconductor (Figure 3.21 (c and d)).

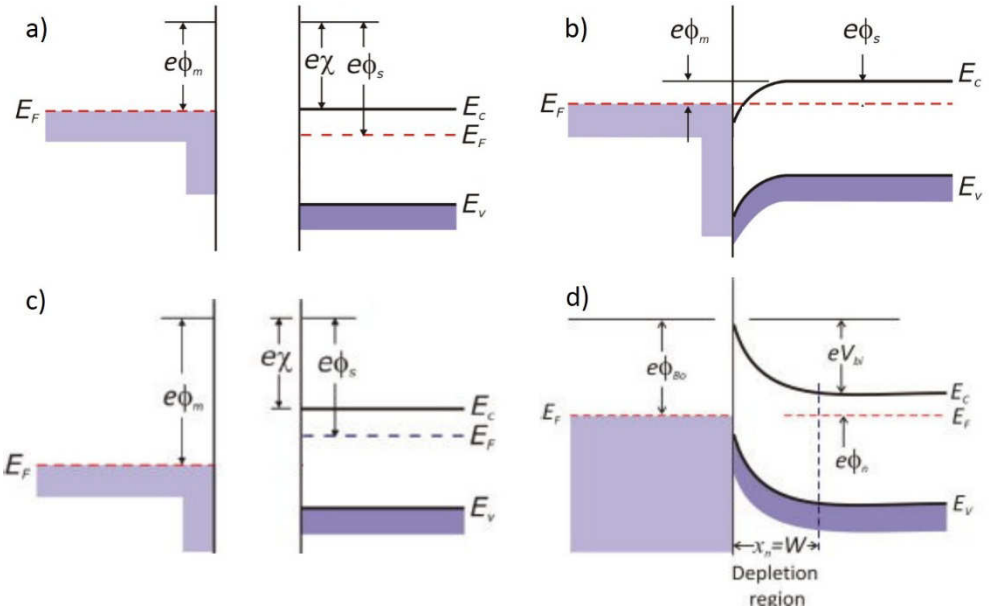

Figure 3.21. Scheme of the band diagram for metal/semiconductor heterojunction: a) metal with small work function and n-type semiconductor before contact; b) ohmic contact with n-type semiconductor; c) metal with large work function and n-type semiconductor; d) Schottky contact of metal and n-type semiconductor.

There are some types of the devices like schottky diodes, metal-semiconductor field effect transistors (MESFET) etc. that require schottky contacts. In the case of the solar cells, an ohmic contact is necessary because it allows current flow without voltage drop.

3.3.4.1 Ohmic contact to n-GaN

Both ohmic and schottky contacts to n-type GaN were widely studied by different groups [Schmitz, 1998; Dobos, 2006]. Usually, ohmic contact is achieved by depositing metals with low work-function such as Al (Φ_m = 4.24 eV) or Ti (Φ_m = 4.33 eV) [Skriver, 1992]. Lin *et al.* showed that the resistivity of Al contact can be significantly improved by insertion of thin Ti layer before Al deposition [Lin, 1993; Luther, 1997]. Two possible mechanisms were proposed to explain a low resistivity of Al/Ti contacts. One of them that Ti forms TiN layer on the top of n-GaN resulting in a creation of nitrogen vacancies that act like donors forming highly-doped n-GaN layer on the metal/semiconductor interface. Heavy doping in the semiconductor causes a very thin depletion width and electron that can tunnel through the Schottky barrier leading to ohmic behavior. And another one is diffusion of silicon to the surface of GaN or/and diffusion of Ti (a potential donor) into semiconductor [Thierry, PhD thesis]. In next works, the resistivity of ohmic contact was even more improved

by inserting Ti/Al/Ni/Au contact [Boudart, 2000; Qin, 2004]. The top Au layer is introduced in order to avoid the oxidation of Al layer and improve the current spreading in the contact. Ni layer between Al and Au was shown to be important to prevent the Au diffusion through Ti/Al layers. In this work, we used Ti/Al/Ni/Au contact with metal thicknesses of 30/70/20/100 nm, respectively. An example of *J(V)* curve for n-contact used in this work is presented in Figure 3.22 showing a good ohmic behavior. The specific resistance of the contact is about 3×10^{-4} Ω*cm^2.

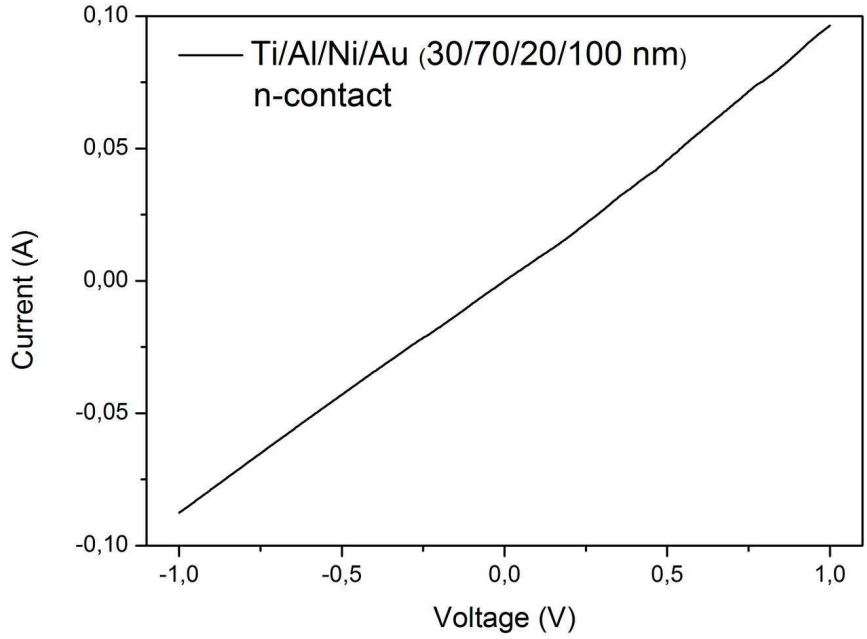

Figure 3.22. Example of J(V) curve for Ti/Al/Ni/Au (30/70/20/100 nm) n-contact used in this work.

3.3.4.2 Ohmic contact to p-GaN

Unlike to n-contact, ohmic contact to p-GaN is very difficult to achieve. It is related to several factors:

- The lack of appropriate metals (as GaN has a large band gap (3.4 eV). Indeed, materials with very high metal work function (normally more than 5 eV) are required.
- Quite low hole concentration in p-GaN (because of high activation energy (about 200 meV) of doping Mg atoms.

And also one of the possible reasons that was not proved or disposed is the losses of nitrogen during fabrication process that can cause a conversion of p-type GaN layer into n-type.

Typically, Ni/Au is used as a contact to p-GaN [Smalc, 2010; Sheu, 1999]. Ni prevents the Au diffusion to the GaN surface and removes hydrogen from the p-GaN surface.

In this work, a thin Ni (5 nm)/Au (5 nm) layer was deposited on p-GaN and annealed in an oxygen atmosphere. After-deposition, the annealing step under oxygen atmosphere was shown to improve the conductivity of the contact by creating NiO/Au [Qiao, 2000]. Contact thickness is choosen to be very thin (overall thickness is only 10 nm) to keep the contact as much transparent as possible. Anyway there are still ways to improve the contact as in our case the transmission is about 50% at the wavelength less than 450 nm (Figure 3.23).

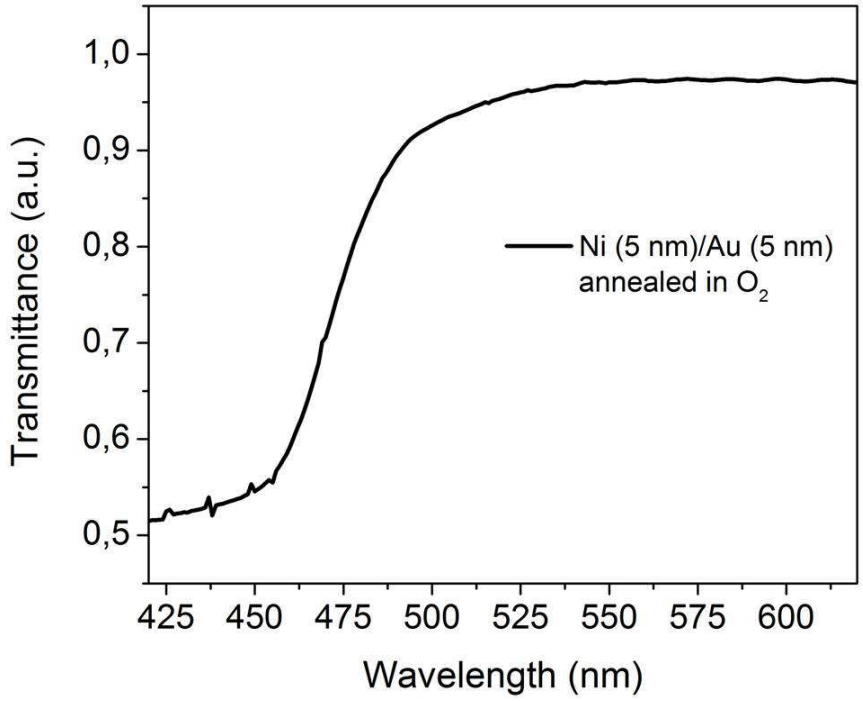

Figure 3.23. Transmission measurements of the Ni (5 nm)/Au (5 nm) contact after annealing in oxygen atmosphere during 5 minutes at 500 ^{0}C.

Note that the resistivity of Ni (5 nm)/Au(5 nm) contact is relatively high because of this small value of thickness. To improve the resistivity, Ni (30 nm)/Au (100 nm) fingers with 5 μm width were deposited on Ni (5nm)/Au(5 nm) semi-transparent contact. After deposition p-contact was annealed at 500 ^{0}C during 5 minutes in oxygen atmosphere. A represantative *J(V)* curve of the p-GaN contact is presented in Figure 3.24.

The specific resistance of the p-contact used in this work was calculated through transmission line method (see in details in Annex 1) at V = 20V (current is 0.2 mA) leading to

the value of 0.11 $\Omega \cdot cm^2$ that is comparable with values obtained in the literature [Moon, 2008]. The value of sheet resistance for p-GaN is about 7.5×10^4 Ω.

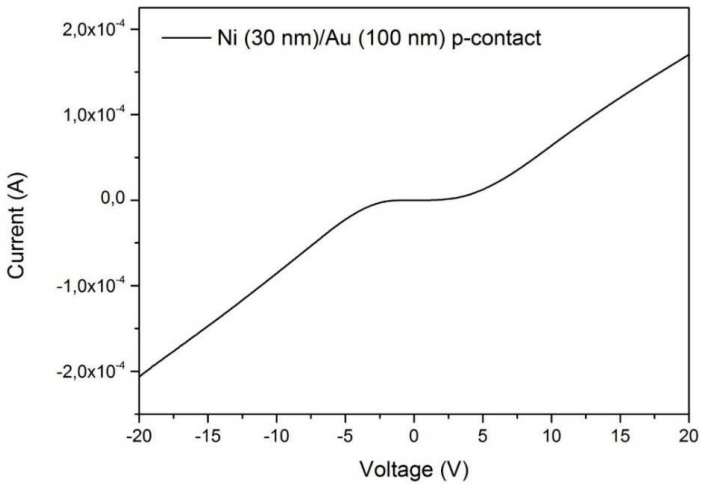

Figure 3.24. J(V) curve of Ni (30 nm)/Au (100 nm) p-contact used in this work.

3.3.4.3 Lift-off

The lift-off is used in this thesis as the last step on the way to form a contact and it includes a removal of metal from the substrate surface for creation of needed pattern. After standard photolithography process and metallization, the metal is both deposited directly on the top of the substrate and on the top of the resist that was left by photolithography. It is necessary to remove the resist together with the metal to form a final pattern. In our case, the lift-off is usually done immediately after metal deposition. Samples are put in a small glass vessel with acetone for 3-5 minutes; the vessel is shaken by hand to remove the resist film with metal on it. Afterwards, if metal was not completely removed, we used ultra-sonic bath for 3-5 seconds. After acetone cleaning, all samples were rinsed in methanol and dehumidified by dry nitrogen.

A top-view image of the device after fabrication is presented in Figure 3.25**.**

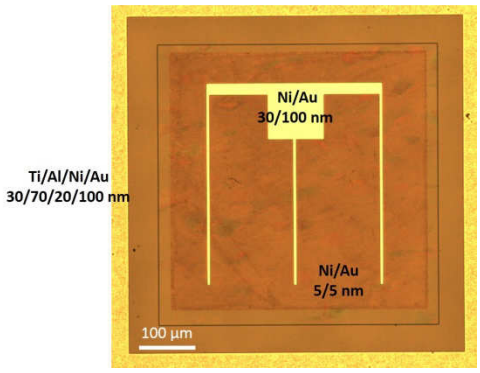

Figure 3.25. Top-view image of the fabricated device with 0.5×0.5 mm^2 mesa size.

3.4 Optimization of the solar cell grid design

The conversion efficiency is mostly determined by the choice of materials for solar cell fabrication and the solar cell design. However, there are still some additional losses that come from the contacts. In our case, we use finger contacts. The distance between fingers is a very important parameter on the way to improve the solar cell efficiency. If the distance between fingers is too small, it shadows the solar cell surface decreasing the amount of absorbed light and therefore, the value of short-circuit current that strongly depends on the light absorption. Too large distance between fingers causes the increase of the contact resistance and losses in the carrier collection. Thus, the space between fingers should be carefully chosen. We fabricated three solar cells with different finger pitches to optimize the contact spacing. The sample structure is presented in Figure 3.26.

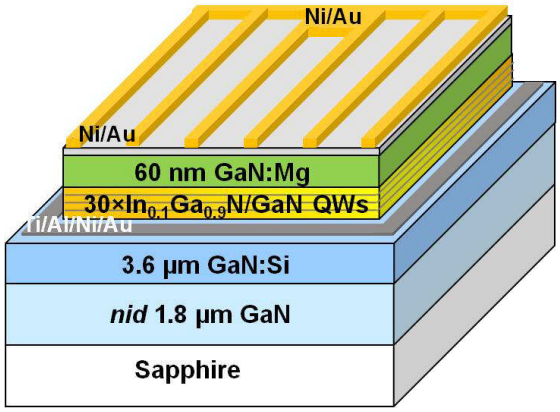

Figure 3.26. Schematic of the device to verify the influence of grid spacing on electrical properties of the solar cell.

The structure consists of 3.6-µm-thick Si-doped ($n = 6\times10^{18}$ cm^{-3}) *n*-GaN layer followed by a 10-nm-thick heavily doped ($n = 2\times10^{19}$ cm^{-3}) GaN layer. The MQW active region is formed by 30×$In_{0.1}Ga_{0.9}N$ (1.3 nm)/GaN (8.5 nm) quantum wells that are capped with a 60-nm-thick Mg-doped ($p = 7\times10^{16}$ cm^{-3}) GaN layer. For device fabrication, 0.5×0.5 mm^2 and 1×1 mm^2 mesas were patterned by Cl_2-based inductively coupled plasma etching. Ohmic contacts to *n*-GaN were deposited around the mesas by electron-beam evaporation of Ti/Al/Ni/Au (30/70/20/100 nm). The *p*-GaN contact consists of a semitransparent layer of Ni/Au (5/5 nm) annealed in O_2 (leading to 96% transmittance in the visible spectral range), and a 130-nm-thick Ni/Au grid (30/100 nm) with 5 µm finger width. The distance between fingers was varied as 100, 150 and 200 µm.

The responsivity spectra together with *J(V)* curves under 1 sun AM1.5G equivalent solar illumination for devices with different grid spacing are presented in Figure 3.27.

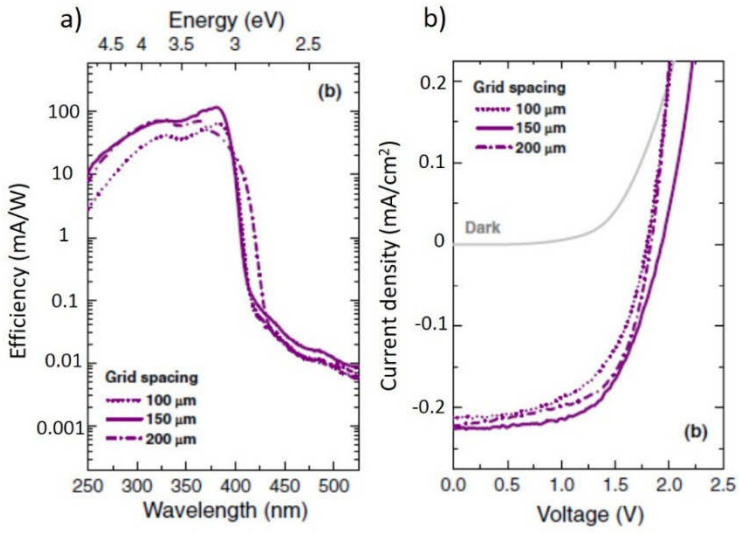

Figure 3.27. a) Responsisivty spectra and b) Current density-voltage characteristics under 1 sun AM1.5G equivalent solar illumination for 30×$In_{0.1}Ga_{0.9}N$/GaN quantum well-based solar cells with different distance between p-contact fingers: 100, 150 and 200 µm [Valdueza, 2013].

All samples show quite the same electrical behavior that points out a good in-plane diffusion length of the minority carriers in Mg-doped GaN. Slight red-shift of the spectral response for sample with 200 µm finger pinch is attributed to In composition fluctuations. Anyway, slightly better results in terms of responsivity and *J(V)* curve are obtained for sample with 150 µm distance between the fingers. This value for finger pitch will be used for further fabrication of solar cells in this work.

3.5 Conclusion

In this chapter we briefly discussed the basics of the nitride-growth by MOVPE: the method of growing GaN buffer-layer, its p- and n-doping and peculiarity of the InGaN/GaN QW growth. We also described the experimental techniques used in this work: HRXRD, PL and transmission setups as well as setups for electrical measurements. The process of device fabrication is detailed. Finally, we investigated the influence of Cp_2Mg flow on the carrier concentration and mobility in p-GaN layers. The best value of Cp_2Mg flow giving a maximum carrier mobility is found to be 500 sccm. Thin top layers grown at higher temperature give higher hole concentration. After p-GaN layer optimization we studied the influence of the grid design for p-contact on the electrical properties of the solar cell. Samples with different grid spacing (100, 150 and 200 µm) show relatively the same electrical characteristics, pointing out a good diffusion length of the holes. Anyway, slightly better characteristics in terms of external quantum efficiency and *J(V)* curves were seen for finger pitch of 150 µm and this value will be used for all the solar cells fabricated in this work. After preliminary optimization of the p-GaN layer and p-contact, we are ready to proceed to the investigation of the influence of the active region parameter.

Chapter 4

Theoretical and experimental study of the InGaN/GaN quantum wells

The growth of high-quality thick InGaN layer is very difficult due to defect creation. It was shown that one of the ways to overcome this problem is to grow pseudomorphic layers [Chen, 1993]. The presence of thin QWs permits to prevent undesired strain relaxation and defect formation keeping the InGaN layer strained. Also, the insertion of the material with a lower band gap (QW) allows absorbing photons with energy lower than the barrier band gap and therefore, increasing the value of short-circuit current. With this method, the absorption can be optimized by varying the QW design (thickness and number). In return, a change of the barrier thickness and doping will also affect the strain state distribution inside the active region and the collection efficiency of the carriers. Consequently, the electrical parameters of the solar cell can be independently adjusted to find an optimum by choosing approriate thicknesses of wells and barriers, In composition, number of QWs and doping level in the active region. In this chapter we are going to discuss the effect of the QW number on the structural, optical and electrical properties of the solar cells.

The number of QWs determines the total thickness of the active region in terms of absorption and carrier generation. Usually in LED devices, the thickness of QWs is chosen to be relatively small (less than 5 nm for In-content less than 30% to manage the strain balance). But in photovoltaic devices, it is necessary to stack as many wells as possible in the structure to get an effective absorption of incoming light. Although the presence of QWs helps to postpone the relaxation, anyway, it still appears when stacking too many periods leading to linear defects (for example threading dislocations and v-pits) [Young, 2013].

There is also another problem showing up with an increase of the period number. The internal electric field created by the *p-n* junction decreases with the active region thickness. This hampers the separation of the electron and hole pairs and their drift to the *n*- and *p*-contacts. Therefore, the determination of the appropriate active region thickness is necessary for the development of an efficient device.

The work presented in this chapter has been published in two papers [Mukhtarova, 2013] and [Valdueza, 2013].

Figure 4.1 present a schematic of the sample structure grown in this chapter. Sampples with 5, 15, 30, 40, 60 and 100 $In_{0.1}Ga_{0.9}N$/GaN QWs were grown on *c*-sapphire substrate[*]. The thicknesses of QW and barrier are 1.3 and 8.5 nm, respectively. To minimize the probability of strain relaxation, we have chosen a sample design with relatively low In-content (about 10%) to be able to investigate the *intrinsic* effect of the QW number.

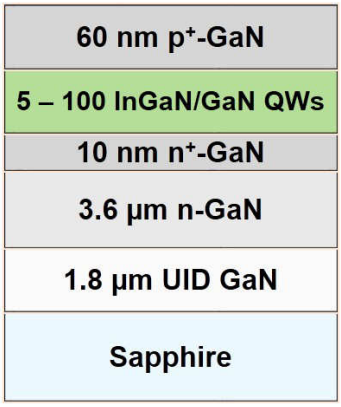

Figure 4.1. General structure for the samples studied in Chapter 4. Target In-composition, QW and QB thicknesses are 10%, 1.3 nm and 8.5 nm.

4.1 Structural and optical properties

4.1.1 Study of crystalline quality (HRXRD and HRTEM)

The growth of QWs is a complicated process. The well/barrier interface roughness, In fluctuations inside the active region, relaxation accompanied with defect formation can damage photovoltaic properties of future solar cells. Before starting a long fabrication process of the device, it is necessary to understand and optimize the structural quality of as-grown samples. In this section, we investigate by X-ray diffraction the crystalline quality, the strain state and In-content of the grown samples depending on the QW number.

Figure 4.2 presents a symmetrical ω-2θ scan around (0002) reflection for samples with different number of QWs (5-100). The measurements are done at the radiation wavelength of

[*] Samples with 5, 15, 30 QWs and samples with 40, 60 and 100 QWs were grown in two different series.

1.54056 Å (copper $K_{\alpha 1}$ emission wavelength) with a high-resolution x-ray diffraction setup (HRXRD equipment). The highest peak corresponds to the thick GaN buffer layer and peaks centered on an "average" superlattice peak (called *SL0*) are coming from the periodicity of QWs. A lot of information about the crystalline structure can be obtained from XRD ω-2θ scan: structural and interfacial quality (from the broadening and sharpness of the peaks and their variation of intensity), *c*-lattice parameter (from the position of *0*-order peak), SL period *T* (from the angle difference between satellite peaks), SL total thickness *H* (from the distance between thickness fringes (indicated by vertical arrows in Figure 4.2) etc. Scans in Figure 4.2 can be analyzed with a simple treatment within the kinematical theory [Holy, 1999]. Values of superlattice period *T* (from Eq. (4.1)), average lattice parameter $<c_{SL}>$ (from Bragg's law, Eq. (3.1)) and total thickness *H* (from Eq. (4.2)) are listed in Table 4.1.

$$T = \frac{\pm n\lambda}{2(sin\theta_{\pm n} - sin\theta_0)}, \tag{4.1}$$

where λ - X-ray wavelength, θ_0 and $\theta_{\pm n}$ - *0*-order and ±n order superlattice satellites.

$$H = \frac{(n_i - n_j)\lambda}{2(sin\theta_i - sin\theta_j)}, \tag{4.2}$$

where θ_i and θ_j - *i* and *j* order superlattice satellites.

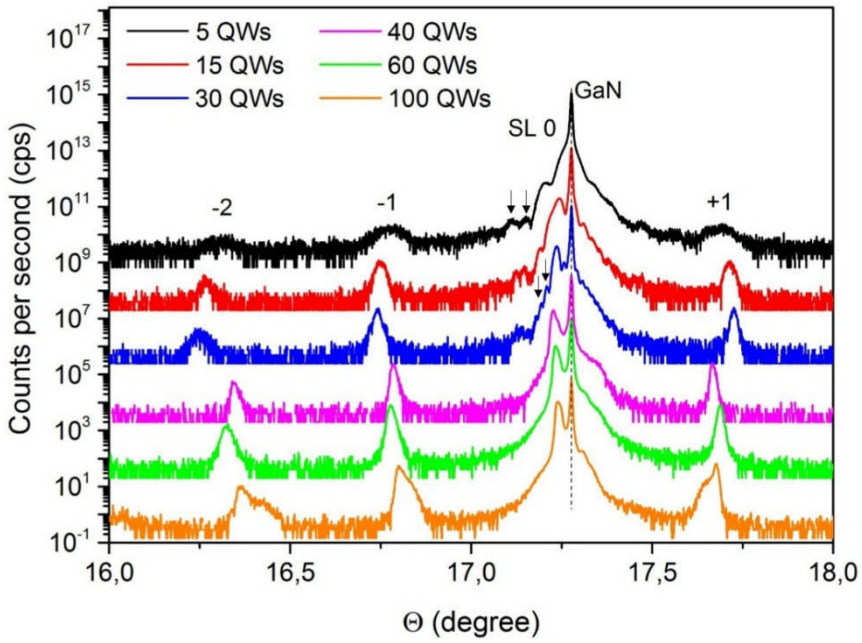

Figure 4.2. X-ray ω-2θ scan around (0002) Bragg peak reflection at 1.54056 Å wavelength for samples with 5-100×$In_{\sim 0.1}Ga_{\sim 0.9}N$(~2 nm)/GaN (~8 nm) QWs. Arrows show the thickness fringes.

If we look at the shape of the satellite peaks, we can notice a peak asymmetry that becomes more evident with increasing the QW number. This asymmetry can come from different reasons such as In-content variation or/and period changes.

To understand the strain state of the samples, the reciprocal space mapping (rsm) around the (10-15) Bragg reflection peak has been performed. Examples of rsm for samples with 30, 60 and 100 QWs are presented in Figure 4.3. The vertical alignment of the superlattice peaks with the GaN peak in the ($K_{||}$, $K_{\perp}$) coordinates indicates a coherent biaxial strain: the in-plane MQW interatomic distance is matched to the GaN buffer layer and the out-of-plane distance is deformed.

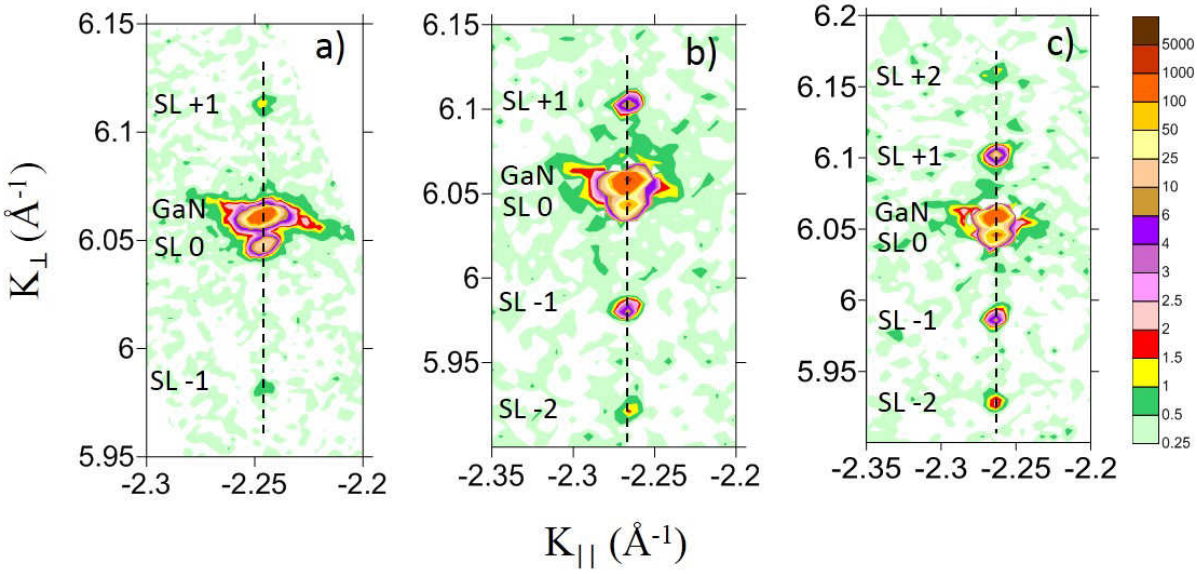

Figure 4.3. Reciprocal space map around (10-15) Bragg reflection peak at the wavelength of 1.54056 Å for $In_{0.11}Ga_{0.89}N$ (~1.7 nm)/GaN (9 nm) samples with: a) 30; b) 60; c) 100 QWs. $K_{||}$ and $K_{\perp}$ are wave vectors in the reciprocal space.

Supposing a biaxial strain approximation of the MQWs on the GaN buffer layer for *c*-orientation, the In-content *x* can be directly estimated from [Vickers, 2003]:

$$\frac{c_{\exp} - c_0^{InGaN}(x)}{c_0^{InGaN}(x)} = -\frac{2C_{13}^{InGaN}(x)}{C_{33}^{InGaN}(x)}\left(\frac{a_{\exp} - a_0^{InGaN}(x)}{a_0^{InGaN}(x)}\right) \qquad (4.3)$$

where $c_0^{InGaN}(x)$ and $a_0^{InGaN}(x)$ - lattice parameters, $C_{13,33}^{InGaN}(x)$ - elastic constants of the relaxed InGaN film, a_{exp}^{InGaN} and c_{exp}^{InGaN} - lattice parameters of the strained InGaN film. In the first approximation, alloy variations of lattice parameters and elastic constants as a

.

function of x are extrapolated linearly from bulk values via Vegard's law Eq. (2.12). For in-plane biaxial strain $a_{exp}^{InGaN} = a_0^{GaN}$, the value of c_{exp}^{InGaN} can be deduced from the position of 0-order peak (SL0) in ω-2θ scan, which depends both on the thickness ratio between well and barrier and the In composition. The total period T is related to the average interplanar spacing d of the MQW by:

$$T = (n_{GaN} + n_{InGaN}) \times d = d_{GaN} \times n_{GaN} + d_{InGaN}(x) \times n_{InGaN} \quad (4.4)$$

where n_{GaN} and n_{InGaN} are the numbers of interatomic planes in the barrier and well (determined from HRTEM measurements (Figure 4.4)), d_{GaN} and $d_{InGaN}(x)$ are the corresponding interatomic distances. d (and consequently c_{exp}) is obtained from the measurement of the 0-order (0002) reflection and the value of $d_{InGaN}(x)$ is obtained from Eq (4.4).

Finally, an In composition is determined by solving Eq. (4.3) with respect to the variable x and results are presented in Table 4.1. Based on these calculations, an average In-content for samples is estimated to be 11 ± 2%.

Table 4.1. Parameters of $In_{0.11}Ga_{0.89}N$/GaN SLs extracted from HRXRD measurements: SL period T, total superlattice thickness H, average c-lattice parameter $<c_{SL}>$, In-content, and degree of relaxation R.

Number of QWs	T, nm	H, nm	$<c_{SL}>$, Å	In-content, %	R, %
5	10.0	55.4	5.194	8.6	0
15	9.55	155.8	5.195	9.0	0
30	9.7	313	5.196	10.1	0
40	10.3	-	5.199	13.5	-
60	10.6	-	5.198	12.9	0.6
100	10.7	-	5.197	12.5	1.7

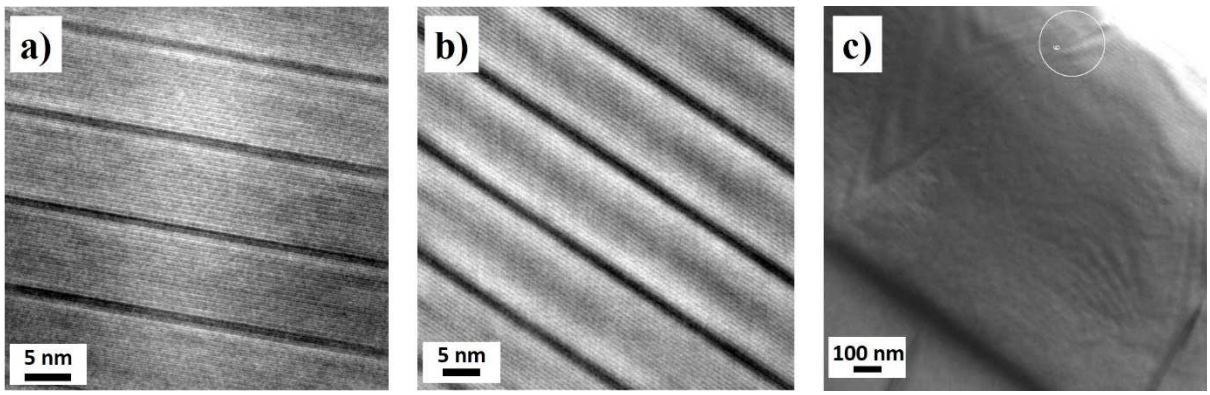

Figure 4.4. HRTEM images of the $In_{0.11}Ga_{0.89}N$ (1.3 nm)/GaN (8-9 nm) QW region for samples with: a) 30 QWs; b)100 QWs; c) HRTEM image of dislocations in the sample with 100 QWs (images are from C. Bougerol).

The in-plane relaxation degree *R* of the superlattice can be estimated knowing the value of In-content via:

$$R = \frac{a_{exp}^{InGaN} - a_0^{GaN}}{a_0^{InGaN} - a_0^{GaN}}, \tag{4.5}$$

where a_0^{GaN} - *a*-lattice parameter of GaN, a_0^{InGaN} - *a*-lattice parameter of InGaN calculated via Vegard's law, a_{exp}^{InGaN} - *a*-lattice parameter of InGaN obtained from the experiment. The values of calculated relaxation are presented in Table 4.1. We can conclude that all samples are coherently biaxially strained on GaN buffer layer.

To improve this structural analysis, samples with larger number of QWs (30, 40, 60 and 100) were measured at the BM02 beamline of the European Synchrotron Radiation Facility using a wavelength λ = 1.28361 Å. Thanks to a large beam flux of the synchrotron radiation it is possible to measure a larger number of satellite peaks and extract more precise information from the fit of the data. X'Pert Epitaxy software has been used to simulate the XRD profiles and to fit the structural properties. Figure 4.5 presents an example of *ω-2θ* simulation for sample with 30 QWs around the (0004) Bragg peak taking into account well and barrier thicknesses from TEM measurements and In-content from Table 4.1.

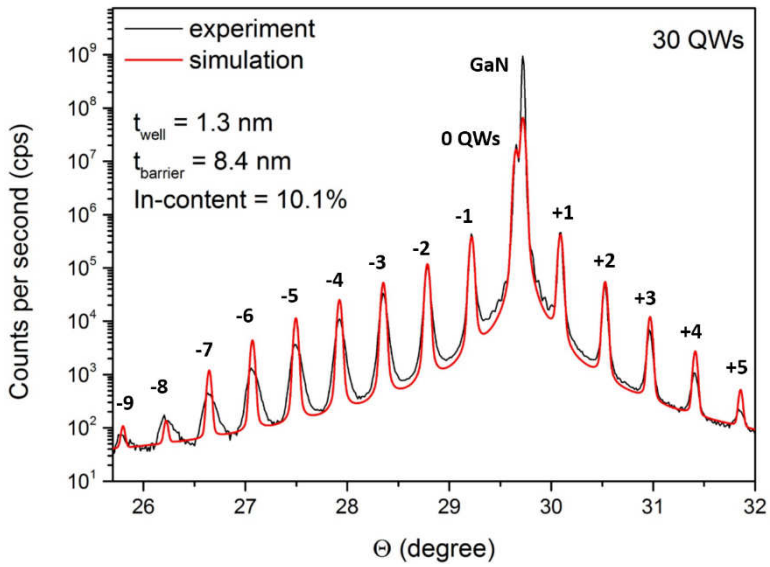

Figure 4.5. X-ray ω-2θ scan around (0004) Bragg's reflection for 30 $In_{0.101}Ga_{0.899}N$/GaN (1.3 nm / 8.4 nm) QWs grown on GaN/sapphire substrate. The measurements (black curve) are carried out at the BM02 beamline of the European Synchrotron Radiation Facility using a wavelength of λ = 1.28361 Å. Simulation (red curve) was performed with X'Pert Epitaxy 4.0 program.

.

The XRD curve is rather well fitted in terms of the peak positions, but the decrease of the simulation peak intensity with the satellite order is slower as compared to experiment. The same effect for CdTe/MnTe superlattices grown by MBE was found in the work of Eymery *et al.* [Eymery, 2000]. It was shown that the change of the interface profile between the well and barrier can be used for better fitting of peak intensities. In their work they supposed a linear gradation of Mn concentration at the QW edges. Figure 4.6 shows an example of the ω-2θ scan around (0004) Bragg's reflection fit for $30\times In_{0.107}Ga_{0.893}N/GaN$ (1.7 nm/8.0 nm) QWs grown on GaN/sapphire substrate. In our case, we fitted XRD curves supposing different profiles of In-content gradation at the well interfaces: linear (Figure 4.6 (a), magenta curve), concave (Figure 4.6 (b), blue curve) and convex (Figure 4.6 (c), red curve). As it can be seen from the fit, the change of the interface profile influences mostly on the intensity of the high-order peaks. The best fit of the peak intensities for all samples under study is obtained for convex shape of the In-content profile.

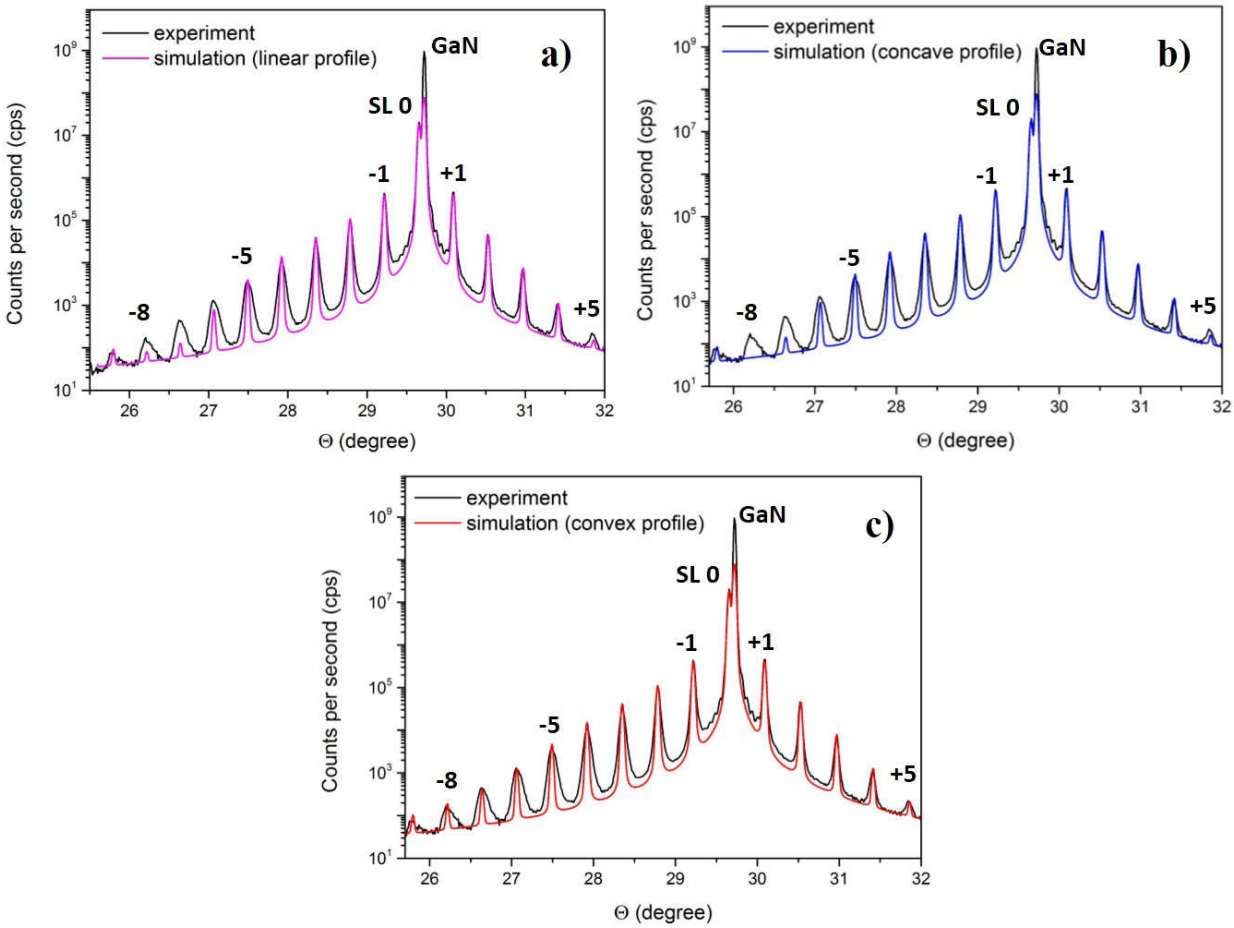

Figure 4.6. X-ray ω-2θ scan around (0004) reflection at the 1.28361 Å radiation wavelength for $30\times In_{0.107}Ga_{0.893}N/GaN$ (1.7 nm / 8.0 nm) QWs. Simulation is done with X'pert Epitaxy 4.0 software supposing different shape of the In-content profile at the well interfaces: (a) linear (magneta curve); (b) concave (blue curve); (c) convex (red curve).

Table 4.2 summarizes the fit parameters of the active region: QW and QB thicknesses and In-content. The thickness of In composition gradient region is called on the bottom of QW: T_{well_1} and on the top of the QW: $T_{well\_3.}$ The thickness of the well zone with constant In composition is called T_{well_2}.

Table 4.2. Structure parameters: In-content, thickness of the barrier T_{bar}, thickness of the well with convex graded In composition: bottom interface T_{well_1} and upper interface $T_{well\_3,}$ well thickness with constant In composition T_{well_2} obtained from the fit of XRD ω - 2θ scans.

Number of QWs	**In-content, %**	**T_{bar}, nm**	**T_{well_1}, nm**	**T_{well_2}, nm**	**T_{well_3}, nm**
30	10.7	7.98	0.48	0.69	0.54
40	12.0	8.49	0.24	1.10	0.41
60	13.0	8.90	0.27	1.04	0.46
100	12.0	8.94	0.41	0.78	0.60

Figure 4.7 shows the final profile of the QW taking into account parameters listed in Table 4.2. The shape of QWs is not rectangular. This fact can be attributed to the peculiarity of the growth process. The growth temperatures T_{gr} of the well and barrier are different. GaN barrier is usually grown at relatively high temperatures (in our case it is 900 ^{0}C), while InGaN well requires a significantly lower T_{gr} (750 ^{0}C). The necessity to use such moderate growth temperature is related to a low thermal stability of InGaN alloys due to a high nitrogen equilibrium vapor pressure and a high volatility of indium [Ju, 2007; MacChesney, 1970]. This temperature change enhances the interdiffusion between In and Ga atoms, especially for the top interface of the well (where the temperature increases) leading to the appearance of In composition gradient at the QW edges.

.

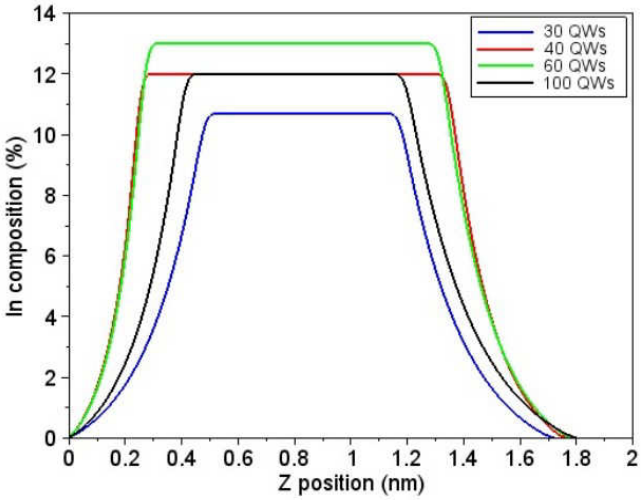

Figure 4.7. Quantum well profiles for $In_{0.11}Ga_{0.89}N$ (1.7 nm)/GaN (8-9 nm) samples with different number of quantum wells (30-100). Convex function is used to describe the In composition profile at the QW edges.

For all samples, the total thickness of QWs has almost not been changed and varies from 1.71 nm (for sample with 30 QWs) to 1.79 nm (for sample with 100 QWs). All variations in the period from sample to sample are mostly related to the variation in the barrier thickness (about 1 nm). The thickness of the barriers slightly increases with QW number (see Table 4.2). The same tendency has been observed for (3-10)×InGaN/GaN QWs grown on Si (111) substrates by Wu *et al.* [Wu, 2006]. These authors explained the increase of the barrier growth rate with the number of periods to be related to the presence of V-defects, supposing that there is a little destruction of reactants in V-defect region that creates an extra supply of precursors in the areas around of V-defect. As the size of V-defects increases with QW number (we also observed this effect experimentally in our samples (see Figure 4.8)), the area outside of the V-defect available for deposition from extra supply of precursors becomes smaller. This leads to the increase of the deposition and, consequently, of the growth rate.

It is known that chemical etching can be used to reveal dislocations in GaN layers [Weyher, 2000]. Figure 4.8 shows scanning electron microscope (SEM) images of the samples with 10 and 20 $In_{0.18}Ga_{0.82}N$/GaN quantum wells without the p-GaN capping layer. Both samples were etched in hot phosphoric H_3PO_4 acid heated to 180 ^{0}C during 20 minutes. The lateral size of "dislocation" traces increases with QW number: $t_{dis} \approx$ 140 nm for 20×$In_{0.18}Ga_{0.82}N$/GaN QWs and about 90 nm for 10×$In_{0.18}Ga_{0.82}N$/GaN QWs. Density of dislocations was relatively the same: $N_{dis} \approx 1.4\times10^8$ cm^{-2} for 10 QWs and 1.5-1.6×10^8 cm^{-2} for 20 QWs.

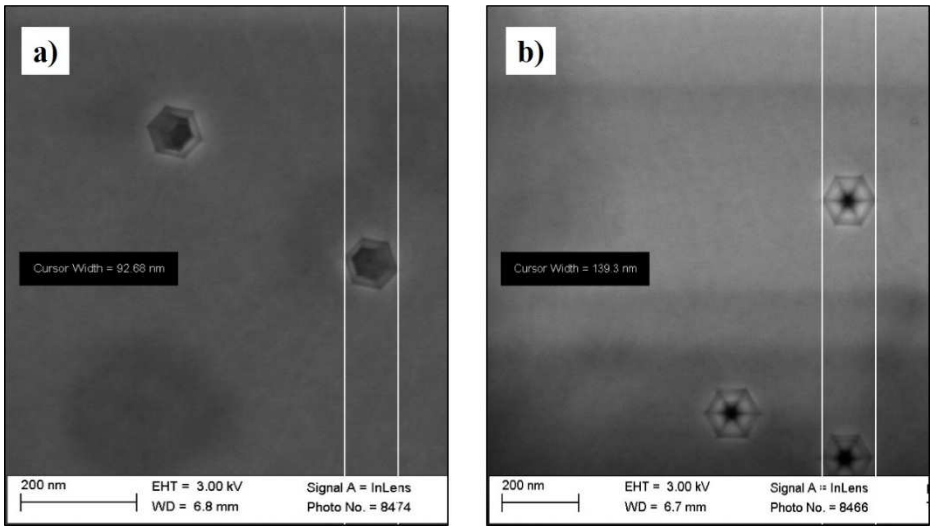

Figure 4.8. SEM images of V-defects for $In_{0.18}Ga_{0.89}N/GaN$ samples with: (a) 10 QWs; (b) 20 QWs.

The period variation ***through the structure*** can be determined by analyzing the full width at half maximum (FWHM) of the satellite peaks [Fewster, 1988]. In the model proposed by Fewster, the measured FWHM broadening of every satellite β_n is deconvoluted by the width of the "zero-order" peak in order to take into account the instrumental broadening and the defects of the samples:

$$\beta_n = ((n\beta_1)^2 + (\beta_0)^2)^{1/2}, \quad (4.6)$$

where β_1 - broadening parameter, β_0 - integral breadth for the "zero-order" satellite.

The FWHMs satellites plotted against the diffraction order for (0004) reflection for samples with 30 – 100 QWs are presented in Figure 4.9.

.

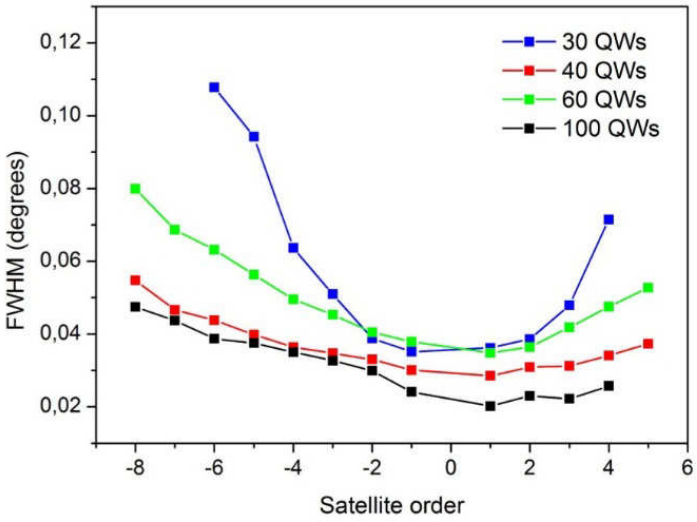

Figure 4.9. Full width at half maximum of the satellite peaks as a function of the peak order at (0004) reflection (λ = 1.28361 Å) for $In_{0.11}Ga_{0.89}N$ (1.7 nm)/GaN (8-9 nm) samples with different number of QWs.

The progressive broadening of the satellite peaks as a function of the order may be interpreted by the presence of a period variation. Quantitatively, the period variation can be found through following formula, directly derived from Bragg's law:

$$\Delta T \approx \lambda\beta_1 / [2\overline{\Delta\omega}\cos(\omega_0)], \quad (4.7)$$

where λ - wavelength, $\overline{\Delta\omega}$ – angle difference between two satellites, ω_0 - angle for *SL0* peak. With this analysis, we obtained the values of period fluctuations of 3.87, 1.45, 2.58 and 2.90 Å for samples with 30, 40, 60 and 100 QWs, respectively. These results show that the period fluctuations remain negligible even for samples with very high number of QWs revealing a good stability of MOVPE techniques during a long time of growth (more than 30 hours of growth for sample with 100 QWs).

Therefore, if the origin of peak broadening seen in ω-2θ scan (Figure 4.2) does not relate to the period fluctuations, it can be related to the composition inhomogenieties. Optical measurements are considered as a good method to verify this assumption.

4.1.2 Analysis of optical properties (PL and transmission)

According to data obtained with XRD analysis, the In-content varies from 9 to 13%. This composition variation should also affect the optical properties of the samples.

Figure 4.10 (a) shows a low temperature (5 K) PL spectra from the $In_{0.11}Ga_{0.89}N$(1.7 nm)/GaN(8-9 nm) samples with different number of QWs.

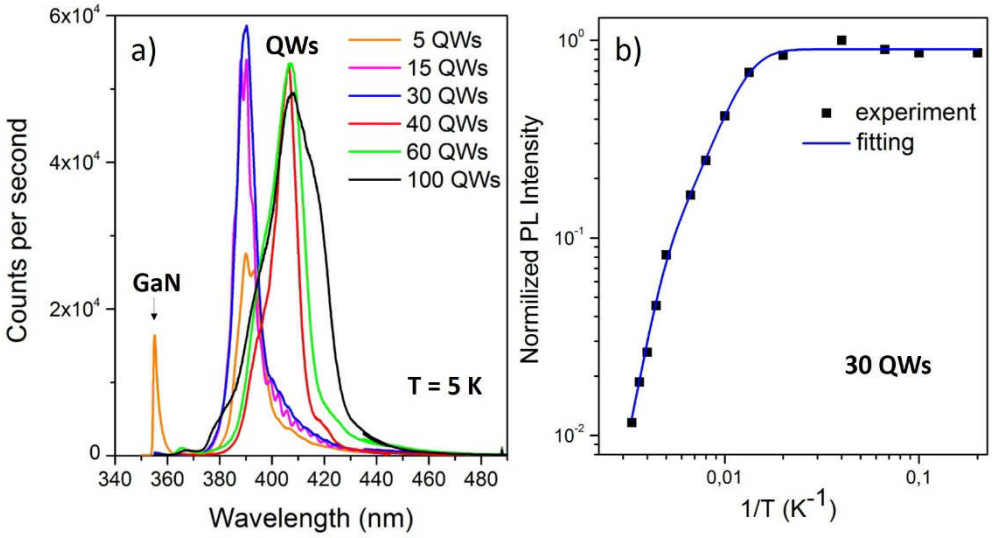

Figure 4.10: (a) Low temperature (T = 5 K) PL measurements for $In_{0.11}Ga_{0.89}N$ (1.7 nm)/GaN (8-9 nm) samples with number of QWs varying from 5 to 100. (b) An example of the PL intensity evolution with the temperature for 30×$In_{0.11}Ga_{0.89}N$ (1.7 nm)/GaN (8-9 nm) QWs. Blue curve shows the fit of experimental data with Eq. (4.12).

The PL emission wavelength change from 390 nm to 408 nm is in a good agreement with the variation of In composition obtained from the structural analysis (from 9 to 13%) [O'Donnell, 2004]. The broadening of PL spectra, with the FWHM change from 70 to 195 meV, indicates an increase in the nonuniformity of the indium composition with the QW number.

Measurements of PL peak intensity dependence on temperature can give an idea about the presence of localization effect inside the QWs. An example of PL intensity evolution with the temperature for sample with 30 QWs is presented in Figure 4.10 (b). Supposing that at low temperature all carriers are localized and recombine only radiatively, the integrated PL intensity can be fitted using the following formula [Wen, 2007]:

$$\frac{I(T)}{I(T=0)} = \frac{1}{1+Ce^{-E_1/kT}}, \tag{4.8}$$

where I - PL intensity, C - fitting constant proportional to the density of the nonradiative recombination centers, E_1 - activation energy (energetic barrier that carriers should overcome to reach nonradiative recombination centers), k - Boltzmann's constant.

The ratio between PL intensities at 0 K and at room temperature (300 K) is generally attributed to the internal quantum efficiency (*IQE*). The carrier localization induced by the presence of potential fluctuations in the QW region introduces an additional term to the Eq. (4.8) [Gacevic, 2011]:

.

$$IQE \approx \frac{I(T)}{I(T=0)} = \frac{R_r}{R_r+R_{nr}} = \frac{1}{(1+C_1 e^{-\frac{E_1}{kT}})(1+C_2 e^{-\frac{E_2}{kT}})}, \quad (4.9)$$

where E_2 - thermal escape energy of the carriers moving out from QWs, R_r and R_{nr} - radiative and nonradiative recombination rates.

Activation energy E_1 extracted from the fit of the data is about 34±1 meV and average localization energy E_2 is in the range of 105 – 140 meV for all samples (Table 4.3). These results are consistent with published data. Na *et al*. obtained the value of E_{a1} = 27 meV for 10 periods of $In_{0.11}Ga_{0.89}N$ (1.4 nm)/GaN (7.5 nm) [Na, 2006]. Sun *et al*. estimated the values of E_{a1} and E_{a2} to be 13 meV and 170 meV, respectively, for 4×$In_{0.2}Ga_{0.8}N$ (3 nm)/GaN (12 nm) QWs [Sun, 2011].

There is not only the variation of the PL intensity with the temperature, but also a shift of the peak position. Figure 4.11 shows an example of the PL peak position dependence on the temperature for samples with 30, 60 and 100 QWs.

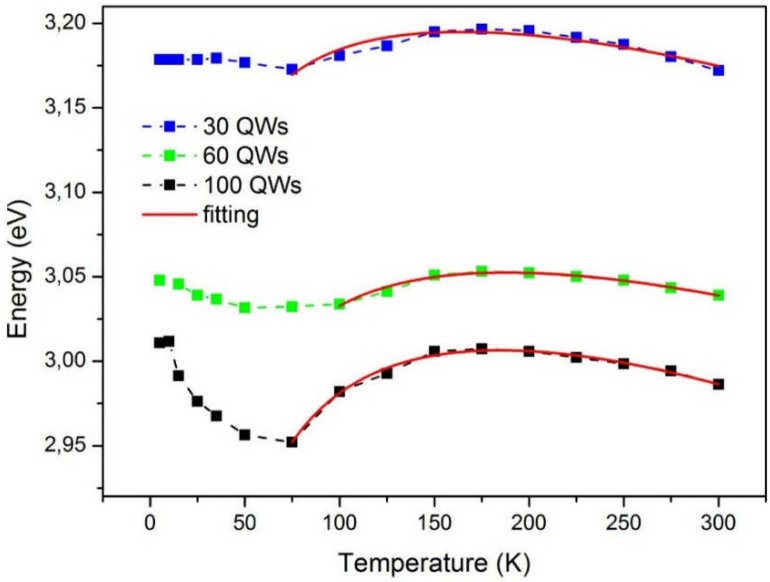

Figure 4.11. The temperature dependence of the PL peak position on temperature for 30, 60 and 100 $In_{0.11}Ga_{0.89}N$ (1.7 nm)/GaN (8-9 nm) QWs. Red curve shows fit of the experimental data with Eq. (4.13).

Normally, the change of the band gap with temperature in semiconductors should follow the Varshni's law (Eq. 2.19). In our case, an anomalous temperature behavior is observed for all investigated samples. This is also known as "s-shaped" temperature dependence (redshift – blueshift – redshift). To explain the origin of the "s-shape" the following model has been proposed by Cho *et al*. [Cho, 1998]. For low temperatures (less than 70 K) the radiative recombination process is dominant, weakly localized carriers are

thermally activated and relaxed down into lower energy tail states induced by potential fluctuations, which results in the initial redshift of the peak energy. With temperature increase (from 70 to 150 K), non-radiative process starts becoming dominant, carriers recombine before reaching the lower energy tail states and their lifetime is decreasing. This behavior leads to the blueshift of the peak energy. For temperatures higher than 150 K, the non-radiative recombination is dominant and carrier's lifetime is almost constant, the blueshift becomes smaller and the temperature-induced bandgap shrinkage becomes responsible for the redshift behavior of the PL peak. The band-tail model is usually used to describe the degree of localization effect. In this model the emission energy dependence on the temperature can be given by the following expression [Eliseev, 1997]:

$$E(T) = E(0) - \frac{\alpha T^2}{T+\beta} - \frac{\sigma^2}{k_B T} \tag{4.10}$$

where *E(0)* - energy gap at 0 K, α - Varshni's parameter, β - Debye temperature. The third term on the right comes from the localization effect. σ represents the degree of localization (the larger value of σ means a stronger localization effect) and k_B is Boltzmann's constant. The values of σ obtained by fitting the experimental data with the equation (4.10) are listed in Table 4.3. Our results are consistent with the literature for InGaN/GaN QWs. Wang *et al*. obtained the values of localization parameter σ = 23 meV for 8×$In_{0.15}Ga_{0.85}N$ (3 nm)/GaN (14 nm) QWs and Murotani *et al*. estimated σ to be in the range from 15 – 35 meV for InGaN/GaN QWs with In-content varied from 0.20 to 0.31 [Wang, 2012; Murotani, 2013]. It is clear that this model fits well the experimental results in the 75 – 300 K temperature range. But it is not valid for low temperatures (less than 75 K). This is related to degeneracy of the carrier occupation at low temperatures (less than 75 K) that is not taken into account in the Eliseev's model [Eliseev, 1997].

It is interesting to notice that localization parameter σ is increasing with QW number, showing an increase of localization effect. In general, the variations of defect density, indium content, well width and interface roughness between the well and barrier may all contribute to the formation of different localization levels. From XRD data we have shown that the relaxation of the samples is negligible as well as the variation in the period. HRTEM images indicate a good quality of the interfaces. Therefore, the origin of the localization effect increase is most possibly related to the nonuniformity of the In composition. This explanation

.

is also consistent with the broadening of FWHM for low temperature PL spectra (Figure 4.10 (a)).

Table 4.3. Values of the band gap E_g, activation energy E_1, localization energy E_2, localization parameter σ and IQE = $I_{PL}(RT)/I_{PL}(T = 5K)$ extracted from the fitting of PL spectra for samples with different number of $In_{0.11}Ga_{0.89}N$/GaN periods.

Sample parameters	30 QWs	60 QWs	100 QWs
E_g (eV)	3.25	3.11	3.09
E_1 (meV)	34	34	34
E_2 (meV)	127	105	139
σ (meV)	23	25	29
IQE (%)	1.3	1.0	2.9

Another indication of the localization presence in the InGaN/GaN QW structure is the existence of so-called Stokes' shift. The Stokes' shift is the difference in the energy between PL and absorption peaks. In order to estimate the value of Stokes' shift, we should first determine the absorption edge. Absorption edge can be attained by fitting the transmission data with a sigmoidal function [Donnell, 1999]:

$$\alpha(E) = \frac{\alpha_0}{1+e^{\frac{(E_g-E)}{\Delta E}}} \tag{4.11}$$

where E_g - effective bandgap energy, α_0 – absorption coefficient, that corresponds to the absorption at energies well above a bandgap energy, ΔE - absorption band edge width, equivalent to the Urbach tailing energy*.

The transmission spectrum of the samples under study is presented in Figure 4.12. A sharp absorption cutoff of GaN (at 365 nm) is followed by the absorption of InGaN/GaN QWs in the 365 – 415 nm region. The absorption increases and the absorption edge broadens with the number of MQWs. But still the absorption is not complete even for sample with 60×$In_{0.11}Ga_{0.89}N$ (1.7 nm)/GaN (8-9 nm) QWs.

As we said before, the thickness of InGaN should be about 300 nm to absorb 95% of incoming light. Indeed, the total absorption thickness (summarized thickness of the InGaN layers) of the sample with 60 QWs is only 102 nm and that is not enough for full absorption. The effective band gap energy obtained through the fitting of the transmission data for all samples under study with the formula (4.14) is 3.11 ± 0.02 eV. This result is consistent with results obtained from PL measurements. The value of ΔE is increasing from 17±2 meV (15 and 30 QWs) to 32±2 meV (40 and 60 QWs), confirming the increase of In-content inhomogeneities with QW number.

From the values of the absorption edge and PL peak positions, the Stokes' shift is estimated to be 40±11 meV. Usually, the presence of the Stokes' shift is attributed to localization [Martin, 1999], quantum-confined Stark effect [Bercowicz, 2000] or a mixture of both.

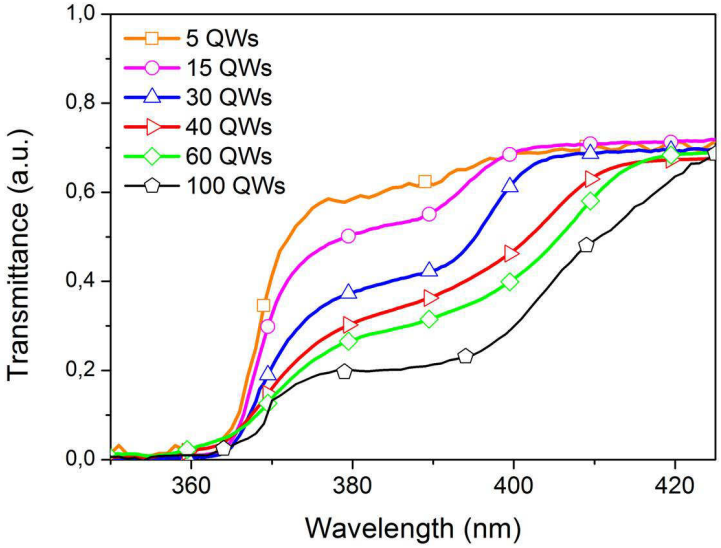

Figure 4.12. Room-temperature transmittance spectra of 5-60×$In_{0.11}Ga_{0.89}N$ (1.7 nm)/GaN (8-9 nm) samples.

Considering that the thickness of QWs is very small (1.7 nm), the influence of QCSE on PL spectra is negligible. Therefore, the most probable nature of the Stokes' shift can be the presence of carrier localization because of In-content fluctuations.

To summarize the results, we show that all samples have a strong PL emission at the wavelength of about 400 nm for the band gap of about 3.1 eV extracted from temperature PL and absorption measurements. The S-shape dependence of the PL emission as a function of the temperature, Stokes' shift presence and the broadening of absorption edge reveal the existence of localization effect in the active region that could be mainly attributed to potential fluctuations in QWs because of In composition inhomogeneities.

4.2 Electrical properties

After structural characterization, all samples have been processed into solar cells using photolithography, plasma etching and metallization processes (see Chapter 3).

.

Photocurrent spectral response of the solar cells under study is presented in Figure 4.13. Measurements were performed at room temperature on the optical transmission spectroscopy setup.

Spectral cutoff is red-shifted in comparison to GaN photodetector because of the InGaN QW presence. The shift of the spectral cutoff with QW number from 398 nm to 416 nm is consistent with transmittance and PL measurements. The efficiency above the GaN bandgap of the devices increases by a factor of 10 when increasing the number of QWs in the active region from 5 to 30. Then, it saturates and remains at the same level for samples with 30, 40 and 60 QWs.

EQE exhibits the ratio of the number of electrons collected by the solar cell to the number of incident photons. So, it includes the efficiencies of three processes happening inside the solar cell under illumination: absorption, carrier separation and collection. The enhancement of the EQE for samples with 5 – 30 QWs can be directly related to the increased absorption with the number of periods. The following saturation of EQE for sample with 40 QWs and slight decreasing of the EQE for sample with 60 and 100 QWs can be related to an increase of collection losses.

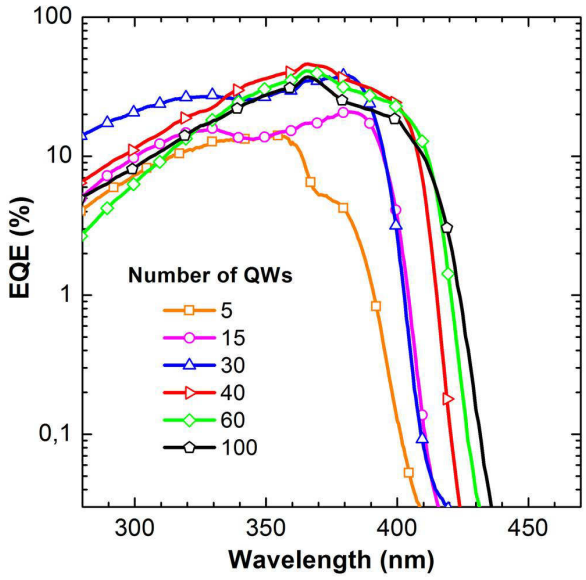

Figure 4.13. Spectral response of the $In_{0.11}Ga_{0.89}N$(1.7 nm)/GaN(8-9 nm) samples varying the number of quantum wells [Valdueza, 2013].

The dependence of the dark current density on the reverse bias for the cells under study is shown in Figure 4.14. It is well known that the reverse dark current is related to the presence of defects in the structure [Kozodoy, 1998]. Therefore, the monotonous decrease of the reverse current with increasing of number of QWs indicates that the dislocation density

generated by misfit relaxation is not critical for our device performance. This is also consistent with XRD data showing no significant strain relaxation with QW number except for sample with 100 QWs. That shows faster increase of the leackage current compared to the samples with 40 and 60 QWs.

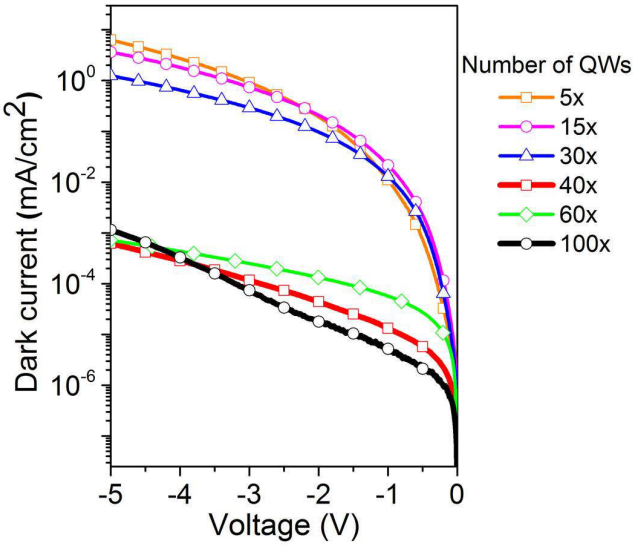

Figure 4.14. Dark current vs reverse bias measurements for $In_{0.11}Ga_{0.89}N$(1.7 nm)/GaN(8-9 nm) samples with different number of periods.

This is further confirmed by the enhancement of V_{oc} from 1.4 V to 2.4 V with the number of QWs, while the fill factor remains almost the same 54-56%. The decrease of open-circuit voltage for sample with 100 QWs can be related to the relaxation and defect formation inside the active region in accordance with HRTEM images. The dependence of J_{sc} on the active region follows the same trend as predicted by the theoretical model in the section 4.1. The J_{sc} increases with the increase of the QW number for thin structures because of absorption improvement. For samples with QW number more than 40, the value of J_{sc} starts saturating reaching the maximum at 0.68 mA/cm^2. This behavior can be related to the appearance of carrier collection losses because of very thick active region (in accordance with EQE measurements). In spite of increased photon absorption, the carriers can be collected only from the first 40-50 QWs. Carriers created in the remaining QWs are lost in the recombination process. The increase of the carrier recombination is also supported by the value of V_{oc} that starts decreasing for sample with 60 and 100 QWs.

The value of optimal active region predicted by the simplified theoretical model is overestimated (1.3 μm instead of about 400-500 nm). This discrepancy can be related to the values of physical parameters (carrier lifetime and mobility) used for plotting theoretical curves that can be different for our samples compared to the values from the literature.

Current density–voltage characteristics of the samples under 1 Sun AM1.5G equivalent illumination are presented in Figure 4.15. All devices showed very homogenious electrical characteristics through the sample. The values of open-circuit voltage, short-circuit current, fill factor, and conversion efficiency for all samples are listed in the Table 4.4.

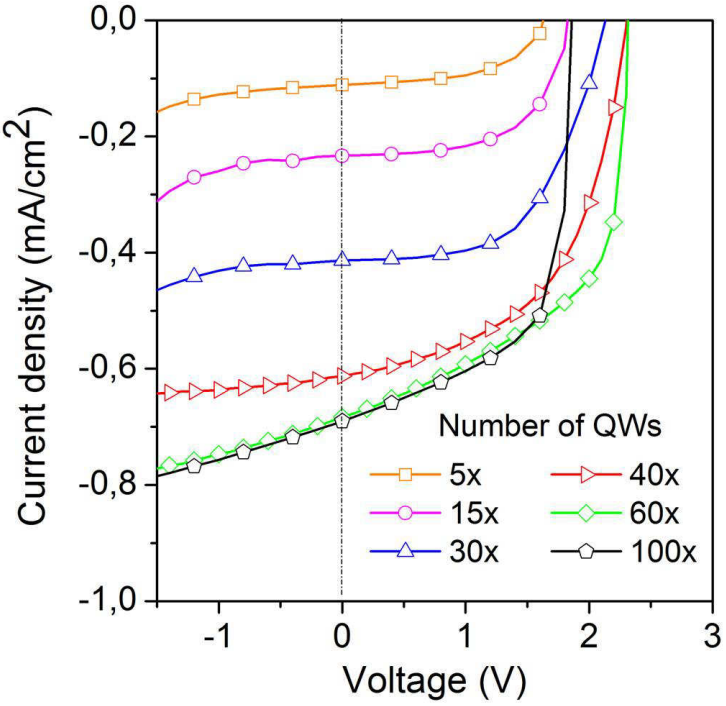

Figure 4.15. Current density – voltage characteristics of $In_{0.11}Ga_{0.89}N$(1.7 nm)/GaN(8-9 nm) solar cells under 1 Sun AM1.5G equivalent illumination.

Table 4.4. Summary of the electrical parameters for $In_{0.11}Ga_{0.89}N$(1.7 nm)/GaN(8-9 nm) QW-based solar cells under 1 Sun AM1.5G illumination: external quantum efficiency EQE, short-circuit current J_{sc}, open-circuit voltage V_{oc}, fill factor FF and conversion efficiency η.

Number of QWs	**EQE at 380 nm**	**V_{oc} (V)**	**J_{sc} (mA/cm^2)**	**FF (%)**	**η (%)**
5	4.1	1.6±0.05	0.11±0.01	54±0.01	0.09
15	16	1.8±0.05	0.24±0.01	56±0.03	0.24
30	38	2.1±0.05	0.42±0.01	54±0.03	0.48
40	36	2.4±0.05	0.63±0.01	56±0.03	0.85
60	31	2.3±0.05	0.68±0.02	56±0.03	0.88
100	25	1.9±0.05	0.68±0.02	60±0.01	0.78

The conversion efficiency was calculated using Eq. (2.10). A low value of conversion efficiency under 1 Sun AM1.5G illumination is related to the lack of absorption at the wavelength higher than 415 nm. An enhancement of η by 1 order of magnitude is observed when increasing the number of QWs from 5 to 60. This increase is mainly associated to the variation of the short-circuit current density, which is enhanced by a factor of 6 with increasing the number of periods.

4.3 Theoretical model of the short-circuit current dependence on the QW number

We developed a simple model to provide an estimation of the value of carrier diffusion length for holes in the active region, assuming a *p*-*i*-*n* MQW structure with similar characteristics as our samples. In particular, we model the evolution of the short-circuit current with the active region thickness using a simple approach based on the following assumptions:

(1) The carrier concentration in *i*-region is small compared to carrier concentration in *p*- and *n*-regions.

(2) Short-circuit current is mostly caused by carriers created in QWs, and the absorption and carrier generation at wavelengths above 380 nm are considered constant through the total thickness of *i*-region. This approximation is based on a simple estimation from the band-edge absorption coefficient for InGaN material (~ 10^5 cm^{-1}) giving 95% absorption of the incoming light for 300 nm thickness [Wu, 2002]. This thickness corresponds to more than 200 QWs with 1.3 nm well thickness.

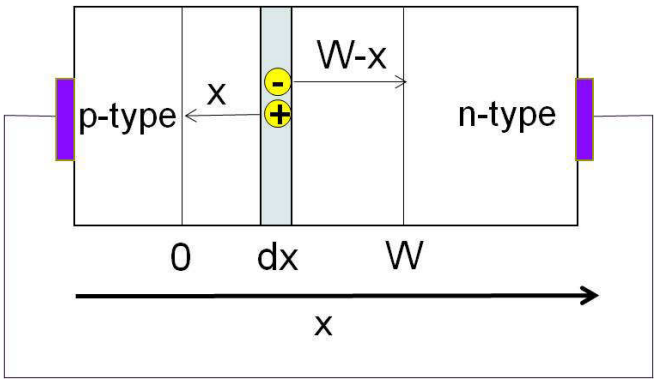

Figure 4.16. Graphical schematic of the electron-hole creation inside i-region in the frame of our model.

In most cases the total current is presented as a sum of hole and electron currents: $J = J_n + J_p$. In this formula two currents are considered as completely independent one from another. In our model we assume that we need both: electron and hole arriving to the *n*- and *p*-zones, respectively. Therefore, we present J_{sc} as a product of two probabilities P_p for holes and P_n for electrons to reach *p*- and *n*-zones for a given photogenerated electron-hole density. We assume the electric field inside *i*-region as $F = V_{bi}/W$ [Raisky, 1997; Mahmood, 2009], where V_{bi} is the built-in voltage and W is the thickness of the depleted region (i.e. intrinsic region with MQWs) which is given by $W = N_w \times (L_w + L_b)$, where N_w is the quantum well number and $L_{w,b}$ are the thicknesses of the well and the barrier. According to Figure 4.16, we express P_p and P_n probabilities as follows:

$$P_p = e^{-\frac{t_p}{\tau_p}} = e^{-\frac{x}{\upsilon_p \tau_p}} = e^{-\frac{xW}{V_{bi}\tau_p\mu_p}} \qquad P_n = e^{-\frac{t_n}{\tau_n}} = e^{-\frac{W-x}{\upsilon_n \tau_n}} = e^{-\frac{x(W-x)}{V_{bi}\tau_n\mu_n}} \tag{4.12}$$

where t_p/t_n is the time that hole/electron needs to reach a *p*/*n* area, respectively, τ_p/τ_n is the hole/electron lifetime, υ_p/υ_n is the hole/electron drift velocity, μ_p/μ_n is the hole/electron mobility.

The equation giving the value of J_{sc} can be written as:

$$J_{sc} = \int_0^W J_0(x) P_p(x) P_n(x) dx \tag{4.13}$$

where $J_0(x)$ is a fitting parameter which includes the number of electron-hole pairs generated per second in *dx* area. Thanks to high mobility and concentration of electrons we assume that all electrons created in QWs are able to reach *n*-side and $P_n(x) = 1$. In the case of homogeneous generation along the active region, *i.e.* $J_0(x)$ = constant, the short-circuit current density can be re-written as follows:

$$J_{sc}(W) = J_0\left(\frac{k_p}{W}\right)\left(1 - e^{\frac{-W^2}{k_p}}\right) \quad (4.14)$$

where $k_p = \mu_p \tau_p V_{bi}$.

Figure 4.17 shows the fit of experimental data with Eq. (4.14). Experimental values of J_{sc} are taken from Table 4.4 and active region thickness W is calculated from HR-XRD for every sample.

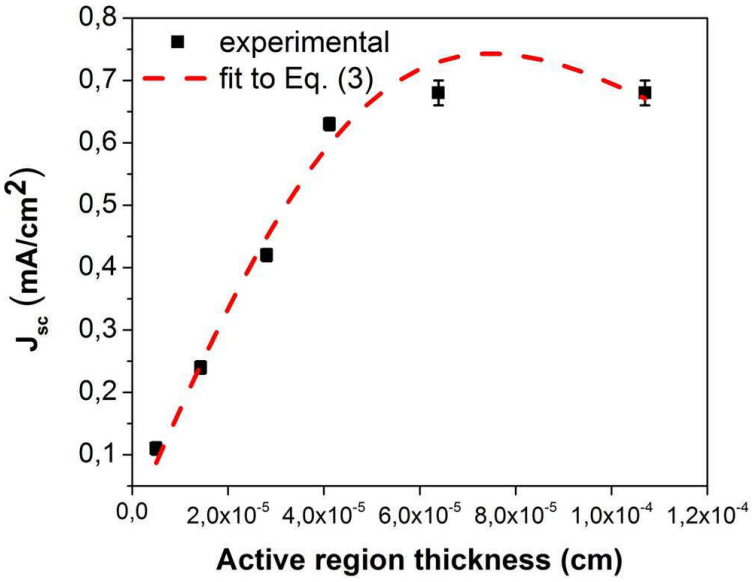

Figure 4.17. Fit of the experimental data with Eq. (4.14).

From the fit we can extract the key parameter k_p, which accounts for the product between the lifetime and mobility for holes in the structure. This allows us to estimate the value of the effective hole diffusion lengths in the MQW region using the formula: $L_p = \sqrt{\frac{kT}{q}\mu\tau}$, where q is the electron charge, k is the Boltzmann constant, and T is the temperature. The obtained effective diffusion length for holes is L_p=64±4 nm. This value is in accordance with the values obtained by others for similar type of structures [Chichibu, 1997].

In the model presented here only drift current is taken into account, but in the samples with thick *i*-region there is also diffusion current exsists that can contribute to the carrier collection. To estimate the value of the effective hole diffusion length taking into account both diffusion and drift currents additional measurements and calculations have also been performed.

Capacitance-voltage measurements have been done to determine the depletion width of the samples under study. The result of the extracted capacitance dependence on the *i*-region

thickness is presented in Figure 4.18. The measurements were done for devices with 1×1 mm^2 mesa size.

Capacitance decreases linearly with the *i*-region thickness for sample with 5-30 QWs and saturates for the sample with 40 QWs. From these measurements we were able to calculate the width of the depleted region (d_{depl}) using the following formula:

$$d_{depl} = \frac{\varepsilon\varepsilon_0 S}{C} \tag{4.15}$$

where ε is the relative dielectric permittivity (here ε = 10), and ε_0 is the electric constant (ε_0 = 8.85×10^{-12} F/m). From these calculations we can say that MQW region is completely depleted in the samples with 5–30 QWs and only partly depleted for samples with 40–100 QWs. Maximum depleted thickness is limited to 340 nm. This can be related to high background doping of the QW region (n~10^{17} cm^{-3}) [Nelson, 2003].

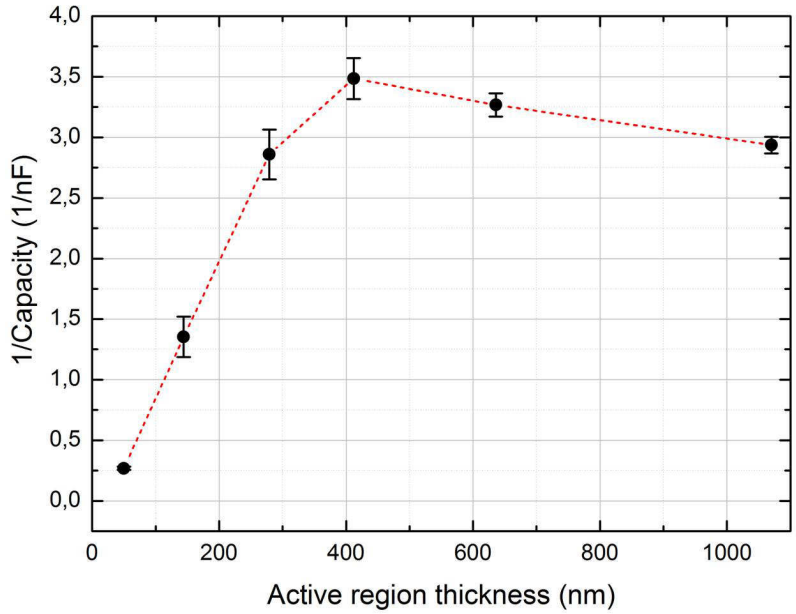

Figure 4.18. Capacitance dependence on the MQW region thickness (V_{appl} = 0V).

Therefore, if MQW region is compeletely depleted for samples with 5-30 QWs, we can assume that the photocurrent obtained for these samples is mostly determined by the drift current. But for samples with thicker active regions (such as with 40-100 QWs) one part of the QW region is left without electric field and contribution of the diffusion current in J_{sc} appears. Formulas used here for diffusion length calculation were taken from [Wee, 2014].

The drift current collected in the depletion region can be expressed as:

$$J_{drift} = q\int_0^{x_d} \varphi(x) G_{opt}(x) dx \tag{4.16}$$

where q is the electron charge, $\varphi(x)$ is the probability of the carrier collection (here it is taken to be equal 1, it means that there is no recombination inside the *i*-region), x_d – thickness of the depleted region, $G_{opt}(x)$ is the generation rate of the electrons for monochromatic radiation. $G_{opt}(x)$ can be expressed as follows:

$$G_{opt}(x) = T_\lambda \Phi_0 \eta_\lambda \alpha e^{-\alpha x} \tag{4.17}$$

where T_λ is the optical transmission factor of the semitransparent contact, Φ_0 is the insident flux density, η_λ is the number of the created electron-hole pairs per one photon (here η_λ is assumed to be 1. It means one photon creates one electron-hole pair), α is the absorption coefficient (here it is taken to be ~ 10^5 cm^{-1}), x is the absorption thickness.

Substituting Eq. (4.17) into Eq. (4.16) we obtain:

$$J_{drift} = qT_\lambda \Phi_0 \alpha \int_0^{x_d} e^{-\alpha x} dx = T_\lambda \Phi_0 q(1 - e^{-\alpha x_d}) \tag{4.18}$$

For samples with thick MQW region (40-100 QWs), a part of *i*-region is not depleted (has no electric field). The schematic of the band diagram for such type of samples is show in Figure 4.19. Therefore, the total J_{sc} is a sum of the drift and diffusion current ($J_{sc} = J_{drift} + J_{diff}$).

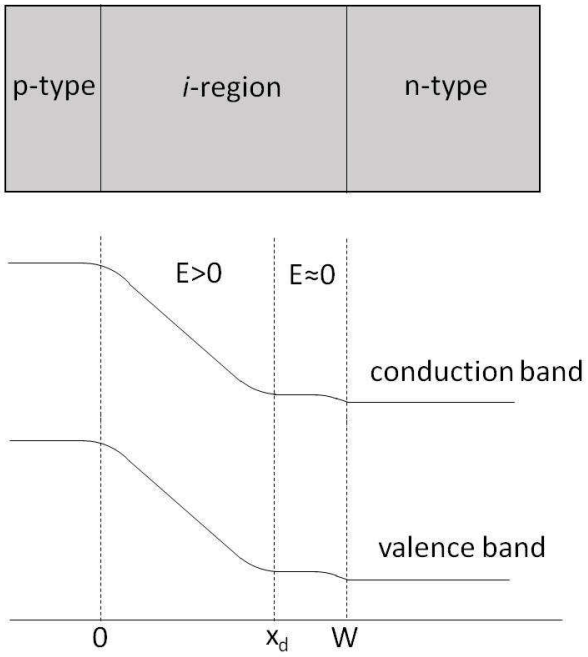

Figure 4.19. A schematic of the band diagram for p-i-n solar cell with a very thick i-region.

Diffusion current for electrons can be expressed as follows (for holes it is done analogically):

$$J_{diff} = -qD_n \frac{dn(x)}{dx}|_{x=x_d} \tag{4.19}$$

where D_n is the diffusion coefficient. $n(x)$ is the electron density distribution in *i*-region where $x \geq x_d$ and it can be obtained through the solving of the minority carrier continuity equation:

$$\frac{dn(x)}{dt} = D_n \frac{d^2n(x)}{dx^2} + G_{opt}(x) - \frac{n(x)-n_{p_0}}{\tau_n} = 0 \tag{4.20}$$

Solution of Eq. (4.20) looks as follows:

$$n(x) = C_0 e^{-\alpha(x-x_d)} - C_0 e^{-(x-x_d)/L_n} + n_{p_0} \tag{4.21}$$

where $C_0 = \frac{T_\lambda \Phi_0 e^{-\alpha x_d} \alpha L_n}{D_n(1-\alpha^2 L_n^2)}$. The description of how the minority carrier continuity equation has been solved is presented in *Annex 2*.

After substituting of Eq. (4.21) into Eq. (4.19), we obtain a formula for diffusion current:

$$J_{diff} = qT_\lambda \Phi_0 e^{-\alpha x_d} (\frac{\alpha L_n}{1+\alpha L_n}) \tag{4.22}$$

The total current is a sum of the drift and diffusion currents and therefore, it can be expressed by:

$$J_{tot} = J_{diff} + J_{drift} = qT_\lambda \Phi_0 (1 - \frac{e^{-\alpha x_d}}{1+\alpha L_n}) \tag{4.23}$$

Rearranging Eq. (4.23) we can extract the value of diffusion length L_n:

$$L_n = \frac{1}{\alpha}\left(\frac{qT_\lambda \Phi_0 e^{-\alpha x_d}}{qT_\lambda \Phi_0 - J_{tot}} - 1\right) \tag{4.24}$$

As it was obtained from capacitance-voltage measurements, *i*-region of the samples with 5–30 QWs is compeletely depleted. Therefore, we can consider that the J_{sc} obtained from these samples is mostly composed from the drift current. Taking the value of the $J_{drift} = J_{sc}$ for samples with 5–30 QWs and using Eq. (4.18), we can estimate the value of $qT_\lambda \Phi_0$ that should

be the same for all samples under study. As it was previously said, in the samples with thick *i*-regions the J_{sc} includes both currents: diffusion and drift. Therefore, setting $J_{tot} = J_{sc}$ for samples with 60 and 100 QWs and taking into account previously obtained $qT_\lambda\Phi_0$ we were able to calculate the value of the effective hole diffusion length L_p = 42 nm that is the same order of magnitude as obtained from the model fitting. The value of diffusion length seems quite small but one should remember that this is effective diffusion length obtained for holes in ***MQW region***.

4.4 Conclusion

In this chapter, samples with different number of $In_{0.11}Ga_{0.89}N$ (1.7 nm)/GaN (8-9 nm) QWs from 5 to 100 have been grown by MOVPE. All samples have a good crystalline quality and sharp interfaces between wells and barriers. There is an interdiffusion process of In-atoms inside the GaN barriers because of temperature change during the growth, leading to the gradation of In composition at the QW edges. Thanks to low In-content we succeeded to grow a large number of QWs without appearance of a significant plastic relaxation (i.e. dislocation occurrence). The variation of the period through the structure was also estimated to be less than 3 Å, revealing a good stability of the growth process during a long time: the growth of 100 QWs lasted more than 30 hours.

The analysis of the optical properties with *s*-shape of the PL energy dependence on the temperature and the presence of a Stokes' shift demonstrated the excistance of In fluctuations in all samples with high number of QWs. The increase of the localization parameter σ points out the enhancement of In inhomogeneities with QW number.

After structural characterization, the samples have been processed into solar cells with 0.5×0.5 mm^2 and 1×1 mm^2 mesa sizes. Devices with both mesa sizes showed a high homogeneity of the photovoltaic characteristics. We showed an enhancement of conversion efficiency with QW number. The maximum value of 0.88% is obtained under 1 Sun AM1.5G equivalent illumination for sample with 60 QWs. The values of J_{sc} and V_{oc} have been improved with the number of periods from 5 to 40. As expected, the increase of the total InGaN thickness in the structure improves the light absorption and positively influences the value of short-circuit current that shows a linear increase with the QW number. Thanks to the absence of the strain relaxation and its related defect formation we do not observe the degradation of V_{oc} and *FF* as it is usually measured by other groups [Young, 2013; Liou,

2011]. It confirms that the control of the strain relaxation is a very important issue in the growth of InGaN-based materials and it must be carefully managed to obtain a high-efficient solar cell. Inspite we managed to postpone the strain relaxation in the samples, nevertheless with increase of the active region thickness the probability of the carrier recombination on the way to the contact increases. This leads to the saturation of J_{sc} and decrease of V_{oc} for structures with thick *i*-region.

A simplified model taking into account the change of the electric field with active region thickness was developed to estimate an effective hole diffusion length (L_p) inside MQW region. According to model fitting of the experimental data L_p = 64 nm. Capacitance-voltage measurements showed that for samples with thick MQW regions (40, 60 and 100 QWs) only a part of MQWs was depleted. It means that diffusion current plays a significant role in the value of the short-circuit current for these samples. Therefore, the value of the effective hole diffusion length has been re-calculated taking into account capacitance-voltage measurements and diffusion current for samples with thick MQW region. Finally, L_p = 42 nm has been estimated that has the same order of magnitude with obtained through the model fitting.

Therefore, we investigated $In_{0.11}Ga_{0.89}N$ (1.7 nm)/GaN (8-9 nm) solar cells with QW number from 5 to 100. The conversion efficiency of 0.88% for sample with 60 QWs under 1 Sun AM1.5G equivalent illumination was reached. This relatively low (compare to Si or GaAs) value shows that such kind of solar cells can not be used as an independent photovoltaic solution because it absorbs light only with the wavelength less than 415 nm, while the peak of solar spectrum on the Earth is in 470-550 nm range. Therefore, it is necessary to increase the absorption wavelength of InGaN-based devices. This can be done by optimizing QW design.

Chapter 5

Active region design optimization of the InGaN/GaN QW-based solar cells

In the previous chapter, we discussed the influence of QW number on photovoltaic properties of $In_{0.11}Ga_{0.89}N$/GaN quantum well-based solar cells. The performance of the best solar cell exhibited promising electrical parameters such as V_{oc} = 2.3 V, FF = 56% and J_{sc} = 0.68 mA/cm^2 that leads to an efficiency of 0.88%. Although, the values of open-circuit voltage and fill factor are comparable with the state-of-the-art [Lang, 2012; Deng, 2011], the short-circuit current value remains quite low and can be further improved by optimizing the design of the active region. Accordingly, in this chapter, we will investigate the effect of InGaN/GaN region design on structural, optical and photovoltaic properties of the devices by tuning the thickness of wells and barriers and In composition inside the wells.

Several papers have been published as a result of the work presented in this chapter. In particular, section 5.1 was reported in [Redaelli, 2014] and section 5.2 was reported in [Valdueza, 2014].

5.1 Variation of quantum well thickness

The light absorption is one of the most critical point of the InGaN/GaN solar cells that determines the value of J_{sc}. One of the ways for light absorption enhancement is to increase the thickness of absorbing InGaN layer. Increasing number of QWs leads to a thicker active region and decreases the internal electric field inside the structure damaging the collection efficiency. Another way to increase the thickness of absorbing layer is to change the QW thickness. We propose to address to this point in this section and discuss structural, optical and electrical features of samples with different QW thickness.

Schematic of the sample structure investigated in this section is presented in details in Figure 5.1: 30×InGaN QWs with thickness 1.3, 3.1 and 5.4 nm keeping the same In composition target equal to 11% have been grown by MOVPE. The rest of the structure is exactly identical to the previous samples described in the Chapter 4. The 30×InGaN/GaN

samples with QW thickness of 1.3, 3.1 and 5.4 nm will be called as *V1*, *V2* and *V3* in the following.

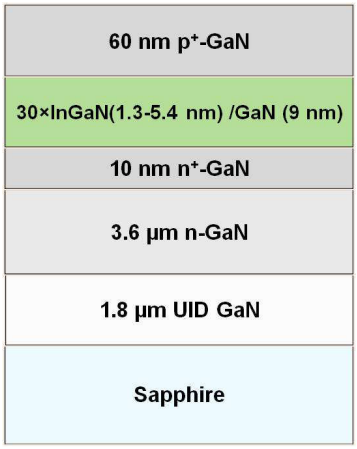

Figure 5.1. The structure of 30×InGaN (T_w nm)/GaN (9 nm) samples with different QW thickness T_w = 1.3, 3.1 and 5 nm.

As it is well known, the increase of the well thickness changes the optical properties of the QWs. To illustrate this point, band diagrams for this batch of samples have been calculated with Nextnano[3] software by Dr. Eva Monroy (Figure 5.2). The calculations were done for three QWs in the middle of the active region supposed fully-strained on a bulk GaN substrate. A lattice temperature of 5 K, an InN bandgap of 0.69 eV and a band gap bowing parameter of 1.4 eV were assumed.

The increase of QW thickness induces a lowering of the energy difference between hole and electron-states together with increased Quantum Confined Stark Effect. That causes the red-shift of PL emission (from 390 nm to 475 nm). Besides, the presence of piezoelectric field leads to the reduction of the electron and hole wave function overlap.

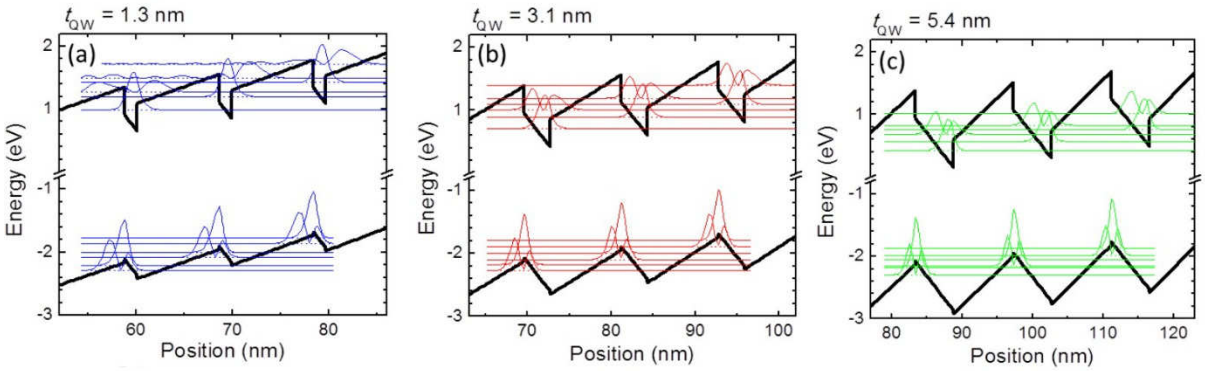

Figure 5.2. Band diagrams of the $In_{0.12}Ga_{0.88}N$/GaN (t_{QW} / 8.5 nm) MQW structure for (a) t_{QW} = 1.3 nm, (b) t_{QW} = 3.1 nm, (c) t_{QW} = 5.4 nm. Two first electronic levels in each QW are shown with their squared wave functions [Redaelli, 2014].

5.1.1 Structural and optical investigation

5.1.1.1 HRXRD

To determine the structural quality of grown samples, XRD analysis was performed at the BM02 beamline of the European Synchrotron Radiation Facility (ESRF) using a wavelength λ = 1.28361 Å. *ω-2θ* scan around the (0004) reflection for *V1*, *V2*, *V3* samples is presented in Figure 5.3 with simulated curves made using X'pert Epitaxy 4.0 software from Philips Analytical.

The values of SL period derived from HRXRD measurements are listed in Table 5.1. In composition obtained from simulation is equal to 12 ± 2 % for all samples under study. The values of QW and QB barrier thicknesses are derived from HRTEM images (Table 5.1).

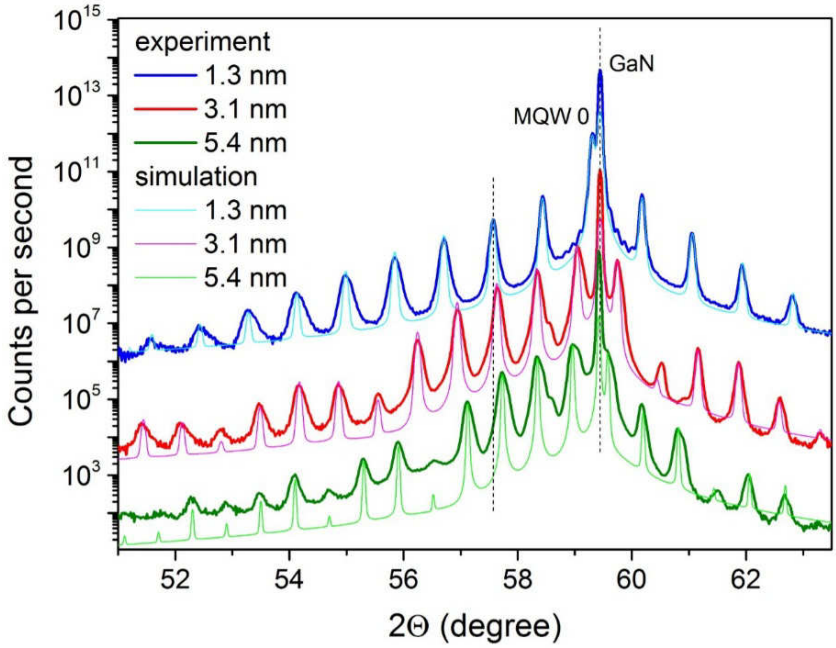

Figure 5.3. ω-2θ scan around (0004) reflection for InGaN/GaN samples with QW thicknesses: 1.3, 3.1 and 5.4 nm measured with radiation wavelength λ = 1.28361 Å. The simulations are presented in thin lines [Redaelli, 2014].

To determine the degree of relaxation[*], we performed a reciprocal space map (rsm) around the (10-15) reflection at the 1.54056 Å radiation wavelength with the HRXRD laboratory setup. Figure 5.4 shows an example of rsm mapping for sample with different QW thickness.

[*] Relaxation is defined as $R = (a_{MQW} - a_{GaN})/(a_{MQW0} - a_{GaN})$, where a_{MQW} is the measured in-plane average lattice parameter of the MQW, a_{MQW0} is the average lattice parameter of the relaxed superlattice and a_{GaN} is the lattice parameter of the GaN buffer layer.

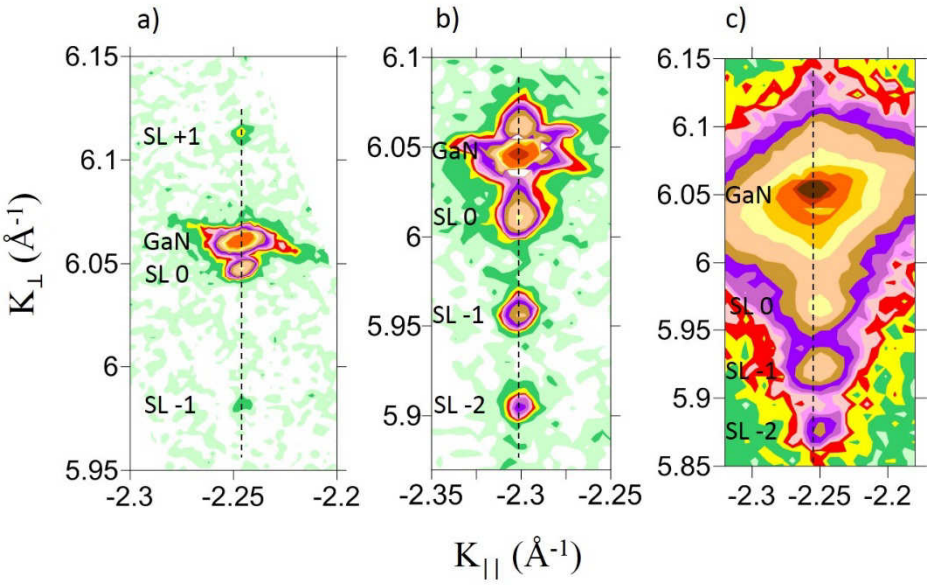

Figure 5.4. Reciprocal space map around (10-15) reflection for the 30×$In_{0.12}Ga_{0.88}N$ (T_w)/GaN (9 nm): a) T_w = 1.3 nm; b) T_w = 3.1 nm; c) T_w = 5.4 nm samples. The measurements are done at HRXRD setup at the 1.54056 Å radiation wavelength [Redaelli, 2014].

Samples with 1.3 and 3.1 nm QW thickness are coherently biaxially strained on GaN buffer layer within the error bar of the experimental technique. This error bar of relaxation is quite large in these samples and is estimated to be ± 20%*. Such large error bar is related to quite low In composition. On the contrary, a quite evident misalignement between GaN and SL peaks is seen in Figure 5.4 for sample with 5.4 nm QW thickness. The relaxation degree is found to be equal to 40 ± 20%. The thicknesses of barrier $T_{barrier}$ and well T_{well} (derived from HRTEM images) are listed in Table 5.1.

Table 5.1. Parameters of 30×$In_{0.12}Ga_{0.88}N$/GaN QWs: SL period T, thickness of well T_{well} and barrier $T_{barrier}$. [a)]Values extracted from XRD ω-2θ scan around (0004) Bragg peak reflection; [b)]Values are extracted from HRTEM images.

Samples	$T^{a)}$, nm (XRD)	$T^{b)}_{well}$, nm	$T^{b)}_{barrier}$, nm
V1	9.7	1.3 ± 0.26	8.0 ± 0.26
V2	12.0	3.1± 0.26	9.3 ± 0.26
V3	13.7	5.4 ± 0.26	9.1 ± 0.26

* Such large value of the error bar in relaxation is related to the low In-content in the samples and small difference in *a*-lattice parameters between GaN and relaxed QWs.

5.1.1.2 HRTEM

High resolution TEM (HRTEM) images were performed to investigate further the structural properties and especially, to study the strain relaxation in the MQW structure. Figure 5.5 shows HRTEM images of the active region for samples with different QW thicknesses. The MQW structure for sample *V1* is well defined with abrupt interfaces and constant well thickness (Figure 5.5 (a)). The interfaces of sample *V2* are still flat (Figure 5.5 (b)) but in some places the misfit relaxations appear, disturbing the MQW structure (Figure 5.5 (c)). This effect increases and takes place on larger areas for the sample *V3* (see Figure 5.5 d and e). In some regions, QWs remain well defined but somewhere they are heavily degraded. This degradation leads to a strong inhomogeneity of In composition and QW thickness.

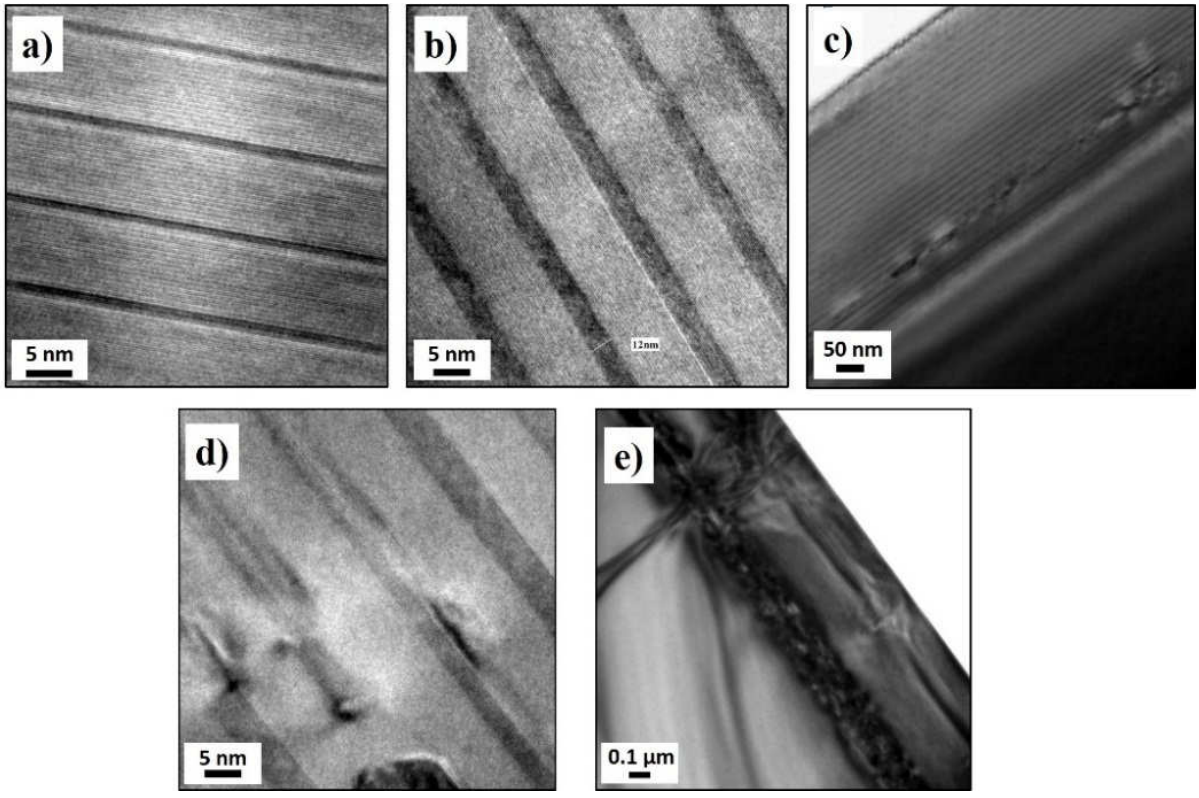

Figure 5.5. HRTEM images of InGaN/GaN QW region for samples with QW thickness: (a) 1.3 nm; (b, c) 3.1 nm; (d, e) 5.4 nm (the images are from C. Bougerol) [Redaelli, 2014].

5.1.1.3 PL measurements

The evidence of In inhomogeneities is also supported by low-temperature (5K) PL measurements (Figure 5.6). There is a noticeable red-shift of PL wavelength together with a

decrease of the PL emission intensity. This effect can be related to a presence of polarization field that reduces an energy difference between hole and electron states together with a decrease of the electron and hole wave function overlap causing a red-shift of PL emission and a drop in emission intensity, respectively. In addition, the FWHM of the PL peaks is significantly increased with QW thickness showing a structural quality degradation of the samples in accordance with TEM images.

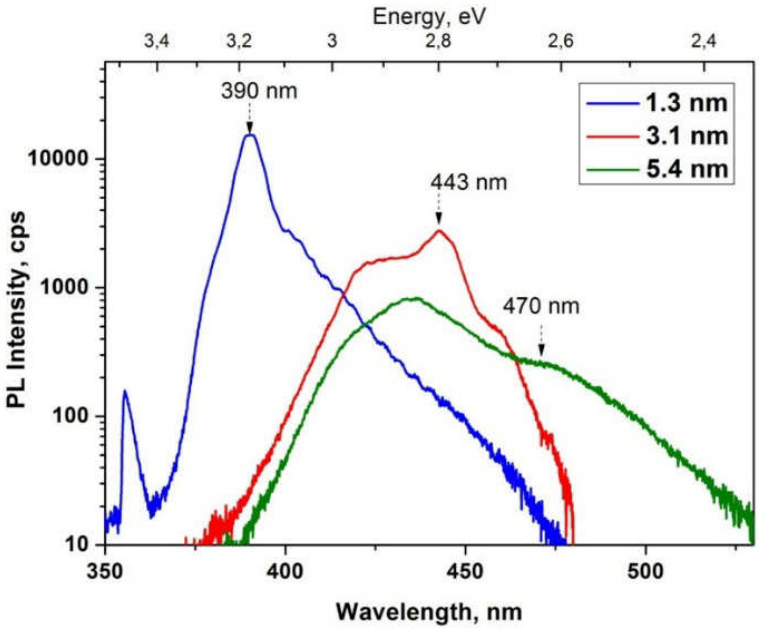

Figure 5.6. Low-temperature (5K) PL measurements from 30×$In_{0.12}Ga_{0.88}N$ (t_w)/GaN (8-9 nm) samples with T_w = 1.3, 3.1, 5.4 nm.

5.1.1.4 Discussion

Figure 5.7 presents the comparison of the experimental data obtained with PL measurements and simulated with Nextnano[3] software data for different QW thickness (T_w = 1.3, 3.1 and 5.4 nm) considering $In_{0.12}Ga_{0.88}N$ (T_w)/GaN (8.5 nm) QWs. Black solid line shows emission wavelength dependence on QW thickness for strained QWs, dotted line corresponds to calculations done for fully-relaxed QWs. The stars indicate the emission wavelength calculated for samples under study taking into account their degree of relaxation (the degree of relaxation for sample *V1*, sample *V2*, sample *V3* is 0, 10* and 40%, respectively). The lattice temperature for simulation calculation is supposed to be 5K.

* For the samples under study, the relaxation error bars were estimated to be ±40% in sample *V1* and ±20% in sample *V2*, due to the relatively low average In content in a MQW period. It is reasonable to assume fully strained QWs in sample *V1*, due to the fact that the wells are very thin in comparison to the barriers. However, the QWs of sample *V2* may be partially relaxed in view of the defect structure observed by HRTEM. Thus, for the calculations in Fig. 5.7, we have assumed 10% relaxation in sample *V2*.

The red-shift of the emission with QW thickness is mostly related to the QCSE that is induced by the presence of piezoelectric fields inside the MQW structure. The relaxation decreases the value of piezoelectric fields and therefore, leads to a smaller red-shift (comparison of the black solid and black dashed lines in Figure 5.7). Experimental results show the same trend as calculated values (taking into account the degree of relaxation), but they are slightly red-shifted. This effect becomes more evident with QW thickness. It can be related to In and QW thickness fluctuations inside the QW structure that increase with QW thickness. This data is in a good agreement with results obtained from HRTEM images and optical measurements.

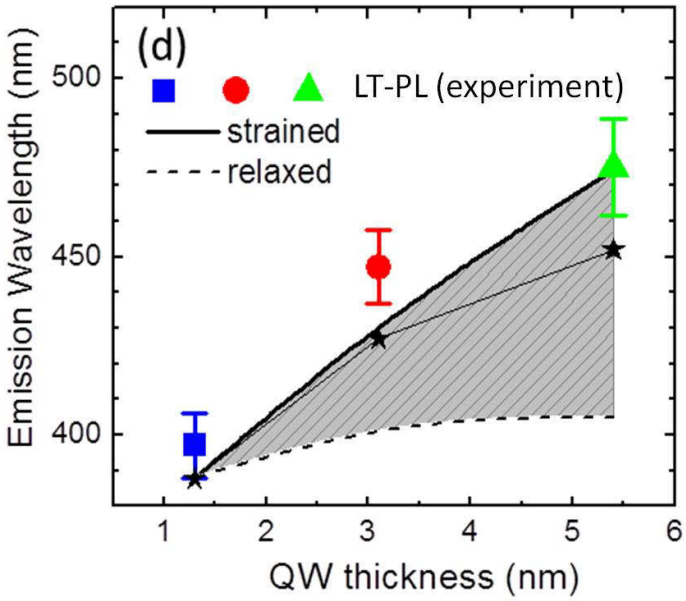

Figure 5.7. Calculated e_1-h_1 transition wavelength as a function of the QW thickness assuming the MQW fully strained on GaN and fully relaxed. The stars indicate the result for the strain state estimated by XRD measurements. The calculations are compared to the PL peak emission wavelength measured at 5 K. The error bars indicate the FWHM of the PL peaks [Redaelli, 2014].

5.1.2 Photovoltaic properties

Figure 5.8 presents the measurements of the spectral response for the 30×$In_{0.12}Ga_{0.88}N(T_w)$/GaN(8-9 nm) under study.

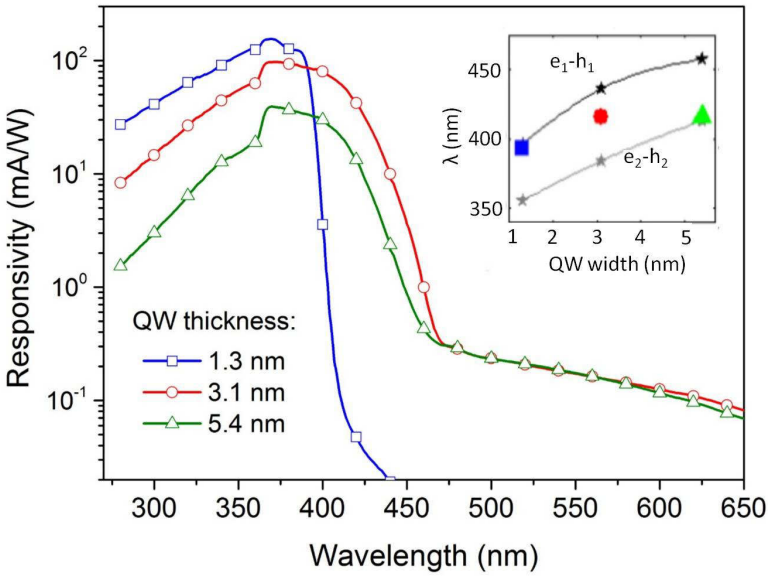

Figure 5.8. Spectral response of the 30×$In_{0.12}Ga_{0.88}N$/GaN(8-9 nm) samples with different QW thickness. Inset: the stars indicate the e_1-h_1 and e_2-h_2 transition wavelengths (λ) as a function of the QW width, calculated with Nextnano[3] by Dr. E. Monroy assuming the lattice at room temperature and the strain states measured by XRD. Points indicate the experimental spectral cutoff of the samples, defined as the wavelength where the photocurrent drops to half of the maximum value [Redaelli, 2014].

As expected from PL measurements, the spectral cutoffs of the samples with thicker QWs are red-shifted with respect to sample *V1*. Surprisingly, the sample *V3* is slightly blue-shifted in comparison with sample *V2*. The peak responsivity measured at about 370 nm for all samples is about 155, 107 and 39 mA/W for QW thickness of 1.3, 3.1 and 5.4 nm. These numbers correspond to 0.52, 0.36, and 0.13 external quantum efficiencies, respectively.

One possible explanation of the unexpected red-shift absence for sample *V3* together with a decrease of the peak responsivity can be proposed. The increase of QW thickness induces the deepening of energetic levels inside the QWs and enhances the carrier confinement. Therefore, it may become difficult for carriers to escape from the deepest levels and most of the carriers collected at the contacts may escape from less-confined high-energetic levels.

Band diagram calculations (inset of Figure 5.8) support this assumption showing the correspondence of the spectral cutoff for sample with thin QWs (1.3 nm) with the energy

difference between e_1-h_1 levels and for sample with thick QWs (5.4 nm) with the energy difference between e_2-h_2 second electron-hole levels.

Current density-voltage curves under 1 Sun AM1.5G equivalent solar illumination are shown in Figure 5.9. The values of electrical parameters extracted from these curves are listed in Table 5.2.

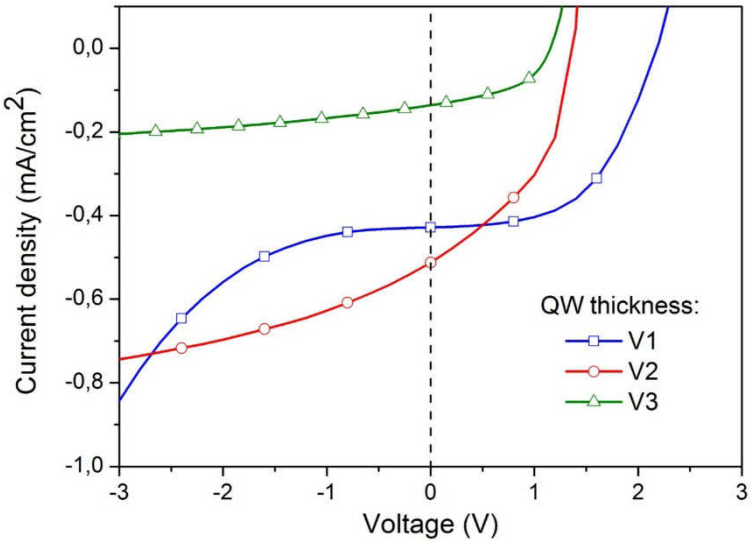

Figure 5.9. Current density-voltage characteristics under 1 Sun AM1.5G equivalent solar illumination for 30×$In_{0.12}Ga_{0.88}N$ (1.3-5.4 nm)/GaN (8-9 nm) solar cells [Redaelli, 2014].

Table 5.2. Electrical characteristics of samples with different QW thicknesses: short-circuit current J_{sc}, open-circuit voltage V_{oc}, fill factor FF and conversion efficiency η.

QW thickness (nm)	J_{sc} (mA/cm^2)	V_{oc} (V)	FF (%)	η (%)
1.3	0.42	2.2	54	0.49
3.1	0.46	1.3	42	0.25
5.4	0.14	1.1	47	0.07

The highest value of short-circuit current is obtained for sample with QW thickness of 3.1 nm: J_{sc} strongly depends on the number of absorbed photons and, as it was shown, the sample with QW thickness of 3.1 nm has a spectral cutoff red-shifted by 30 nm as compared to sample *V1*. It means that the sample *V2* is able to absorb more photons and to create a larger number of carriers. Nevertheless, the spectral cutoff of the sample *V3* (with 5.4 nm QW thickness) is about the same as for sample *V*2, but the value of J_{sc} is lower. This fact is related to a high number of dislocations created by strain relaxation in sample *V3* as shown by XRD diffraction and HRTEM images. Carriers are created inside the QWs, but they can not be collected because of recombination with the defects.

A high dislocation density observed in TEM images has an effect on the value of open-circuit voltage as well. The highest open-circuit voltage is obtained for sample *V1* with the thinnest QWs. The value of V_{oc} constantly decreases with QW thickness because of increased carrier recombination. Finally, the best conversion efficiency of 0.49% is obtained for sample with the thinnest QWs, attributed to the high structural quality of this sample compared to the others.

It is also interesting to notice that the current for sample *V1* significantly increases at the voltage higher than -2 V. This effect can be related to the increase of tunneling effect, because of higher electric field inside thinner active region [Watanabe, 2012; Wierer, 2012].

5.1.3 Summary of the role of QW thickness

We investigated the structural and photovoltaic properties of the $30\times In_{0.12}Ga_{0.88}N/GaN$ (8–9 nm)-based solar cells with different QW thickness (1.3, 3.1 and 5.4 nm). A theoretical simulation with Nextnano^3 software predicts a red-shift of the emission wavelength of about 80 nm by increasing the QW thickness from 1.3 to 5.4 nm due to the presence of the piezoelectric field inside the MQW structure. But experimentally, it was shown that the effect of the effective band gap decrease can not be completely used in photovoltaic cells. The deepening of the energetic levels with QW thickness increases the confinement of the carriers and prevents their escape from the well. Also, the enhancement of the strain inside the QW structure causes plastic relaxation and dislocation formation, as confirmed from XRD and TEM measurements. Dislocations degrade the collection efficiency of the devices and induce a decrease of the EQE from 0.52 for the sample with 1.3 nm QW thickness to 0.13 for the sample with 5.4 nm QW thickness. Therefore, in spite of the increased absorption, the collection of the carriers is very poor. It induces a strong decrease in the values of open-circuit voltage and fill-factor leading to conversion efficiency degradation. Consequently, the best value of conversion efficiency of 0.49% is obtained for sample with the thinnest QWs (1.3 nm).

5.2 Variation of In composition

There is one more way to improve the light absorption and the value of short-circuit current. It is well-known that an increase of the In-content helps to red-shift the absorption wavelength permitting to absorb a larger part of the solar spectrum [Wu, 2002; Wetzel, 1998]. Nevertheless, the growth of In-rich layers by MOVPE faces a lot of difficulties [Pantzas, 2013; El Gmili, 2013]. The first one comes from the growth temperature that must be low enough for a sufficient incorporation of In atoms ($T < 800\ ^0C$). But at the same time, the quality of InGaN layers degrades at low growth temperature because of insufficient diffusion rate of metal atoms and poor decomposition rate of ammonia (NH_3) [Mesrine, 1998]. The second difficulty comes from the InGaN lattice mismatch that increases with In-content causing the strain accumulation inside the QW structure. Beyond the critical thickness, the strains relieve by forming numerous dislocations that damages the quality of future solar cells.

This section will investigate the influence of In-content on the solar cell properties. The In composition inside QWs was changed from 10 to 18% by decreasing the growth temperature (from 750 ^{0}C for samples with 10% of target In-content to 720 ^{0}C for samples with 18% of target In-content) and by increasing the TMIn flow (from 120 sccm to 200 sccm), simultaneously. The temperature of barriers was kept the same (900 ^{0}C) for all samples. The schematic of the samples investigated in this section is presented in Figure 5.10.

Based on the previous studies, the number of QWs was chosen to be 15 and 30 (to limit the strain relaxation with the increase of In-content). Because of increased TMIn flow the QW growth rate was also enhanced. Therefore, QW thickness for the samples with high In composition is larger (2 nm) compared to the samples with lower In-composition (1.3 nm). In the following we will call the four samples as:

A1: N=15 QWs, In-content = 10%, QW thickness = 1.3 nm,

A2: N=30 QWs, In-content = 10%, QW thickness = 1.3 nm,

A3: N=15 QWs, In-content = 18%, QW thickness = 2 nm,

A4: N=30 QWs, In-content = 18%, QW thickness = 2 nm.

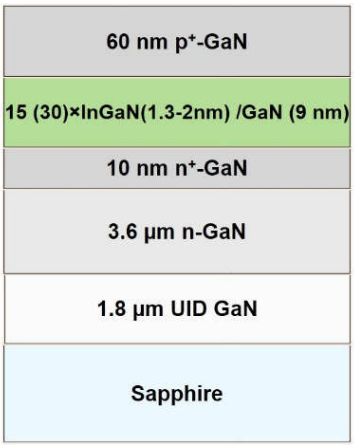

Figure 5.10. Structure schematic for 15(30)×InGaN (1.3-2 nm)/GaN (9 nm) samples with different In composition x = 10 and 18%.

Band diagrams calculated with Nextnano[3] software are presented in Figure 5.11. The increase of In-content induces the deepening of the QWs and, respectively, energetic levels causing a red-shift of the emission wavelength and absorption cut-off. The simulation is done for $In_{0.1}Ga_{0.9}N$ (1.3 nm)/GaN (8.5 nm) and $In_{0.18}Ga_{0.82}N$ (2 nm)/GaN (9 nm) QWs, supposing them fully strained. (The lattice temperature is 300 K).

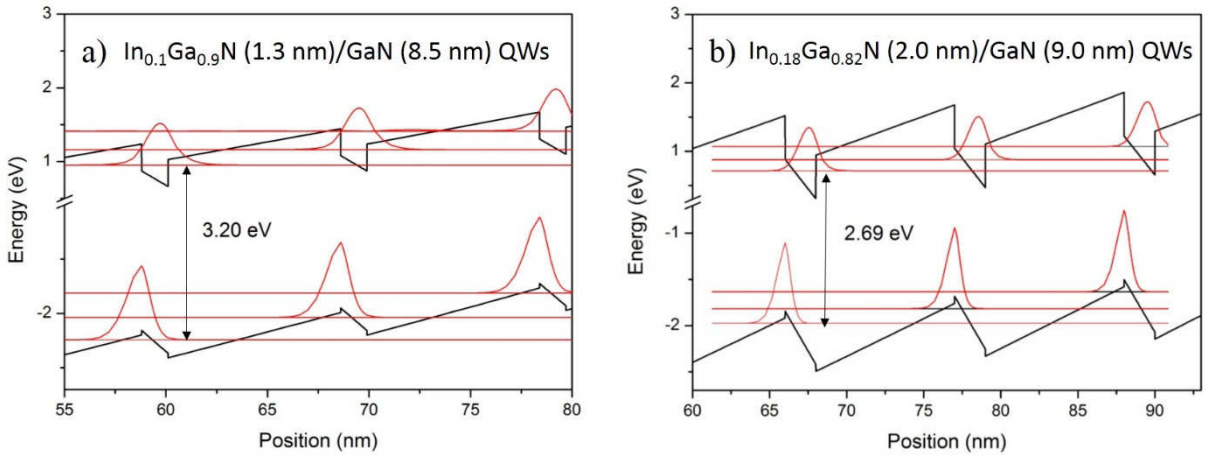

Figure 5.11. Band diagrams of the a) $In_{0.1}Ga_{0.9}N$ (1.3 nm)/GaN (8.5 nm) MQW structure and b) $In_{0.18}Ga_{0.82}N$ (2.0 nm)/GaN (9.0 nm) QWs. The first electronic levels are shown with their squared wave functions.

5.2.1 Structural and optical investigation

5.2.1.1 HRXRD

Figure 5.12 (a) presents *ω-2θ* scans for samples with 30×$In_xGa_{1-x}N$ (1.3-2 nm)/GaN (9 nm) QWs. Measurements are done at the BM02 beamline of the European Synchrotron Radiation Facility using the λ = 0.442959 Å wavelength.

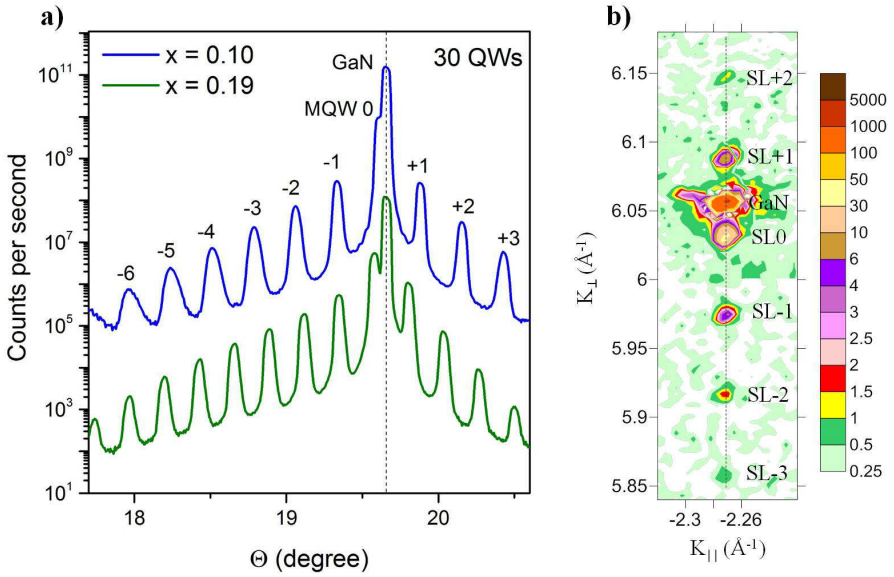

Figure 5.12. (a)ω-2θ scans around the (0004) reflection at the emission wavelength λ = 0.442959 Å for 30×$In_xGa_{1-x}N$ (1.3 -2 nm)/GaN (9 nm) samples with target In composition x = 10 and 18%. (b) Reciprocal space map around (10-15) reflection for 30×$In_{0.18}Ga_{0.82}N$/GaN sample. $K_{||}$ and $K_\perp$ are reciprocal space vectors.

Distinct and well-defined peaks for both samples confirm a good periodicity of the MQW structure. There is a slight variation in the period between the samples appearing as a shift of the satellite peaks induced by different QW thickness (see hereafter). To examine the strain state of the samples with higher In-content, reciprocal space mappings have been done. They demonstrated that all samples were coherently biaxially-strained on the GaN buffer layer regardless the In composition. Figure 5.12 (b) shows an example of rsm for sample with 30×$In_{0.18}Ga_{0.82}N$/GaN QWs.

Values of In-content were extracted using *c*-lattice parameter derived from HRXRD measurements and assuming a biaxial strain approximation, QW and QB thicknesses are obtained from HRTEM images (Figure 5.13). In-contents were calculated using Eq. (4.6) and correspond to the values of 10 ± 2% and 18 ± 2% for QW structures grown at 750 ^{0}C and 720 ^{0}C, respectively.

5.2.1.2 HRTEM

Typical HRTEM images show parallel QWs with abrupt interfaces confirming a good quality of the MQW structure for samples with both In-contents. An example of HRTEM image for 15×$In_{0.18}Ga_{0.82}N$ (2 nm)/GaN (9 nm) is presented in Figure 5.13. Table 5.3 presents the values of In-content and SL period extracted from HRXRD measurements and well and barrier thicknesses derived from HRTEM images.

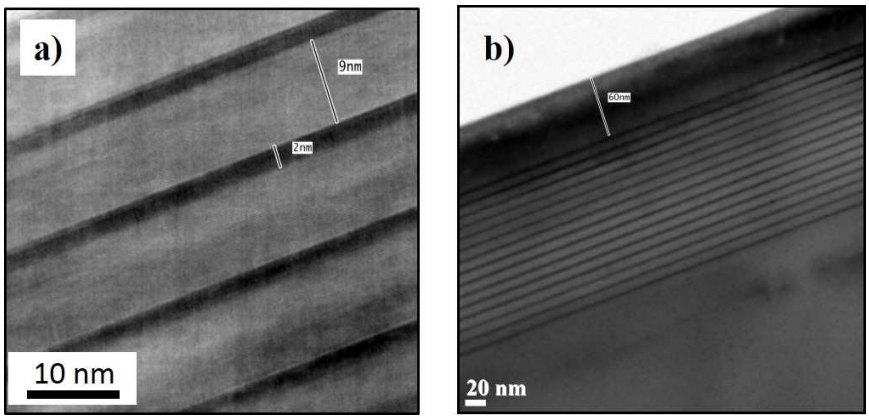

Figure 5.13. TEM images of the 15×$In_{0.18}Ga_{0.82}N$ (2 nm)/GaN (9 nm) QWs: a) active region; b) active region and p-GaN layer (the images are made by C. Bougerol).

Table 5.3. Structural parameters of the active region for $In_xGa_{1-x}N$/GaN MQW-based samples: In-content and SL period T are extracted from HRXRD measurements, QW T_{well} and QB T_{bar} thicknesses are derived from HRTEM images.

Sample	QW number	In-content (%)	T (nm)	T_{well} (nm)	T_{bar} (nm)
A1	15	9.0	9.6	1.3	8.5
A2	30	10.7	9.7	1.3	8.4
A3	15	19.1	10.8	2.0	9.0
A4	30	16.4	11.2	2.0	9.0

5.2.1.3 PL and transmission measurements

The increase of In-content is also confirmed by low-temperature (5 K) PL measurements. The shift of PL peak emission wavelength is about 50 nm with increasing In-content from 10 to 18%. For sample with 15 QWs and In-content of 18% the high intensity main peak is accompanied by a tail at shorter wavelengths. This effect may be related to an increase of In inhomogeneities inside the wells that often appear when increasing the In-content [Lin, 2000].

From simulation we obtained $\lambda \approx 390$ nm for 1.3 nm QW thickness with 10% of In and $\lambda \approx 460$ nm for 2 nm QW thickness with 18% of In. The difference of 10 nm with experimental data can be related to In inhomogeneities inside the wells and an error bar in the In-content calculations.

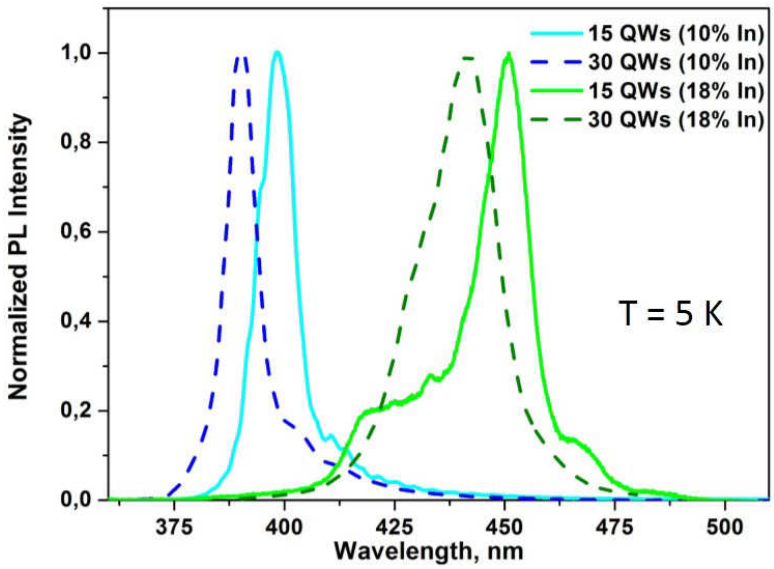

Figure 5.14. Low-temperature (5K) PL measurements of the 15(30)×$In_xGa_{1-x}N$(1.3-2 nm)/GaN(8-9 nm) samples with x = 10 and 18% [Valdueza, 2014].

An average band gap energy E_g and absorption edge broadening ΔE were estimated using Eq. (4.14) to fit room-temperature transmission data (Figure 5.15). The results are listed in Table 5.4.

The increase of In-content from 10 to 18% leads to the decrease of the average band gap of 0.28 eV, redshifting the emission wavelength of about 50 nm. The enhancement of the absorption edge broadening confirms the presence of In-content fluctuations inside the active region that increases with In-content. Based on the data derived from the fit of transmission measurements and room-temperature PL, the value of the Stokes' shift is obtained to be about 40 ± 12 meV and 200 ± 25 meV for low and high In-content samples, respectively.

Table 5.4. Optical properties of N×$In_xGa_{1-x}N$ (1.3-2 nm)/GaN (8-9 nm) solar cells: λ emission PL wavelength at 5K, full-width-half-maximum of the PL curves at 5K, average band gap E_g, broadening of absorption edge ΔE and the Stokes' shift.

Sample	QW number, N/ In-content, %	λ at 5 K, nm	FWHM at 5K, meV	E_g, eV	ΔE, meV	Stokes' shift, meV
A1	15/10%	398.3	76.6	3.12 ± 0.01	18 ± 1	40 ± 10
A2	30/10%	390.1	70.1			
A3	15/18%	450.8	83.0	2.84 ± 0.02	31 ± 1	57 ± 5
A4	30/18%	441.8	131.0			

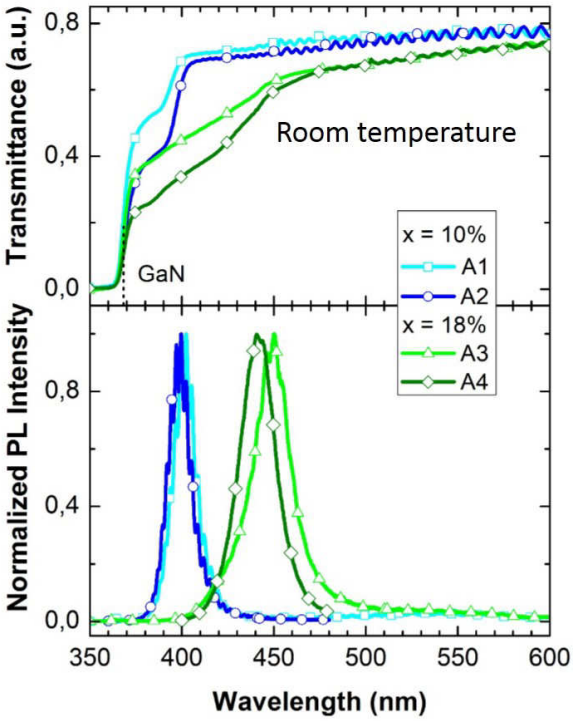

Figure 5.15. Room-temperature transmittance and normalized PL measurements for samples with 15(30)×$In_xGa_{1-x}N$ (1.3-2 nm)/GaN(8-9 nm) with x = 10 and 18% [Valdueza, 2014].

5.2.2 Electrical properties of solar cells

After their structural characterizations, the samples were processed into devices with 0.5×0.5 mm^2 and 1×1 mm^2 mesa sizes by using Cl_2-based inductively coupled plasma etching (all detailed information about device structure and contacts have been previously presented in Chapter 3).

Figure 5.16 shows the EQE spectrum. For samples *A1* and *A2*, the spectral cutoff is shifted to 380 nm and for samples *A3* and *A4* to 465 nm in relation to GaN photodetector

(~365 nm). The peak EQE of the devices increases a factor of 2.3−2.4 when increasing the number of QWs from 15 to 30 for both In-contents. But for samples with higher In-content, the values of EQE are always lower than for samples with In-content of 10%, probably because of carrier localization in In inhomogeneities that were observed with optical measurements.

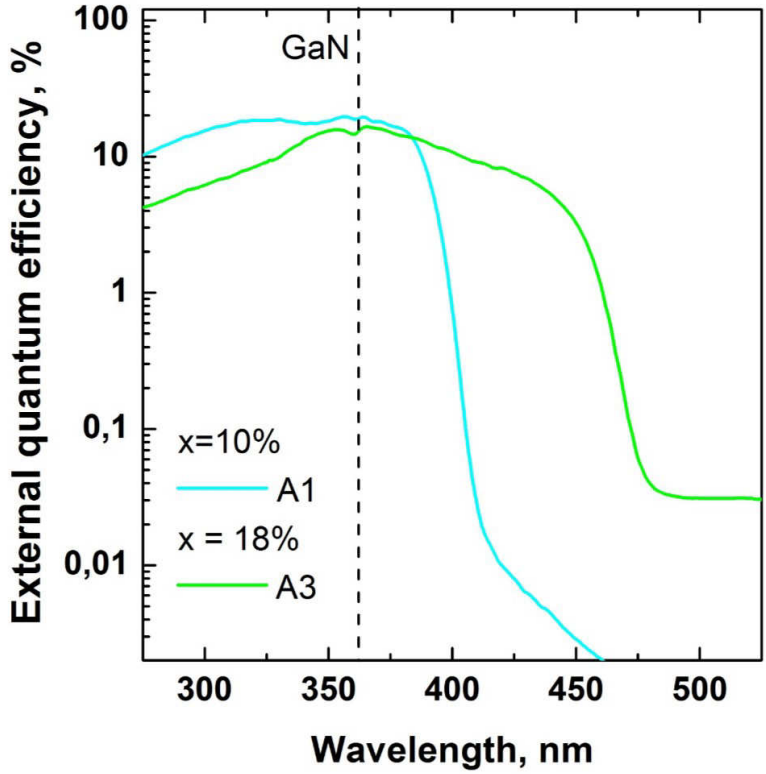

Figure 5.16. External quantum efficiency for 15×$In_xGa_{1-x}N$ (1.3-2 nm)/GaN (9 nm) with x = 10 and 18% solar cells as a function of the wavelength [Valdueza, 2014].

From electrical characteristics in the dark (not shown here), we can extract the values of parallel (given by the tangent to the *J-V* curve at $V = 0$ V) and series (given by the tangent to the *I-V* curve at high voltages ($V > E_g/e$)) resistances. The value of parallel resistance is caused by the leakage across the junction typically due to the presence of defects. The average values of parallel resistance extracted from electrical measurements in the dark (not shown here) is about $R_{SH} = (13\pm12)\times10^6$ Ωcm^2 for samples with both In-contents showing that QWs were not significantly damaged because of higher In-content in agreement with HRTEM and HRXRD measurements. The calculated values of series resistance are $R_S = 0.19$ (±0.05) Ωcm^2 and $R_S = 0.64$ (±0.05) Ωcm^2 for samples with 10% and 18% of In, respectively.

Figure 5.17 shows the *J-V* characteristics for 0.5×0.5 mm^2 devices, with 15/30 MQWs, and 10/18%-In under 1 sun AM1.5G equivalent illumination (1 kW/m^2). Relatively high values of open-circuit voltage $V_{oc} = 2.0$ V and fill factor $FF = 58.9\%$ are obtained for devices

with 30 MQWs and 10% of In-content. However, the short spectral cutoff wavelength limits the performance of the device with low In-content. The conversion efficiency raises a factor of ~20 by increasing the In-content in the QWs from 10% to 18%, obtaining a maximum J_{sc} = 3.00 mA/cm^2 and η = 2.00% for 15 MQW devices with 18% of In, at the price of the reduction of the *FF* to 39.3%. The electrical performance of the four structures is summarized in Table 5.5.

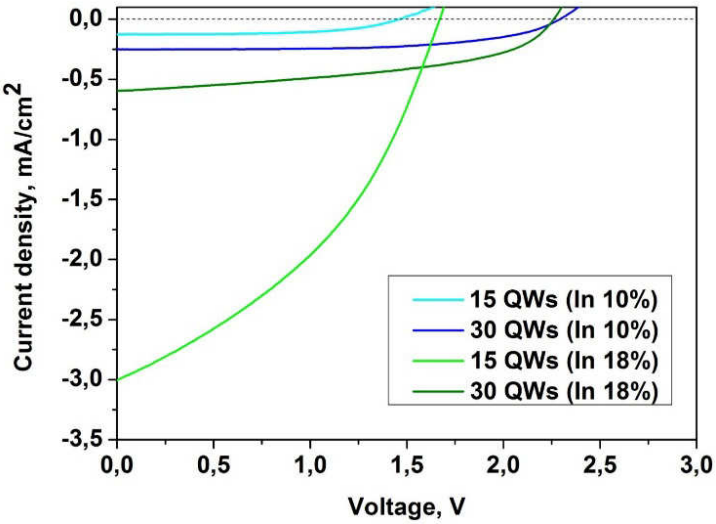

Figure 5.17. J-V characteristics under 1 Sun AM1.5G equivalent illumination for 15(30)×$In_xGa_{1-x}N$/GaN samples with x = 10 and 18% with 0.5×0.5 mm^2 size of mesa [Valdueza, 2014].

The decrease of the fill-factor with In composition is mostly related to the increase of the series resistance. Nevertheless, from Figure 5.17, there is a definite increase of the *J(V)* curve slope around 0V for samples with higher In-content (green lines) compare to samples with low In-content (blue lines). The appearance of this kind of slope is generally attributed to a R_{sh} decrease. However, as it was calculated from dark measurements, R_{sh} is not changed significantly with In-content for our samples. It means that there is another reason for increasing the slope at 0V, which is related to In composition and it can be probably attributed to the change of the carrier collection efficiency with bias.

Surprisingly, the value of V_{oc} is improved with an increase of the In-content. Open-circuit voltage is related to the value of short-circuit current J_{sc} and saturation current J_0 through Eq. (2.8).

Values of saturation current J_0 ("leakage current" in the device in the absence of light) extracted from the fit of dark *ln(J)-V* curves decreases with In composition pointing out the absence of the structural degradation for the samples with higher In-content (Table 5.5).

Table 5.5. Electrical parameters of solar cells having 15(30)×$In_xGa_{1-x}N$ (1.3-2 nm)/GaN (9 nm) MQWs with x = 10 and 18% and measured under 1 Sun AM1.5G equivalent illumination: external quantum efficiency EQE, saturation current J_0, open-circuit voltage V_{oc}, fill factor FF, short-circuit current J_{sc} and conversion efficiency η.

Sample	EQE at 380 nm, %	J_0, mA/cm^2	V_{oc}, V	FF, %	J_{sc}, mA/cm^2	η, %
A1	16±1	2.4×10^{-5}	1.5	57.8	0.13	0.11
A2	38±1	5.4×10^{-5}	2.0	58.9	0.23	0.29
A3	14±1	2.0×10^{-7}	1.7	39.3	3.00	2.00 (inhomogeneous)
A4	32±1	7.6×10^{-8}	2.2	47.0	0.60	0.65

The decrease of the fill factor for high In-content devices is a consequence of both the threefold increase in series resistance, and of the lower carrier collection efficiency (in agreement with EQE values). The drop in EQE is probably related to the existing hole blocking barrier* at the *i*-InGaN/*p*-GaN interface that increases with In-content [Jani, 2006]. In spite of higher V_{oc} and *FF*, the overall photovoltaic performance of *A4* is limited by the lower value of short-circuit current. This could be due to slightly lower In-content for sample with 30 QWs (16.4% in comparison with 19.1% for sample with 15 QWs). Also it is worth to notice that samples A3 with the highest In-content showed quite inhomogeneous electrical characteristics from device to device. This discrepancy of the data is related to the In fluctuations at a large lateral scale in agreement with PL data.

5.2.3 Summary of the role of In-content

(15 and 30)×$In_xGa_{1-x}N$/GaN samples with different In composition x = 10 and 18% have been investigated from structural and electrical point of view. All samples were coherently biaxially-strained on the GaN buffer layer as demonstrated by X-ray diffraction. The increase of In composition, checked by PL and absorption measurements, gives a 50 nm red-shift of the emission wavelength and absorption cutoff. The absorption edge broadening and Stokes' shift show the presence of In fluctuations inside the active region that increases with In-content.

EQE is improved by 2.3-2.4 times increasing the number of QWs from 15 to 30 for both In-contents, whereas a small reduction of EQE is measured for samples with In-content x =

18% as compared with x = 10%. This can be induced by the losses in collection efficiency because of the hole blocking barrier* at the *i*-InGaN/*p*-GaN interface that increases with In-content and the difficulty for carriers to escape from deeper QWs. Increase of In-content also negatively influences the *FF* of the devices. This phenomenon can be related to the change in the collection efficiency with bias that becomes more critical for samples with higher In-content. The value of V_{oc} was not damaged indicating a similar level of structural quality. In addition, J_{sc} was significantly improved thanks to a decrease of the band gap and an increase of the absorption (as Sun illumination intensity rises almost linearly with the wavelength in the 400-550 nm spectral range). It is also worth to notice that samples with higher In-content showed quite strong inhomogeneity of the photovoltaic characteristics that can be related to In composition fluctuations. The best value of conversion efficiency of 2.0% was reached for $15\times In_{0.18}Ga_{0.82}N$/GaN QWs.

5.3 Variation of barrier thickness

The increase of In-content induces several problems that have to be overcome to avoid any damage of the device electrical properties. One of them is the enhancement of the carrier confinement because of energy level deepening in the QWs. It becomes more difficult for carriers to escape and to be collected at the electrical contacts. As said before, there are two main ways for carriers to escape from the QWs: thermal emission and tunneling [Young, 2013]. Thermal emission is efficient for low In-content devices, because carriers can move easily out from the well at room temperature, but as the energy levels go deeper (as it was shown for thicker QWs) the thermal emission becomes insufficient. Normally, for GaN barrier thicknesses of 9 nm, the tunneling effect is negligible as it was shown in the literature [Deng, 2011; Lang, 2012]. Therefore, it is necessary to decrease the barrier thickness to enhance the tunneling probability of the carriers from the QWs. In this section, we will investigate the samples having a $15\times In_{0.17}Ga_{0.83}N$ (2 nm)/GaN (T_b) structure with a tuning barrier thickness (T_b) as depicted in Figure 5.18. To avoid a strong inhomogeneity of the photovoltaic properties that was observed in the previous series of samples with high indium composition, the growth temperature of the barriers was slightly decreased (from 900 ^{0}C to 885 ^{0}C) for this series of samples. It is believed that it helps to avoid strong fluctuations inside

* Hole blocking barrier is created by bending of the bands in the *i*-InGaN/*p*-GaN interfaces due to the piezoelectric field.

the QWs and improve the homogeneity of the sample. In the following, the samples with 9 nm, 5.5 nm and 3.7 nm GaN barrier thickness will be called as *D1*, *D2* and *D3*, respectively.

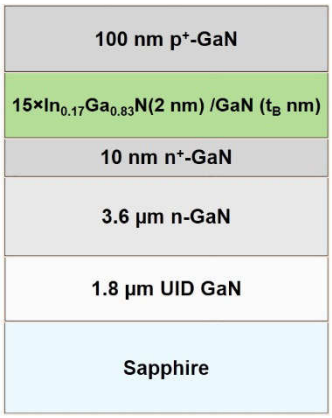

Figure 5.18. Structure schematic for 15×$In_{0.17}Ga_{0.83}N$ (2 nm)/GaN QW-based samples with thickness of GaN barriers: 3.7, 5.5 and 9.0 nm.

Band diagrams for this series of samples have been also calculated with the Nextnano[3] software (Figure 5.19). Calculations are done for $In_{0.17}Ga_{0.83}N$ (2 nm)/GaN (T_b) samples changing the thickness of the barrier T_b = 3.7, 5.5 and 9.0 nm. The lattice-temperature is supposed to be 5 K.

With the increase of the barrier thickness, the piezoelectric field inside wells also increases inducing the tilt of the QW energy band. The difference in energy between electron and hole ground states decreases leading to a red-shift in spectral emission.

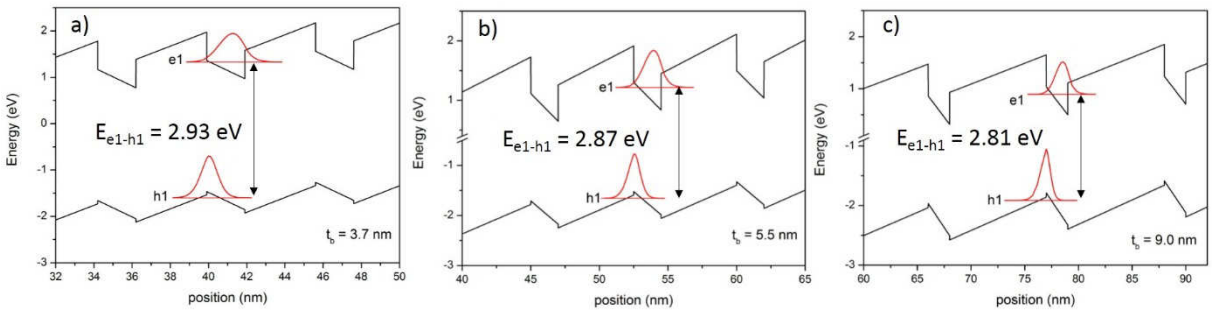

Figure 5.19. Calculations of conduction and valence band diagrams with Nextnano[3] software for 15×$In_{0.17}Ga_{0.83}N$ (2 nm)/GaN QWs with barrier thickness: (a) 3.7 nm; (b) 5.5 nm and (c) 9.0 nm. Red curves show the deepest energy level for electrons and the highest energy level for holes.

5.3.1 Structural and optical properties of as-grown samples

5.3.1.1 HRXRD

Figure 5.20 presents XRD ω-2θ scans that have been performed with the laboratory HRXRD setup to assess the structural parameters of the 15×$In_{0.17}Ga_{0.83}N$(2 nm)/GaN (T_b) samples. The presence of several satellite peaks around GaN peak (the most intense) confirms a good periodicity of the structure.

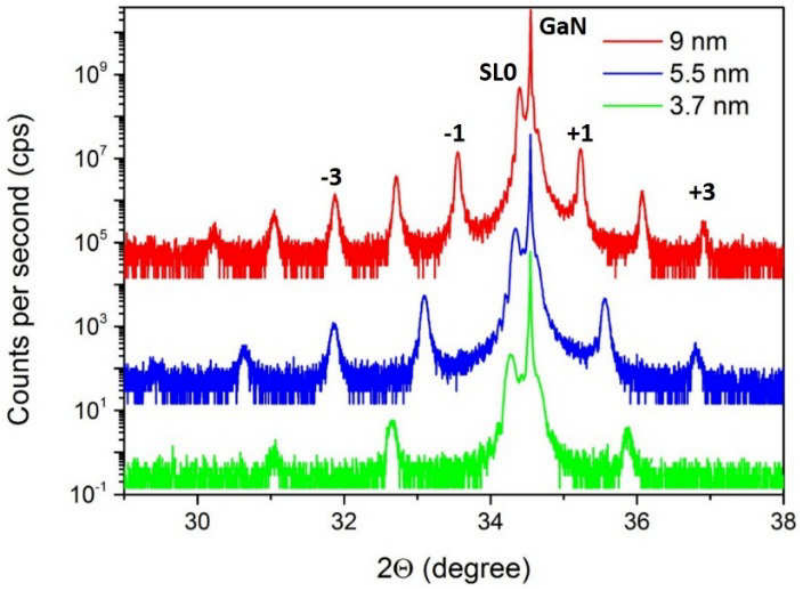

Figure 5.20. ω-2θ scan around the (0002) Bragg peak reflection at 1.54056 Å emission wavelength for 15×$In_{0.17}Ga_{0.83}N$ (2 nm)/GaN (3.7–9.0 nm).

The superlattice period *T* and average *c*-lattice parameter extracted from ω-2θ scans in Figure 5.20 are presented in Table 5.6. The value of In-content was calculated using Eq. (4.6) supposing that all samples are biaxially strained on GaN buffer layer. The thickness of QW is supposed to be 2 nm (by analogy with previous samples).

Table 5.6. Structural parameters of 15×$In_{0.17}Ga_{0.83}N$ (2 nm)/GaN (3.7–9 nm) samples: period T, total SL thickness H, average c-lattice parameter $<c_{SL}>$, In-content and relaxation degree R.

Sample	T, nm	H, nm	$<c_{SL}>$, Å	In-content, %	R, %
D1	11.0	167	5.2084	15.0	-
D2	7.5	110	5.2158	17.1	2.3
D3	5.7	79	5.2241	17.1	20

To investigate the strain state of the samples under study the reciprocal space mapping has been done. The examples of reciprocal space maps for all samples are shown in Figure 5.21. The extracted values of relaxation are listed in Table 5.6. The sample *D1* and *D2* are

biaxially strained on GaN buffer layer, but for sample *D3* there is a slight shift of *SL0* peak relatively GaN peak in the (10-15) rsm, pointing out the relaxation appearance. In spite of the small visible misalignment, the value of relaxation* *R* reaches 20% for sample *D3* supposing In composition of 17%.

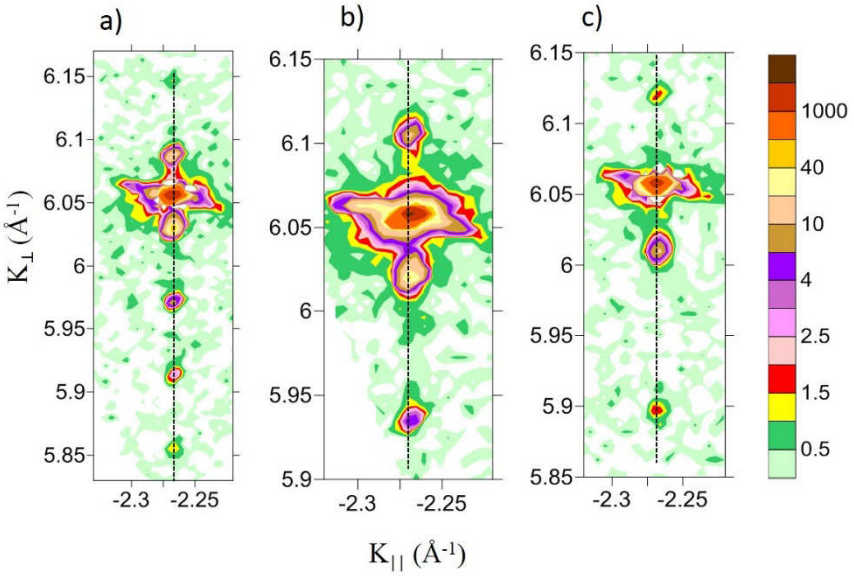

Figure 5.21. Reciprocal space maps around (10-15) Bragg's peak reflection for 15×$In_{0.17}Ga_{0.83}N$ (2nm) QW-based samples with the thickness of GaN barrier: (a) 9.0 nm, (b) 5.5 nm and (c) 3.7 nm. $K_{||}$ and $K_{\perp}$ are reciprocal space vectors.

5.3.1.2 PL and transmission

As shown in band diagram simulations, the change of the barrier thickness should influence the optical emission wavelength of investigated samples. Low-temperature (5 K) PL measurements are presented in Figure 5.22.

A red-shift of emission wavelength of 12 nm appears with increasing of barrier thickness from 3.7 nm to 9.0 nm in a good agreement with a value of 18 nm obtained with Nextnano[3] simulation.

In spite of the increase of the QCSE with QB thickness, the PL intensity for thicker barriers is higher. This can be related to the increase of non-radiative recombination because of defect formation induced by the strain relaxation of QWs with thinner barriers in accordance with XRD measurements.

* Relaxation is defined as $R = (a_{MQW} - a_{GaN})/(a_{MQW0} - a_{GaN})$, where a_{MQW} is the measured in-plane average lattice parameter of the MQW, a_{MQW0} is the average lattice parameter of the relaxed superlattice and a_{GaN} is the lattice parameter of the GaN buffer layer.

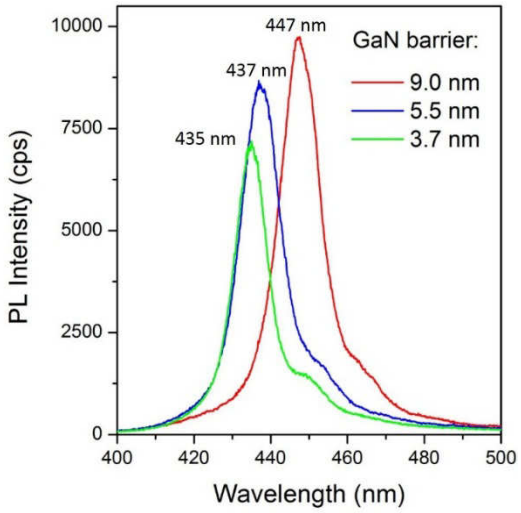

Figure 5.22. Low-temperature (5K) PL measurements of the $In_{0.17}Ga_{0.83}N$(2 nm)/GaN (3.7 – 9.0 nm) QW-based samples.

The influence of the barrier thickness on the transmittance spectra is shown in Figure 5.23. In agreement with low-temperature PL measurements, we see a slight red-shift of the absorption edge for samples with thicker barriers.

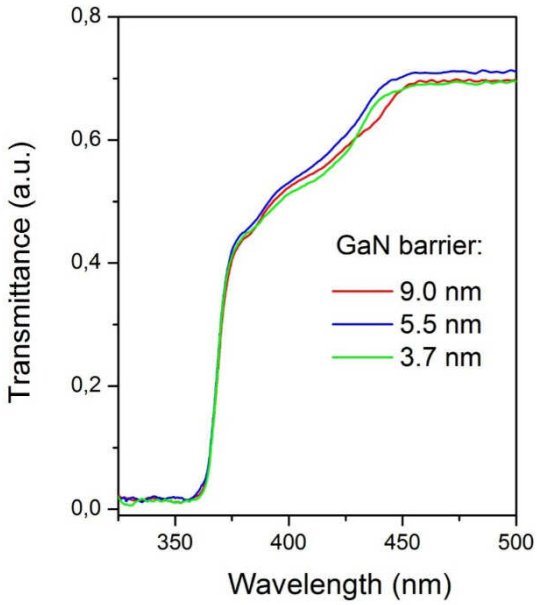

Figure 5.23. Transmission spectra for 15×$In_{0.17}Ga_{0.83}N$(2nm)/GaN(3.7–9 nm) QW structures.

By fitting transmission data with Eq. (4.14), we obtained the value of the effective band gap energy E_g and absorption edge width ΔE (Table 5.7). The presence of energetic states inside the band gap induces a smoothing of the absorption edge. The value of ΔE increases from sample *D1* to samples *D2* and *D3*. This can be related to the defects appearing inside the QW structure because of strain relaxation confirmed by XRD measurements. Comparing the

E_g obtained from the fit of the transmittance spectra with room-temperature PL spectra, we calculate the value of the Stokes' shift. As expected, the Stokes' shift increases with barrier thickness pointing out the enhancement of the QCSE that red-shifts the PL emission wavelength.

Table 5.7. Values obtained from optical measurements for 15×$In_{0.17}Ga_{0.83}N$(2nm)/GaN(3.7 – 9.0 nm): effective band gap E_g, absorption edge width ΔE, Stokes' shift.

Sample	E_g, eV	ΔE, meV	Stokes' shift, meV
D1	2.84	31.6	64.6
D2	2.90	40.7	54.0
D3	2.90	40.8	41.6

5.3.2 Influence of the barrier thickness on photovoltaic characteristics

The external quantum efficiencies for 15×$In_{0.17}Ga_{0.83}N$ (2nm)/GaN (3.7–9 nm) MQW samples are presented in Figure 5.24. Below 365 nm, the EQE values result from the GaN material, but the EQE for wavelength higher than 365 nm can be attributed to the $In_{0.17}Ga_{0.83}N$/GaN QWs. The values of EQE at 380 nm wavelength are 34.5, 30 and 27% for barrier thickness of 3.7, 5.5 and 9.0 nm.

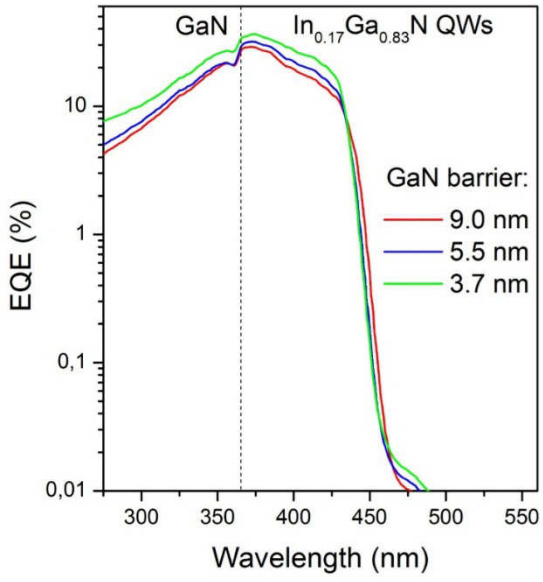

Figure 5.24. Spectral response of 15×$In_{0.17}Ga_{0.83}N$(2nm)/GaN(3.7 – 9.0 nm). Xe-arc lamp is used for 250-400 nm and halogen lamp is for 360-700 nm spectral range. The dotted line corresponds to the GaN spectral cutoff.

EQE is slightly improved by decreasing the barrier thickness. It can be related to the improvement of the collection efficiency due to tunneling effect. We have measured the same tendency for the short-circuit current values, that also increased with the decrease of the barrier thickness.

J(V) characteristics of three samples under 1 Sun AM1.5G equivalent illumination are shown in Figure 5.25.

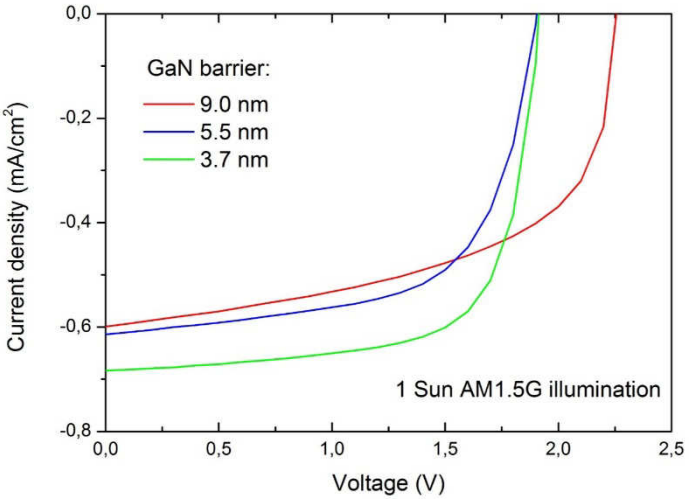

Figure 5.25. Current density-voltage dependence for 15×$In_{0.17}Ga_{0.83}N$(2nm)/GaN with different barrier thickness under 1 Sun AM1.5G equivalent illumination.

Main electrical parameters extracted from Figure 5.25 are listed in Table 5.8. The best value of conversion efficiency is obtained for sample with thinnest barriers. This is mostly related to the increase of J_{sc} and fill factor. Fill factor increases with decreasing of the barrier thickness. The same effect was also observed by Wierer *et al* [Wierer, 2012].

Table 5.8. Summary of the electrical characteristics: external quantum efficiency EQE, open-circuit voltage V_{oc}, short-circuit current J_{sc}, fill factor FF, conversion efficiency η for 15×$In_{0.17}Ga_{0.83}N$(2nm)/GaN-based devices with different barrier thicknesses under 1 Sun AM1.5G equivalent illumination.

Sample	EQE at 380 nm, %	V_{oc}, V	FF, %	J_{sc}, mA/cm^2	η, %
D1	27	2.2	57	0.60	0.78
D2	30	1.9	63	0.61	0.73
D3	35	1.9	70	0.69	0.92

A possible explanation could be the following. As shown by the band diagrams, the barriers have a triangular shape because of the piezoelectric field. This shape reduces an "effective" height of the barrier inducing the enhancement of the tunneling probability

through the barriers. The increase of the forward voltage partly compensates the piezoelectric fields and decreases the probability of tunneling. For thin barriers, the tunneling current does not depend on the barrier shape and therefore, on bias. For structures with thick barriers, the impact from tunneling component decreases with bias, leading to the current reduction. This effect appears as an increase of the *J(V)* curve slope at voltages higher *0*, leading to the decrease of *FF*.

The value of open-circuit voltage, in opposite to *FF*, diminishes with the barrier thickness decrease. Using Eq. (2.8) and plotting the dependence of $ln(J_{sc})$ as a function of bias *V*, we can extract the values of ideality factor *n* (from the slope of the curve) and saturation current J_0 (from the straight line intercept of $ln(J_{sc})$-*V* plot at a zero voltage).

The values of J_0 extracted from $ln(J_{sc})$-*V* curves measured in the dark are about 4×10^{-19}, 3×10^{-7} and 6×10^{-7} mA/cm^2 for samples with 9.0, 5.5 and 3.7 nm barrier thicknesses. The increase of J_0 with a decrease of the barrier thickness denotes the increase of carrier recombination in QW region. As shown from XRD data, the samples with thin barriers show an appearance of relaxation. As a rule, the strain relaxation induces the defect formation that can be responsible for the increase of recombination in the active region. The ideality factor *n* also increases from 2.1 to 5.2 with a decrease of the barrier thickness for voltage range 2 - 2.5 V. The values of *n* more than 2 for GaN-based materials were also reported by other groups [Casey, 1996; Perlin, 1996]. Such high ideality factor is normally attributed to the presence of tunneling as a main transport mechanism [Chitnis, 2000].

5.3.3 Summary of the role of barrier thickness

We investigated $15\times In_{0.17}Ga_{0.83}N$ (2 nm)/GaN QW-based solar cells with barrier thickness of 3.7, 5.5 and 9.0 nm. As it was predicted by band-to-band Nextnano^3 calculations, we observed the PL emission red-shift (from 435 to 447 nm) induced by the increased polarization fields with barrier thickness. The polarization fields deform the QW band profile and lead to the change of the energetic difference between electron and hole levels (i.e. standard QCSE). From the fit of transmittance spectra, a value of average band gap $E_g \approx 2.9$ eV is estimated.

From device point of view, the decrease of the barrier thickness enhances the carrier tunneling. This creates an additional way for carriers to escape from QW improving the values of external quantum efficiency, short-circuit current and fill factor. But on the other

hand, a thinning of the barriers causes the appearance of strain relaxation (in agreement with XRD rsm data) accompanied by defect formation. This increases the leakage current through the active region of the device and reduces the value of open-circuit voltage (which falls down from 2.2 V to 1.9 V for samples under study).

Finally, the best solar cell is obtained for 15×$In_{0.17}Ga_{0.83}N$ (2 nm)/GaN (3.7 nm) sample with thinnest barriers showing the electrical parameters: J_{sc} = 0.69 mA/cm^2; V_{oc} = 1.9 V; FF = 70% leading to an overall conversion efficiency of 0.92%. This result is lower than obtained for previous series of samples (2%). But it is worth to notice that homogeneity of the samples was significantly improved in spite of high In-content.

5.4 Conclusion

In this chapter, we investigated the influence of the active region design on the structural, optical and photovoltaic characteristics of InGaN/GaN-based solar cells.

The most important limitation for InGaN-based photovoltaics is a small value of short-circuit current. The J_{sc} strongly depends on absorption of the light. One of the way to increase absorption is to increase the thickness of InGaN layers, in our case the thickness of QWs. Samples with QW thicknesses of 1.3, 3.1 and 5.4 nm and 10% of In composition have been studied. The increase of QW thickness red-shifts the emission and absorption wavelength of about 70 nm increasing the absorption. But this effect can not be completely explored in solar cells because of losses in collection efficiency induced by the deepening of the electron and hole energy levels and defect formation due to strain relaxation enhancement with QW thickness. The best value of conversion efficiency of 0.49% is obtained for 30×$In_{0.12}Ga_{0.88}N$ (1.3 nm)/GaN(9.0 nm) QWs with the thinnest QWs.

The other way of absorption improvement is to increase In-content inside the active region. The samples with 18% of In have been grown by MOVPE. The increase of In composition from 10 to 18% gives a red-shift of the spectral cut-off of about 50 nm. High quality of the samples in spite of the increased In-content was confirmed with HRXRD and HRTEM measurements. From electrical point of view, high inhomogeneity of the electrical characteristics was observed. The increase of In-content causes the reduction of fill-factor, which is related to the rise of series resistance and losses in collection efficiency. On the other hand, the value of short-circuit current that usually limits conversion efficiency of the InGaN-

based devices was significantly improved leading to the maximum performance of 2.0% for $15\times In_{0.18}Ga_{0.82}N$ (2 nm)/GaN (9.0 nm).

The decrease of barrier thickness can also improve the collection efficiency and electrical performance of the InGaN QW-based solar cells with high In-content by stimulating the carrier tunneling. $15\times In_{0.17}Ga_{0.83}N$/GaN samples with barrier thicknesses of 9.0, 5.5 and 3.7 nm have been studied. To improve the homogeneity of the samples the growth temperature of the barriers was decreased by 15 ^{0}C. From the band diagram calculated with Nextnano^3 software, a lowering of the polarization field inside the QWs is expected with a decrease of the barrier thickness. The reduction of the polarization fields blue-shifts the absorption cutoff and emission wavelength in our structures. In spite of decreased absorption wavelength, the value of the short-circuit current was improved with barrier thickness decrease. This is related to enhanced carrier tunneling fraction in the total value of J_{sc} in addition to carriers that escaped QWs through thermionic emission. Thanks to carrier tunneling, the current under illumination becomes less sensitive to the change of the band diagram with applied bias and this improves the value of fill factor as well. These effects lead to conversion efficiency enhancement from 0.78 to 0.92% with a decrease of the barrier thickness from 9.0 to 3.7 nm. This efficiency is lower compared to the previous series with high In-content. Therefore, the homogeneity of the sample was significantly improved at the price of the conversion efficiency averaging.

Chapter 6

Conclusion and perspectives

This thesis has reported on the growth, characterization and optimization of the InGaN/GaN multiple quantum wells (QWs) for photovoltaic applications. All samples have been grown by metal-organic vapor phase epitaxy (MOVPE) on *c*-plane sapphire substrate.

It has been shown that InGaN/GaN QW-based solar cell can efficiently convert solar energy into electricity in blue-violet spectral range. In spite of that, quite low values of conversion efficiency for InGaN-based solar cells were published in the literature. This low value of performance is related to a poor absorption of solar spectrum by InGaN layers with low In-content and high dislocation density in In-rich InGaN layers. Therefore, the optimization of the solar cell structure design is required to improve the device efficiency.

The aim of this work was to grow and fabricate InGaN/GaN quantum well-based solar cells as well as to understand the influence of the different structural parameters on the cell performance.

In the first part of this thesis, we investigated the influence of the number of $In_{0.1}Ga_{0.90}N$/GaN QWs (from 5 to 100) on the structural, optical and photovoltaic properties of the devices. The detailed structural characterization of the samples by X-ray diffraction and transmission electron microscopy showed their good crystalline quality. Optical measurements by photoluminescence spectroscopy demonstrated an increase of In-inhomogeneities with QW number that, by the way, did not significantly damaged their electrical properties. Thanks to low In-composition (10%) and small thickness (1.3 nm) of QWs, the active region for all the samples was strained on the GaN buffer-layer. This allows us to determine the intrinsic properties of the materials because strain relaxation usually induces numerous defects inside the structure damaging the device performance. The value of J_{sc} was linearly improved with QW number from 5 to 60 reaching a maximum value of 0.68 mA/cm^2 for samples with 60×$In_{0.1}Ga_{0.9}N$/GaN QWs. The following saturation of J_{sc} is attributed to the collection losses in very thick active region. This explanation is in agreement with the measurements of external quantum efficiency (EQE) that was enhanced from 0.04 for samples with 5 QWs to 0.38 for samples with 30 QWs followed by the saturation and decrease for larger number of QWs (0.31 for samples with 60 QWs). The increase of the

carrier recombination inside the active region is also confirmed by the decrease of V_{oc} for samples having more than 40 QWs.

There are several possible ways to avoid the losses in collection efficiency because of very thick active region and keeping a good absorption. One of them is to change the ratio between barrier and well thicknesses growing thicker QWs. In the second part of the thesis, we investigated the influence of QW thickness on the properties of the samples. A deepening of the energetic levels inside thicker QWs redshifts the absorption wavelength. Strain relaxation appeared in spite of low In-composition (~12%) for samples with QW thickness more than the critical thickness (in our case, 3 nm) causing defect formation and quality degradation of the active region. Numerous defects serve as centers of recombination for the carriers reducing the value of V_{oc}. The deepening of the energetic levels hinders the carrier escape from QWs damaging the external quantum efficiency of the devices. Therefore, the increase of the QW thickness is not a very efficient way for device optimization.

We explored another solution to improve the absorption conserving moderate overall thickness of active region: the change of the In-content. By decreasing the growth temperature and increasing the TMIn flow, we were able to incorporate 18% of indium keeping a good quality of the samples. The increase of the In content induces composition fluctuations in the wells. In spite of that and thanks to better absorption, the value of J_{sc} was significantly improved reaching more than 2 mA/cm^2 for some devices. But the values of external quantum efficiency were lowered for In-rich samples compared to low In-content QWs pointing out the difficulty of the carrier escape from deeper QWs.

The problem of thermal emission of the carriers from deep QWs can be solved by stimulating carrier tunneling. To verify this assumption, a series of samples with different barrier thickness was grown. In-content was kept to be about 18% as in the previous series. As it was expected, the value of J_{sc} is improved by a decrease of the barrier thickness evidencing the enhancement of the tunneling process in short-circuit current J_{sc}. The best value of conversion efficiency of 0.92% was obtained for sample with the thinnest (3.7 nm) barriers.

To conclude, the best structure for solar cell should include quite thin QWs (2 nm) to avoid the strain relaxation that appeared in QWs thicker than 3 nm significantly damaging the value of open-circuit voltage (and also the conversion efficiency). The barriers should also be quite thin (less than 4 nm) to enable the carrier tunneling as an additional mechanism to improve the carrier collection. The increase of the In-content is, of course, the most effective

way for the improvement of the solar cell performance thanks to enhanced light absorption. Figure 6.1 presents the optimized structure of InGaN-based solar cell.

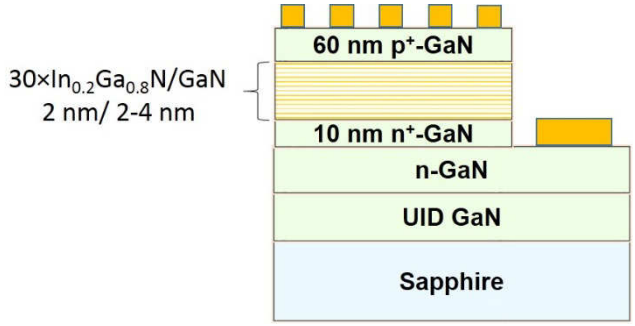

Figure 6.1. Optimized structure of the InGaN/GaN QW-based solar cell.

Finally, the best performance of 2.00% for 15×$In_{0.18}Ga_{0.82}N$/GaN QWs grown on sapphire was obtained. This value is comparable with the current state-of-the-art of the literature, where the best conversion efficiency for InGaN/GaN QW-based solar cells grown on sapphire has been reported to be 2.95% for samples with 12×$In_{0.35}Ga_{0.65}N$/GaN QWs [Dahal, 2010]. There are still some additional ways for conversion efficiency improvement that were not performed in the frame of this thesis. For example, it was shown that the device performance can be improved on more than 50% by roughening the sample surface [Farrell, 2011] or more than 35% by introducing of top-antireflection or back reflection coatings [Young, 2014]. The growth on less defective GaN substrate also ameliorates the performance of InGaN-based solar cells, but increases the price as well.

While the present work was focused on the conversion efficiency enhancement of pure InGaN QW-based solar cell, it is clear from published works, that optimized structure should include multi-junction solar cells to be able to use the absorption advantages of several materials. Therefore, future works should involve the integration of InGaN materials in the multi-junction solar cell. InGaN can be integrated in two ways: by a direct growth of InGaN-based p-n junction on the top of multi-junction solar cell or by an electrical connection of several types of solar cells with wires. The first method is very limited by the high growth temperature imposed by the MOVPE technique and by the need of lattice-matched materials. The use of MBE technique can be a good alternative to overcome this drawback. The second method is more promising because it allows connecting two semiconductors that can not be grown on the top of each other. Therefore, this technique reduces the requirements for lattice matched materials and tunnel junctions. Figure 6.2 presents the schematic of the integration of InGaN-based solar cell with non-nitride based photovoltaics.

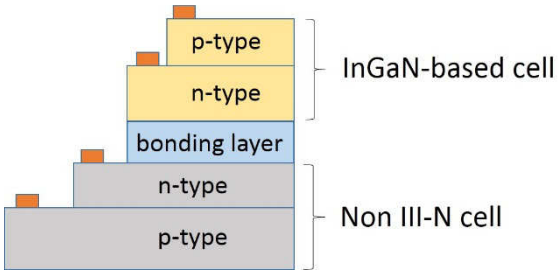

Figure 6.2. Tandem 2-junction solar cell based on InGaN.

InGaN can be a complement to either GaAs or silicon solar cell [Hsu, 2008; Toledo, 2012]. A link with optimized silicon solar cells can be a solution for high volume manufacturing. In particular, the crystalline/amorphous silicon heterojunctions (E_g (c-Si) = 1.2 eV, E_g (a-Si) = 1.7 eV) can provide a good choice in terms of band gap adjustments with the structure developed in this work.

The best result for solar cell conversion efficiency of 44.7% is obtained for 4-junction III-V material-based solar cell by Fraunhofer Institute for Solar Energy Systems ISE, Soitec, CEA-Leti and the Helmholtz Center. Next step is 5-junction solar cell and it requires a material with 2.68 eV band gap [Bhuiyan, 2012]. It means that emission wavelength should be around 460 nm. In our case, we were able to grow $In_{0.18}Ga_{0.82}N$/GaN QW-based samples with a spectral cut-off extending to 465 nm that is quite close to the calculated optimum value of the InGaN band gap for integration with GaAs-based 4 junction solar cell (about 2.65 eV that corresponds to In-content of about 20%) [Farrell, 2013]. One more perspective for this work can be an extension of the present results to nanowire-based solar cells, eventually on flexible substrates to add a new function to the devices [Messanvi, PhD thesis].

Annex 1

Transmission length method

Transmission length method (TLM) is a way used in semiconductor engineering to estimate the resistvity of the contacts. An array of the contacts with different distance between them is formed on the surface of semiconductor (Figure A1.1 (a)).

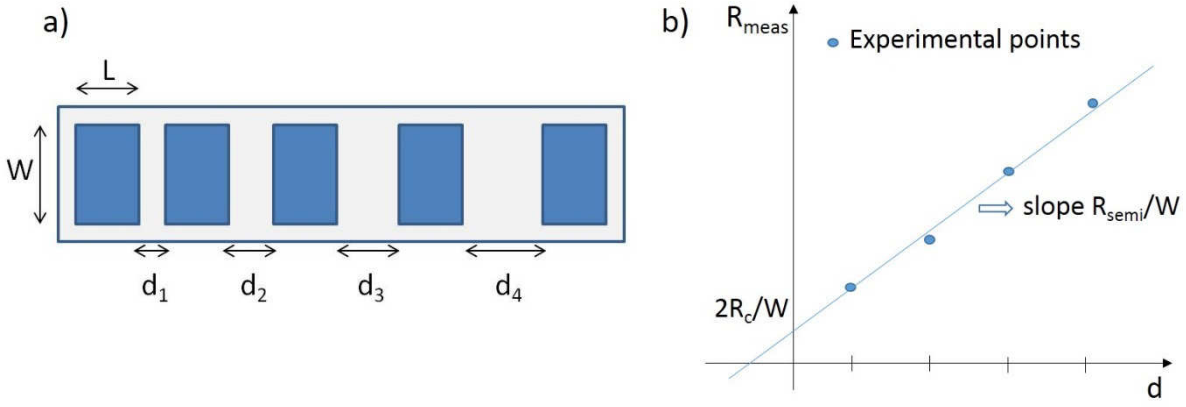

Figure A1.1. a) The array of contacts to measure the contact resistivity by TLM; b) Graphical method to determine the values of contact and sheet resistances.

The current-voltage dependence is measured between every pair of contacts. The obtained from these measurements resistance includes the resistance of the both contacts and the resistance of the semiconductor layer between two contacts:

$$R_{meas} = 2\frac{R_c}{W} + d\frac{R_{semi}}{W},$$

where R_c is the contact resistance, R_{semi} is the resistance of semiconductor layer, W is the width of the contacts, d is the distance between two contacts.

Plotting the measured value of resistance on the distance between the contacts and making a linear interpolation, the intercept of the line interpolation with x=0 gives the value of R_c and the curve slope gives the value of R_{semi} (Figure A1.1 (b)).

Annex 2

Solution of the minority carrier continuity equation

The rate of the carrier concentration change inside the *i*-region *n(x)* where $x \geq x_d$ (region without electric field inside) (Figure A2.1) can be calculated as incoming flux, outgoing flux, generation, recombination and other processes (such as light).

$$\frac{dn(x)}{dx} = \left(\frac{J_n(x)}{q} - \frac{J_n(x+dx)}{q}\right) + G_n(x,t) - R_n(x,t) + other\ processes \quad \text{(A2.1)}$$

The outcoming and incoming fluxes consist from drift and diffusion currents: $J_n = J_{diff} + J_{drift}$. We can assume zero drift current ($J_{drift} = 0$) because there is no electric field in the QW region with $x \geq x_d$.

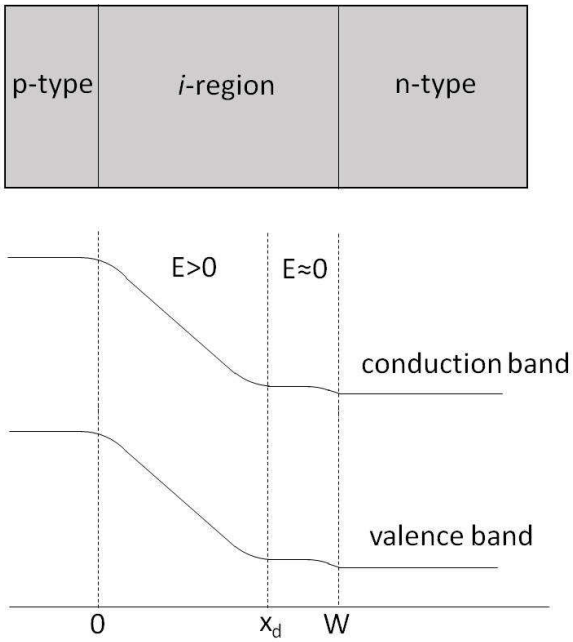

Figure A2.1. A schematic of the band diagram for p-i-n structure with thick i-region.

Diffusion current can be expressed as follows:

$$J_{diff} = -qD_n \frac{dn(x)}{dx}\Big|_{x=x_d} \quad \text{(A2.2)}$$

where q is the electron charge, D_n is the diffusion coefficient and $dn(x)/dx$ is the electron density distribution.

$$J_n(x+dx) = J_n(x) + \frac{dJ_n(x)}{dx}dx \tag{A2.3}$$

Substituting Eq. (A2.3) into Eq. (A2.1) we obtain:

$$\frac{dn(x)}{dx} = -\frac{1}{q}\frac{dJ_n(x)}{dx} + G_n(x,t) - R_n(x,t) + other\ processes \tag{A2.4}$$

The recombination rate is proportional to the excess of the carrier density:

$$R_n - G_n = \frac{n(x)-n_{p_0}}{\tau_n} \tag{A2.5}$$

where n_{p0} is the electron density in the equilibrium, τ_n is the electron lifetime. Therefore, the minority carrier continuity equation can be written as follows:

$$\frac{dn(x)}{dt} = D_n\frac{d^2n(x)}{dx^2} + G_{opt}(x) - \frac{n(x)-n_{p_0}}{\tau_n} = 0 \tag{A2.6}$$

The equation (A2.6) is the second order differential nonhomogeneous equation and the solution can be found as a sum of the solution of homogeneous differential equation and particular solution. The general solution of Eq. (A2.6) is:

$$n(x) = C_0e^{-\alpha(x-x_d)} + C_1e^{-(x-x_d)/L_n} + C_2e^{(x-x_d)/L_n} + n_{p_0} \tag{A2.7}$$

Constants C_0, C_1 and C_2 can be found applying boundary conditions: one at the depletion edge $x = x_d$ and one at the boarder of the *i*-region and *n*-doped region. We consider that $n(x = x_d) = n_{p0}$ and $n(x=W) = n_{p0}$. It means that electrons arriving at the edge of the depletion region are swept away by the electric field and there is no excess of the electron concentration at $x = x_d$. The second condition implys the electrons arriving to the *n*-doped region do not significantly change the equilibrium concentration because of high initial doping of the *n*-region. Applying these conditions we obtain the following values for constants of Eq. (A2.7):

$$C_0 = \frac{T_\lambda \Phi_0 e^{-\alpha x_d} \alpha L_n}{D_n(1-\alpha^2 L_n^2)} \quad \text{(A2.8)}$$

$$C_1 = -C_0 \left(\frac{e^{(W-x_d)/L_n} - e^{-\alpha(W-x_d)/L_n}}{e^{(W-x_d)/L_n} - e^{-(W-x_d)/L_n}} \right) \quad \text{(A2.9)}$$

$$C_2 = C_0 \left(\frac{e^{-(W-x_d)/L_n} - e^{-\alpha(W-x_d)/L_n}}{e^{(W-x_d)/L_n} - e^{-(W-x_d)/L_n}} \right) \quad \text{(A2.10)}$$

However, if the active region is thick enough, that $W - x_d >> L_n$ and $W - x_d >> \alpha^{-1}$, then $C_2 \approx 0$ and $C_1 = -C_0$.

Therefore, the solution of the minority carrier continuity equation for distribution of the electron density can be re-written as follows:

$$n(x) = C_0 e^{-\alpha(x-x_d)} - C_0 e^{-(x-x_d)/L_n} + n_{p_0} \quad \text{(A2.11)}$$

Bibliography

[Aleksiejunas, 2003] R. Aleksiejūnas, M. Sūdžius, V. Gudelis, T. Malinauskas, K. Jarašiūnas, Q. Fareed, R. Gaska, M. S. Shur, J. Zhang, J. Yang, E. Kuokštis, and M. a. Khan, "Carrier transport and recombination in InGaN/GaN heterostructures, studied by optical four-wave mixing technique," *Phys. Status Solidi*, vol. 2690, no. 7, pp. 2686–2690, Dec. 2003.

[Amano, 1986] H. Amano, N. Sawaki, I. Akasaki, and Y. Toyoda, "Metalorganic vapor phase epitaxial growth of a high quality GaN film using an AlN buffer layer," vol. 48, no. 5, p. 353, 1986.

[Amano, 1989] H. Amano, M. Kito, K. Hiramatsu, and I. Akasaki, "P-Type Conduction in Mg-Doped GaN Treated with Low-Energy Electron Beam Irradiation (LEEBI)," *Jpn. J. Appl. Phys.*, vol. 28, no. 12, p. L2112, 1989.

[Ambacher, 1998] O. Ambacher, "Growth and applications of group III-nitrides," *J. Phys. D: Appl. Phys.*,vol. 31, p. 2653, 1998.

[Ambacher, 2002] O. Ambacher, J. Majewski, C. Miskys, A. Link, M. Hermann, M. Eickhoff, M. Stutzmann, F. Bernardini, V. Fiorentini, and V. Tilak, "Pyroelectric properties of Al (In) GaN / GaN hetero- and quantum well structures," *J. Phys.: Condens. Matter.*, vol. 14, pp. 3399–3434, 2002.

[Andre, 2007] Y. Andre, A. Trassoudaine, J. Tourret, R. Cadoret, E. Gil, D. Castelluci, O. Aoude, and P. Disseix, "Low dislocation density high-quality thick hydride vapour phase epitaxy (HVPE) GaN layers," *J. Cryst. Growth*, vol. 306, no. 1, pp. 86–93, Aug. 2007.

[Angerer, 1997] H. Angerer, D. Brunner, F. Freudenberg, O. Ambacher, M. Stutzmann, R. Höpler, T. Metzger, E. Born, G. Dollinger, a. Bergmaier, S. Karsch, and H.-J. Körner, "Determination of the Al mole fraction and the band gap bowing of epitaxial $Al_xGa_{1-x}N$ films," *Appl. Phys. Lett.*, vol. 71, no. 11, p. 1504, 1997.

[Ayers, 2007] J. E. Ayers, "Heteroepitaxy of semiconductors: theory, growth, and characterization," 2007.

[Bae, 2011] S.-Y. Bae, J.-P. Shim, D.-S. Lee, S.-R. Jeon, and G. Namkoong, "Improved photovoltaic effects of a vertical-type InGaN/GaN multiple quantum well solar cell," *Jpn. J. Appl. Phys.*, vol. 50, p. 092301, 2011.

[Bandic, 1998] Z. Z. Bandić, P. M. Bridger, E. C. Piquette, and T. C. McGill, "Minority carrier diffusion length and lifetime in GaN," *Appl. Phys. Lett.*, vol. 72, no. 24, p. 3166, 1998.

[Barnham, 1990] K. W. J. Barnham, G. Duggan, "A new approach to high-efficiency multi-band-gap solar cells," *J. Appl. Phys.*, 67, p. 3490, 1990.

[Beach, 1999] R. A. Beach, T. C. Mcgill, and G. A. Gan, "Piezoelectric fields in nitride devices," *J. Vac. Sci. Technol. B*, vol. 17 no. 4, pp. 1753–1756, 1999.

[Bercowicz, 2000] F. Bercowicz, D. Gershoni, G. Bahir, F. Lakin, D. Shilo, F. Zolotoyabko, A. C. Abare, S. P. Denbaars, and L. A. Coldren "Measured and calculated optical absorption of $In_xGa_{1-x}N$/GaN

quantum structures," *Phys. Rev. B.*, vol. 61, no. 16, p. 10994 – 11008, 2000.

[Bernardini, 1997] F. Bernardini, V. Fiorentini, D. Vanderbilt, "Spontaneous polarization and piezoelectric constants of III-V nitrides," *Phys. Review B*, vol. 56, p. 10024, 1997.

[Bernardini, 1999] F. Bernardini and V. Fiorentini, "Spontaneous versus Piezoelectric Polarization in III-V Nitrides: Conceptual Aspects and Practical Consequences," *Phys. Status Solidi*, vol. 216, no. 1, pp. 391–398, Nov. 1999.

[Bernardini, 2001] F. Bernardini, V. Fiorentini, D. Vanderbilt, "Nonlinear macroscopic polarization in III-V nitride alloys," *Phys. Review B*, vol. 64, p. 085207, 2001.

[Bhuiyan, 2012] A. G. Bhuiyan, K. Sugita, A. Hashimoto, and A. Yamamoto, "InGaN Solar Cells : Present State of the Art and Important Challenges," *IEEE Journal of photovoltaics*, vol. 2, no. 3, pp. 276–293, 2012.

[Birner, 2006] S. Birner, S. Hackenbuchner, and M. Sabathil, "Modeling of Semiconductor Nanostructures with nextnano 3," *Acta Physica Polonica A*, vol. 110, no. 2, pp. 111–124, 2006.

[Boney, 2011] C. Boney, I. Hernandez, R. Pillai, D. Starikov, A. Bensaoula, M. Henini, M. Syperek, and J. Misiewicz, "Growth and characterization of InGaN photovoltaic devices," *Phys. Stat. Sol. C*, vol. 8, no. 7-8, pp. 2466–2668, 2011.

[Boudart, 2000] B. Boudart, S. Trassaert, X. Wallart, J. C. Pesant, O. Yaradou, D. Théron, Y. Crosnier, H. Lahreche, and F. Omnes, "Comparison between TiAl and TiAlNiAu ohmic contacts to n-type GaN," *J. Electron. Mater.*, vol. 29, no. 5, pp. 603–606, May 2000.

[Cai, 2009] X.-M. Cai, S.-W. Zeng, and B.-P. Zhang, "Favourable photovoltaic effects in InGaN pin homojunction solar cell," *Electron. Lett.*, vol. 45, no. 24, p. 1266, 2009.

[Cai, 2013] X. Cai, Y. Wang, B. Chen, M. Liang, W. Liu, J. Zhang, X. Lv, L. Ying, and B. Zhang, "Investigation of InGaN p-i-n Homojunction and Heterojunction Solar Cells," *IEEE Photonics technology letters*, vol. 25, no. 1, pp. 59–62, 2013.

[Cakmak, 2012] H. Cakmak, PhD Thesis "Growth and characterization of In rich Indium-Gallium-Nitride solar cell epitaxial structures by Metal Organic Chemical Vapor Deposition," 2012.

[Cakmak, 2014] H. Çakmak, E. Arslan, M. Rudziński, P. Demirel, H. E. Unalan, W. Strupiński, R. Turan, M. Öztürk, and E. Özbay, "Indium rich InGaN solar cells grown by MOCVD," *J. Mater. Sci. Mater. Electron.*, vol. 25, no. 8, pp. 3652–3658, Jun. 2014.

[Casey, 1996] H. C. Casey, J. Muth, S. Krishnankutty, and J. M. Zavada, "Dominance of tunneling current and band filling in InGaN/AlGaN double heterostructure blue light-emitting diodes," *Appl. Phys. Lett.*, vol. 68, no. 20, p. 2867, 1996.

[Cavassilas, 2014] N. Cavassilas, F. Michelini, and M. Bescond, "Theoretical comparison of multiple quantum wells and thick-layer designs in InGaN/GaN solar cells," *Appl. Phys. Lett.*, vol. 105, no. 6, p. 063903, Aug. 2014.

[Chen, 1993] Y. C. Chen, J. Singh, and P. K. Bhattacharya, "Suppression of defect propagation by pseudomorphic layers," *J. Appl. Phys.*, vol. 74, no. 6, pp. 3800–3804, 1993.

[Chen, 2008] X. Chen, K. D. Matthews, D. Hao, W. J. Schaff, and L. F. Eastman, "Growth, fabrication, and characterization of InGaN solar cells," *Phys. Status Solidi*, vol. 205, no. 5, pp. 1103–1105, May 2008.

[Chichibu, 1997] S. Chichibu, K. Wada, and S. Nakamura, "Spatially resolved cathodoluminescence spectra of InGaN quantum wells," *Appl. Phys. Lett.*, vol. 71, no. 16, p. 2346, 1997.

[Chichibu, 1998] S. F. Chichibu, a. C. Abare, M. S. Minsky, S. Keller, S. B. Fleischer, J. E. Bowers, E. Hu, U. K. Mishra, L. a. Coldren, S. P. DenBaars, and T. Sota, "Effective band gap inhomogeneity and piezoelectric field in InGaN/GaN multiquantum well structures," *Appl. Phys. Lett.*, vol. 73, no. 14, p. 2006, 1998.

[Chitnis, 2000] A. Chitnis, A. Kumar, M. Shatalov, V. Adivarahan, A. Lunev, J. W. Yang, G. Simin, M. A. Khan, R. Gaska, and M. Shur, "High-quality p–n junctions with quaternary AlInGaN/InGaN quantum wells," *Appl. Phys. Lett.*, vol. 77, no. 23, p. 3800, 2000.

[Cho, 1998] Y.-H. Cho, G. H. Gainer, A. J. Fischer, J. J. Song, S. Keller, U. K. Mishra, and S. P. DenBaars, "'S-shaped' temperature-dependent emission shift and carrier dynamics in InGaN/GaN multiple quantum wells," *Appl. Phys. Lett.*, vol. 73, no. 10, p. 1370, 1998.

[Christmas, 2005] U. M. E. Christmas, a. D. Andreev, and D. a. Faux, "Calculation of electric field and optical transitions in InGaN/GaN quantum wells," *J. Appl. Phys.*, vol. 98, no. 7, p. 073522, 2005.

[Chung, 2002] S. J. Chung, E.-K. Suh, H. J. Lee, H. B. Mao, and S. J. Park, "Photoluminescence and photocurrent studies of p-type GaN with various thermal treatments," *J. Cryst. Growth*, vol. 235, no. 1–4, pp. 49–54, Feb. 2002.

[Dadgar, 2011] A. Dadgar, J. Blasing, A. Diez, and A. Krost, "Crack-free, highly conducting GaN layers on Silicon substrates by Ge doping," *Appl. Phys. Exp.*, vol. 4, p. 011001, 2011.

[Dahal, 2009] R. Dahal, B. Pantha, J. Li, J. Y. Lin, and H. X. Jiang, "InGaN/GaN multiple quantum well solar cells with long operating wavelengths," *Appl. Phys. Lett.*, vol. 94, no. 6, p. 063505, 2009.

[Dahal, 2010] R. Dahal, J. Li, K. Aryal, J. Y. Lin, and H. X. Jiang, "InGaN/GaN multiple quantum well concentrator solar cells," *Appl. Phys. Lett.*, vol. 97, no. 7, p. 073115, 2010.

[Das, 2012] A. Das, PhD thesis "Boite quantiques des semi-conducteurs nitrures pour des applications aux capteurs opto-chimiques," 2012.

[Davydov, 2002] V. Y. Davydov, A. A. Klochikhin, R. P. Seisyan, and V. V Emtsev, "Rapid Research Note Absorption and Emission of Hexagonal InN. Evidence of Narrow Fundamental Band Gap," *Phys. Stat. Solidi (b)*, vol. 229, no. 3, pp. R1–R3, 2002.

[Della-Sala, 1999] F. Della Sala, A. Di Carlo, P. Lugli, F. Bernardini, V. Fiorentini, R. Scholz, and J.-M. Jancu, "Free-carrier screening of polarization fields in wurtzite GaN/InGaN laser structures," *Appl. Phys. Lett.*, vol. 74, no. 14, p. 2002, 1999.

[Deng, 2011] Q. Deng, X. Wang, H. Xiao, C. Wang, H. Yin, H. Chen, Q. Hou, D. Lin, J. Li, Z. Wang, and X. Hou, "An investigation on In x Ga 1− x N/GaN multiple quantum well solar cells," *J. Phys. D. Appl. Phys.*, vol. 44, no. 26, p. 265103, 2011.

[Dobos, 2006] L. Dobos, B. Pécz, L. Tóth, Z. J. Horváth, Z. E. Horváth, a. Tóth, E. Horváth, B. Beaumont, and Z. Bougrioua, "Metal contacts to n-GaN," *Appl. Surf. Sci.*, vol. 253, no. 2, pp. 655–661, Nov. 2006.

[Donnell, 1999] K. O'Donnell, R. Martin, and P. Middleton, "Origin of Luminescence from InGaN Diodes," *Phys. Rev. Lett.*, vol. 82, no. 1, pp. 237–240, Jan. 1999.

[Eiting, 1998] C. J. Eiting, P. A. Grudowski, and R. D. Dupuis, "P- and N-Type Doping of GaN and AlGaN Epitaxial Layers Grown by Metalorganic Chemical Vapor Deposition," *Journal of Electronic Materials*, vol. 27, no. 4, pp. 206–209, 1998.

[El Gmili, 2013] Y. El Gmili, PhD thesis "Etude et caractérisations par cathodoluminescence de couches minces d'InGaN pour le photovoltaïque," 2013.

[Eliseev, 1997] P. G. Eliseev, P. Perlin, J. Lee, and M. Osiński, "Blue' temperature-induced shift and band-tail emission in InGaN-based light sources," *Appl. Phys. Lett.*, vol. 71, no. 5, p. 569, 1997.

[Eymery, 2000] J. Eymery, J. M. Hartmann, and G. T. Baumbach, "Interface dilution and morphology of CdTe/MnTe superlattices studied by small- and large-angle x-ray scattering," *J. Appl. Phys.*, vol. 87, no. 10, p. 7266, 2000.

[Farrell, 2011] R. M. Farrell, C. J. Neufeld, S. C. Cruz, J. R. Lang, M. Iza, S. Keller, S. Nakamura, S. P. DenBaars, U. K. Mishra, and J. S. Speck, "High quantum efficiency InGaN/GaN multiple quantum well solar cells with spectral response extending out to 520 nm," *Appl. Phys. Lett.*, vol. 98, no. 20, p. 201107, 2011.

[Farrell, 2013] R. M. Farrell, D. J. Friedman, N. Young, E. Perl, N. Singh, J. Lang, C. Neufeld, M. Iza, S. Cruz, S. Keller, W. E. McMahon, S. Nakamura, S. P. DenBaars, U. K. Mishra, J. E. Bowers, and J. S. Speck, "InGaN-Based Solar Cells and High-Performance Broadband Optical Coatings for Ultrahigh Efficiency Hybrid Multijunction Device Designs," *Conference on Laser and electro-optics*, vol. 1, p. ATh4N.4, 2013.

[Fedison, 1998] J. B. Fedison, T. P. Chow, H. Lu, and I. B. Bhat, "Electrical characteristics of magnesium-doped gallium nitride junction diodes," *Appl. Phys. Lett.*, vol. 72, no. 22, p. 2841, 1998.

[Feng, 2010] S.-W. Feng, C.-M. Lai, C.-H. Chen, W.-C. Sun, and L.-W. Tu, "Theoretical simulations of the effects of the indium content, thickness, and defect density of the i-layer on the performance of p-i-n InGaN single homojunction solar cells," *J. Appl. Phys.*, vol. 108, no. 9, p. 093118, 2010.

[Fewster, 1988] P. F. Fewster, "Interface roughness and period variations in MQW structures determined by X-ray diffraction," *J. Appl. Crystallogr.*, vol. 21, no. 5, pp. 524–529, Oct. 1988.

[Gacevic, 2011] Z. Gačević, A. Das, J. Teubert, Y. Kotsar, P. K. Kandaswamy, T. Kehagias, T. Koukoula, P. Komninou, and E. Monroy, "Internal quantum efficiency of III-nitride quantum dot superlattices grown by plasma-assisted molecular-beam epitaxy," *J. Appl. Phys.*, vol. 109, no. 10, p. 103501, 2011.

[Gmili, 2013] Y. El Gmili, G. Orsal, K. Pantzas, T. Moudakir, S. Sundaram, G. Patriarche, J. Hester, A. Ahaitouf, J.P. Salvestrini, and A. Ougazzaden, "Multilayered InGaN/GaN structure vs. single InGaN layer for solar

cell applications: A comparative study," *Acta Materialia*, vol. 61, p. 6587, 2013.

[Goano(1), 2000] M. Goano, E. Bellotti, E. Ghillino, G. Ghione, and K. F. Brennan, "Band structure nonlocal pseudopotential calculation of the III-nitride wurtzite phase materials system. Part I. Binary compounds GaN, AlN, and InN," *J. Appl. Phys.*, vol. 88, no. 11, p. 6467, 2000.

[Goano(2), 2000] M. Goano, E. Bellotti, E. Ghillino, C. Garetto, G. Ghione, and K. F. Brennan, "Band structure nonlocal pseudopotential calculation of the III-nitride wurtzite phase materials system. Part II. Ternary alloys $Al_xGa_{1-x}N$, $In_xGa_{1-x}N$, and $In_xAl_{1-x}N$," *J. Appl. Phys.*, vol. 88, no. 11, p. 6476, 2000.

[Gotz, 1996] W. Goetz, N.M. Johnson, J. Walker, and D.P. Bour, "Activation of acceptors in Mg-doped, p-type GaN," Proceedings of the MRS Spring Symposium, San Francisco, April 8-12, 1996.

[Gou, 2010] Y. Guo, X. L. Liu, H. P. Song, a. L. Yang, X. Q. Xu, G. L. Zheng, H. Y. Wei, S. Y. Yang, Q. S. Zhu, and Z. G. Wang, "A study of indium incorporation in In-rich InGaN grown by MOVPE," *Appl. Surf. Sci.*, vol. 256, no. 10, pp. 3352–3356, Mar. 2010.

[Grandjean, 1999] N. Grandjean, B. Damilano, S. Dalmasso, M. Leroux, M. Laügt, and J. Massies, "Built-in electric-field effects in wurtzite AlGaN/GaN quantum wells," *J. Appl. Phys.*, vol. 86, no. 7, p. 3714, 1999.

[Green, 1982] M. Green, "Solar cells: Opertaing principles, Technology, and System Applications," Englewood Cliffs: Prentice-Hall, Inc., 1982.

[Hammersley, 2012] S. Hammersley, D. Watson-Parris, P. Dawson, M. J. Godfrey, T. J. Badcock, M. J. Kappers, C. McAleese, R. a. Oliver, and C. J. Humphreys, "The consequences of high injected carrier densities on carrier localization and efficiency droop in InGaN/GaN quantum well structures," *J. Appl. Phys.*, vol. 111, no. 8, p. 083512, 2012.

[Hangleiter, 2003] A. Hangleiter, F. Hitzel, S. Lahmann, and U. Rossow, "Composition dependence of polarization fields in GaInN/GaN quantum wells," *Appl. Phys. Lett.*, vol. 83, no. 6, p. 1169, 2003.

[Ho, 1996] I. Ho, and G. B. Stringfellow, "Solid phase immiscibility in GaInN," *Appl. Phys. Lett.*, vol. 69, p. 2701, 1996.

[Holec, 2008] D. Holec, Y. Zhang, D. V. Sridhara Rao, M. J. Kappers, C. McAleese, and C. J. Humphreys, "Equilibrium critical thickness for misfit dislocations in III-nitirdes," *J. Appl. Phys.*, vol. 104, no. 12, p. 123514-1, 2008.

[Holy, 1999] V. Holy, U. Pietsch, T. Baumbach, "High-resolution X-ray scattering from thin films and multilayers," Springer, vol. 149, 256, 1999.

[Horng, 2009] R. Horng, S. Lin, Y. Tsai, M. Chu, W. Liao, M. Wu, R. Lin, and Y. Lu, "Improved Conversion Efficiency of GaN/InGaN Thin-Film Solar Cells," *IEEE Electron Device Letters*, vol. 30, no. 7, pp. 724–726, 2009.

[Hsu, 2008] L. Hsu and W. Walukiewicz, "Modeling of InGaN/Si tandem solar cells," *J. Appl. Phys.*, vol. 104, no. 2, p. 024507, 2008.

[Iliopuolos, 2006] E. Iliopoulos, M. Zervos, A. Adikimenakis, T. Tsagaraki, A. Georgakilas, "Properties of Si-doped GaN and AlGaN/GaN heterostructures grown by RF-MBE on high resistivity Fe-doped GaN," *Superlat. and Microstruct.*, vol. 40, p. 313, 2006.

[Islam, 2013] Md. R. Islam, Md. R. Kaysir, Md. J. Islam, A. Hashimoto, and A. Yamamoto,"MOVPE Growth of $In_xGa_{1-x}N$ (x ~ 0.4) and Fabrication of Homo-junction Solar Cells," *J. Mater. Sci. Technol.*, vol. 29, no. 2, p. 128, 2013.

[Jampana(1), 2010] B. R. Jampana, A. G. Melton, M. Jamil, N. N. Faleev, R. L. Opila, I. T. Ferguson, and C. B. Honsberg, "Design and Realization of Wide-Band-Gap (~ 2.67 eV) InGaN p-n junction solar cells," *IEEE Electron Device Lett.*, vol. 31, no. 1, pp. 32–34, 2010.

[Jampana(2), 2010] B. Jampana, T. Xu, A. Melton, M. Jamil, R. Opila, C. Honsberg, and I. Ferguson, "Relaization of InGaN solar cells on (111) silicon substrate," *35th IEEE Photovoltaic Specialists Conf (PVTC)*, p. 457, 2010.

[Jani, 2005] O. Jani, C. Honsberg, A. Asghar, D. Nicol, I. Ferguson, A. Doolittle, and S. Kurtz, *31st IEEE Photovoltaic Specialists Conf.*, pp 37–42, 2005.

[Jani, 2006] O. Jani, C. Honsberg, Y. Huang, J. Song, I. Ferguson, G. Namkoong, E. Trybus, A. Doolittle, and S. Kurtz, "Design, Growth, Fabrication and Characterization of High-Band Gap InGaN/GaN Solar Cells," *2006 IEEE 4th World Conf. Photovolt. Energy Conf.*, pp. 20–25, 2006.

[Jani(1), 2007] O. Jani, H. Yu, E. Trybus, B. Jampana, I. Ferguson, A. Doolittle, and C. Honsberg, "Effect of phase separation on performance of III-V nitride solar cells," *22nd European Photovoltaic Solar Energy Conference* , 3-7 September 2007 , Milan , Italy, pp. 64–67, 2007.

[Jani(2), 2007] O. Jani, I. Ferguson, C. Honsberg, and S. Kurtz, "Design and characterization of GaN/InGaN solar cells," *Appl. Phys. Lett.*, vol. 91, no. 13, p. 132117, 2007.

[Jani, 2008] O. Jani, M. Mehta, H. Yu, I. Ferguson, R. Opila, and C. Honsberg, "Optimization of GaN window layer for InGaN solar cells using polarization effect," *33rd IEEE Photovoltaic Specialists Conf.*, San-Diego, May, 12-16, 2008.

[Jeng, 2009] M.-J. Jeng, Y.-L. Lee, and L.-B. Chang, "Temperature dependences of In x Ga 1− x N multiple quantum well solar cells," *J. Phys. D. Appl. Phys.*, vol. 42, no. 10, p. 105101, May 2009.

[Ju, 2007] J.-W. Ju, J. Zhu, H.-S. Kim, C.-R. Lee, and I.-H. Lee, "Effects of p-GaN Growth Temperature on a Green InGaN/GaN Multiple Quantum Well," *J. Korean Phys. Soc.*, vol. 50, no. 3, p. 810, Mar. 2007.

[Kaneta, 2003] A. Kaneta, T. Mutoh, Y. Kawakami, S. Fujita, G. Marutsuki, Y. Narukawa, and T. Mukai, "Discrimination of local radiative and nonradiative recombination processes in an InGaN/GaN single-quantum-well structure by a time-resolved multimode scanning near-field optical microscopy," *Appl. Phys. Lett.*, vol. 83, no. 17, p. 3462, 2003.

[Kaufmann, 2000] U. Kaufmann, P. Schlotter, H. Obloh, K. Kohler, and M. Maier, "Hole conductivity and compensation in epitaxial GaN:Mg layers," *Phys. Rew. B*, vol. 62, no. 16, pp. 867–872, 2000.

[Kaun, 2013] S. W. Kaun, M. H. Wong, U. K. Mishra, and J. S. Speck, "Molecular beam epitaxy for high-performance Ga-face GaN electron devices," *Semicond. Sci. Technol.*, vol. 28, no. 7, p. 074001, Jul. 2013.

[Keller, 1996] S. Keller, B. P. Keller, Y.-F. Wu, B. Heying, D. Kapolnek, J. S. Speck, U. K. Mishra, and S. P. DenBaars, "Influence of sapphire nitridation on

properties of gallium nitride grown by metalorganic chemical vapor deposition," *Appl. Phys. Lett.*, vol. 68, no. 11, p. 1525, 1996.

[Kim, 1998] I. H. Kim, H. S. Park, Y. J. Park, and T. Kim, "Formation of V-shaped pits in InGaN/GaN quantum wells and bulk InGaN films," *Appl. Phys. Lett.*, vol. 73, p. 1634, 1998.

[Kozodoy, 1998] P. Kozodoy, J.P. Ibbetson, H. Marchand, P.T. Fini, S. Keller, J.S. Speck, S.P. DenBaars, U.K. Mishra, "Electrical characterization of GaN p-n junctions with and without threading dislocations," *Appl. Phys. Lett*., vol. 73, p. 975, 1998.

[Koster, 2010] R. Koster, PhD thesis "Croissance auto-assemblée de fils de GaN sans catalyseur par epitaxie en phase vapeur d'organo-metalliques," 2010.

[Koukitu, 1999] A. Koukitu, T. Taki, N. Takahashi, and H. Seki, "Thermodynamic study on the role of hydrogen during the MOVPE growth of group III nitrides," *J. of Cryst. Growth,* vol. 197, pp. 99–105, 1999.

[Kumakura, 2005] K. Kumakura, T. Makimoto, N. Kobayashi, T. Hashizume, T. Fukui, and H. Hasegawa, "Minority carrier diffusion length in GaN: Dislocation density and doping concentration dependence," *Appl. Phys. Lett.*, vol. 86, no. 5, p. 052105, 2005.

[Kung, 2000] P; Kung, M. Razeghi, "III-nitride wide bandgap semiconductors: a survey of the current status and future trends of the material and deivce technology," *Opto-Electr.,* vol. 8, no. 3, p. 201, 2000.

[Kuwahara, 2010] Y. Kuwahara, T. Fujii, Y. Fujiyama, T. Sugiyama, M. Iwaya, T. Takeuchi, S. Kamiyama, I. Akasaki, and H. Amano, "Realization of Nitride-Based Solar Cell on Freestanding GaN Substrate," *Appl. Phys. Express*, vol. 3, no. 11, p. 111001, Oct. 2010.

[Kuwahara, 2011] Y. Kuwahara, T. Fujii, T. Sugiyama, D. Iida, Y. Isobe, Y. Fujiyama, Y. Morita, M. Iwaya, T. Takeuchi, S. Kamiyama, I. Akasaki, and H. Amano, "GaInN-Based Solar Cells Using Strained-Layer GaInN/GaInN Superlattice Active Layer on a Freestanding GaN Substrate," *Appl. Phys. Express*, vol. 4, no. 2, p. 021001, Jan. 2011.

[Lai, 2010] K. Y. Lai, G. J. Lin, Y. L. Lai, Y. F. Chen, and J. H. He, "Effect of indium fluctuation on the photovoltaic characteristics of InGaN/GaN multiple quantum well solar cells," *Appl. Phys. Lett.*, vol. 96, p. 081103, 2010.

[Lang, 2012] J. R. Lang, N. G. Young, R. M. Farrell, Y.-R. Wu, and J. S. Speck, "Carrier escape mechanism dependence on barrier thickness and temperature in InGaN quantum well solar cells," *Appl. Phys. Lett.*, vol. 101, no. 18, p. 181105, 2012.

[Lee, 1998] W. J. Lee, H. S. Kim, J. W. Lee, T. I. Kim, and G. Y. Yeom, "Etch Properties of Gallium Nitride Using Chemically Assisted Ion Beam Etching (CAIBE)," *Jpn. J. Appl. Phys.*, vol. 37, p. 7006, 1998.

[Lee, 2011] H. C. Lee, Y. K. Su, W. H. Lan, J. C. Lin, K. C. Huang, W. J. Lin, Y. C. Cheng, and Y. H. Yeh, "Study of Electrical Characteristics of GaN-Based Photovoltaics With Graded In Ga Absorption Layer," *IEEE Photonics Technology Letters,* vol. 23, no. 6, pp. 347–349, 2011.

[Leyer, 2008] M. Leyer, J. Stellmach, Ch. Meissner, M. Pristovsek, and M. Kneissl, "The critical thickness of InGaN on (0001) GaN," *J. of Cryst. Growth*., vol. 310, p. 4913, 2008.

[Li, 2012] X. Li, X. Z. A, D. Zhang, and Y. Wu, "InGaN / GaN Multiple Quantum Well Solar Cells with Good Open-Circuit Voltage and Concentrator Action InGaN / GaN Multiple Quantum Well Solar Cells with Good Open-Circuit Voltage and Concentrator Action," *Jpn. J. Appl. Phys.*, vol. 51, p. 092301, 2012.

[Lin, 1993] M. E. Lin, Z. Ma, F. Y. Huang, Z. F. Fan, L. H. Allen, and H. Morkoç, "Low resistance ohmic contacts on wide band-gap GaN," *Appl. Phys. Lett.*, vol. 64, no. 8, p. 1003, 1993.

[Lin, 1994] M. E. Lin, Z. F. Fan, Z. Ma, L. H. Allen, and H. Morkoç, "Reactive ion etching of GaN using W I3," *Appl. Phys. Lett.*, vol. 64, no. 7, p. 887, 1994.

[Lin, 2000] Y.-S. Lin, K.-J. Ma, C. Hsu, S.-W. Feng, Y.-C. Cheng, C.-C. Liao, C. C. Yang, C.-C. Chou, C.-M. Lee, and J.-I. Chyi, "Dependence of composition fluctuation on indium content in InGaN/GaN multiple quantum wells," *Appl. Phys. Lett.*, vol. 77, no. 19, p. 2988, 2000.

[Lin, 2003] Y. C. Lin, S. J. Chang, C. W. Kuo, and S. C. Chen, "InGaN / GaN light emitting diodes with Ni / Au , Ni / ITO and ITO p-type contacts," *Solid-State Electron.*, vol. 47, pp. 849–853, 2003.

[Liou, 2011] B. W. Liou, "Design and fabrication of InxGa1−xN/GaN solar cells with a multiple-quantum-well structure on SiCN/Si(111) substrates," *Thin Solid Films*, vol. 520, no. 3, pp. 1084–1090, Nov. 2011.

[Liu, 2013] C. Y. Liu, C. C. Lai, J. H. Liao, L. C. Cheng, H. H. Liu, C. C. Chang, G. Y. Lee, J.-I. Chyi, L. K. Yeh, J. H. He, T. Y. Chung, L. C. Huang, K. Y. Lai, "Nitred-based concentrator solar cells grown on Si substrates," *Solar Energy Materials and Solar Cells*, vol. 117, p.54, 2013.

[Lu, 2003] C. J. Lu, L. A. Bendersky, H. Lu, and W. J. Schaff, "Threding dislocations in epitaxial InN thin films grown on (0001) sapphire with a GaN buffer layer," *Appl. Phys. Lett.*, vol. 83, no. 14, p. 2817, 2003.

[Lu, 2013] N. Lu and I. Ferguson, "III-nitrides for energy production: photovoltaic and thermoelectric applications," *Semicond. Sci. Technol.*, vol. 28, no. 7, p. 074023, Jul. 2013.

[Luther, 1997] B. P. Luther, S. E. Mohney, T. N. Jackson, M. Asif Khan, Q. Chen, and J. W. Yang, "Investigation of the mechanism for Ohmic contact formation in Al and Ti/Al contacts to n-type GaN," *Appl. Phys. Lett.*, vol. 70, no. 1, p. 57, 1997.

[MacChesney, 1970] J. B. MacChesney, P. M. Bridenbaugh, and P. B. O'Connor, "Thermal stability of indium nitiride at elevated temepartures and nitrogen pressures," Mat. Res. Bull. Vol. 5, pp. 783-792, 1970.

[Mahmood, 2009] S. A. Mahmood and M. Z. Kabir, "Modeling of transient and steady-state dark current in amorphous silicon p–i–n photodiodes," *Curr. Appl. Phys.*, vol. 9, no. 6, pp. 1393–1396, Nov. 2009.

[Martin, 1999] R. W. Martin, P. G. Middleton, K. P. O'Donnell, and W. Van der Stricht, "Exciton localization and the Stokes' shift in InGaN epilayers," *Appl. Phys. Lett.*, vol. 74, no. 2, p. 263, 1999.

[Maruska, 1969] H. P. Maruska, "The preparation and properties of vapor-deposited single-crystal-line GaN," *Appl. Phys. Lett.*, vol. 15, no. 10, p. 327, 1969.

[Matioli, 2011] E. Matioli, C. Neufeld, M. Iza, S. C. Cruz, A. a. Al-Heji, X. Chen, R. M. Farrell, S. Keller, S. DenBaars, U. Mishra, S. Nakamura, J. Speck, and C. Weisbuch, "High internal and external quantum efficiency

InGaN/GaN solar cells," *Appl. Phys. Lett.*, vol. 98, no. 2, p. 021102, 2011.

[Meng, 2008] F. Meng, "Phase separation, atomic ordering and defects in quaternary indium aluminium gallium nitride epitaxial layers," ProQuest, 2008.

[Mesrine, 1998] M. Mesrine, N. Grandjean, J. Massies, M. Mesrine, N. Grandjean, and J. Massies, "Efficiency of NH 3 as nitrogen source for GaN molecular beam epitaxy," *Appl. Phys. Lett.*, vol. 72, p. 350, 1998.

[Messanvi, PhD] A. Messanvi, "'Composant photonique à base de nanofils uniques de nitrures".

[Misra, 2008] P. Misra, C. Boney, N. Medelci, D. Starikov, A. Freundlich, and A. Bensaoula, "Fabrication and characterization of 2.3 eV InGaN photovoltaic devices," *33rd IEEE Photovoltaic Specialists Conf.*, San Diego, CA, May, 12-16, 2008.

[Monroy, 2003] E. Monroy and F. Omnes, F. Calle, "Wide-bandgap semiconductor ultraviolet photodetectors," *Semicond. Sci. Technol.* 18, pp. R33-R51, 2003.

[Monroy, 2004] E. Monroy, E. Sarigiannidou, F. Fossard, N. Gogneau, E. Bellet-Amalric, J.-L. Rouvière, S. Monnoye, H. Mank, and B. Daudin, "Growth kinetics of N-face polarity GaN by plasma-assisted molecular-beam epitaxy," *Appl. Phys. Lett.*, vol. 84, no. 18, p. 3684, 2004.

[Moon, 2008] J. Y. Moon, J. H. Kim, and H. S. Lee, "Effect of Thermal Annealing on Ni / Au Contact to p-GaN," *Journal of the Korean Physical Society*, vol. 53, no. 6, pp. 3681–3684, 2008.

[Moscatelli, 2007] D. Moscatelli, and C. Cavallotti, "Theoretical investigation of the gas-phase kinetics active during the GaN MOVPE," *J. Phys. Chem. A*, 111 (21), p. 4620, 2007.

[Mukhtarova, 2013] A. Mukhtarova, S. Valdueza-Felip, C. Durand, Q. Pan, L. Grenet, D. Peyrade, C. Bougerol, W. Chikhaoui, E. Monroy, and J. Eymery, "InGaN/GaN multiple-quantum well heterostructures for solar cells grown by MOVPE: case studies," *Phys. Status Solidi*, vol. 10, no. 3, pp. 350–354, Mar. 2013.

[Murotani, 2013] H. Murotani, Y. Yamada, T. Tabata, Y. Honda, M. Yamaguchi, and H. Amano, "Effects of exciton localization on internal quantum efficiency of InGaN nanowires," *J. Appl. Phys.*, vol. 114, no. 15, p. 153506, 2013.

[Na, 2006] J. H. Na, R. A. Taylor, K. H. Lee, T. Wang, A. Tahraoui, P. Parbrook, A. M. Fox, S. N. Yi, Y. S. Park, J. W. Choi, and J. S. Lee, "Dependence of carrier localization in InGaN⁄GaN multiple-quantum wells on well thickness," *Appl. Phys. Lett.*, vol. 89, no. 25, p. 253120, 2006.

[Nakamura, 1991] S. Nakamura, "GaN Growth Using GaN Buffer Layer," *Jpn. J. Appl. Phys.*, vol. 30, no. 10A, p. L1705, 1991.

[Nakamura(1), 1992] S. Nakamura, T. Mukai, and M. Senoh, "In situ monitoring and Hall measurements of GaN grown with GaN buffer layers," *J. Appl. Phys.*, vol. 71, no. 11, p. 5543, 1992.

[Nakamura(2), 1992] S. Nakamura, N. Iwasa, M. Senoh, and, T. Mukai, "Hole Compensation Mechanism of P-Type GaN Films," *Jpn. J. Appl. Phys.*, vol. 31, p. 1258, 1992.

[Nakamura(3), 1992] S. Nakamura, T. Mukai, M. Senoh, and N. Iwasa, "Thermal Annealing Effects on P-Type Mg-Doped GaN Films," *Jpn. J. Appl. Phys.*, vol. 31, p. L139, 1992.

[Nakao, 2011] T. Nakao, T. Fujii, T. Sugiyama, S. Yamamoto, D. Iida, M. Iwaya, T. Takeuchi, S. Kamiyama, I. Akasaki, and H. Amano, "Fabrication of Nonpolar a-Plane Nitride-Based Solar Cell on r-Plane Sapphire Substrate," *Appl. Phys. Express*, vol. 4, no. 10, p. 101001, Oct. 2011.

[Nelson, 2003] J. Nelson, "The physics of solar cells," Imperial College Press, 2003.

[Neufeld, 2008] C. J. Neufeld, N. G. Toledo, S. C. Cruz, M. Iza, S. P. DenBaars, and U. K. Mishra, "High quantum efficiency InGaN/GaN solar cells with 2.95 eV band gap," *Appl. Phys. Lett.*, vol. 93, no. 14, p. 143502, 2008.

[Neufeld, 2011] C. J. Neufeld, S. C. Cruz, R. M. Farrell, M. Iza, J. R. Lang, S. Keller, S. Nakamura, S. P. DenBaars, J. S. Speck, and U. K. Mishra, "Effect of doping and polarization on carrier collection in InGaN quantum well solar cells," *Appl. Phys. Lett.*, vol. 98, no. 24, p. 243507, 2011.

[O'Donnell, 2004]] K. P. O'Donnell, I. Fernandez-Torrente, P. R. Edwards, and R. W. Martin, "The composition dependence of the $In_xGa_{1-x}N$ bandgap," *J. Cryst. Growth*, vol. 269, no. 1, pp. 100–105, Aug. 2004.

[Oliver, 2010] R. A. Oliver, S. E. Bennett, T. Zhu, D. J. Beesley, M. J. Kappers, D. W. Saxey, a Cerezo, and C. J. Humphreys, "Microstructural origins of localization in InGaN quantum wells," *J. Phys. D. Appl. Phys.*, vol. 43, no. 35, p. 354003, Sep. 2010.

[O'Steen, 1999] M. L. O'Steen, F. Fedler, and R. J. Hauenstein, "Effect of substrate temperature and V/III flux ratio on In incorporation for InGaN/GaN heterostructures grown by plasma-assisted molecular-beam epitaxy," *Appl. Phys. Lett.*, vol. 75, no. 15, p. 2280, 1999.

[Qiao, 2000] D. Qiao, L. S. Yu, S. S. Lau, J. Y. Lin, H. X. Jiang, and T. E. Haynes, "A study of the Au/Ni ohmic contact on p-GaN," *J. Appl. Phys.*, vol. 88, no. 7, p. 4196, 2000.

[Qin, 2004] Z. X. Qin, Z. Z. Chen, Y. Z. Tong, X. M. Ding, X. D. Hu, T. J. Yu, and G. Y. Zhang, "Study of Ti/Au, Ti/Al/Au, and Ti/Al/Ni/Au ohmic contacts to n-GaN," *Appl. Phys. A Mater. Sci. Process.*, vol. 78, no. 5, pp. 729–731, Mar. 2004.

[Pantha, 2010] B. N. Pantha, J. Li, J. Y. Lin, and H. X. Jiang, "Evolution of phase separation in In-rich InGaN alloys," *Appl. Phys. Lett.*, vol. 96, p. 232105, 2010.

[Pantzas, 2013] K. Pantzas, PhD thesis "Elaboration par MOVPE et caractérisation des matériaux InGaN pour les cellules solaires de 3ième génération," 2013.

[Parikh, 2006] R. P. Parikh, R. A. Adomaitis, "An overview of gallium nitride growth chemistry and its effect on reactor design: Application to a planetary radial-flow CVD reactor," *J. Cryst Growth*, 286, p. 259, 2006.

[Park, 2008] I.-K. Park, J.-Y. Kim, M.-K. Kwon, C.-Y. Cho, J.-H. Lim, and S.-J. Park, "Phosphor-free white light-emitting diode with laterally distributed multiple quantum wells," *Appl. Phys. Lett.*, vol. 92, no. 9, p. 091110, 2008.

[Pearton, 2000] M. O. Manasreh, "Optoelectronic properties of semiconductors and superlattices", vol. 7, Science, 2000.

[Perlin, 1996] P. Perlin, M. Osiński, P. G. Eliseev, V. a. Smagley, J. Mu, M. Banas, and P. Sartori, "Low-temperature study of current and electroluminescence in InGaN/AlGaN/GaN double-heterostructure blue light-emitting diodes," *Appl. Phys. Lett.*, vol. 69, no. 12, p. 1680, 1996.

[Raisky, 1997] O. Y. Raisky, W. B. Wang, R. R. Alfano, C. L. Reynolds, Jr., and V. Swaminathan, "Investigation of photoluminescence and photocurrent in InGaAsP/InP strained multiple quantum well heterostructures," *J. Appl. Phys.*, vol. 81, no. 1, p. 394, 1997.

[Rawal, 2012] D. S. Rawal, H. Arora, V. R. Agarwal, S. Vinayak, A. Kapoor, B. K. Sehgal, R. Muralidharan, D. Saha, and H. K. Malik, "GaN etch rate and surface roughness evolution in Cl2/Ar based inductively coupled plasma etching," *Thin Solid Films*, vol. 520, no. 24, pp. 7212–7218, Oct. 2012.

[Redaelli, 2014] L. Redaelli, A. Mukhtarova, S. Valdueza-Felip, A. Ajay, C. Bougerol, C. Himwas, J. Faure-Vincent, C. Durand, J. Eymery, and E. Monroy "Effect of the quantum well thickness on the performance of InGaN photovoltaic cells," *Appl. Phys. Lett., 105, p. 131105, 2014.*

[Rezaei, 2006] B. Rezaei, a. Asgari, and M. Kalafi, "Electronic band structure pseudopotential calculation of wurtzite III-nitride materials," *Phys. B Condens. Matter*, vol. 371, no. 1, pp. 107–111, Jan. 2006.

[Ruterana, 2006] P. Ruterana, M. Albrecht, J. Neugebauer, "Nitride Semiconductors: Handbook on Materials and Devices," Wiley-VCH, 686p., 2006.

[Schmitz, 1988] A. C. Schmitz, A. T. Ping, M. A. Khan, Q. Chen, and J. W. Yang, "Metal Contacts to n-Type GaN," *J. Electron. Mat.*, vol. 27, no. 94, pp. 255–260, 1998.

[Shah, 2003] J. M. Shah, Y.-L. Li, T. Gessmann, and E. F. Schubert, "Experimental analysis and theoretical model for anomalously high ideality factors ($n \gg 2.0$) in AlGaN/GaN p-n junction diodes," *J. Appl. Phys.*, vol. 94, no. 4, p. 2627, 2003.

[Shen, 2000] X. Q. Shen, T. Ide, S. H. Cho, M. Shimizu, S. Hara, and H. Okumura, "Stability of N- and Ga-polarity GaN surfaces during the growth interruption studied by reflection high-energy electron diffraction," *Appl. Phys. Lett.*, vol. 77, no. 24, p. 4013, 2000

[Shen, 2012] K.-C. Shen, T.-Y. Wang, D.-S. Wuu, and R.-H. Horng, "High thermal stability of high indium content InGaN films grown by pulsed laser deposition.," *Opt. Express*, vol. 20, no. 19, pp. 21173–80, Sep. 2012.

[Sheu, 1999] J. K. Sheu, Y. K. Su, G. C. Chi, P. L. Koh, M. J. Jou, C. M. Chang, C. C. Liu, and W. C. Hung, "High-transparency Ni/Au ohmic contact to p-type GaN," *Appl. Phys. Lett.*, vol. 74, no. 16, p. 2340, 1999.

[Sheu, 2002] J. K. Sheu, G.C. Chi, "The doping process and dopant characteristics of GaN," *J. Phys.: Condens. Matter.*, vol. 14, p. R657, 2002.

[Sheu, 2009] J. Sheu, C. Yang, S. Tu, K. Chang, M. Lee, W. Lai, and L. Peng, "Demonstration of GaN-Based Solar Cells With," *IEEE Electron Dvice Letters*, vol. 30, no. 3, p. 225, 2009.

[Shim, 2011] J.-P. Shim, M. Choe, S.-R. Jeon, D. Seo, T. Lee, and D.-S. Lee, "InGaN-Based p–i–n Solar Cells with Graphene Electrodes," *Appl. Phys. Express*, vol. 4, no. 5, p. 052302, May 2011.

[Shul, 1998] R. J. Shul, C. G. Willison, M. M. Bridges, J. Han, J. W. Lee, S. J. Pearton, C. R. Abernathy, J. D. Mackenzie, and S. M. Donovan, "High-density plasma etch selectivity for the III-V nitrides," *Solid-State Electron.*, vol. 42, no. 12, pp. 2269–2276, 1998.

[Sugahara, 1998] T. Sugahara, H. Sato, M. Hao, Y. Naoi, S. Kurai, and S. Tottori, K. Yamashita, K. Nishino, L. T. Romano, and S. Sakai, "Direct Evidence

that Dislocations are Non-Radiative Recombination Centers in GaN," *Jpn. J. Appl. Phys.*, vol. 37, p. 398, 1998.

[Singh, 1997] R. Singh, D. Doppalapudi, T. D. Moustakas, and L. T. Romano, "Phase separation in InGaN thick films and formation of InGaN/GaN double heterostructures in the entire alloy composition," *Appl. Phys. Lett.*, vol. 70, no. 9, p. 1089, 1997.

[Skriver, 1992] H.L. Skriver, N. M. Rosengaard, "surface energy and work function of elemental metals", *Phys. Rew. B*, vol. 46, no. 11, p. 7157, 1992.

[Smalc, 2010] J. Smalc-Koziorowska, S. Grzanka, E. Litwin-Staszewska, R. Piotrzkowski, G. Nowak, M. Leszczynski, P. Perlin, E. Talik, J. Kozubowski, and S. Krukowski, "Ni–Au contacts to p-type GaN – Structure and properties," *Solid. State. Electron.*, vol. 54, no. 7, pp. 701–709, Jul. 2010.

[Smith, 1996] L. L. Smith, S. W. King, R. J. Nemanich, R. F. Davis, "Cleaning of GaN surface," *J. Elec. Mat.*, vol. 25, no. 5, p. 805, 1996.

[Steigerwald, 1997] D. Steigerwald, S. Rudaz, H. Liu, R. S. Kern, W. Götz, and R. Fletcher, "III–V Nitride semiconductors for high-performance blue and green light-emitting devices," *JOM*, vol. 49, no. 9, pp. 18–23, Sep. 1997.

[Sugiura, 1998] L. Sugiura, M. Suzuki, and J. Nishio, "p-type conduction in as-grown Mg-doped GaN grown by metalorganic chemical vapor deposition," *Appl. Phys. Lett.*, vol. 72, no. 14, p. 1748, 1998.

[Sun, 2011] G. Sun, G. Xu, Y. J. Ding, H. Zhao, G. Liu, J. Zhang, and N. Tansu, "Investigation of fast and slow decays in InGaN/GaN quantum wells," *Appl. Phys. Lett.*, vol. 99, no. 8, p. 081104, 2011.

[Sun, PhD thesis] Y.-J. Sun, "Growth and characterization of m-plane GaN and (In,Ga)N/GaN multiple quantum wells," 2004.

[Svensk, 2007] O. Svensk, S. Suihkonen, T. Lang, H. Lipsanen, M. Sopanen, M. a. Odnoblyudov, and V. E. Bougrov, "Effect of growth conditions on electrical properties of Mg-doped p-GaN," *J. Cryst. Growth*, vol. 298, pp. 811–814, Jan. 2007.

[Takeuchi, 1997] T. Takeuchi, S. Sota, M. Katsuragawa, M. Komori, H. Takeuchi, H. Amano, and I. Akasaki, "Quantum-Confined Stark Effect due to Piezoelectric Fields in GaInN Strained Quantum Wells," *Jpn. J. Appl. Phys.*, vol. 36, p.382, 1997.

[Takeuchi, 1998] T. Takeuchi, C. Wetzel, S. Yamaguchi, H. Sakai, H. Amano, I. Akasaki, Y. Kaneko, S. Nakagawa, Y. Yamaoka, and N. Yamada, "Determination of piezoelectric fields in strained GaInN quantum wells using the quantum-confined Stark effect," *Appl. Phys. Lett.*, vol. 73, no. 12, p. 1691, 1998.

[Thierry, PhD thesis] N. Thierry-Jebli, "Caractérisation et modélisation physique de contacts entre phases métalliques et Nitrure de Gallium semi-conducteur," 2012.

[Toledo, 2012] N. G. Toledo, D. J. Friedman, R. M. Farrell, E. E. Perl, C.-T. (Tony) Lin, J. E. Bowers, J. S. Speck, and U. K. Mishra, "Design of integrated III-nitride/non-III-nitride tandem photovoltaic devices," *J. Appl. Phys.*, vol. 111, no. 5, p. 054503, 2012.

[Tsai, 2010] C.-L. Tsai, G.-S. Liu, G.-C. Fan, and Y.-S. Lee, "Substrate-free large gap InGaN solar cells with bottom reflector," *Solid. State. Electron.*, vol. 54, no. 5, pp. 541–544, May 2010.

[Tuna, 2013] O. Tuna, H. Hahn, H. Kalisch, G. Ciesen, A. Vescan, M. V. Rzheutcki, V. N. Pavlovskii, E. V. Lutsenko, G. P. Yablonskii, and M. Heuken,

"MOVPE growth, optical and electrical characterization of thick Mg-doped InGaN layers," *J. Cryst. Growth*, vol. 370, p. 2, 2013.

[Tuomisto, 2005] F. Tuomisto, K. Saarinen, B. Lucznik, I. Grzegory, H. Teisseyre, T. Suski, S. Porowski, P. R. Hageman, and J. Likonen, "Effect of growth polarity on vacancy defect and impurity incorporation in dislocation-free GaN," *Appl. Phys. Lett.*, vol. 86, no. 3, p. 031915, 2005.

[Valdueza, 2013] S. Valdueza-Felip, A. Mukhtarova, Q. Pan, G. Altamura, L. Grenet, C. Durand, C. Bougerol, D. Peyrade, F. Gonzalez-Posada, J. Eymery, and E. Monroy, "Photovoltaic response of InGaN/GaN multiple-quantum well solar cells," *Jpn. J. of Appl. Phys.*, vol. 52, p. 08JH05, 2013.

[Valdueza, 2014] S. Valdueza-Felip, A. Mukhtarova, L. Grenet, C. Bougerol, C. Durand, J. Eymery, and E. Monroy, "Improved conversion efficiency of as-grown InGaN/GaN quantum-well solar cells for hybrid integration," *Appl. Phys. Express*, vol. 7, p. 032301, 2014.

[Varshni, 1967] P. Varshni, "Temperature dependence of the energy gap in semiconductors," *Physica*, vol. 34, no. 1, pp. 2–7, 1967.

[Vegard, 1921] L. Vegard, Die *Konstitution der Mischkristalle und die Raumfullung der Atome*, Zeitschrift fur Physik, 5, 17, 1921.

[Vickers, 2003] M. E. Vickers, M. J. Kappers, T. M. Smeeton, E. J. Thrush, J. S. Barnard, and C. J. Humphreys, "Determination of the indium content and layer thicknesses in InGaN/GaN quantum wells by x-ray scattering," *J. Appl. Phys.*, vol. 94, no. 3, p. 1565, 2003.

[Vurgaftman, 2003] I. Vurgaftman and J. R. Meyer, "Band parameters for nitrogen-containing semiconductors," *J. Appl. Phys.*, vol. 94, no. 6, p. 3675, 2003.

[Wang, 2012] H. Wang, Z. Ji, S. Qu, G. Wang, Y. Jiang, B. Liu, X. Xu, and H. Mino, "Influence of excitation power and temperature on photoluminescence in InGaN/GaN multiple quantum wells.," *Opt. Express*, vol. 20, no. 4, pp. 3932–40, Feb. 2012.

[Watanabe, 2012] N. Watanabe, H. Yokoyama, N. Shigekawa, K. Sugita, and A. Yamamoto, "Barrier Thickness Dependence of Photovoltaic Characteristics of InGaN / GaN Multiple Quantum Well Solar Cells," *Jpn. J. of Appl. Phys.* 51, p. 10ND10, 2012.

[Wee, 2014] D. Wee, PhD thesis "Characterization of the minority carrier diffusion length using the photocurrent technique in extrinsically doped GaN", 2014.

[Wen, 2007] X. Wen, J. A. Davis, L. Van Dao, P. Hannaford, V. A. Coleman, H. H. Tan, C. Jagadish, K. Koike, S. Sasa, M. Inoue, and M. Yano, "Temperature dependent photoluminescence in oxygen ion implanted and rapid thermally annealed ZnO/ZnMgO multiple quantum wells," *Appl. Phys. Lett.*, vol. 90, no. 22, p. 221914, 2007.

[Wetzel, 1998] C. Wetzel, T. Takeuchi, S. Yamaguchi, H. Katoh, H. Amano, and I. Akasaki, "Optical band gap in $Ga_{1-x}In_xN(0<x<0.2)$ on GaN by photoreflection spectroscopy," *Appl. Phys. Lett.*, vol. 73, no. 14, p. 1994, 1998.

[Weyher, 2000] J. L. Weyher, P. D. Brown, J. L. Rouvie, T. Wosinski, A. R. A. Zauner, and I. Grzegory, "Recent advances in defect-selective etching of GaN," *J. of Cryst. Growth*, vol. 210, pp. 151–156, 2000.

[Wierer, 2010] J. J. Wierer, a. J. Fischer, and D. D. Koleske, "The impact of piezoelectric polarization and nonradiative recombination on the performance of (0001) face GaN/InGaN photovoltaic devices," *Appl. Phys. Lett.*, vol. 96, no. 5, p. 051107, 2010.

[Wierer, 2012] J. J. Wierer, D. D. Koleske, and S. R. Lee, "Influence of barrier thickness on the performance of InGaN/GaN multiple quantum well solar cells," *Appl. Phys. Lett.*, vol. 100, no. 11, p. 111119, 2012.

[Wright, 1997] A. F. Wright, "Elastic properties of zinc-blende and wurtzite AlN, GaN, and InN," *J. Appl. Phys.*, vol. 82, p. 2833, 1997.

[Wu, 2002] J. Wu, W. Walukiewicz, K. M. Yu, J. W. Ager, E. E. Haller, H. Lu, and W. J. Schaff, "Small band gap bowing in In_{1-x} Ga_xN alloys," *Appl. Phys. Lett.*, vol. 80, no. 25, p. 4741, 2002.

[Wu, 2003] J. Wu, W. Walukiewicz, K. M. Yu, W. Shan, J. W. Ager, E. E. Haller, H. Lu, W. J. Schaff, W. K. Metzger, and S. Kurtz, "Superior radiation resistance of $In_{1-x}Ga_xN$ alloys: Full-solar-spectrum photovoltaic material system," *J. Appl. Phys.*, vol. 94, no. 10, p. 6477, 2003.

[Wu, 2006] G. M. Wu and Y. L. Kao, "Defect structures in InGaN / GaN multiple quantum wells on Si (111) substrates," *Journal of achievements in materials and manufacturing engineering*, vol. 18, no. 1, pp. 195–198, 2006.

[Yamamoto, 2008] A. Yamamoto, K. Sugita, M. Horie, Y. Ohmura, Md. R. Islam, and A. Hashimoto, "Mg-doping and N^+-P junction formation in MOVPE-grown $In_xGa_{1-x}N$ (x~0.4)," *33rd IEEE Photovoltaic Specialists Conf.*, San Diego, CA, May, 12-16, 2008.

[Yamamoto, 2014] A. Yamamoto, T. Hasan, A. Mihara, N. Narita, and N. Shigekawa, "Phase separation of thick (~1µm) $In_xGa_{1-x}N$ (x~0.3) grown on AlN/Si(111): Simultaneous emergence of metallic In–Ga and GaN-rich InGaN," *Appl. Phys. Exp.*, vol. 7, p. 035502, 2014.

[Yang, 2010] C. C. Yang, J. K. Sheu, X.-W. Liang, M.-S. Huang, M. L. Lee, K. H. Chang, S. J. Tu, F.-W. Huang, and W. C. Lai, "Enhancement of the conversion efficiency of GaN-based photovoltaic devices with AlGaN/InGaN absorption layers," *Appl. Phys. Lett.*, vol. 97, no. 2, p. 021113, 2010.

[Young, 2013] N. G. Young, R. M. Farrell, Y. L. Hu, Y. Terao, M. Iza, S. Keller, S. P. DenBaars, S. Nakamura, and J. S. Speck, "High performance thin quantum barrier InGaN/GaN solar cells on sapphire and bulk (0001) GaN substrates," *Appl. Phys. Lett.*, vol. 103, no. 17, p. 173903, 2013.

[Young, 2014] N. G. Young, E. E. Perl, R. M. Farrell, M. Iza, S. Keller, J. E. Bowers, S. Nakamura, S. P. DenBaars, and J. S. Speck, "High-performance broadband optical coatings on InGaN/GaN for multijunction device integration," *Appl. Phys. Lett.*, vol. 104, p. 163902, 2014.

[Zeng, 2009] S. W. Zeng, B. P. Zhang, J. W. Sun, J. F. Cai, C. Chen, and J. Z. Yu, "Substantial photo-response of InGaN p–i–n homojunction solar cells," *Semicond. Sci. Technol.*, vol. 24, no. 5, p. 055009, May 2009.

[Zeman] M. Zeman, Cours of lections "Solar cells", Delft University of Technology.

[Zhang, 2013] Z.-H. Zhang, S. Tiam Tan, Z. Kyaw, W. Liu, Y. Ji, Z. Ju, X. Zhang, X. Wei Sun, and H. Volkan Demir, "p-doping-free InGaN/GaN light-

emitting diode driven by three-dimensional hole gas," *Appl. Phys. Lett.*, vol. 103, no. 26, p. 263501, Dec. 2013.

[Zheng, 2008] X. Zheng, R.-H. Horng, D.-S. Wuu, M.-T. Chu, W.-Y. Liao, M.-H. Wu, R.-M. Lin, and Y.-C. Lu, "High-quality InGaN/GaN heterojunctions and their photovoltaic effects," *Appl. Phys. Lett.*, vol. 93, no. 26, p. 261108, 2008.

[Zhihao, 2009] X. Zhihao, Z. Jincheng, D. Huantao, Z. Zhongfen, Z. Qingwei, X. Hao, and H. Yue, "Stress, structural and electrical properties of Si-doped GaN film grown by MOCVD," *J. Semicond.*, vol. 30, no. 12, p. 123003, Dec. 2009.

[Zhu, 2009] D. Zhu, J. Xu, A. N. Noemaun, J. K. Kim, E. F. Schubert, M. H. Crawford, and D. D. Koleske, "The origin of the high diode-ideality factors in GaInN/GaN multiple quantum well light-emitting diodes," *Appl. Phys. Lett.*, vol. 94, no. 8, p. 081113, 2009.

In this work we report on epitaxial growth and characterization of InGaN/GaN multi-quantum wells (MQWs) heterostructures for application in photovoltaic devices. The samples were grown by metal-organic vapor phase epitaxy (MOVPE) on (0001) sapphire substrate. The structural and optical characterization is performed by X-ray diffraction, transmission electron microscopy, photoluminescence spectroscopy and transmission measurements. To investigate the presence of photovoltaic effect and estimate the electrical performance of the samples, they were processed into solar cells by means of the photolithography, inductively coupled plasma reactive-ion etching and metallization to manage n and p contacts.

We studied the influence of different InGaN/GaN active region designs on the structural, optical and electrical properties of the samples, i.e. number of InGaN quantum wells, QW and quantum barrier thicknesses and indium composition in the wells. Two main mechanisms have to be taken into account for an efficient optimization of photovoltaic devices: photon absorption and carrier collection. We showed that an increase of the MQWs number, their thickness and the In-content allows absorption improvement, but causes losses in the carrier collection efficiency due to: the increase of the active region thickness (lower electric field), the difficulty of the carrier to escape from deeper QWs and the strain relaxation (structural defect creation). The decrease of the barrier thickness can solve the first two issues, but the problem with strain relaxation remains. In the best design, we report the value of 2.00% of conversion efficiency for $15\times In_{0.18}Ga_{0.82}N/GaN$ samples with spectral response extending to 465 nm.
Keywords: InGaN/GaN, quantum well, MOVPE, solar cell.

Ce travail traite de la croissance épitaxiale et de la caractérisation d'hétérostructures à base de multi-puits quantiques (MPQ) pour des applications dans le photovoltaïque. Les échantillons ont été obtenus par la technique d'épitaxie en phase vapeur aux organo-métalliques (EPVOM) sur des substrats de saphir (0001). La caractérisation structurale et optique est réalisée par diffraction de rayons X, microscopie électronique en transmission, spectroscopie de photoluminescence et de transmission. Pour étudier la présence de l'effet photovoltaïque et pour estimer la performance électrique des échantillons, les MPQ ont été intégrés dans la géométrie de cellules solaires en utilisant de la photolithographie, des attaques réactives ioniques assistées par plasma inductif et des métallisations pour contacter les parties dopées n et p.

Nous avons étudié l'influence de différents designs des régions actives InGaN/GaN sur les propriétés optiques et électriques des échantillons, c'est-à-dire le nombre de puits quantiques InGaN, les épaisseurs des puits et des barrières et la composition en indium dans les puits. Deux mécanismes principaux doivent être pris en compte pour une optimisation efficace de composants photovoltaïques: l'absorption des photons et la collections des porteurs. Nous avons montré qu'une augmentation du nombre de MPQ, de leur épaisseur et de la composition d'In améliorait l'absorption, mais causait aussi des pertes dans l'efficacité de collection du fait de l'augmentation de l'épaisseur de la couche active (champ électrique plus faible), de la difficulté des porteurs pour s'échapper de puits plus profonds et de relaxation des contraintes (création de défauts structuraux). La décroissance de l'épaisseur des barrières peut résoudre les deux premiers points, mais le problème de la relaxation de la contrainte reste entier. Pour notre meilleur design, nous obtenons une efficacité de conversion de 2 % pour des couches $15\times In_{0.18}Ga_{0.82}N/GaN$ qui ont une réponse spectrale qui s'étend jusqu'à 465 nm.
Mots clés: InGaN/GaN, puits quantiques, EPVOM, cellules solaires.